

The background of the entire page is a dramatic, apocalyptic landscape. A massive, intense fire burns across the horizon, sending thick, dark smoke billowing into a sky filled with orange and yellow light. In the foreground, a herd of cattle and sheep stands on a dry, brownish field, looking towards the viewer. The scene conveys a sense of environmental crisis and extreme weather events.

EXPLAINING EXTREME EVENTS OF 2017

From A Climate Perspective

Special Supplement to the
Bulletin of the American Meteorological Society
Vol. 100, No. 1, January 2019

EXPLAINING EXTREME EVENTS OF 2017 FROM A CLIMATE PERSPECTIVE

Editors

Stephanie C. Herring, Nikolaos Christidis, Andrew Hoell,
Martin P. Hoerling, and Peter A. Stott

Special Supplement to the

Bulletin of the American Meteorological Society

Vol. 100, No. 1, January 2019

AMERICAN METEOROLOGICAL SOCIETY

CORRESPONDING EDITOR:

Stephanie C. Herring, PhD
NOAA National Centers for Environmental Information
325 Broadway, E/CC23, Rm 1B-131
Boulder, CO, 80305-3328
E-mail: stephanie.herring@noaa.gov

COVER CREDIT:

©Dean Sewell/Fairfax Syndication—Sir Ivan Bushfire, February 2017. A bushfire that started near Leadvill, east of Duneedoo in the New South Wales (NSW) Central tablelands, ripped through bush and grasslands in a day that NSW fire authorities classified as catastrophic. Sheep and cattle maneuver around a dam to avoid a fast running bushfire as the fire front moved east. Photograph by Dean Sewell/Oculi.

HOW TO CITE THIS DOCUMENT

Citing the complete report:

Herring, S. C., N. Christidis, A. Hoell, M. P. Hoerling, and P. A. Stott, Eds., 2019: Explaining Extreme Events of 2017 from a Climate Perspective. *Bull. Amer. Meteor. Soc.*, **100** (1), S1–S117, <https://doi.org/10.1175/BAMS-ExplainingExtremeEvents2017.1>.

Citing a section (example):

Hope, P., M. T. Black, E.-P. Lim, A. Dowdy, G. Wang, A. S. Pepler, and R. J. B. Fawcett, 2019: On determining the impact of increasing atmospheric CO₂ on the record fire weather in eastern Australia in February 2017 [in “Explaining Extremes of 2017 from a Climate Perspective”]. *Bull. Amer. Meteor. Soc.*, **100** (1), S111–S117, <https://doi.org/10.1175/BAMS-D-18-0135.1>.

TABLE OF CONTENTS

1. Introduction to Explaining Extreme Events of 2017 from a Climate Perspective.....	S1
2. Actuaries are Paying Attention to Climate Data	S5
3. Hydroclimatic Extremes as Challenges for the Water Management Community: Lessons from Oroville Dam and Hurricane Harvey	S9
4. Observations of the Rate and Acceleration of Global Mean Sea Level Change	S15
5. Anthropogenic Contributions to the Intensity of the 2017 United States Northern Great Plains Drought.....	S19
6. Attribution of the 2017 Northern High Plains Drought	S25
7. The Extremely Wet March of 2017 in Peru.....	S31
8. Contribution of Anthropogenic Climate Change to April–May 2017 Heavy Precipitation over the Uruguay River Basin.....	S37
9. December 2016: Linking the Lowest Arctic Sea-Ice Extent on Record with the Lowest European Precipitation Event on Record	S43
10. The Exceptional Summer Heat Wave in Southern Europe 2017	S49
11. Examining the Potential Contributions of Extreme “Western V” Sea Surface Temperatures to the 2017 March–June East African Drought	S55
12. Risks of Pre-Monsoon Extreme Rainfall Events of Bangladesh: Is Anthropogenic Climate Change Playing a Role?	S61
13. The Effects of Natural Variability and Climate Change on the Record Low Sunshine over Japan during August 2017	S67
14. Anthropogenic Contribution to 2017 Earliest Summer Onset in South Korea	S73
15. Anthropogenic Influence on the Heaviest June Precipitation in Southeastern China since 1961	S79
16. Attribution of the Persistent Spring–Summer Hot and Dry Extremes over Northeast China in 2017.....	S85
17. Anthropogenic Warming has Substantially Increased the Likelihood of July 2017–Like Heat Waves over Central Eastern China	S91
18. Attribution of a Record-Breaking Heatwave Event in Summer 2017 over the Yangtze River Delta.....	S97
19. The Role of Natural Variability and Anthropogenic Climate Change in the 2017/18 Tasman Sea Marine Heatwave.....	S105
20. On Determining the Impact of Increasing Atmospheric CO ₂ on the Record Fire Weather in Eastern Australia in February 2017	S111

INTRODUCTION TO EXPLAINING EXTREME EVENTS OF 2017 FROM A CLIMATE PERSPECTIVE

STEPHANIE C. HERRING, NIKOLAOS CHRISTIDIS, ANDREW HOELL, MARTY HOERLING, AND PETER A. STOTT

This year's report includes climate change attribution assessments of seventeen different extreme events from around the world during 2017 (Table S1) and once again illustrates that both terrestrial and oceanic heat events are becoming more frequent and intense as a consequence of human-induced climate change. For example, climate change increased the odds at least threefold since 1950 of a heat wave like the one that impacted southern Europe (Kew et al. 2019). The November 2017/18 Tasman Sea marine heatwave was found to be virtually impossible without anthropogenic influence (Perkins-Kirkpatrick et al. 2019). Ocean heat events have wide-ranging impacts; for example, warm sea surface temperatures in the west Pacific Ocean, which were found to not be possible without human-caused climate change, doubled the probability of African drought, which contributed to food insecurity (Funk et al. 2008). These results continue to build the body of evidence that the oceans experience extreme heat events and the heat events in turn drive extreme events on land.

On land, analyses of drought events continues to illustrate the nuanced way in which climate change can impact the drivers of an extreme event. Two independent studies using different methodological approaches found that the 2017 U.S. northern Great Plains drought was made more intense due to long-term soil moisture decreases resulting from anthropogenically forced increases in evapotranspiration and temperature (Hoell et al. 2019; Wang et al. 2019).

Those studies, however, found that climate change has not reduced the overall amount of precipitation during spring and summer over the northern Great Plains, normally the rainiest time of the year in that region.

In addition to the usual analyses of specific events found in this report, the editors also wanted to further explore the relevance of climate change attribution science to decision support. This year, several Perspective pieces illustrate how attribution results are relevant across a broad range of sectors that incorporate information on extreme events. This ranges from those looking to the future to address changing risk exposure, as well as looking towards the past to understand what caused an event and, potentially, to determine who was responsible for it.

In the articles *Actuaries are Paying Attention to Climate Data* (Owen 2019) and *Hydroclimatic Extremes as Challenges for the Water Management Community: Lessons from Oroville Dam and Hurricane Harvey* (Vano et al. 2019), the authors explore how attribution results are relevant in a risk management context. In Owen's article, written from her experience as both a professional actuary and researcher with the Society of Actuaries, Owen notes that "the actuarial profession is responding strongly to the challenges presented with climate change." She points to the Actuaries Climate Index (<http://actuariesclimateindex.org/home/>), which was the result of the combined effort of the four major actuarial organizations in North America. As the impacts of climate change continue to have financial consequences, actuaries are increasingly asking "What does the future look like for the financial risks associated with climate change?" An interesting point from Owen's article is her observation that for those actuarial decisions that have consequences over long time periods even "small deviations from estimations of future costs have considerable financial consequences." Thus, when considering the impacts of climate change on extremes understanding how that risk might change in the future can significantly impact predicted risk exposure.

Vano and coauthors are members of the AMS Water Resources Committee and author backgrounds

AFFILIATIONS: HERRING—NOAA/National Centers for Environmental Information, Boulder, Colorado; HOELL AND HOERLING—NOAA/Earth System Research Laboratory, Physical Sciences Division, Boulder, Colorado; CHRISTIDIS AND STOTT—Met Office Hadley Centre, Exeter, United Kingdom, and University of Exeter, Exeter, United Kingdom

CORRESPONDING AUTHOR: Stephanie Herring, stephanie.herring@noaa.gov

DOI:10.1175/BAMS-D-18-0307.1

© 2019 American Meteorological Society

For information regarding reuse of this content and general copyright information, consult the [AMS Copyright Policy](#).

	ANTHROPOGENIC INFLUENCE ON EVENT			METHOD USED	Total Events
	INCREASE	DECREASE	NOT FOUND or UNCERTAIN		
Heat	Ch 11: Southern Europe Ch 18: China Ch 19: China			Ch 11: weather@home, EC-Earth, HadGEM-3A, and EURO-CORDEX Ch 18: HadGEM3-GA6-N216 Ch 19: CMIP5	3
Heat & Dryness	Ch 17: China			Ch 17: CMIP5	1
Marine Heat	Ch 20: Tasman Sea Ch 12: East Africa			Ch 20: CESM1, CMIP5 Ch 12: CESM1, CMIP5	2
Heavy Precipitation	Ch 8: Peru Ch 9: Uruguay Ch 10: Western Europe Ch 13: Bangladesh Ch 16: China			Ch 8: HadGEM3-A Ch 9: HadGEM3-A Ch 10: EC-Earth3 in forecast mode Ch 13: weather@home HadRM3P RCM nested in the global atmosphere-only HadAM3P Ch 16: CanESM2	5
Drought	Ch 6: U.S. Northern Plains Ch 7: U.S. Northern Plains Ch 12: East Africa			Ch 6: CESM Ch 7: AMIP GEOS-5 Ch 12: CESM 1, CMIP5	3
Fire Season	Ch 15: South Korea		Ch 21: Australia	Ch 21: McArthur Forest Fire Danger Index (FFDI) and seasonal forecast model, POAMA2	1
Seasonal Changes				Ch 15: weather@home East Asia project, CMIP5	1
Poor Sunshine	Ch 14: Japan			Ch 14: MIROC5, CMIP5	1
Total Events	16		1		17

Acronyms:

AMIP: Atmospheric Model Intercomparison Project
 CAM: Community Atmosphere Model
 CanESM: Canadian Earth System Model
 CESM: Community Earth System Model, www.cesm.ucar.edu/
 CMIP: Coupled Model Intercomparison Project
 EURO-CORDEX: Coordinated Downscaling Experiment—European Domain

GEOS: Goddard Earth Observing System Model
 HadAM: Hadley Center Atmospheric General Circulation Model
 HadGEM: Hadley Centre Global Environmental Model
 MIROC: Model for Interdisciplinary Research on Climate
 POAMA: Predictive Ocean Atmosphere Model for Australia
 Weather@Home: www.climateprediction.net/weatherathome/

include government and academic researchers and consulting and municipal engineers. They used case studies of the Oroville Dam and New Don Pedro incidents and flooding from Hurricane Harvey to explore concerns and questions water managers confronted, and then “list some lessons those experiences offered about framing attribution studies to serve management needs.” One lesson they identified as important is to more clearly address the duration characteristics of precipitation events. For example, most attribution papers tend to deal with the amount of rain that has fallen over a particular period, and less frequently explore whether the duration of rain events is changing. Vano and colleagues are encouraging the attribution community to explore this duration question because of the relevance to water resource managers.

Also, Marjanac et al. (2018) assess the role attribution science could play in a range of legal challenges that could be classed as ‘climate change litigation’. They conclude that attribution scientists need to communicate probabilistic findings in a way that is accessible for decision-makers who work to differing standards of proof. They also highlight a need for the insurance industry to take account of changing climate when drawing up their catastrophe models for commercial use.

LOOKING AHEAD. This annual special edition of the *Bulletin of the American Meteorological Society* is now in its seventh year, and over this time has seen explosive growth in the field of event attribution. In the first year the editors managed to recruit six papers, which at the time seemed like an extraordinary success (Peterson et al. 2012). All the papers either dealt with temperature or precipitation, or the combination of the two factors in impacting drought. Today, the report is being published in a new landscape of attribution research that involves a much broader range of scientists, methodologies, and event types. In addition, numerous attribution papers are now being published much closer to the occurrence of the event itself, especially for high-impact events such as Hurricane Harvey (Emanuel 2017; van Oldenborgh et al. 2017; Risser and Wehner 2017). Increasingly attribution research is being done using initialized forecast systems, and there is a move toward real-time release of attribution results (www.nature.com/articles/d41586-018-05849-9). This leads to the question of the role this report has within the attribution community going forward.

The original motivation of this report was twofold. One goal was to support the attribution research community by providing a place to look across event

types and methodological approaches and explore what works, and where improvements can be made. It was always meant as a tool to advance the science and increase its relevancy, with a mission larger than the examination of any single event. The second driver was to improve communication and understanding of attribution results not only to the public, but to other sectors that will hopefully integrate attribution results into their decision making. This communication driver was the motivation behind making these reports 1,500 words and “readable” to an external audience. These two original reasons remain the primary focus of this report, and in next year’s report we will continue to look for papers on individual events while using this platform to advance the overall research. For example, we will continue to include Perspective pieces that provide the attribution community with feedback from other sectors to help shape and drive research relevancy. In addition, the editors will be looking to synthesize research from across events and methodological approaches to assess broader human-caused changes in the earth system that drive extreme events. At the same time, the outreach and communication effort will continue as we work to not only expand the scope of who and how attribution research is utilized, but also promote informed discourse around how human-caused climate change is impacting extreme events. The editors welcome comments and feedback from both readers and contributors on how this report can continue to advance the science and adaptation response to climate change impacts on extremes. We look forward to embarking on this in partnership with the attribution community, and with those who use the results of attribution research.

REFERENCES

- Emanuel, K., 2017: Assessing the present and future probability of Hurricane Harvey’s rainfall. *Proc. Natl. Acad. Sci. USA*, **114**, 12 681–12 684, <https://doi.org/10.1073/pnas.1716222114>.
- Funk, C., and Coauthors, 2019: Examining the potential contributions of extreme ‘Western V’ sea surface temperatures to the 2017 March–June East African drought [in “Explaining Extremes of 2017 from a Climate Perspective”]. *Bull. Amer. Meteor. Soc.*, **100** (1), S55–S60, <https://doi.org/10.1175/BAMS-D-18-0108.1>.
- Hoell, A., J. Perlwitz, C. Dewes, K. Wolter, I. Rangwala, X.-W. Quan, and J. Eischeid, 2019: Anthropogenic contributions to the intensity of the 2017 United States northern Great Plains drought [in “Explaining Extremes of 2017 from a Climate Perspective”].

- Bull. Amer. Meteor. Soc.*, **100** (1), S19–S24, <https://doi.org/10.1175/BAMS-D-18-0127.1>.
- Kew, S. F., S. Y. Philip, G. J. van Oldenborgh, F. E. L. Otto, R. Vautard, and G. van der Schrier, 2019: Attribution study of the exceptional summer heatwave in southern Europe 2017 [in “Explaining Extremes of 2017 from a Climate Perspective”]. *Bull. Amer. Meteor. Soc.*, **100** (1), S49–S53, <https://doi.org/10.1175/BAMS-D-18-0109.1>.
- Owen, R., 2019: Actuaries are paying attention to climate data [in “Explaining Extremes of 2017 from a Climate Perspective”]. *Bull. Amer. Meteor. Soc.*, **100** (1), S5–S8, <https://doi.org/10.1175/BAMS-D-18-0293.1>.
- Peterson, T. C., P. A. Stott, and S. Herring, 2012: Explaining Extreme Events of 2011 from a Climate Perspective. *Bull. Amer. Meteor. Soc.*, **93**, 1041–1067, <https://doi.org/10.1175/BAMS-D-12-00021.1>.
- Risser, M., and M. Wehner, 2017: Attributable human-induced changes in the likelihood and magnitude of the observed extreme precipitation during Hurricane Harvey. *Geophys. Res. Lett.*, **44**, 12 457–12 464, <https://doi.org/10.1002/2017GL075888>.
- van Oldenborgh, G. J., and Coauthors, 2017: Attribution of extreme rainfall from Hurricane Harvey, August 2017. *Environ. Res. Lett.*, **12**, 124009, <https://doi.org/10.1088/1748-9326/aa9ef2>.
- Vano, J. A., M. D. Dettinger, R. Cifelli, D. Curtis, A. Dufour, K. Miller, J. R. Olsen, and A. M. Wilson, 2019: Hydroclimatic extremes as challenges for the water management community: Lessons from Oroville Dam and Hurricane Harvey [in “Explaining Extremes of 2017 from a Climate Perspective”]. *Bull. Amer. Meteor. Soc.*, **100** (1), S9–S14, <https://doi.org/10.1175/BAMS-D-18-0219.1>.
- Wang, H., S. D. Schubert, R. D. Koster, and Y. Chang, 2019: Attribution of the 2017 northern high plains drought [in “Explaining Extremes of 2017 from a Climate Perspective”]. *Bull. Amer. Meteor. Soc.*, **100** (1), S25–S29, <https://doi.org/10.1175/BAMS-D-18-0115.1>.

ACTUARIES ARE PAYING ATTENTION TO CLIMATE DATA

REBECCA OWEN

Imagine it is July in a city in the upper Midwestern United States. Usually it is hot and muggy in the summer, with bugs flying and the lush greenery steaming. But this week the temperatures have soared far above the usual high 80s, and the nights bring no relief. Day after day triple-digit heat leaves most everyone limp and tired. But for some people, the heat is more than just a tiresome nuisance; it is life threatening. The city has a large low-income elderly population, with a large percentage suffering from chronic obstructive pulmonary disease, diabetes, congestive heart failure, and kidney disease. Their old houses and apartments do not have functioning air-conditioning and they are reluctant to go outside or to ask for help. The heat wave is life threatening for them and they have few resources and amenities to cope with the heat stress. The hospitals that serve them are stretched to capacity normally; now the emergency rooms need to turn away ambulances and there are no more vacant beds for patients in extremis. The euphemism for the result is “increased morbidity and mortality due to heat-related causes.” The blunt statement is that the heat is making people very sick or even killing them. This is of course, not a far-fetched scenario, since we have read the news stories including from Chicago, Paris, and Sydney. Nor are scenarios featuring floods in the Southeast or tornados in Oklahoma or drought-exacerbated fire in the West. These events are all driven by climate, and in a world where the climate is changing, so is the risk of any of these scenarios occurring. In this article I provide an overview of how and why actuaries assess various risks, and the role a changing climate can have in those calculations. For climate scientists, I hope this provides insight into how event attribution research can be relevant to actuaries. In addition, for other actuaries I hope this article will contribute to

an awareness as to why considering climate change, and research such as extreme event attribution, is important for our profession to effectively finance future risk.

WHY IS IT IMPORTANT FOR ACTUARIES TO BE AWARE OF RISKS ASSOCIATED WITH CLIMATE CHANGE IN THEIR PROFESSIONAL CAPACITY?

For years actuaries have used the motto “risk is opportunity” to describe the ways that their analytic techniques offer our clients and employer’s ways to offset, hedge, or exploit risk to their advantage. But not all risk is good, especially when the risk contemplated involves financial or personal harm to a large portion of our population, risk that can only be mitigated and not avoided. Insurance helps all of us face and finance this risk.

The actuarial profession is more diverse than most people realize and nearly all actuaries pick a specialty and confine their practice to areas in which they have specific experience. There are many kinds of actuaries and each looks at different types of risk, and at risk across different time scales. For example, some look at property and casualty risk, such as crop insurance or flood insurance. Most people are familiar with this through auto or homeowner’s insurance policies. These policies often look in the short term for issues that have more frequency, but the cost of each event can vary from small to large. Actuaries who work in life insurance, disability, or casualty insurance study a singular or rare life-changing event. The cost of each event is more certain and here the probability of the event is low, so the timing of the event is important. Another kind of actuary works with health insurance, which combines a bit of both short-term and long-term risk, with very large variations in the size of each individual health claim, from a \$2.00 antibiotic prescription to the expense of life-saving multiple organ transplants. Many people will have at least one prescription over a year, while very few will need a new heart and lungs simultaneously. Other actuaries look at the risk associated with financial instruments.

Insurance is a promise that a premium paid today will cover some or all the expense of an unfortuitous

AFFILIATION: OWEN—HCA Solutions, Bend, Oregon

CORRESPONDING AUTHOR: Rebecca Owen,
rebecca@hcasolutions.com

DOI:10.1175/BAMS-D-18-0293.1

© 2019 American Meteorological Society

For information regarding reuse of this content and general copyright information, consult the [AMS Copyright Policy](#).

event happening tomorrow. This means there needs to be enough financial resources available to pay for the event when the event happens, even if the event is far into the future or a rare catastrophic event. Actuaries calculate these premiums. In general, actuaries look backward to think forward, by using historical experience to predict future events. What if the past does not prepare us for a future event? What if the pattern and severity of the variability of these events is changing so much faster than before, so fast that the past, instead of being a guide, will seriously underestimate the future?

To put things in context, here are some basics. There are three components of risk for insured events: the probability the event will occur, the timing of the event, and the distribution of the severity of the expense of the event. When actuaries price for the risk, they take all these things into account. If there is a low likelihood of loss and a predictable outcome, then it is easy to manage the risk. For instance, you do not expect your toaster to stop functioning and the replacement cost is easy to estimate. But other risks are harder to predict and the outcomes much more uncertain. A tornado tearing through a small town leaving devastation in its path is an example of an event that is much less likely to predict with certainty, and the severe consequences are suffered by many residents and business. A consistent feature of actuarial work is the idea that there needs to be a large enough population or group of events to make a consistent and accurate prediction. The impact to the overall financial risk of any component needs to be large enough to make a difference to the total predicted financial picture. Nearly all actuarial work includes a provision for exceptional experience, sometimes using an explicit margin, or in surplus capital, which functions like a rainy-day fund.

Nearly every kind of actuary will have some part of their analysis impacted by climate change and so they are asking the question: What does the future look like for the financial risks associated with climate change and are they different than the experience in the near past? Some climate risk will be absorbed into the actuarial models organically. If the change is gradual, the models will also change gradually and reflect the increased general risk of, for example, higher overall temperatures and drought. However not all change will be as predictable.

An actuary may be pricing with an assumption, based on historical analysis, that 100-yr floods are a rarity, and that only a few houses in a neighborhood will be affected. But what if 100-yr floods are now 20-yr floods or 5-yr floods, and those floods are larger and more damaging than before? And places

that did not flood in years past now begin to flood. Or what if the sea level rises so that flood damage due to tidal shifts can happen even without a severe storm (Jacobs et al. 2018; Sweet et al. 2018)? The U.S. National Climate Assessment has documented some of these changes in precipitation that are already being experienced (Walsh et al. 2014).

An actuary may be examining the risk of interruption of normal business operations. The list of risks sounds like a biblical litany of the apocalypse; fire, flood, pestilence, infrastructure collapse. These losses may be severe, if regional, and the impact may go on for a long time. Storm losses due to hurricanes can take decades to repair, so if big regional storms are larger and more frequent, this is of great concern.

The concept of additional risks from hurricanes, flood, fire and drought to physical structures, crops, infrastructure, or ongoing business may be something we can all imagine, but climate variation does not just bring changes that impact our belongings, dwellings, and infrastructure. It also damages the health and well-being of the population. The author is a health actuary, which means most of the risk models she works with focus on the short term for annual rating. Misunderstanding the role of climate change in any rating cycle may not have implications that reach out for decades, but on the other hand, the size of the health delivery system means that even very small deviations from estimations of future costs have considerable financial consequences. Consider the example in Table S1 that is a generalized financial model that considers an event, such as the Paradise fire, that increases both the cost of care for a person with a chronic disease as well as the prevalence/severity of the chronic disease in a 1-yr period.

For a state with a million Medicaid members this sort of change in average costs and disease severity, something that is conceivable as climate extremes become more frequent, could result in budget shortfalls of hundreds of millions of dollars. For Medicare coverage the risk is even more severe due to the prevalence in the beneficiary population of chronic diseases that are negatively impacted by high temperatures or severe events.

This change in variability comes at the same time as other rapid developments in potential financial chaos, such as global pandemic, the sudden emergence of drug-resistant organisms, or the emergence of expensive therapies. Estimating future costs, even for something as short term as health insurance, is complicated by the variability of climate change, and the financial implications have the potential to be staggering.

TABLE S1. Estimates of annual costs for care: A straw model.

	Total members	Members with complex disease (10% of the population)	All other members
Members	75,000	7,500	67,500
Average monthly cost per member	\$600	\$2,450	\$394
Total annual cost	\$540,000,000	\$220,500,000	\$319,500,000
Suppose the cost of care for the complex 10% is 1% higher than expected			
	Total members	Members with complex disease (10% of the population)	All other members
Members	75,000	7,500	67,500
Average monthly cost per member	\$602	\$2,475	\$394
Total annual cost	\$542,205,000	\$222,705,000	\$319,500,000
Excess annual cost	\$2,205,000		
Suppose further that the percent of the population identified as complex chronic grows by 5%			
	Total members	Members with complex disease (10% of the population)	All other members
Members	75,000	7,875	67,125
Average monthly cost per member	\$613	\$2,475	\$394
Total annual cost	\$551,565,250	\$233,840,250	\$317,725,000
Excess annual cost	\$11,565,250		
	13		
If it were a million people this would translate into			
	\$154,203,333		

HOW IS THE ACTUARIAL PROFESSION RESPONDING?

The actuarial profession is responding to the challenges presented by climate change or, if you must, increased climate variability. The profession may not publish articles or studies in academic journals as much as it folds changes into models to reflect the increased risk to clients and employers based on historical studies. The profession is conservative and carefully studies credible and demonstrated experience before making changes to their models. The studies and changes are unfolding both locally and privately, for specific needs and for the profession as a whole. The effort may be as local as an actuary with a regional-based plan with a specific issue and as broad as international work groups looking at global effects. The Resources and Environment Working Group of the International Actuarial Association has been working to connect actuaries from across the globe working on actuarial aspects of climate change. We are seeing articles appear in actuarial journals that are starting to raise awareness among actuaries (e.g., Hall 2017; Stryker 2018). The Society of Actuaries has also established

a Climate Index Working Group that produced a technical report entitled “Determining the impact of climate change on insurance risk and the global community Phase 1: Key Climate Indicators.”¹

Most of the actuarial profession is privately employed and so much of the body of work is not published, but rather used internally on behalf of clients and employers. Academic actuarial research is very much focused on the development of advanced predictive statistical models; many actuaries are focused on the examination and understanding of the vast amounts of proprietary data used to develop pricing, reserving, trend, and capital models for their insured populations. Actuaries convene for conferences and webinars to discuss observations and changes in practice patterns, but collaboration is often difficult because of the nature of our employment. However, there are concerted efforts across the profession to start integrating the best available climate science into risk assessments. In particular,

¹ www.soa.org/research-reports/2012/research-2012-climate-change-reports/

attribution of specific losses to particular events could be more impactful with access to broader studies over larger populations within a particular type of event such as heat waves or forest fire.

Another example of how the profession is making progress in integrating climate change information is in North America, where the four major actuarial organizations have joined forces to create and maintain the Actuaries Climate Index (ACI; <http://actuariesclimateindex.org/home/>). The climate index was officially launched 30 November 2016, although it was several years in development. The ACI uses six components to create a summary index to measure the relative change in climate measures over history. The components are the frequency of temperatures above the 90th percentile, the frequency of temperatures below the 10th percentile, the maximum rainfall per month of five consecutive days, annual maximum consecutive dry days, the frequency of wind speed above the 90th percentile, and sea level change.

Furthermore, all four organizations—the Canadian Institute of Actuaries, the American Academy of Actuaries, the Casualty Actuarial Society, and the Society of Actuaries—have active committees sponsoring studies, articles, and talks about the role of a changing climate in the actuarial practices to manage financial risk. All of these organizations have devoted sections of their websites to document and discuss what actuaries think about when they are modeling for the variations in weather events including focusing on likelihood of an event, when the event might happen, and the severity of an event, all in the context of financial implications. There are regular presentations to the profession at meetings and in webinars, especially about the ACI.

The profession is beginning to absorb the financial impact of changes in the extent and severity of climate changes as exhibited in losses due to weather extremes and the body of actuarial work on climate is growing rapidly. While some may remain skeptical, losses and statistics will make even the cautious actuary think twice.

REFERENCES

- Hall, R. D., 2017: Defining and understanding climate change for actuaries. *Actuary Mag.*, August/September 2017, <https://theactuarymagazine.org/defining-understanding-climate-change-actuaries/>.
- Jacobs, J. M., L. R. Cattaneo, W. Sweet, and Y. Mansfield, 2018: Recent and future outlooks for nuisance flooding impacts on roadways on the US East Coast. *Transp. Res. Rec.*, March 2018, <https://doi.org/10.1177/0361198118756366>.
- Stryker, R., 2018: Turning up the heat: Understanding the risks and potential implications of a changing climate. *Actuary Mag.*, December 2017/January 2018, <https://theactuarymagazine.org/turning-up-the-heat/>.
- Sweet, W. V., G. Dusek, J. Obeysekera, and J. J. Marra, 2018: Patterns and projections of high tide flooding along the U.S. coastline using a common impact threshold. NOAA Tech. Rep. NOS CO-OPS 086, 44 pp., https://tidesandcurrents.noaa.gov/publications/techrpt86_PaP_of_HTFlooding.pdf.
- Walsh, J., and Coauthors, 2014: Our changing climate. *Climate Change Impacts in the United States: The Third National Climate Assessment*, J. M. Melillo, T. C. Richmond, and G. W. Yohe, Eds., U.S. Global Change Research Program, 19–67, <https://doi.org/10.7930/J0KW5CXT>.

HYDROCLIMATIC EXTREMES AS CHALLENGES FOR THE WATER MANAGEMENT COMMUNITY: LESSONS FROM OROVILLE DAM AND HURRICANE HARVEY

JULIE A. VANO, MICHAEL D. DETTINGER, ROB CIFELLI, DAVID CURTIS, ALEXIS DUFOUR,
KATHLEEN MILLER, J. ROLF OLSEN, AND ANNA M. WILSON

PROBLEM STATEMENT. Record-breaking extreme storms were a hallmark of 2017 in the United States. An extremely wet winter on the West Coast and brutally damaging hurricane season in the U.S. Southeast and the Caribbean challenged communities and power-, water- and flood-management systems in ways that raised climate change concerns. Among the most severe were two periods of heavy precipitation and high runoff that exposed dangerous weaknesses in water management infrastructure and land use practices in California and Texas. In California, a record-breaking string of atmospheric river landfalls and remarkably wet winter conditions came close to causing a catastrophic failure of the emergency spillway at Oroville Dam (France et al. 2018; Abbott 2018; White et al. 2019) and less publicized concerns elsewhere (Holland et al. 2018; CNRFC 2017). In Texas, near record-doubling rainfall accumulations from Hurricane Harvey led to massive flooding (Blake and Zelinsky 2018) and dam safety challenges in Houston (Wax-Thibodeaux et al. 2017). We use these events as examples to ground the concept that attribution studies, with careful management-focused framing, can help water management better navigate such unprecedented extremes.

As members of the AMS Water Resources Committee, we and our contacts include government and academic researchers, and consulting and municipal engineers. We approached this topic by leveraging our collective experiences and expertise regarding the hydroclimatology, meteorology, and hydrology of these events and others like them. We reviewed post-assessment and media reports and had conversations with managers who worked to reduce risks and damages during these events. In this essay, we briefly describe each event, highlighting concerns water managers confronted, and then list some lessons those experiences offered about framing attribution studies to serve management needs.

CASE STUDY: OROVILLE DAM AND NEW DON PEDRO INCIDENTS. On 12 February 2017, the structural integrity of the main and emergency spillways at the Oroville Dam (the tallest dam in the United States) was compromised, prompting an evacuation of nearly 200,000 people in northern California. Although not headlining national news, other California reservoirs were facing similar challenges, including controlled flooding downstream of New Don Pedro Reservoir on the Tuolumne River. Events that led to these incidents involved both hydroclimatic extremes and water management decisions (CNRFC 2017; White et al. 2019), the details of which provide insights into how attribution studies can help water managers.

The series of events that led to Oroville's evacuation began with unusual warmth in October–December 2016, which resulted in high snowlines where larger than normal areas of the upstream catchment received rainfall rather than snowfall. For water managers, this early season snow drought (snowpack in the Sierra Nevada was well below normal by 1 January) was particularly concerning following the extremely dry and snow-poor conditions of the previous five years. Snow droughts confront water managers with a tension between maintaining empty space for flood-management purposes and desire to capture early-season

AFFILIATIONS: VANO AND MILLER—NCAR, Boulder, Colorado; DETTINGER—U.S. Geological Survey, Water Cycle Branch, Carson City, Nevada; CIFELLI—NOAA/ESRL/Physical Sciences Division, Boulder, Colorado; CURTIS—WEST Consultants, Folsom, California; DUFOUR—San Francisco Public Utilities Commission, Water Enterprise, San Francisco, California; OLSEN—Institute for Water Resources, U.S. Army Corps of Engineers, Alexandria, Virginia; WILSON—Center for Western Weather and Water Extremes, Scripps Institution of Oceanography, University of California, San Diego, La Jolla, California

CORRESPONDING AUTHOR: Julie A. Vano, jvano@ucar.edu

DOI:10.1175/BAMS-D-18-0219.1

© 2019 American Meteorological Society

For information regarding reuse of this content and general copyright information, consult the [AMS Copyright Policy](#).

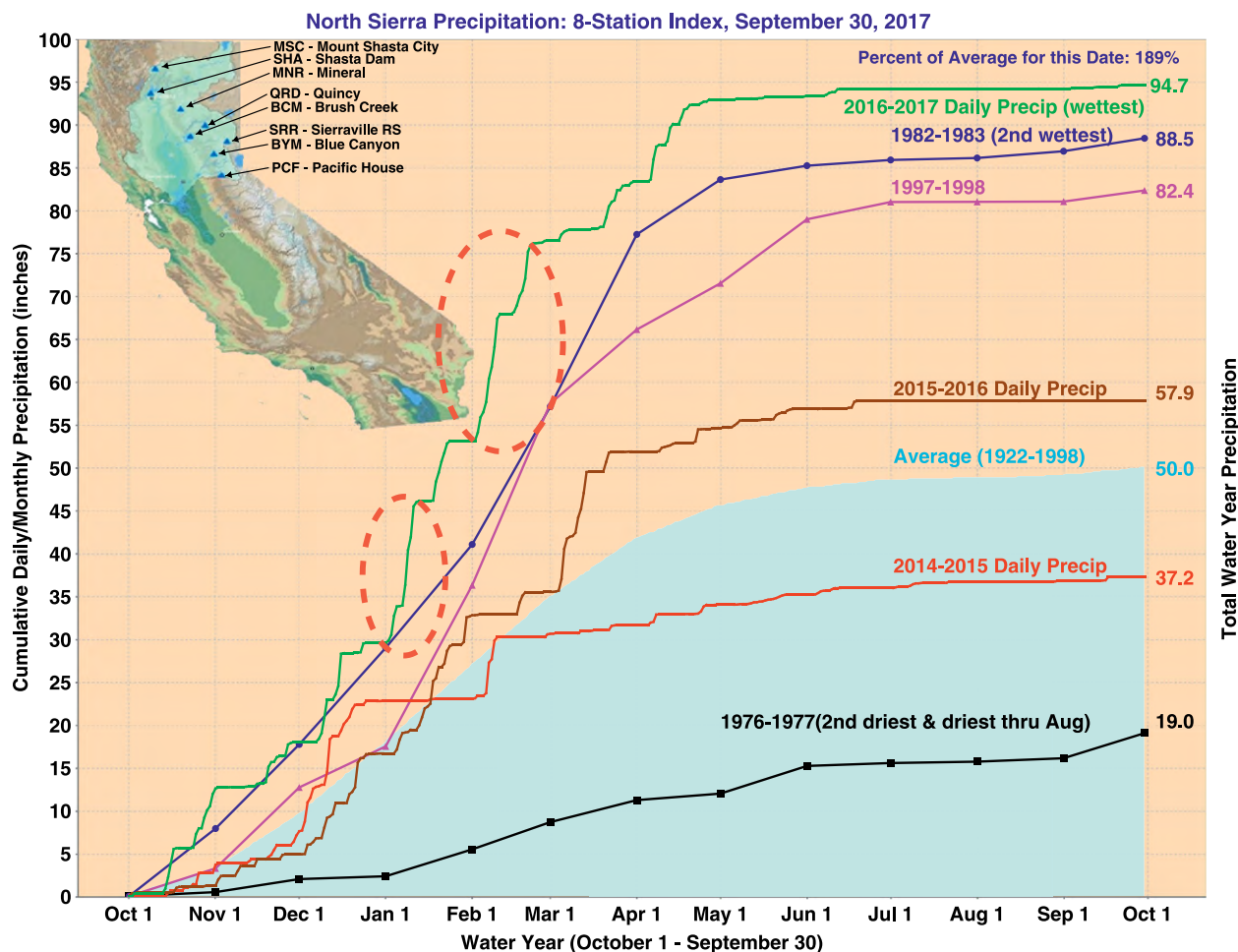


FIG. 1. 2016–17 precipitation accumulation for an average of precipitation observations at eight northern Sierra stations, the Northern Sierra 8 Station Index, compared to water years 1983, 1996, 2016, 2015, and 1977 and a long-term average (100 inches = 2540 mm; dashed ovals highlight major January and February storm sequences).
Source: https://cdec.water.ca.gov/cgi-progs/lproducts/PLOT_ESI.

streamflows since limited snow-fed runoff is less likely to meet warm-season water demands.

Major storms in early January ended the snow drought, and normal water volumes were stored in Lake Oroville when the intense precipitation arrived. In events that followed (Fig. 1), no single storm broke records or approached probable maximum precipitation (PMP) status. Although the storm that triggered Oroville’s evacuation was an extreme landfalling atmospheric river, it was the unusually large number of storms (e.g., 49 atmospheric rivers made landfall between 1 October 2016 and 12 April 2017) and their record-breaking cumulative precipitation total that were hard to manage and threatened infrastructure throughout northern California. By the end of April, snow water equivalent in the northern Sierra was ~170% of normal. Total main spillway outflow from Oroville Dam during the 2016/17 season was nearly 2.5 times the previous record.

The remarkable string of storms that set the stage for the near-disaster at Oroville impacted all of northern California. For example, at New Don Pedro Reservoir farther south, operators also struggled with flood challenges, but without structural damages that hampered operations at Oroville. By careful use of forecast tools, operators at New Don Pedro limited flows to 16,000 cubic feet per second (cfs; $450 \text{ m}^3 \text{ s}^{-1}$) instead of 31,000 cfs ($880 \text{ m}^3 \text{ s}^{-1}$), which would have resulted in more downstream flooding. Reservoir operators, including even Oroville in hindsight, weathered 2017 successfully. Thus the near-disaster at Oroville cannot be strictly attributed to the meteorological extremes that unfolded there but rather owed much to engineering (e.g., compromised spillways) and other non-meteorological challenges (e.g., people living below the dam) that are likely to increase as infrastructure ages and development continues.

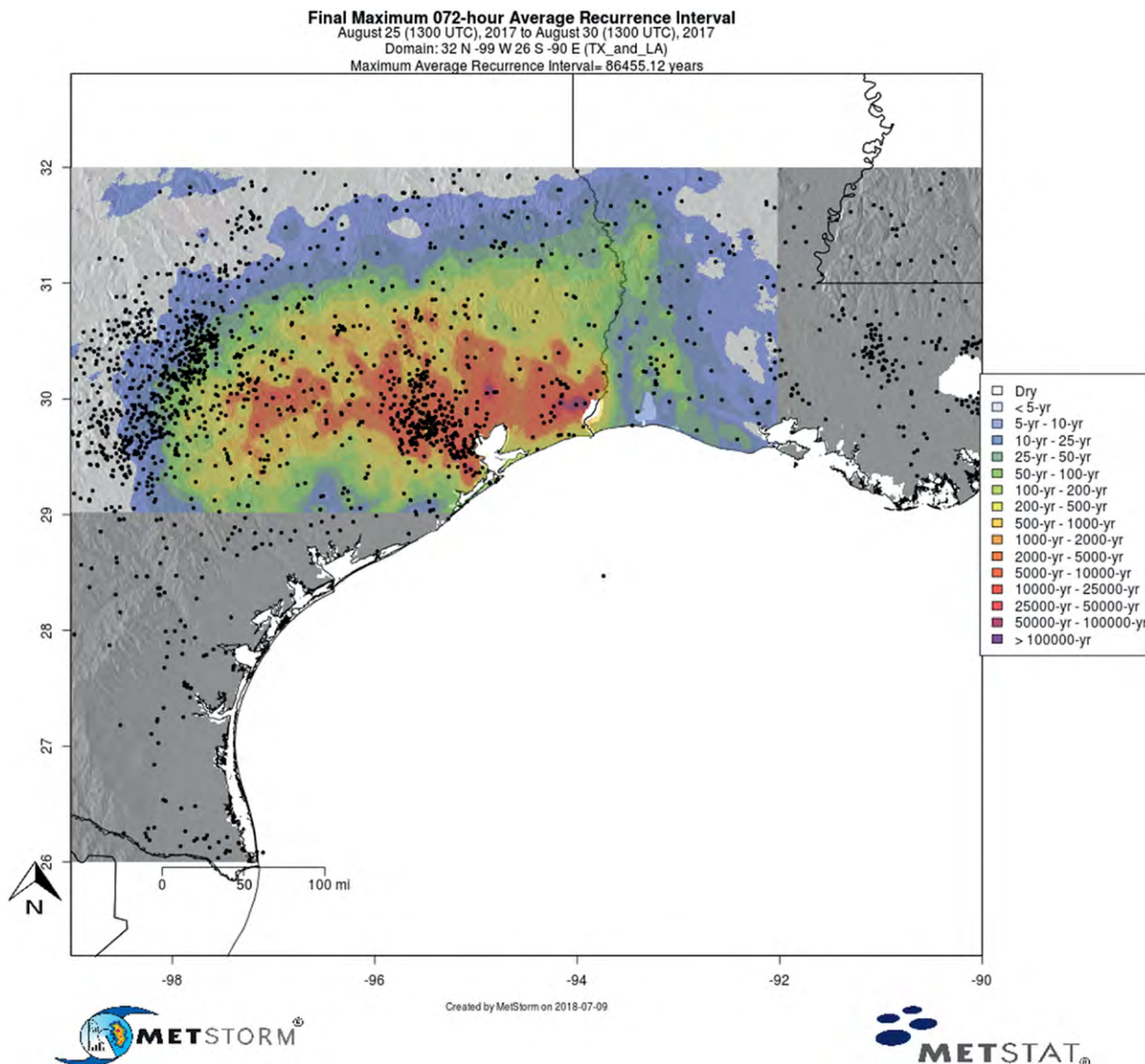


FIG. 2. Estimated average recurrence interval (ARI) of maximum (worst case) 72-h precipitation associated with Hurricane Harvey. Underlying precipitation from MetStorm, a storm precipitation analysis system operated by MetStat, Inc. that integrates radar, satellite, and precipitation gauge data into seamless, high-resolution GIS grids. The underlying precipitation frequency information is from a detailed regional precipitation frequency study conducted for the U.S. Army Corps of Engineers by MetStat, Inc. in 2017–18. Source: MetStat, Inc.

Lessons for attribution studies. On the basis of challenges water managers across northern California faced during winter 2017, we suggest that climate-change attribution studies address whether management should expect future changes in 1) seasons with unusually large numbers of atmospheric-river storms, 2) unusually warm storm conditions with unusually high attendant snowlines (e.g., Hatchett and McEvoy 2018), 3) preceding-year(s) and early-season snow-drought conditions, and 4) the nexus of storm precipitation totals and storm temperatures.

Additionally, the current validity of design storms and return intervals, which were estimated half a century ago when dams were built and operating rule curves were developed, is increasingly being questioned by water managers, and thoroughly vetted guidance in the form of studies that describe how much out of date current curves already are would be helpful.

CASE STUDY: FLOODING FROM HURRICANE HARVEY. In August 2017, a landfalling/

land-stalling category-4 hurricane became one of the most destructive in Texas history, causing major flooding from Houston to Beaumont (Blake and Zelinsky 2018). Similar to Oroville, events involved both hydroclimatic extremes and management decisions. The situations differ, yet have common themes that highlight aspects of meteorology that would be beneficial for attribution studies to explore.

Hurricane Harvey broke U.S. precipitation records, both in peak intensity and geographic extent, since records began in the 1880s (Blake and Zelinsky 2018). Maximum precipitation totals exceeded 60 inches (1500 mm) at several sites with over 20 inches (500 mm) falling in 24 h near Houston. A large swath of southeast Texas from Houston to Beaumont had 4-day rain totals that were > 1-in-1000 events (ftp://hdsc.nws.noaa.gov/pub/hdsc/data/aep/201708_Harvey/AEP_HurricaneHarvey_August2017.pdf). Preliminary estimates of the average recurrence interval (ARI) for rainfall over 72 h had maxima near 86,000 years (Fig. 2). Rainfall totals approached and, perhaps, exceeded PMP values for coastal Texas.

Addicks and Barker Reservoirs, designed to reduce flood flows through Houston, were overwhelmed by rainfall totals. Reservoir levels rose dramatically in both, peaking on 30 August. Local topography drove water to flow out of the northern end of Addicks Reservoir, creating a potentially catastrophic situation. Homes that had been built within the usually dry reservoir below the maximum flood pool elevation flooded for the first time (Wallace et al. 2018). Water managers had to increase releases downstream (creating additional downstream flooding) to prevent an emergency spillway overflow. Thus, although the extraordinary precipitation amounts surely drove the disaster, impacts were magnified by land-use decisions decades in the making, decisions that placed people, homes, and infrastructures in harm's way (Satija et al. 2017).

Overall, rainfall forecasts for Harvey showed remarkable skill in capturing duration and geographic extent. For several days in advance and during the event, quantitative precipitation forecasts (QPFs) were measured in feet (hundreds of millimeters), which is exactly what materialized; for example, on 26 August, the 72-h QPF showed

ACTIONABLE ATTRIBUTION SCIENCE

Water managers and agencies tasked with flood management and dam safety are confronted with the question of whether these remarkable storms and storm sequences were fueled in part by long-term continuing climate trends. Existing designs and plans are based on historical conditions. Therefore, information on how storms have already changed, and may change in the future, is crucial for assessing current flood and dam-safety risks and planning for recovery, remedial actions, and climate-change adaptations.

The Oroville and Harvey cases suggest some ways to make attribution studies more relevant to the water management community by considering real-world decision making context when designing studies:

Duration characteristics are critical to determining event severity for water management. A key meteorological factor in both Oroville and

Harvey was storm duration. No single storm (Oroville) or instantaneous precipitation rate (Harvey) was to blame; rather, the damages were caused by precipitation that did not seem to stop. In addition to changes in instantaneous precipitation rates—which can be meteorologically or climatically interesting and significant for local stormwater management—durations and storm totals are often more relevant to reservoir and flood managers.

Temperature characteristics can significantly change the magnitude of the water management impact. As illustrated in Oroville, the combination of storm precipitation totals and temperatures prior to and during the storm played a critical role in determining the amount of water already in the reservoir and runoff-contributing area of the watershed during the storm. In watersheds impacted by snow, climatological changes in storm temperatures can be as important to

water management as storm precipitation totals, and the likelihood of combined effects is even more important to understand.

Attribution studies can improve real-world relevance by including case-specific criteria and targets.

These case studies illustrate that risk exposure goes beyond maximum precipitation intensities or station-based storm precipitation totals. While PMPs are criteria that engineers use to increase dam safety, events can impact systems without being anywhere near PMP. At Oroville, the precipitation/streamflow volume from a series of storms contributed to the incident. In Harvey, PMPs may have been exceeded, but the duration/storm speed and geographic extent had greater impact. Conversations with water (and other) managers when designing attribution studies could help identify criteria most relevant to risk exposure and result in more actionable science.

up to 28 inches (715 mm) (NOAA 2018). Station records across the United States rarely show a single station 3-day total above 20 inches (500 mm) (Ralph and Dettinger 2012), let alone an entire region, yet Harvey's 72-h QPF's had >20 inches (508 mm) over a 100-km-wide area. In addition, models were stubbornly consistent day to day in forecasting this large rainfall event.

The first-order challenge for water managers was whether to believe these extraordinary QPFs, which were without precedent even for a region with a recent history of major floods. The resulting rainfall produced flooding beyond anyone's experience locally and well beyond standard floodplain mapping. Emergency managers were challenged both by the magnitude of the event and the difficulty of conveying the severity of what was happening.

Lessons for attribution studies. All attribution studies to date, by Emanuel (2017), Risser and Wehner (2017), van Oldenborgh et al. (2017), and Wang et al. (2018), indicate increased precipitation intensity caused by anthropogenic warming. For example, Emanuel (2017) found likelihoods of storm

occurrences with area-averaged precipitation totals of 20 inches (500 mm), like Harvey, have already increased by 6% compared to likelihoods in the late twentieth century. This quantification (or others that are even more to the point) can provide managers with a better context for deciding what confidence to place in the most extreme forecasts and how much to rely on existing flood-management infrastructures. In the case of Harvey, unprecedented precipitation intensities and totals "made" the hazard, but the meteorological events and hydrological catastrophe were exacerbated by its arrival onshore, its speed and duration as an intact severe storm, and its geographic extent. These "other" factors are beginning to be explored (e.g., Gutmann et al. 2018; Kossin 2018) and suggest that, for flood and water managers, climate-change attribution studies could also address whether and how much climate change contributes to 1) numbers of landfalling hurricanes per year, 2) speed and duration of hurricanes both offshore and on, 3) rates of intensification, 4) geographic extent of (landfalling) hurricanes, and 5) relationships between Saffir category status and maximum precipitation.

Attribution studies should be careful about how results are expressed, because both meteorological and operational factors are important in many extreme events. Damages from extreme events are usually not just functions of climatological extremity (Klotzbach et al. 2018). Non-climatological factors such as locations and integrity of infrastructure and communities, reservoir operations, and land-use patterns are also important. When water systems perform well, they can operate safely in the midst of extremes. For example, the Oroville event would have garnered little notice if a purely structural problem with the emergency spillway had not developed early in the storm sequence. Also, planning and management decisions can elevate vulnerabilities, such as allowing homes to be built below the maximum flood pool elevation in reservoirs in Houston. Thus, results of attribution studies need to be communicated with realistic humility regarding the mix of

meteorological and human contributions to disasters resulting from meteorologically extreme events.

Attribution studies can help management navigate an important paradigm shift. Water planners and engineers build and operate to specific safety standards, including PMPs and design storms with various likelihoods of recurrence. Most projects were planned in an era where optimality and economic efficiency were accepted objectives based on the assumption that probabilities of extreme events could be estimated reasonably by extrapolation of the historical record (Brown 2010). Events like Oroville and Harvey naturally raise questions whether historical records and their derived statistics still provide reliable estimates of risks, and whether some design criteria and reservoir operations guidelines should be revised. Unprecedented magnitudes of forecasted rainfall can leave operators doubting the validity of forecasts:

Can the atmosphere hold that much rainfall? Are this many extreme storms really likely in a single year? These are questions attribution studies can be designed to address, leading, with careful consideration and collaboration, to information that managers can use to guide their interpretations of forecasts and their estimates of long-term probabilities that they use in their operations and planning processes.

From our collective experience, we see potential for attribution studies to better inform water management decisions and enhance public safety to reduce impacts of extreme hazards. However, for studies to be actionable for water management, attention to those aspects of extremes that make them most challenging to management will be needed, requiring improved understanding and engagement with the water management community. We encourage future Explaining Extreme Events studies to take on this challenge.

REFERENCES

- Abbott, J., 2018, Impacts, lessons from Oroville spillway crisis. *Appeal-Democrat* (Marysville, CA), accessed 12 Feb 2018, www.govtech.com/em/disaster/Impacts-Lessons-from-Oroville-Spillway-Crisis.html.
- Blake, E. S., and D. A. Zelinsky, 2018. National Hurricane Center Tropical Cyclone Report: Hurricane Harvey (AL092017). NHC, 77 pp., www.nhc.noaa.gov/data/tcr/AL092017_Harvey.pdf.
- Brown, C., 2010: The end of reliability. *J. Water Resour. Plann. Manage.*, **136** (2), [https://doi.org/10.1061/\(ASCE\)WR.1943-5452.65](https://doi.org/10.1061/(ASCE)WR.1943-5452.65).
- CNRFC, 2017: Heavy precipitation events California and northern Nevada: January and February 2017. California Nevada River Forecast Center, accessed 12 February 2018, www.cnrfc.noaa.gov/storm_summaries/janfeb2017storms.php.
- Emanuel, K., 2017: Assessing the present and future probability of Hurricane Harvey's rainfall. *Proc. Natl. Acad. Sci. USA*, **114**, 12681–12684, <https://doi.org/10.1073/pnas.1716222114>.
- France, J. W., I. A. Alvi, P. A. Dickson, H. T. Falvey, S. J. Rigbey, and J. Trojanowski, 2018: Oroville Dam spillway incident independent forensic team final report (5 January 2018). 584 pp., www.ussdams.org/our-news/oroville-dam-spillway-incident-independent-forensic-team-final-report.
- Gutmann, E., and Coauthors, 2018: Changes in hurricanes from a 13-yr convection-permitting pseudo-global warming simulation. *J. Climate*, **31**, 3643–3657, <https://doi.org/10.1175/JCLI-D-17-0391.1>.
- Hatchett, B. J., and D. J. McEvoy, 2018: Exploring the origins of snow drought in the northern Sierra Nevada, California. *Earth Interact.*, **22**, <https://doi.org/10.1175/EI-D-17-0027.1>.
- Holland J., R. Ahumada and D. Farrow, 2018. Last year, all eyes were on the Don Pedro spillway as a nervous Modesto waited. *The Modesto Bee* (Modesto, CA), 17 February 2018, www.modbee.com/news/article199926454.html.
- Klotzbach, P., S. Bowen, R. Pielke, and M. Bell, 2018: Continental U.S. hurricane landfall frequency and associated damage: Observations and future risks. *Bull. Amer. Meteor. Soc.*, **99**, 1359–1376, <https://doi.org/10.1175/BAMS-D-17-0184.1>.
- Kossin, J. P., 2018: A global slowdown of tropical-cyclone translation speed. *Nature*, **558**, 104–107, <https://doi.org/10.1038/s41586-018-0158-3>.
- NOAA, 2018: Quantitative precipitation forecasts. Accessed 2 July 2018, www.wpc.ncep.noaa.gov/qpf/qpf2.shtml.
- Ralph, F. M., and M. D. Dettinger, 2012: Historical and national perspectives on extreme West Coast precipitation associated with atmospheric rivers during December 2010. *Bull. Amer. Meteor. Soc.*, **93**, 783–790, <https://doi.org/10.1175/BAMS-D-11-00188.1>.
- Risser, M. D., and M. F. Wehner, 2017: Attributable human-induced changes in the likelihood and magnitude of the observed extreme precipitation during Hurricane Harvey. *Geophys. Res. Lett.*, **44**, 12 457–12 464, <https://doi.org/10.1002/2017GL075888>.
- Satija, N., K. Collier, and A. Shaw, 2017: Houston officials let developers build homes inside reservoirs. But no one warned buyers. *The Texas Tribune*, 12 October 2017, <https://apps.texastribune.org/harvey-reservoirs>.
- van Oldenborgh, G. J., and Coauthors, 2017: Attribution of extreme rainfall from Hurricane Harvey, August 2017. *Environ. Res. Lett.*, **12**, 124009, <https://doi.org/10.1088/1748-9326/aa9ef2>.
- Wallace, T., D. Watkins, H. Park, A. Singhvi, and J. Williams, 2018. How one Houston suburb ended up in a reservoir. *The New York Times*, 22 March 2018, www.nytimes.com/interactive/2018/03/22/us/houston-harvey-flooding-reservoir.html.
- Wang, S.-Y. S., L. Zhao, J.-H. Yoon, P. Klotzbach, and R. Gillies, 2018: Quantitative attribution of climate effects on Hurricane Harvey's extreme rainfall in Texas. *Environ. Res. Lett.*, **13**, 054014, <https://doi.org/10.1088/1748-9326/aabb85>.
- Wax-Thibodeaux, E., A. Horton, and A. B. Wang, 2017. Houston dam spills over for the first time in history, overwhelmed by Harvey rainfall. *The Washington Post*, 29 August 2017, www.washingtonpost.com/news/post-nation/wp/2017/08/28/houston-releases-water-from-two-dams-in-attempt-to-prevent-uncontrolled-overflow.
- White, A., B. Moore, D. Gattas, and P. Neiman, 2019: Winter storm conditions leading to excessive runoff above California's Oroville Dam during January and February 2017. *Bull. Amer. Meteor. Soc.*, <https://doi.org/10.1175/BAMS-D-18-0091.1>, in press.

OBSERVATIONS OF THE RATE AND ACCELERATION
OF GLOBAL MEAN SEA LEVEL CHANGE

R. S. NEREM AND J. FASULLO

Climate models and basic physical principles project that global mean sea level (GMSL) will increase and the rate of increase will accelerate under anthropogenic climate change (Church et al. 2013). There is now substantial evidence for this in the observational record, which consists of tide gauge measurements, satellite altimeter measurements, and, indirectly, satellite gravity measurements. Both tide gauge sea level reconstructions and satellite altimetry show that the current rate of global mean sea level change is about 3 mm yr^{-1} , and both show that this rate is accelerating. Usually, this change in the rate of sea level rise is modeled as a quadratic, but other functions (e.g., an exponential) may be equally valid, and in either case one must be careful interpreting these simple functional fits to what are likely to be temporally complex climate responses. Nonetheless, the character of future changes is of enormous socioeconomic consequence.

The tide gauge sea level record is now more than a century long, but it suffers from poor spatial sampling and is sensitive to vertical land motion and coastal effects. In addition, the number of tide gauges decreases dramatically as one goes back in time. Recent papers have argued that the rate of sea level rise as measured by tide gauges during the early part of the century is less than previously understood, perhaps as low as 1.1 mm yr^{-1} over 1900–90 (Hay et al. 2015; Dangendorf et al. 2017), but there is still no consensus on this value due to data quality, estimation, and sampling issues (Hamlington and Thompson 2015; Thompson et al. 2016), with others preferring a value

closer to 1.5 mm yr^{-1} . However, over the altimeter era (1992–present), tide gauges show a rate of about 3 mm yr^{-1} , suggesting that global mean sea level has accelerated over the last century (e.g., Merrifield et al. 2009; Church and White 2006), although the tide gauge record also shows higher rates ($\sim 2 \text{ mm yr}^{-1}$) in the 1940s. Acceleration estimates averaged over the last century vary from 0.01 to 0.02 mm yr^{-2} (e.g., Dangendorf et al. 2017), but for much of this time period GMSL was probably accelerating very little because ice sheet melt did not start making a substantial contribution to sea level change until the early 1990s (e.g., Bamber et al. 2018). Also decadal variability in the tide gauge record (Haigh et al. 2014), due to both poor spatial sampling and real variability, increases the uncertainty of these estimates. Different analyses of the tide gauge record give different acceleration values depending on the methods used [see Dangendorf et al. (2017) for a summary].

The satellite altimeter record from TOPEX/Poseidon, *Jason-1*, *Jason-2*, and *Jason-3* has observed a rate of sea level rise of $\sim 3 \text{ mm yr}^{-1}$ over 1993–2018 (e.g., Nerem et al. 2010; Ablain et al. 2017; Beckley et al. 2017). The satellite altimeter record is short (25 yr) and thus great care must be taken when trying to extract any climate-driven acceleration from variability due to volcanic activity, climate variability (ENSO, PDO, etc.), and interannual variability driven by water storage variations. However, the altimeter record provides nearly global coverage between $\pm 66^\circ$ latitude (biases due to non-polar coverage are currently small; Lickley et al. 2018). A number of recent papers have detected increases in the decadal rates of sea level change from the altimeter record (e.g., Watson et al. 2015; Chen et al. 2017; Dieng et al. 2017). Fasullo et al. (2016) showed that the eruption of Mount Pinatubo in 1991 had a profound effect on the altimeter GMSL record, causing the rate of sea level rise to be higher in the early part of the record (a negative acceleration over the altimeter era).

For the relatively short sea level records available from satellite altimetry, it is helpful to try to remove different sources of variability to reveal the “climate-driven” sea level changes. Nerem et al. (2018) used a model to correct the altimeter record for the effects of

AFFILIATIONS: NEREM—Smead Aerospace Engineering Sciences, Colorado Center for Astrodynamics Research, Cooperative Institute for Research in Environmental Sciences, University of Colorado, Boulder, Colorado; FASULLO—National Center for Atmospheric Research, Boulder, Colorado

CORRESPONDING AUTHOR: R. S. Nerem, nerem@colorado.edu

DOI:10.1175/BAMS-D-18-0247.1

© 2019 American Meteorological Society

For information regarding reuse of this content and general copyright information, consult the [AMS Copyright Policy](#).

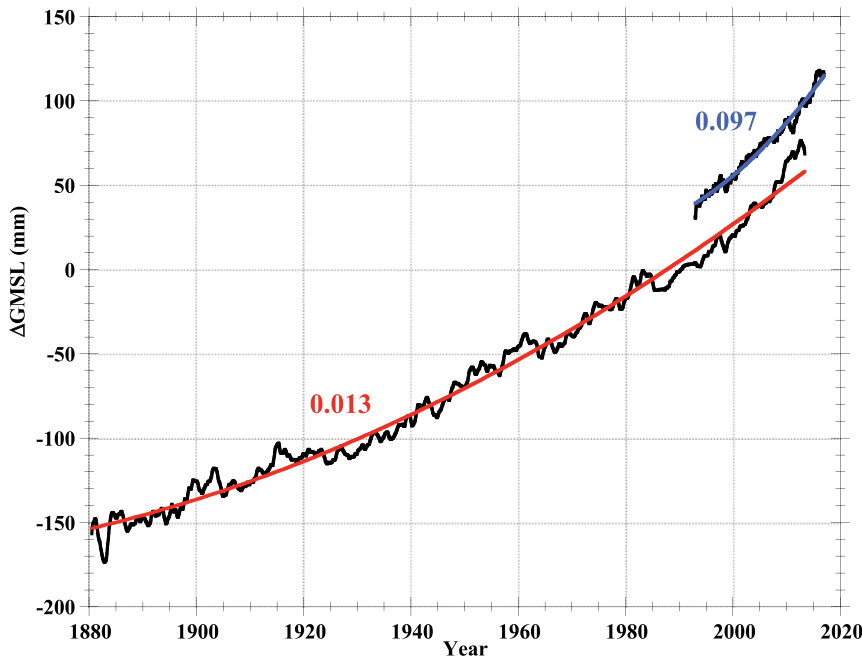


FIG. 1. Global mean sea level variations from a tide gauge sea level reconstruction (Church and White 2011) and satellite altimetry (Beckley et al. 2017) before correcting for Pinatubo and ENSO, with quadratic fits covering 1880–2015 and 1993–2017 respectively. Quadratic fits are summarized in Table I [updated from Nerem et al. (2018)]. Curves are offset for readability.

Mount Pinatubo and removed interannual variability due to ENSO and PDO. They found a climate-driven acceleration of $0.084 \pm 0.025 \text{ mm yr}^{-2}$, which is comparable to tide gauge estimates post-1970 but higher than them over the last century because for most of the century the ice sheets were largely in balance (Bamber et al. 2018).

Figure 1 shows some of the time series used to determine the rates and accelerations discussed

era, largely because of the GRACE mission and the Argo network of profiling floats to measure heat content. Nevertheless, different analyses may give different amounts of attribution (e.g., Dieng et al. 2017). The attribution of the changes in sea level can be directly tied to increases in surface land and sea temperatures, because the changes are due almost entirely to the melting of land ice (Bamber et al. 2018) and increasing heat content of the oceans (leading to

here. Table 1 shows a summary of some of these rate and acceleration estimates. Nerem et al. (2018) also used the gravity record from the GRACE mission (2002–17) to determine that ~45% of the rate and ~90% of the acceleration observed in the altimeter record is due to ice mass loss from Greenland, Antarctica, and mountain glaciers and small ice caps, with the rest being due mainly to thermal expansion.

The closing of the sea level budget for the rate has been a subject of much study and is often the basis for statements of attribution. There is much uncertainty in closing the budget of the tide gauge record (e.g., Jevrejeva et al. 2017), but we have a much better understanding of the altimeter

TABLE 1. GMSL acceleration estimates from tide gauges and satellite altimetry [updated from Nerem et al. (2018)].

Component	Time period	Rate epoch	Rate (mm yr^{-1})	Acceleration (mm yr^{-2})
Greenland	2002.3–2017.0	2005	0.66	0.0236
Antarctica	2002.3–2017.0	2005	0.19	0.0332
Mountain glaciers and small ice caps	2002.3–2017.0	2005	0.51	0.0094
Thermosteric ¹	1993.0–2016.0	2005	1.65	0.0076
Components total		2005	3.01	0.0738
Altimeter observed	1993.0–2017.0	2005	3.1	0.097
Altimeter observed ¹	1993.0–2017.0	2005	2.9	0.117
Altimeter observed ²	1993.0–2017.0	2005	2.9	0.084
Tide gauges ³	1880–2015	1950	1.6	0.012

¹ Corrected for Pinatubo.

² Corrected for Pinatubo and ENSO effects (climate change–driven acceleration).

³ From updated results of Church and White (2011).

thermal expansion). Therefore, most of the observed sea level change is anthropogenic (e.g., Slangen et al. 2016) although a secondary role for internal climate variability also exists (Swart et al. 2015).

As a thought experiment, Nerem et al. (2018) extrapolated the quadratic fit to the altimeter record to 2100 and found 65 ± 12 cm of sea level rise by 2100 relative to 2005, which agrees well with the IPCC AR5 projections (Church et al. 2013). This extrapolation suggests that the rate of sea level rise in 2100 could be ~ 10 mm yr⁻¹. While extrapolation of this simple functional fit is not a physically based way of projecting future sea level change, it does provide a data-driven method of representing past changes so that they can be compared to climate models. Various physical realizations of twenty-first-century climate change are potentially associated with the range of statistical assumptions and relate in particular to cryospheric instabilities in Antarctica and Greenland and the estimated range of polar amplification, cloud feedbacks, and climate sensitivity.

On the whole, the available observational evidence suggests that the rate of global mean sea level is accelerating in response to anthropogenic forcing roughly as the climate models have predicted. However, there is still much uncertainty regarding how fast the ice sheets will respond to warming, and what this response will look like over time. As the observational record continues to grow, in part made possible with the launches of *Jason-3* in January 2016 and *GRACE-FO* in May 2018, and as climate models are coupled to ice sheet models such as in the CMIP6 multimodel ensemble now being generated at major climate centers, the observational record will become increasingly useful for validating models and ultimately reducing the uncertainty in future sea level change projections. While we have focused here on global mean sea level, satellite altimetry also provides the spatial variations of sea level change and these may soon be useful for attribution studies, as the different contributions to sea level change have distinctive regional patterns. In addition, regional estimates of climate-driven sea level change will be more useful for sea level impact studies than the global average.

REFERENCES

- Ablain, M., J. F. Legeais, P. Prandi, M. Marcos, L. Fenoglio-Marc, H. B. Dieng, J. Benveniste, and A. Cazenave, 2017: Satellite altimetry-based sea level at global and regional scales. *Surv. Geophys.*, **38**, 7–31, <https://doi.org/10.1007/s10712-016-9389-8>.
- Bamber, J., R. M. Westaway, B. Marzeion, and B. Wouters, 2018: The land ice contribution to sea level during the satellite era. *Environ. Res. Lett.*, **13**, 063008, <https://doi.org/10.1088/1748-9326/aac2f0>.
- Beckley, B. D., P. S. Callahan, D. W. Hancock, G. T. Mitchum, and R. D. Ray, 2017: On the “Cal-Mode” correction to TOPEX satellite altimetry and its effect on the global mean sea level time series. *J. Geophys. Res. Oceans*, **122**, 8371–8384, <https://doi.org/10.1002/2017JC013090>.
- Chen, X., X. Zhang, J. A. Church, C. S. Watson, M. A. King, D. Monselesan, B. Legresy, and C. Harig, 2017: The increasing rate of global mean sea-level rise during 1993–2014. *Nat. Climate Change*, **7**, 492–495, <https://doi.org/10.1038/nclimate3325>.
- Church, J. A., and N. J. White, 2006: A 20th century acceleration in global sea-level rise. *Geophys. Res. Lett.*, **33**, L01602, <https://doi.org/10.1029/2005GL024826>.
- , and —, 2011: Sea-level rise from the late 19th to the early 21st century. *Surv. Geophys.*, **32**, 585–602, <https://doi.org/10.1007/s10712-011-9119-1>.
- , and Coauthors, 2013: *Sea level change. Climate Change 2013: The Physical Science Basis*, T. F. Stocker et al., Eds., Cambridge University Press, 1137–1216.
- Dangendorf, S., M. Marcos, G. Wöppelmann, C. P. Conrad, T. Frederikse, and R. Riva, 2017: Reassessment of 20th century global mean sea level rise. *Proc. Natl. Acad. Sci. USA*, **114**, 5946–5951, <https://doi.org/10.1073/pnas.1616007114>.
- Dieng, H. B., A. Cazenave, B. Meyssignac, and M. Ablain, 2017: New estimate of the current rate of sea level rise from a sea level budget approach. *Geophys. Res. Lett.*, **44**, 3744–3751, <https://doi.org/10.1002/2017GL073308>.
- Fasullo, J. T., R. S. Nerem, and B. Hamlington, 2016: Is the detection of accelerated sea level rise imminent? *Sci. Rep.*, **6**, 31245, <https://doi.org/10.1038/srep31245>.
- Haigh, I. D., T. Wahl, E. J. Rohling, R. M. Price, C. B. Pattiaratchi, F. M. Calafat, and S. Dangendorf, 2014: Timescales for detecting a significant acceleration in sea level rise. *Nat. Commun.*, **5**, 3635, <https://doi.org/10.1038/ncomms4635>.
- Hamlington, B. D., and P. R. Thompson, 2015: Considerations for estimating the 20th century trend in global mean sea level. *Geophys. Res. Lett.*, **42**, 4102–4109, <https://doi.org/10.1002/2015GL064177>.
- Hay, C. C., E. Morrow, R. E. Kopp, and J. X. Mitrovica, 2015: Probabilistic reanalysis of twentieth-century sea-level rise. *Nature*, **517**, 481–484, <https://doi.org/10.1038/nature14093>.
- Jevrejeva, S., A. Matthews, and A. Slangen, 2017: The twentieth-century sea level budget: Recent progress and challenges. *Surv. Geophys.*, **38**, 295–307, <https://doi.org/10.1007/s10712-016-9405-z>.
- Lickley, M. J., C. C. Hay, M. E. Tamisiea, and J. X. Mitrovica, 2018: Bias in estimates of global mean

- sea level change inferred from satellite altimetry. *J. Climate*, **31**, 5263–5271, <https://doi.org/10.1175/JCLI-D-18-0024.1>.
- Merrifield, M. A., S. T. Merrifield, and G. T. Mitchum, 2009: An anomalous recent acceleration of global sea level rise. *J. Climate*, **22**, 5772–5781, <https://doi.org/10.1175/2009JCLI2985.1>.
- Nerem, R. S., D. P. Chambers, C. Choe, and G. T. Mitchum, 2010: Estimating mean sea level change from the TOPEX and Jason altimeter missions. *Mar. Geod.*, **33** (S1), 435–446, <https://doi.org/10.1080/01490419.2010.491031>.
- , B. D. Beckley, J. T. Fasullo, B. D. Hamlington, D. Masters, and G. T. Mitchum, 2018: Climate-change-driven accelerated sea-level rise detected in the altimeter era. *Proc. Natl. Acad. Sci. USA*, **115**, 2022–2025, <https://doi.org/10.1073/pnas.1717312115>.
- Slangen, A. B. A., J. A. Church, C. Agosta, X. Fettweis, B. Marzeion, and K. Richter, 2016: Anthropogenic forcing dominates global mean sea-level rise since 1970. *Nat. Climate Change*, **6**, 701–705, <https://doi.org/10.1038/nclimate2991>.
- Swart, N. C., J. C. Fyfe, E. Hawkins, J. E. Kay, and A. Jahn, 2015: Influence of internal variability on Arctic sea-ice trends. *Nat. Climate Change*, **5**, 86–89, <https://doi.org/10.1038/nclimate2483>.
- Thompson, P. R., B. D. Hamlington, F. W. Landerer, and S. Adhikari, 2016: Are long tide gauge records in the wrong place to measure global mean sea level rise? *Geophys. Res. Lett.*, **43**, 10 403–10 411, <https://doi.org/10.1002/2016GL070552>.
- Watson, C. S., N. J. White, J. A. Church, M. A. King, R. J. Burgette, and B. Legresy, 2015: Unabated global mean sea-level rise over the satellite altimeter era. *Nat. Climate Change*, **5**, 565–568, <https://doi.org/10.1038/nclimate2635>.

ANTHROPOGENIC CONTRIBUTIONS TO THE INTENSITY OF THE 2017 UNITED STATES NORTHERN GREAT PLAINS DROUGHT

ANDREW HOELL, JUDITH PERLWITZ, CANDIDA DEWES, KLAUS WOLTER, IMTIAZ RANGWALA, XIAO-WEI QUAN, AND JON EISCHEID

Anthropogenic forcing made the occurrence of observed 2017 northern Great Plains drought intensity up to 1.5 times more likely through aridification due to long-term increases in evapotranspiration over precipitation.

INTRODUCTION. Drought conditions developed rapidly during the spring and summer of 2017 over the northern Great Plains states of South Dakota, North Dakota, and Montana (Fig. 1a). On 2 May 2017, the U.S. Drought Monitor (USDM) reported no drought, with only two small areas of abnormal dryness in the central part of the region (Fig. 1b). By 1 August 2017, the USDM depicted widespread drought over all of eastern Montana and the Dakotas, highlighted by areas of extreme and exceptional drought (Fig. 1c). Deemed a “billion dollar disaster,”¹ this drought sparked widespread wildfires² and compromised water resources, which led to the destruction of property, livestock sell-offs, and reduced agricultural production.³ While this region is no stranger to drought (e.g., Woodhouse and Overpeck 1998),

the last comparable event occurred as far back as 1987–89 [described in Riebsame et al. (1991)].⁴ Here, we investigate anthropogenic contributions to the intensity of this drought during May–July 2017 using climate model simulations.

DATA. *Drought monitoring and estimates of observed conditions.* Expert drought assessments are from the USDM. The National Drought Mitigation Center⁵ archives these USDM maps, which blend observations of the hydrology and climate with reported local impacts to produce estimates of drought severity coverage.

Estimates of observed 1-m soil moisture, precipitation, evapotranspiration, and 2-m air temperature are from the North American Land Data Assimilation System version 2 (NLDAS-2; Xia et al. 2012). We use the median of three models from NLDAS-2: Mosaic (Koster and Suarez 1994), Noah-2.8 (Xia et al. 2012), and the Variable Infiltration Capacity model (VIC-4.0.3; Wood et al. 1997).

Climate model simulations. Two 40-member ensembles of historical climate simulations are diagnosed for 1920–2016. The first ensemble, called AOGCM for atmosphere–ocean general circulation model, is carried out with the Community Earth System Model (CESM) version 1 (Kay et al. 2015), a fully coupled climate model. CESM utilizes the Community Atmosphere Model version 5 (CAM5; Neale et al. 2010) and the Community Land Surface Model version 4 (CLM4; Lawrence et al. 2011), both of which are run at an approximately 1° resolution. The second ensemble, called AGCM, is carried out with CAM5 and CLM4. While ocean and sea ice conditions are calculated

¹ www.ncdc.noaa.gov/billions/

² www.nytimes.com/2017/09/07/us/montana-wildfire-drought.html

³ www.usda.gov/media/blog/2017/10/03/million-acres-scorched-montana-wildfires

AFFILIATIONS: HOELL—NOAA/Earth System Research Laboratory Physical Sciences Division, Boulder, Colorado; PERLWITZ, DEWES, WOLTER, RANGWALA, QUAN, AND EISCHEID—NOAA/Earth System Research Laboratory Physical Sciences Division and Cooperative Institute for Research in the Environmental Sciences, University of Colorado, Boulder, Colorado

CORRESPONDING AUTHOR: Andrew Hoell, andrew.hoell@noaa.gov

DOI:10.1175/BAMS-D-18-0127.1

A supplement to this article is available online (10.1175/BAMS-D-18-0127.2)

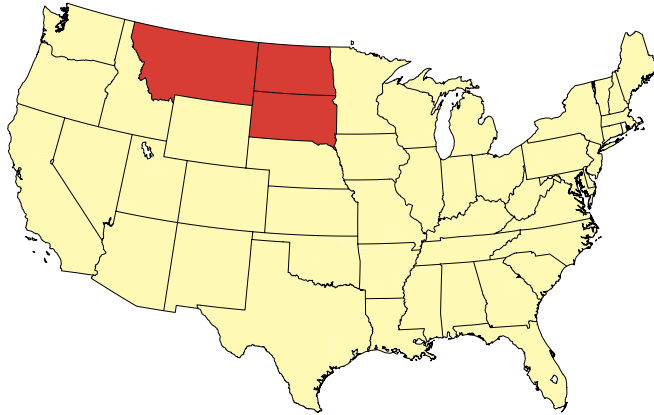
© 2019 American Meteorological Society

For information regarding reuse of this content and general copyright information, consult the [AMS Copyright Policy](#).

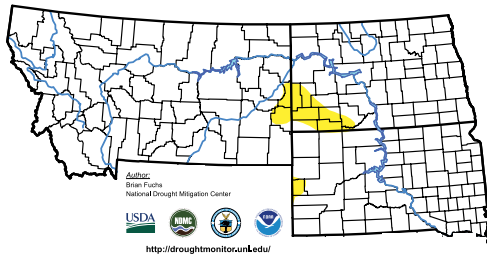
⁴ www.ncdc.noaa.gov/billions/events/US/1980-2017

⁵ <http://droughtmonitor.unl.edu/>

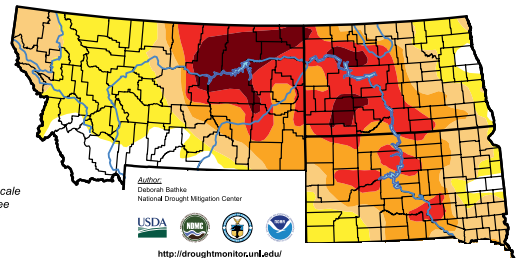
(a) Northern Plains Region Within the United States



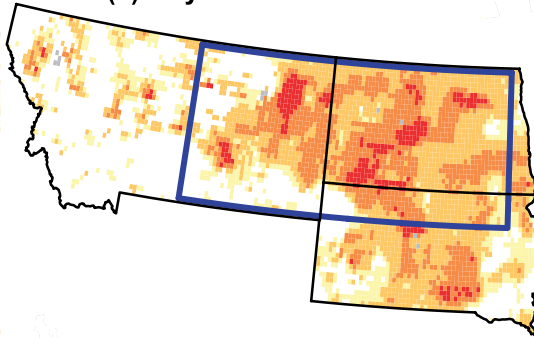
(b) 2 May 2017 USDM



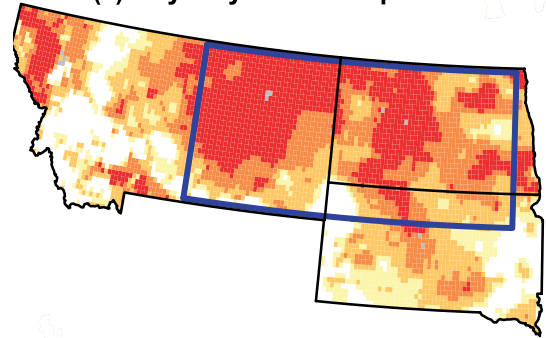
(c) 1 August 2017 USDM



(d) July 2017 Soil Moisture



(e) May-July 2017 Precipitation



Percentile Rank Relative to 1979-2017

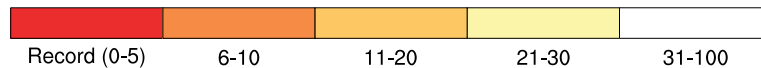


FIG. 1. (a) Location of the northern Plains. (b),(c) U.S Drought Monitor on 2 May and 1 Aug 2017, respectively. Also shown are percentile ranks of (d) July 2017 1-m soil moisture and (e) May-July 2017 precipitation based on the NLDAS-2 data. The blue box in (d) and (e) encloses the domain considered in the analysis of climate model simulations.

in AOGCM, AGCM is forced with observed time-evolving sea surface temperature and sea ice concentrations from Hurrell et al. (2008), which combines data from HadISST version 1 (Rayner et al. 2003) and NOAA OI SST version 2 (Reynolds et al. 2007). Both experiments are externally forced by the same anthropogenic (e.g., greenhouse gases and aerosols)

and natural (solar and volcanic) drivers, according to the design protocol for phase 5 of the Coupled Model Intercomparison Project (CMIP5), historical forcing for 1920–2005 (Lamarque et al. 2010), and the representative concentration pathway 8.5 (RCP8.5) scenario (Meinshausen et al. 2011; Lamarque et al. 2011) thereafter.

METHODS. We compare conditions between 1920–49 and 1987–2016, referred to as the *past* and *current* climates, respectively. The comparison between past and current climates in the AOGCM and AGCM ensembles isolates the effect of changes in the prescribed external forcing, which is mostly anthropogenic (Bindoff et al. 2013). It is important to note that while the AOGCM and AGCM ensembles employ different experimental designs, they still utilize the same atmosphere and land surface models.

Our choice of past climate overlaps the “Dust Bowl” era of the 1930s. Conflicting results exist as to whether the Dust Bowl over the northern Plains was forced by sea surface temperatures (cf. Schubert et al. 2004; Hoerling et al. 2009). The choice of past climate period does not affect our results since neither experiment indicates that the severity and duration of the Dust Bowl was forced by the boundary conditions (sea surface temperatures in the case of AGCM and external forcing in the case of both AGCM and AOGCM).

We compare histograms of 1-m soil moisture, precipitation, evapotranspiration, and 2-m air temperature—and the relationships among those variables—between the simulated past and current climates over the northern Plains. The term “northern Plains” hereafter refers to areal averages over the region bounded by the blue box in Figs. 1d and 1e, the area in which soil moisture was lowest across the region during July 2017. Four classes of agricultural drought intensity are considered based on 1-m soil moisture percentile ranges (0–2, 3–5, 6–10, and 11–20), which are analogous to those considered by USDM.⁶ Soil moisture thresholds associated with these percentiles are calculated relative to the past climate. The Kolmogorov–Smirnov test is used to examine whether the probability estimated from sample values between the past and current climates are of the same distribution. The change in drought risk and associated confidence intervals between past and current climates is also examined.

RESULTS. Soil moisture during July 2017 for the northern Plains region was the fifth lowest (12th percentile) between 1979 and 2017 (Fig. 1d). Widespread soil moisture in the lowest 20th percentile was observed across the region. Some areas were especially affected, as Glasgow in northeast Montana and Bismarck in central North Dakota experienced their lowest July soil moisture in 2017 since at least 1979. The

climate model experiments suggest that anthropogenic greenhouse forcing has contributed to the intensity of the drought by driving long-term reductions in soil moisture (referred to hereafter as aridification). From past to current climate, the simulations exhibit significant ($p < 0.001$) northern Plains soil moisture declines of 2%, which corresponds to 0.5 standard deviations (σ) of the past climate’s interannual variability (Fig. 2a; see also Fig. ES1a in the online supplemental material). The aridification of July soil moisture is also notable in the scatter of soil moisture, as there is a clear shift to lesser values in the current climate relative to the past (Figs. 2e,f and ES2e,f).

Consistently, the aridification during July increased the risk of summertime northern Plains agricultural droughts (Table 1). Specifically, droughts in the 11th–20th soil moisture percentile, such as during July 2017, are found to occur 1.2–1.5 times more often in the current climate than in the past climate. For more intense droughts, the risk of occurrence is even more enhanced with droughts in the 3rd–5th and 0th–2nd soil moisture percentiles occurring 1.7–2 times and 3–5 times more frequently in the current climate than in the past climate, respectively.

The observed drought was largely driven by low May–July precipitation over the northern Plains (Fig. 1e). Record low precipitation since 1979 was observed over at least 50% of the northern Plains region, mainly over northeastern Montana and North Dakota. However, the climate model experiments show a slight but significant increase (at $p < 0.04$) in northern Plains precipitation (Figs. 2b and ES1b), indicating that an anthropogenically driven increase in risk of specific drought intensities is not caused by precipitation changes. Rather, the aridification of the northern Plains during July is forced by statistically significant ($p < 0.001$) increases in evapotranspiration (0.4σ ; Fig. ES2c) during May–July associated with statistically significant ($p < 0.001$) increases in May–July 2-m air temperature by 0.5 – 0.6 K (0.5σ ; Figs. 2d and ES2d). Previous studies show that many of the twentieth-century temperature changes over North America are attributable to human influences in coupled climate models (e.g., Knutson et al. 2013). Our findings are consistent with a body of literature that suggests that anthropogenic influences decrease soil moisture and increase the risk of agricultural drought over North America through increases in evaporation as a result of human-induced warming (e.g., Hoerling et al. 2008; Sheffield and Wood 2011).

May–July precipitation and July soil moisture are closely linked ($r = 0.76$; Figs. 2e,f and ES2e,f) in both past and current climates. Taking into account the

⁶ <http://droughtmonitor.unl.edu/AboutUSDM/DroughtClassification.aspx>

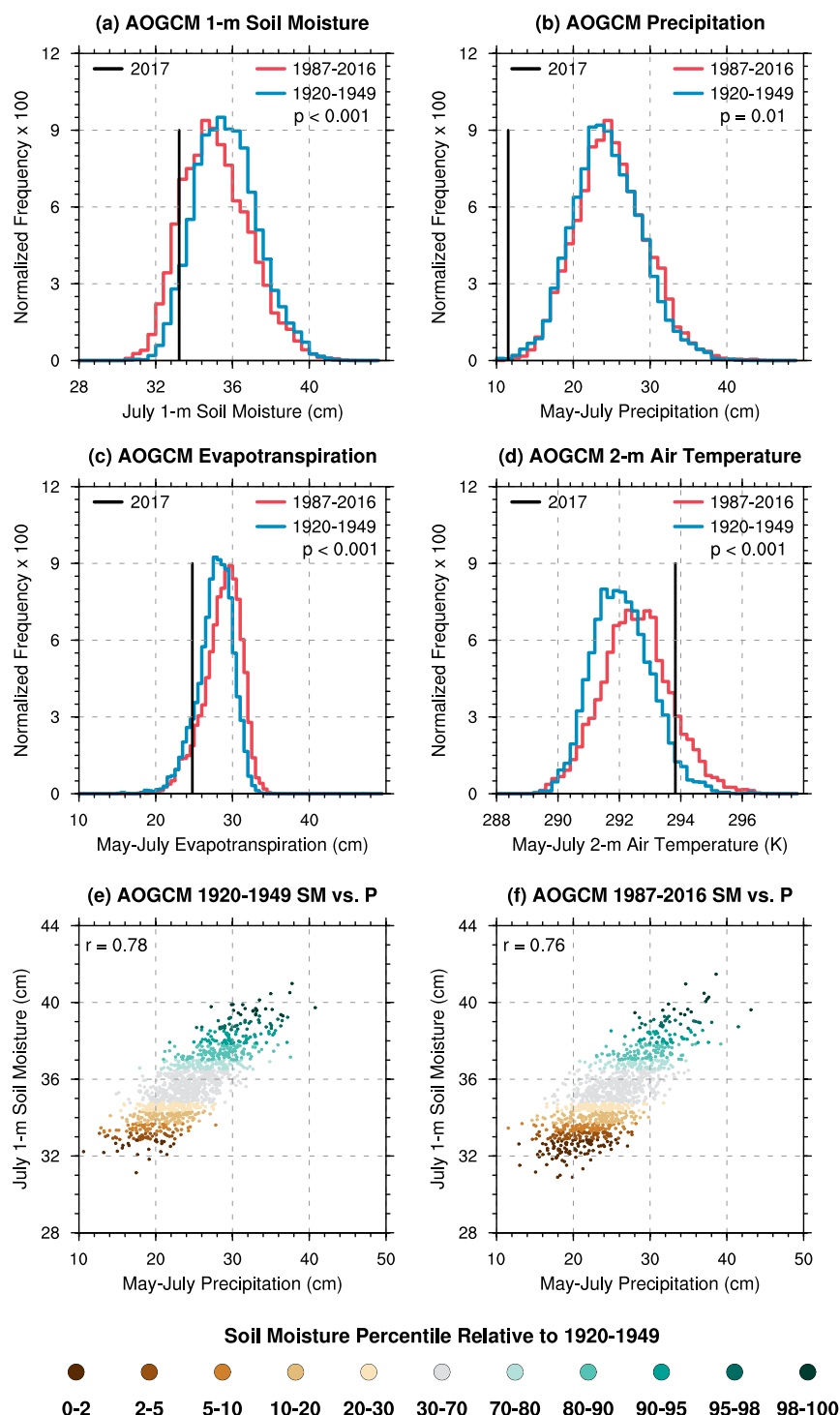


FIG. 2. Results from AOGCM areally averaged over the northern Plains. Normalized histograms of (a) July 1-m soil moisture, (b) May–July precipitation, (c) May–July evapotranspiration, and (d) May–July 2-m air temperature (cm) for 1987–2016 (red) and 1920–49 (blue). Black line in (a)–(d) displays NLDAS-2 percentile rank for 2017 at the value corresponding to the same percentile rank in the model simulations of the current climate. Also shown are scatter diagrams of July 1-m soil moisture and May–July precipitation during (e) 1920–49 and (f) 1987–2016.

small precipitation change between past and current climates, we can illustrate, however, that specific precipitation amounts above certain percentiles are less effective at keeping the northern plain regions out of drought (see Table ES1 in the online supplemental material; shift in scatter to lower soil moisture values from past to current climate in Figs. 2e,f and ES2e,f). For example, there is up to a 3.5-fold increased risk in drought occurrence when precipitation falls in the 40th–50th percentile range. Even for lower precipitation percentiles (e.g., 2nd–10th), where it is expected that drought occurs more frequently in general, there is still a 30% increase in drought occurrence from the past to the current climate.

For May–July 2017, which was the driest since at least 1979 over the northern Plains (Fig. 1e), both the AGCM and AOGCM experiments reveal that drought during July 2017 would have likely occurred regardless of external forcing (Table ES2). We found that in both past and current climates there is a 92% chance that simulated 1-m soil moisture falls in the lower 20th percentile when May–July precipitation values are in the lower second percentile.

CONCLUSIONS. We estimated the anthropogenic contributions to the intensity of agricultural drought over the United States northern Great Plains during May–July 2017 using model simulations. The experiments

TABLE 1. Relative risk of drought intensity between current and past climates as a function of July soil moisture percentiles in AOGCM and AGCM simulations.

Soil moisture percentile	AOGCM			AGCM		
	Lower 95% CI	Risk	Upper 95% CI	Lower 95% CI	Risk	Upper 95% CI
21–30	0.8	1.0	1.3	1.0	1.2	1.5
11–20	1.0	1.2	1.5	1.3	1.5	1.9
6–10	1.1	1.5	2.0	1.3	1.8	2.4
3–5	1.4	2.0	3.0	1.27	1.7	2.6
0–2	2.2	3.4	5.4	3.4	5.2	8.0

reveal that climate change made droughts with an intensity similar to that observed in May–July 2017 up to 1.5 times more likely as a result of aridification due to increases in evapotranspiration over precipitation. However, the principal cause of the 2017 drought was record low precipitation. We found that for such record low May–July 2017 (0th–2nd percentile) precipitation, drought (as defined by soil moisture below the 20th percentile) occurs with the same frequency in the simulated current and past climates.

ACKNOWLEDGMENTS. This research was jointly supported by the National Integrated Drought Information System⁷ and federally appropriated funds. Climate model simulations used in this study can be obtained from the NOAA/Earth System Research Laboratory Physical Sciences Division Facility for Climate Assessments.⁸

REFERENCES

- Bindoff, N. L., and Coauthors, 2013: Detection and attribution of climate change: From global to regional. *Climate Change 2013: The Physical Science Basis*, T. F. Stocker et al, Eds., Cambridge University Press, 867–952.
- Hoerling, M., G. Hegerl, D. Karoly, A. Kumar, and D. Rind, 2008: Attribution of the causes of climate variations and trends over North America during the modern reanalysis period. *Reanalysis of Historical Climate Data for Key Atmospheric Features: Implications for Attribution of Causes of Observed Change*, R. Dole, M. Hoerling, and S. Schubert, Eds., National Climatic Data Center, 47–92.
- , X.-W. Quan, and J. Eischeid, 2009: Distinct causes for two principal U.S. droughts of the 20th century. *Geophys. Res. Lett.*, **36**, L19708, <https://doi.org/10.1029/2009GL039860>.
- Hurrell, J. W., J. J. Hack, D. Shea, J. M. Caron, and J. Rosinski, 2008: A new sea surface temperature and sea ice boundary dataset for the Community Atmosphere Model. *J. Climate*, **21**, 5145–5153, <https://doi.org/10.1175/2008JCLI2292.1>.
- Kay, J. E., and Coauthors, 2015: The Community Earth System Model (CESM) Large Ensemble Project: A community resource for studying climate change in the presence of internal climate variability. *Bull. Amer. Meteor. Soc.*, **96**, 1333–1349, <https://doi.org/10.1175/BAMS-D-13-00255.1>.
- Knutson, T. R., F. Zeng, and A. T. Wittenberg, 2013: Multimodel assessment of regional surface temperature trends: CMIP3 and CMIP5 twentieth-century simulations. *J. Climate*, **26**, 8709–8743, <https://doi.org/10.1175/JCLI-D-12-00567.1>.
- Koster, R. D., and M. J. Suarez, 1994: The components of a ‘SVAT’ scheme and their effects on a GCM’s hydrological cycle. *Adv. Water Resour.*, **17**, 61–78, [https://doi.org/10.1016/0309-1708\(94\)90024-8](https://doi.org/10.1016/0309-1708(94)90024-8).
- Lamarque, J. F., and Coauthors, 2010: Historical (1850–2000) gridded anthropogenic and biomass burning emissions of reactive gases and aerosols: Methodology and application. *Atmos. Chem. Phys.*, **10**, 7017–7039, <https://doi.org/10.5194/acp-10-7017-2010>.
- , G. P. Kyle, M. Meinshausen, K. Riahi, S. J. Smith, D. P. van Vuuren, A. J. Conley, and F. Vitt, 2011: Global and regional evolution of short-lived radiatively-active gases and aerosols in the representative concentration pathways. *Climatic Change*, **109**, 191–212, <https://doi.org/10.1007/s10584-011-0155-0>.
- Lawrence, D. M., and Coauthors, 2011: Parameterization improvements and functional and structural advances in version 4 of the Community Land Model. *J. Adv. Model. Earth Syst.*, **3**, M03001, <https://doi.org/10.1029/2011MS00045>.
- Meinshausen, M., and Coauthors, 2011: The RCP greenhouse gas concentrations and their extension from 1765 to 2300. *Climatic Change*, **109**, 213–241, <https://doi.org/10.1007/s10584-011-0156-z>.

⁷ www.drought.gov/drought/

⁸ www.esrl.noaa.gov/psd/repository/alias/facts

- Neale, R. B., and Coauthors, 2010: Description of the NCAR Community Atmosphere Model (CAM5.0). NCAR/TN-486+STR, 274 pp., www.cesm.ucar.edu/models/cesm1.0/cam/docs/description/cam5_desc.pdf.
- Rayner, N. A., D. E. Parker, E. B. Horton, C. K. Folland, L. V. Alexander, D. P. Rowell, E. C. Kent, and A. Kaplan, 2003: Global analyses of sea surface temperature, sea ice, and night marine air temperature since the late nineteenth century. *J. Geophys. Res.*, **108**, 4407, <https://doi.org/10.1029/2002JD002670>.
- Reynolds, R. W., T. M. Smith, C. Liu, D. B. Chelton, K. S. Casey, and M. G. Schlax, 2007: Daily high-resolution-blended analyses for sea surface temperature. *J. Climate*, **20**, 5473–5496, <https://doi.org/10.1175/2007JCLI1824.1>.
- Riebsame, W. E., S. A. Changnon, and T. R. Karl, 1991: *Drought and Natural Resources Management in the United States: Impacts and Implications of the 1987–89 Drought*. Westview Press, 174 pp.
- Schubert, S. D., M. J. Suarez, P. J. Pegion, R. D. Koster, and J. T. Bacmeister, 2004: On the cause of the 1930s Dust Bowl. *Science*, **303**, 1855–1859, <https://doi.org/10.1126/science.1095048>.
- Sheffield, J., and E. Wood, 2011: *Drought: Past Problems and Future Scenarios*. Earthscan, 210 pp.
- Wood, E. F., D. Lettenmaier, X. Liang, B. Nijssen, and S. W. Wetzel, 1997: Hydrologic modeling of continental-scale basins. *Annu. Rev. Earth Planet. Sci.*, **25**, 279–300, <https://doi.org/10.1146/annurev.earth.25.1.279>.
- Woodhouse, C. A., and J. T. Overpeck, 1998: 2000 years of drought variability in the central United States. *Bull. Amer. Meteor. Soc.*, **79**, 2693–2714, [https://doi.org/10.1175/1520-0477\(1998\)079<2693:YODVIT>2.0.CO;2](https://doi.org/10.1175/1520-0477(1998)079<2693:YODVIT>2.0.CO;2).
- Xia, Y., and Coauthors, 2012: Continental-scale water and energy flux analysis and validation for the North American Land Data Assimilation System project phase 2 (NLDAS-2): 1. Intercomparison and application of model products. *J. Geophys. Res.*, **117**, D03109, <https://doi.org/10.1029/2011JD016048>.

ATTRIBUTION OF THE 2017 NORTHERN HIGH PLAINS DROUGHT

HAILAN WANG, SIEGFRIED D. SCHUBERT, RANDAL D. KOSTER, AND YEHUI CHANG

The 2017 northern High Plains precipitation deficits were largely the result of internal atmospheric variability. Global warming may have exacerbated the dry condition by producing surface warming and increasing the probability of heat waves there.

INTRODUCTION. The northern High Plains, particularly much of Montana and the Dakotas, had extreme to exceptional drought conditions develop during the summer of 2017. When the months of May, June, and July are combined, the year 2017 received 60% of normal precipitation and is ranked as the second driest (only after 1936) of the period 1901–2017 (Fig. 1a; see also Fig. ES1a in the online supplemental material). It also had anomalously warm temperatures relative to the 1901–2017 record (Figs. 1b and ES1b). The exceptional dryness combined with the unusual heat over central and eastern Montana resulted in a rapidly declining Palmer Severity Drought Index, which, although of short duration, reached extreme drought levels comparable to those of historical droughts (e.g., during the 1930s). The occurrence of the drought over Montana and the Dakotas, an important spring wheat-growing region in the country, during the crop growing season caused agricultural losses of \$2.5 billion and contributed to one of Montana's worst wildfire seasons on record (NOAA/NCEI 2018).

This study investigates the causes of the 2017 northern High Plains drought, particularly the roles of the 2017 sea surface temperature (SST) anomalies and atmospheric internal variability. It also assesses the impact of the post-1901 long-term warming trend on the frequency of drought occurrence in the area.

DATA AND METHODS. This study makes use of various observational datasets, including the NOAA Extended Reconstructed SST (ERSST) version 5 (Huang et al. 2017), the Global Precipitation Climatology Project (GPCP) precipitation (Adler et al. 2003), and the Global Precipitation Climatology Centre (GPCC) land precipitation (Schneider et al. 2014). Data from the NASA Modern-Era Retrospective Analysis for Research and Applications, version 2 (MERRA-2; Gelaro et al. 2017) are used as well.

The study also utilizes two sets of Atmospheric Model Intercomparison Project (AMIP) simulations performed with the NASA Goddard Earth Observing System Model, version 5 (GEOS-5) atmospheric general circulation model (AGCM) (Rienecker et al. 2008; Molod et al. 2012), forced with observed monthly SST, sea ice, and time-varying greenhouse gases (Schubert et al. 2014). The first set is used to investigate the impacts of the 2017 SST anomalies and atmospheric internal variability on the drought event in the context of current climate; here, a GEOS-5 (tag: Ganymed 4.0) AMIP simulation covering 1980–2014 provided a climatology, and a 90-member ensemble of AMIP simulations performed for 2017 provided a robust estimate of model atmospheric internal variability during that year. These AMIP runs employed a tendency bias correction to the basic state variables (estimated from the time-mean MERRA-2 analysis increments) that removes much of the model bias in the mean climate and its variability (Wang et al. 2018). The second set of AMIP simulations consists of 12 archived long-

AFFILIATIONS: WANG—Science Systems and Applications, Inc., Lanham, Maryland; SCHUBERT—Global Modeling and Assimilation Office, NASA Goddard Space Flight Center, Greenbelt, and Science Systems and Applications, Inc., Lanham, Maryland; KOSTER—Global Modeling and Assimilation Office, NASA Goddard Space Flight Center, Greenbelt, Maryland; CHANG—Global Modeling and Assimilation Office, NASA Goddard Space Flight Center, Greenbelt, and Morgan State University, Baltimore, Maryland

CORRESPONDING AUTHOR: Dr. Hailan Wang, hailan.wang-1@nasa.gov

DOI:10.1175/BAMS-D-18-0115.1

A supplement to this article is available online (10.1175/BAMS-D-18-0115.2)

© 2019 American Meteorological Society

For information regarding reuse of this content and general copyright information, consult the [AMS Copyright Policy](#).

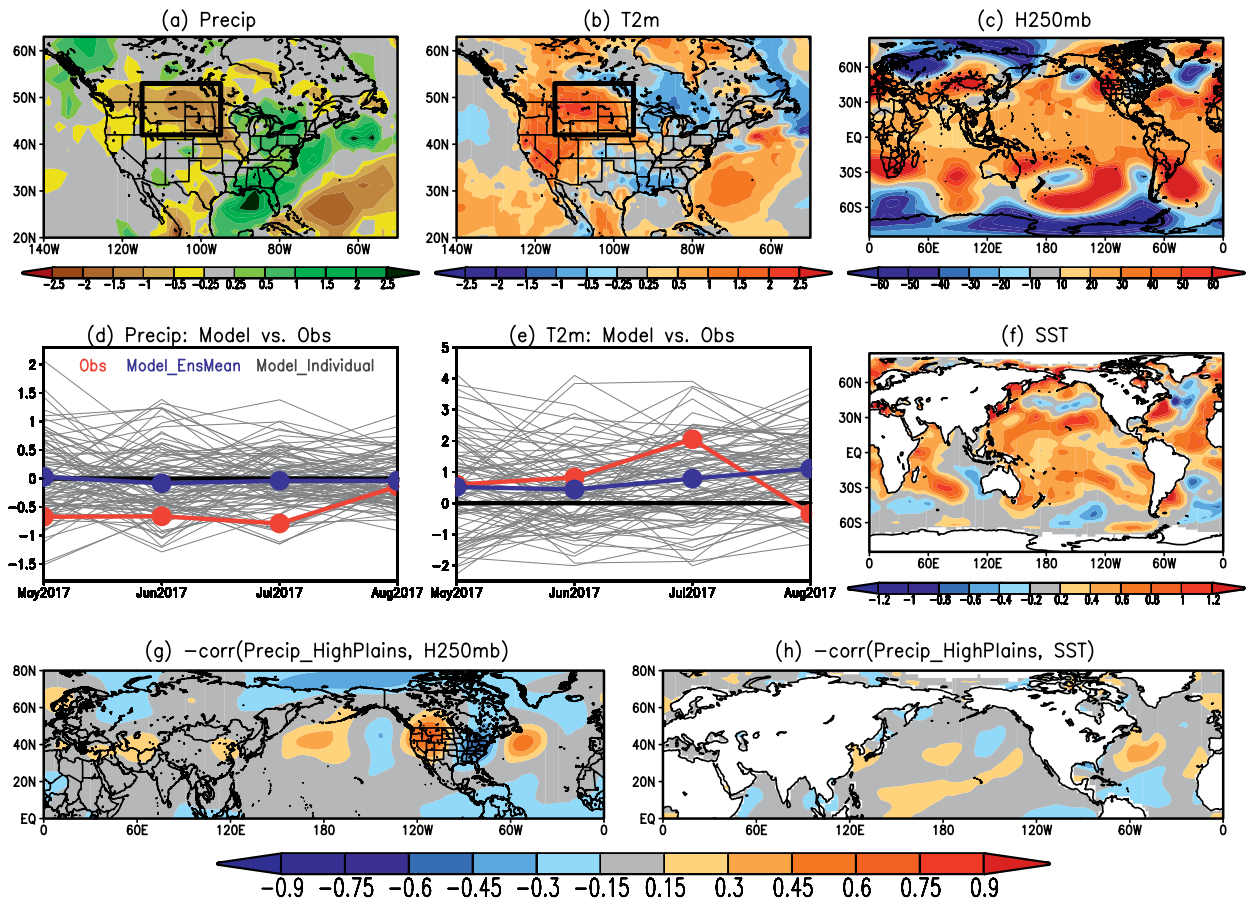


FIG. 1. The observed May–July 2017 anomalies in (a) precipitation from GPCP (mm day^{-1}), (b) surface air temperature anomalies (K) from MERRA-2, and (c) 250-mb geopotential height (m) from MERRA-2. (d) The comparison between observations (GPCP), the 90 GEOS-5 AMIP members, and their ensemble mean for monthly precipitation anomalies (mm day^{-1}) averaged over the 2017 drought region ($245^{\circ}\text{--}265^{\circ}\text{E}$, $42^{\circ}\text{--}53^{\circ}\text{N}$) for May–August 2017. (e) As in (d), but for surface air temperature (K). (f) As in (a), but for NOAA SST (unit: K). (g) The temporal correlation between GPCP precipitation averaged over the 2017 drought region and MERRA-2 250-mb geopotential height for May–July averages for 1980–2017; (h) as in (g), but for NOAA SST. The above anomalies are obtained as deviations from their climatology over the period 1980–2014. The 2017 drought region is indicated using a black box in (a) and (b).

term simulations (1901–2014) performed with an earlier version of the GEOS-5 AGCM (tag: Fortuna 2.4) (Schubert et al. 2014); it is used to assess the effects of historical warming. The dependence of the attribution analysis on climatologies used and the model dependence of our assessments are examined by also considering long-term NCAR CAM5 AMIP simulations (1901–2017; 40 members).¹ Since the precipitation deficit and surface warming anomalies in the northern High Plains mainly occurred during May–July 2017, our analyses focus on the average of these three months.

¹ The long-term NCAR CAM5 AMIP simulations are produced by the NOAA ESRL Attribution and Predictability Assessments Team and are made available at the NOAA/ESRL/PSD Climate Data Repository (www.esrl.noaa.gov/psd/repository/alias/facts).

RESULTS. Figure 1 examines the 2017 northern High Plains drought relative to the 1980–2014 climatology. The observed May–July averaged precipitation deficits occurred over the northern Plains and southern Canadian prairies (Fig. 1a). Meanwhile, much of the western half of the United States experienced warmer-than-normal temperatures, with peak warming over Montana, the Dakotas, and the southwestern United States (Fig. 1b). The accompanying geopotential height anomalies in the upper troposphere consisted of widespread warming in the tropics and much of the midlatitudes, a reflection of global SST warming trends during recent decades (e.g., Schubert et al. 2014), as well as a zonal wave train that spans the North Pacific and North America, with an anomalous barotropic high centered over the northwestern United States (Fig. 1c). The high anomaly, which

persisted throughout much of May–July 2017 (not shown), contributed to the local surface warming by suppressing the formation of local convection and clouds and leading to increased solar radiation at the surface. Meanwhile, the northerly anomaly at its east flank in the lower troposphere weakened the Great Plains low-level jet (LLJ) and inhibited northward atmospheric moisture transport by the jet, leading to precipitation deficits in the northern High Plains.

To investigate the physical processes for the 2017 drought event, we compared anomalies from the first set of GEOS-5 AMIP simulations with observations (Figs. 1d,e). Here the model ensemble average highlights the SST-forced signal, whereas the spread among the ensemble members reflects the unforced variability generated by processes internal to the atmosphere. The observed SST anomalies show warming over much of the tropical and subtropical oceans (Fig. 1f). When forced with these SST anomalies, the ensemble mean of the GEOS-5 AGCM simulations shows little change in precipitation but a notable surface warming in the northern High Plains. The observed anomalies fall within the fairly large model ensemble spread, with the observed precipitation anomalies falling near the dry edge of the spread. Only three ensemble members (out of 90) show persistent dry and warm responses similar to the observations. These results suggest that the 2017 warm SST anomalies encouraged surface warming in the northern High Plains, while atmospheric internal variability explains much of the precipitation deficits. A parallel analysis using the CAM5 AMIP simulations (1901–2017) shows that the above conclusion is not changed when viewed in the context of the century long (1901–2014) climate (cf. Figs. 1d,e with Figs. ES1c–f); furthermore, it appears that much of the 2017 SST-forced surface warming in the northern High Plains is a response to the long-term SST warming trend (see the online supplemental information). Figure 1g shows that the year-to-year variation of summertime precipitation in the northern High Plains is typically associated with a zonal wave train (of roughly wavenumber 5) in the NH midlatitudes; its connection to SST is weak overall (Fig. 1h). Such a wave train resembles the leading patterns of upper-level circulation variability within the jet waveguide during boreal summer (Ding and Wang 2005; Schubert et al. 2011). The nature of the drought-inducing atmospheric internal variability is yet unclear and needs further research.

In our second analysis, we investigate the effect of historical warming on the occurrence of extreme dry events in the northern High Plains by compar-

ing two time periods from the long-term GEOS-5 AMIP simulations: 1901–70 and 1980–2014, with the latter period coinciding with the start of a period of enhanced global warming. The May–July mean SST differences between the two periods (Fig. 2a) reflects the long-term warming trend over the twentieth century, as evidenced by its resemblance to the SST warming trend pattern that is obtained as the leading rotated empirical orthogonal function (REOF) of annual mean SST over 1901–2004 (Schubert et al. 2009). Most of the effects of decadal to multidecadal oscillations (e.g., the Pacific decadal oscillation and Atlantic multidecadal oscillation) are thus averaged out in the two periods. Relative to the early period, the ensemble mean upper-level geopotential height in the latter period (Fig. 2b) increases nearly everywhere, with local maxima occurring over the northwestern United States and the Bering Sea, presumably forced by the long-term SST changes (Fig. 2a). In fact, such atmospheric circulation changes resemble the responses of this model and four other AGCMs participating in the U.S. CLIVAR drought working group (Schubert et al. 2009) to the above-mentioned SST warming trend pattern (not shown), suggesting that the circulation changes in Fig. 2b are a robust dynamical response to the warming trend pattern.

We investigate the effects of historical global warming on the occurrence of drought extremes in the northern High Plains by comparing the probability density functions (PDFs) of drought-related variables in the two periods. The precipitation PDFs in the northern High Plains for the two periods are very similar (Fig. 2c), consistent with indications from GPCC observations (not shown). There are, however, clear indications of an increased probability of warmer surface air temperature in the recent period (Fig. 2d), which leads to a modest increase in the risk for drier soil (Fig. 2e). The AMIP simulations thus suggest that agricultural droughts (soil moisture deficits) are more probable during recent times. Evapotranspiration shows a slight net decrease (not shown), a reflection of the slight decrease in precipitation. There are also clear indications of an increased probability of a moister atmosphere over the central United States (Fig. 2f) and increased eddy height anomalies over the northwestern United States (Fig. 2g). While the moister atmosphere tends to increase atmospheric moisture transport to the northern High Plains and thus precipitation there, the increased eddy height anomalies tend to reduce this precipitation by inducing subsidence in the northern High Plains as well as by weakening the Great Plains LLJ. In other words, the modest

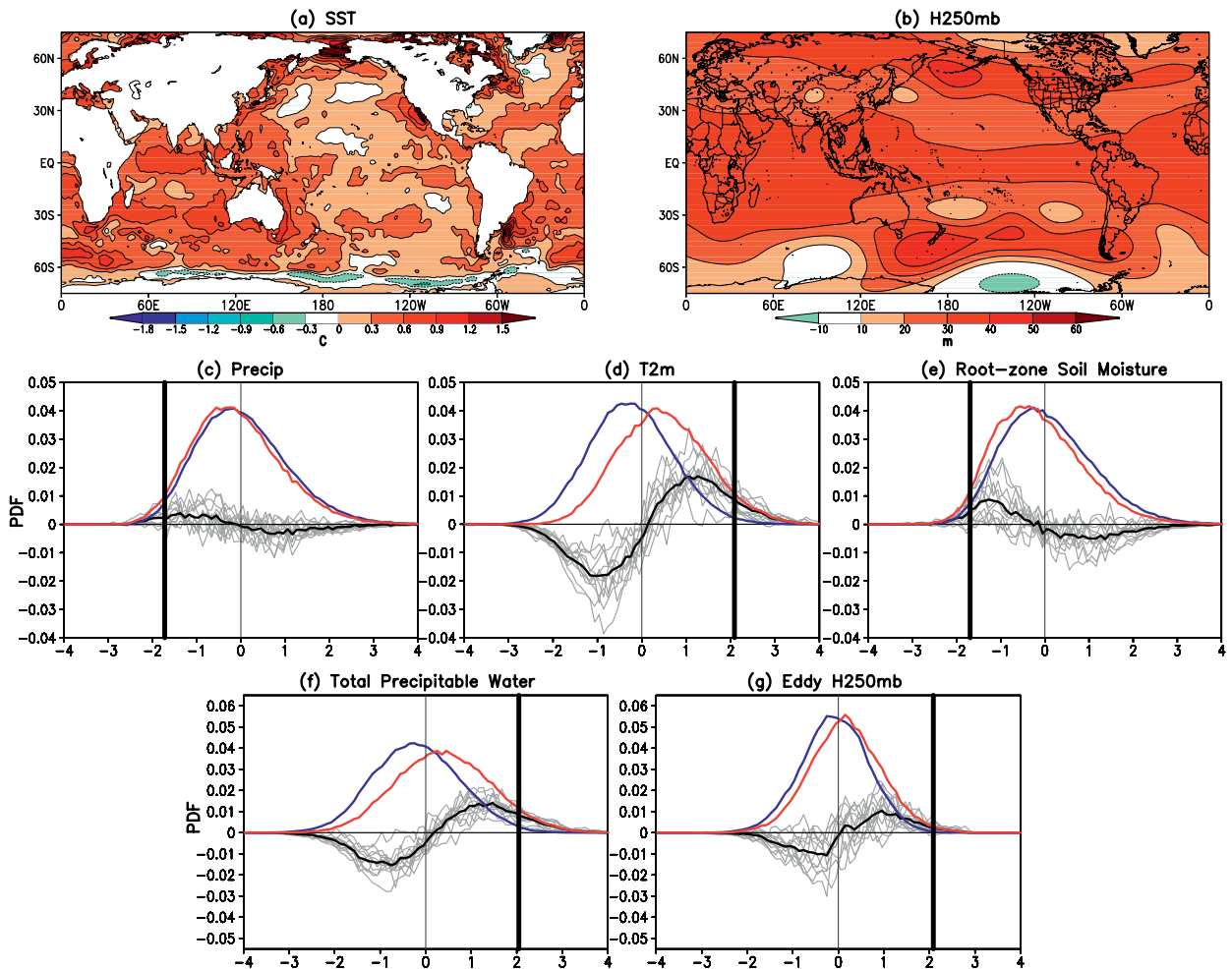


FIG. 2. (a) The observed climatology difference of May–July SST between the periods 1901–70 and 1980–2014. (b) As in (a), but for the 250-mb geopotential height in the GEOS-5 AMIP ensemble mean simulation. (c) The PDF of precipitation over the 2017 drought region (245° – 265° E; 42° – 53° N) for the periods 1901–70 (blue) and 1980–2014 (red) using the 12 GEOS-5 AMIP simulations combined, the PDF difference between the two time periods using the 12 AMIP simulations combined (black), and each of the 12 AMIP simulations (gray). (d),(e) As in (c), but respectively for surface air temperature and root-zone soil moisture (moisture in the top meter of soil, as determined from soil moisture prognostic states in the GEOS-5 land surface model). (f),(g) As in (c), but respectively for total column water vapor over the central United States (245° – 265° E; 30° – 45° N) and the 250-mb zonally asymmetric geopotential height over the northwestern United States (232° – 257° E, 35° – 52° N). The critical values of 2.5% associated with dry conditions based on the distribution over 1901–2014 are shown using thick black vertical lines. [Note that the PDF analysis in (c)–(g) uses data at all grid points in the selected domains. Anomalies used in the PDF analysis are normalized deviations from the climatology over the period 1901–2014.]

change in the precipitation PDF (Fig. 2c) appears to reflect counteracting impacts of the thermodynamic and dynamical processes. A parallel analysis using the CAM5 simulations (Fig. ES2) produces results similar to those based on the GEOS-5 model (Fig. 2), supporting that our findings are not model dependent. We also emphasize that the impact of dynamical processes examined here reflects the model's response to the observed SST changes that occurred during the period of 1901–2014. As such, the dynamical impact may be different in models

(e.g., CMIP5 historical simulations) that simulate mean SST changes different from the observed.

CONCLUSIONS. The 2017 northern High Plains drought and associated heat waves were induced in part by a positive height anomaly that persisted over the northwestern United States and the northern High Plains throughout much of May–July 2017. Our model results show that while the observed 2017 SST anomalies provided a predilection for drought by inducing surface warming, internal atmospheric vari-

ability accounts for the extreme precipitation deficits.

An assessment of the role of historical global warming shows no appreciable increase in the risk of precipitation deficits but an increased risk of heat waves in the northern High Plains. In fact, a substantial fraction of the 2017 SST-forced surface warming appears to be a response to the global warming signal. The small change in the probability of precipitation deficits over the historical period appears to reflect counteracting effects of thermodynamic processes (increased atmospheric moisture over the United States) and dynamical processes (increased eddy height over the northwestern United States). The increased risk for heat waves may have increased the likelihood of agricultural (soil moisture) drought in the region, and contributed to exacerbating the 2017 drought.

ACKNOWLEDGMENTS. This work has been supported by the NOAA Climate Program Office Modeling, Analysis, Prediction, and Projections (MAPP) program and the NASA Modeling, Analysis and Prediction (MAP) program. We thank Peter Stott, Martin Hoerling, and two anonymous reviewers for their constructive comments and suggestions, which have greatly improved the paper.

REFERENCES

- Adler, R. F., and Coauthors, 2003: The version-2 Global Precipitation Climatology Project (GPCP) monthly precipitation analysis (1979–present). *J. Hydro-meteor.*, **4**, 1147–1167, [https://doi.org/10.1175/1525-7541\(2003\)004<1147:TVGPCP>2.0.CO;2](https://doi.org/10.1175/1525-7541(2003)004<1147:TVGPCP>2.0.CO;2).
- Ding, Q., and B. Wang, 2005: Circumglobal teleconnection in the Northern Hemisphere summer. *J. Climate*, **18**, 3483–3505, <https://doi.org/10.1175/JCLI3473.1>.
- Gelaro, R., and Coauthors, 2017: The Modern-Era Retrospective Analysis for Research and Applications, version 2 (MERRA-2). *J. Climate*, **30**, 5419–5454, <https://doi.org/10.1175/JCLI-D-16-0758.1>.
- Huang, B., and Coauthors, 2017: Extended Reconstructed Sea Surface Temperature version 5 (ERSSTv5), Upgrades, validations, and intercomparisons. *J. Climate*, **30**, 8179–8205, <https://doi.org/10.1175/JCLI-D-16-0836.1>.
- Molod, A., L. Takacs, M. Suarez, J. Bacmeister, I.-S. Song, and A. Eichmann, 2012: The GEOS-5 atmospheric general circulation model: Mean climate and development from MERRA to Fortuna. NASA Technical Report Series on Global Modeling and Data Assimilation, NASA TM-2012-104606, Vol. 28, 117 pp.
- NOAA/NCEI, 2018: Billion-dollar weather and climate disasters. NOAA National Centers for Environmental Information, www.ncdc.noaa.gov/billions/.
- Rienecker, M. M., and Coauthors, 2008: The GEOS-5 data assimilation system—Documentation of versions 5.0.1, 5.1.0, and 5.2.0. NASA Tech. Rep. Series on Global Modeling and Data Assimilation, NASA/TM-2007-104606, Vol. 27, 95 pp.
- Schneider, U., A. Becker, P. Finger, A. Meyer-Christoffer, M. Ziese, and B. Rudolf, 2014: GPCC's new land surface precipitation climatology based on quality-controlled in situ data and its role in quantifying the global water cycle. *Theor. Appl. Climatol.*, **115**, 15–40, <https://doi.org/10.1007/s00704-013-0860-x>.
- Schubert, S., and Coauthors, 2009: A U.S. CLIVAR project to assess and compare the responses of global climate models to drought-related SST forcing patterns: Overview and results. *J. Climate*, **22**, 5251–5272, <https://doi.org/10.1175/2009JCLI3060.1>.
- , H. Wang, and M. Suarez, 2011: Warm season subseasonal variability and climate extremes in the Northern Hemisphere: The role of stationary Rossby waves. *J. Climate*, **24**, 4773–4792, <https://doi.org/10.1175/JCLI-D-10-05035.1>.
- , —, R. Koster, M. Suarez, and P. Groisman, 2014: Northern Eurasian heat waves and droughts. *J. Climate*, **27**, 3169–3207, <https://doi.org/10.1175/JCLI-D-13-00360.1>.
- Wang, H., S. D. Schubert, Y. Chang, and R. D. Koster, 2018: Subseasonal prediction of warm season drought in North America. *42nd NOAA Climate Diagnostics and Prediction Workshop*, Norman, OK, National Weather Service, www.cpc.ncep.noaa.gov/products/outreach/CDPW42/11-Wang.pdf.

THE EXTREMELY WET MARCH OF 2017 IN PERU

NIKOLAOS CHRISTIDIS, RICHARD A. BETTS, AND PETER A. STOTT

While extreme rainfall of March 2017 in Peru was favored by the anomalously warm ocean, human influence is also estimated to make such events at least 1.5 times more likely.

INTRODUCTION. Peru's rainy season falls in the first quarter of the year, often dubbed the "landslide season," with the direst downpours typically occurring in March (Lavado Casimiro et al. 2012). The rains of March 2017, however, were deadlier than usual and wreaked unprecedented havoc, leaving half of the country in a state of emergency. Widespread flooding and landslides affected 1.7 million people, while the death toll reached 177 and an estimated total damage of \$3.1 billion was reported (EM-DAT 2017). Anomalously warm sea surface temperatures (SSTs) in the region, characteristic of El Niño conditions, favor extreme rainfall (Sanabria et al. 2018). Although a marked SST anomaly was present off the Peruvian coast at the time of the event (Fig. 1a), the strong global El Niño of 2015–16 had already come to an end, as demonstrated in the time series of the Southern Oscillation index (SOI; CPC 2017) shown in Fig. 1b. The ocean at the peak of the March rains was warmer than during the preceding El Niño (Fraser 2017), creating conditions that are commonly referred to as a "local" or "coastal" El Niño, also reflected in the anomalously high value of the Niño 1 + 2 index in March (Trenberth et al. 2016). A possible atmospheric triggering mechanism of the 2017 coastal warming was proposed by Garreaud (2018). While the presence of a warm SST anomaly increases the likelihood of extreme rainfall in the region, anthropogenic climate change may also make a contribution, for example, via a long-term warming of the ocean (Rhein et al. 2013)

that could intensify the local El Niño. A similarly catastrophic event associated with the El Niño of 1998 amassed more rainfall in the region, but, as reported in the media, what made March 2017 distinct was the fact that heavier rainfall fell in shorter periods. This study employs a well-established probabilistic event attribution methodology (Stott et al. 2016) to examine the effect of man-made climate change on extreme rainfall events in Peru similar to 2017, over the entire month of March, as well as on shorter, submonthly time scales.

Data and methods. Attribution analyses use classes of extreme events that share some basic characteristics with the event under investigation (Christidis et al. 2018). Here, extreme rainfall averaged over the Peruvian region (69° – 83° E, 0° – 20° S) is defined as the exceedance of a high threshold. Three climatological thresholds are employed to examine extremes of different rarity, namely the 1-in-10-, 1-in-50-, and 1-in-100-yr events during 1960–2015. This period is modeled by 15 ensemble simulations of the historical climate with HadGEM3-A, the model underpinning the Hadley Centre's event attribution system (Christidis et al. 2013; Ciavarella et al. 2018). Different event durations are also considered by computing the average rainfall over the month of March, the 10 and 5 wettest consecutive days in March (R10x and R05x), and the wettest day of that month (R01x). The monthly mean anomaly pattern in March 2017 computed with data from the NCEP–NCAR reanalysis (Kalnay et al. 1996) is illustrated in Fig. 1c. The total rainfall over the reference region is about 5 standard deviations above the historical mean estimated with the reanalysis data and this is also the case in subregions over the mountains and to the east of the Andes (see the online supplemental material). March rainfall time series constructed with NCEP–NCAR and HadGEM3-A data are shown in Fig. 1d. Year 2017 stands out as a record in the reanalysis, which is also found to be the case in the shorter GPCP dataset (Huffman et al. 2009), but not in the GPCC record

AFFILIATIONS: CHRISTIDIS, BETTS, AND STOTT—Met Office Hadley Centre, Exeter, United Kingdom

CORRESPONDING AUTHOR: Nikolaos Christidis, nikos.christidis@metoffice.gov.uk

DOI:10.1175/BAMS-D-18-0110.1

A supplement to this article is available online (10.1175/BAMS-D-18-0110.2)

© 2019 American Meteorological Society

For information regarding reuse of this content and general copyright information, consult the [AMS Copyright Policy](#).

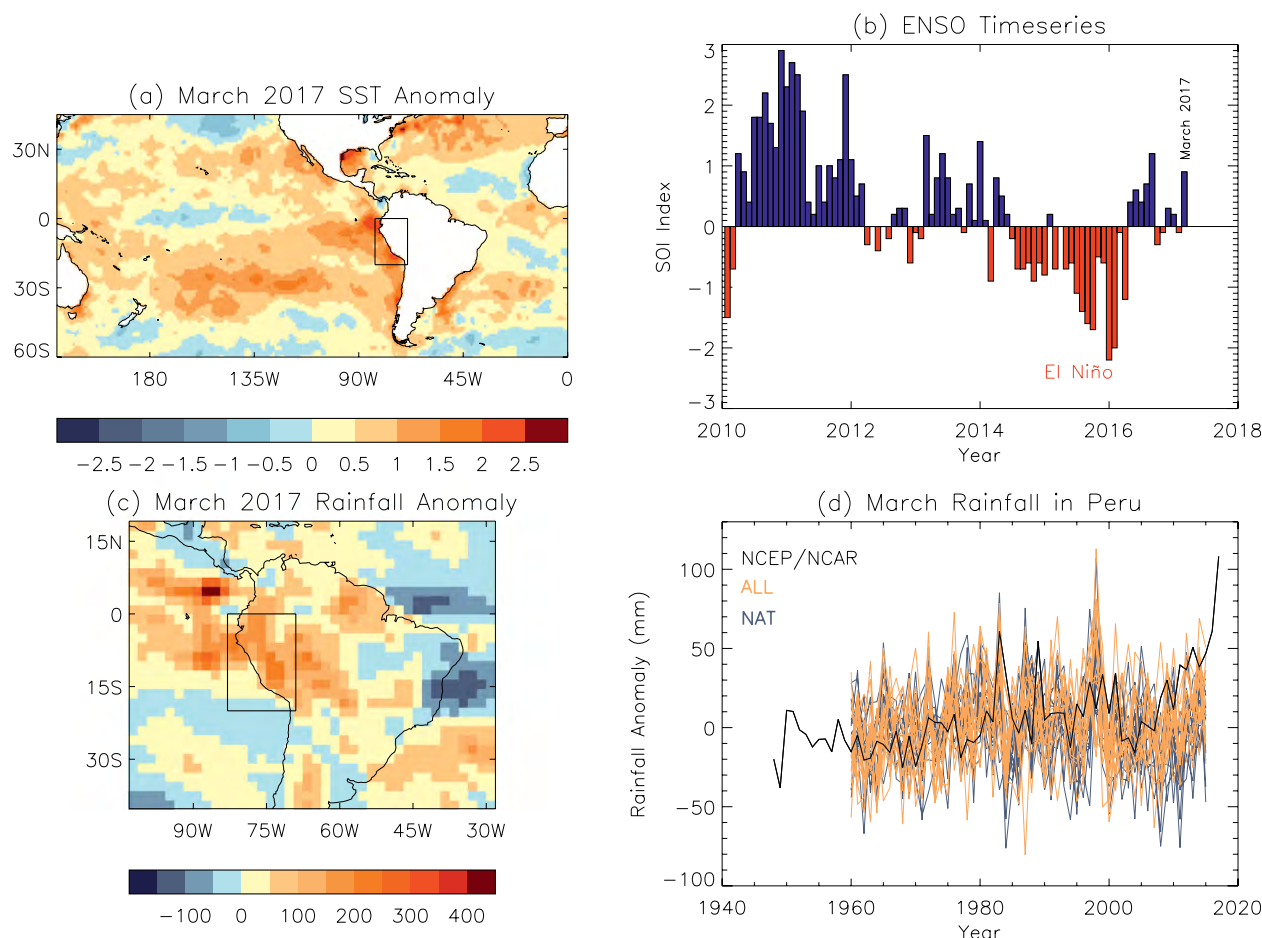


FIG. 1. (a) Mean SST anomalies (°C) in March 2017 from HadISST. (b) Time series of monthly SOI values in recent years. Negative values (in red) indicate El Niño and positive values (in blue) La Niña conditions. (c) Mean rainfall anomalies (mm) in March 2017 estimated with NCEP–NCAR reanalysis data. (d) Time series of the March mean rainfall anomaly in the region of Peru constructed with NCEP–NCAR reanalysis data (black line) and HadGEM3-A data from the ALL (orange lines) and NAT (blue lines) multidecadal simulations. All anomalies are relative to 1961–90. The black box in (a) and (b) marks the study area.

(Schneider et al. 2016). Rainfall over shorter time scales (R10x, R05x, R01x) is found to reach record levels in 2017 as well. Time series from the long (multidecadal) HadGEM3-A simulations are also shown in Fig. 1d. In addition to the experiment representing the historical climate that includes all (both natural and anthropogenic) external forcings (experiment ALL), a second set of 15 simulations has also been produced, representing a hypothetical natural climate without anthropogenic forcings (NAT). HadGEM3-A is an atmospheric model and therefore oceanic conditions need to be prescribed. In the ALL experiment these come from the HadISST dataset (Rayner et al. 2003). In the NAT simulations, an estimate of the anthropogenic SST change is subtracted from the observations, obtained from simulations with 19 coupled models (<http://portal.nersc.gov/c20c/experiment.html>) and simple empirical relationships are used to adjust the sea

ice to cooler SSTs (Christidis et al. 2013). The rainfall time series display characteristic peaks during major El Niño events (e.g., 1982/83), also evident in the model simulations which retain the ENSO signal through the prescribed boundary conditions. Interestingly, the 1997/98 El Niño, which had devastating impacts in Peru, is more pronounced in the model, probably indicating a reanalysis shortcoming.

This study addresses two questions: 1) Has anthropogenic influence altered the likelihood of the 2017 extreme rainfall in Peru, given the warm oceanic anomaly present at the time? 2) How does the presence of such an SST anomaly affect the current likelihood of extreme rainfall in the region? To answer these questions the Hadley Centre’s event attribution system is employed. Large 525-member ensembles of ALL and NAT simulations of the first quarter of 2017 were generated, as part of the sys-

tem's quasi-operational setup. The coastal El Niño is also manifest in the NAT simulations, although the cooler ocean under preindustrial conditions takes the edge off the intensity of the 2017 anomaly (see the online supplemental material). The first question of the study is addressed by comparing estimated probabilities of extremes obtained with the ALL and NAT simulations of March 2017 (525 estimates per experiment). The impact of the coastal El Niño in the present-day climate is examined by comparing the 525 ALL simulations for 2017 with their counterparts of the historical climate, from which the last 10 years (2006–15) are extracted. The selected years provide a sample of 150 (15 runs \times 10 yr) probability estimates and are used as a proxy of the current climate under any oceanic conditions. Near-zero mean March SST anomalies over this decade (see the supplemental material) indicate no SST bias in the near-present-day climate. As in previous work, extreme probabilities are computed with the generalized Pareto distribution and their associated uncertainties with a Monte Carlo bootstrap procedure (Christidis et al. 2013). It is essential that models in attribution studies are evaluated to establish whether they are fit for the purpose (Vautard et al. 2018). Despite the lack of long and reliable observational rainfall records for Peru available to the authors, standard evaluation assessments against reanalysis data applied to HadGEM3-A indicate that the model's representation of rainfall variability and extremes in the region is consistent with the reanalysis (see the supplemental material).

While it cannot be established beyond doubt that the modeled rainfall over the complex topography of the study region is reliable, the attribution results presented below ought to be viewed in the light of this uncertainty.

Results. Return times (reverse probabilities) of extreme rainfall events are reported in Table 1. A comparison between the ALL and NAT estimates for 2017 indicates that anthropogenic forcings unambiguously increase the likelihood of extremes across events of different rarity and duration. Human influence leads to a shift in the March rainfall distribution illustrated in Fig. 2a (similar shifts also found for shorter rainfall durations). The estimated risk ratios plotted in Fig. 2b reveal greater anthropogenic influence on rarer events (1 in 100 yr), although the uncertainty in the likelihood of these events also increases. The effect of the warm SSTs is inferred by comparing ALL simulations of 2017, when a strong anomaly was present, with ALL simulations of recent years representing a wider range of oceanic conditions. Figures 2c and 2d show that the SST anomaly of 2017 leads to a marked shift in the rainfall distribution and in most cases increases the likelihood of extremes by at least a factor of 3. The probabilities of the rarer events without the effect of a strong SST anomaly are very small and hence their estimates suffer from large uncertainties (Table 1). Risk ratios estimated in subregions with different topography indicate no peculiar orographic effect on the attribution findings (supplemental material). It should be noted that

TABLE 1. Return times (in years) of high rainfall events in Peru estimated using the ALL and NAT experiments for year 2017 and the multidecadal ALL simulations for years 2006–15. Estimates are provided for the total rainfall in March, the 10 and 5 wettest consecutive days, and the wettest day in March. The best estimate (50th percentile) of the return time is reported together with the 5%–95% uncertainty range (in parentheses).

	March	R10x	R05x	R01x
1-in-10-yr events				
ALL 2017	1.99 (1.85 to 2.14)	2.10 (1.95 to 2.27)	2.22 (2.06 to 2.43)	3.62 (3.14 to 4.08)
NAT 2017	3.44 (3.08 to 3.90)	3.40 (3.05 to 3.83)	4.26 (3.79 to 4.74)	6.91 (5.88 to 8.25)
ALL 2006–15	10.23 (6.88 to 17.08)	9.41 (7.02 to 13.65)	12.25 (7.48 to 19.40)	10.39 (5.75 to 22.64)
1-in-50-yr events				
ALL 2017	6.02 (5.23 to 6.98)	8.71 (7.45 to 10.22)	10.19 (8.71 to 12.24)	14.48 (11.78 to 18.47)
NAT 2017	19.51 (15.33 to 25.97)	22.02 (17.10 to 29.91)	46.92 (33.06 to 72.72)	34.92 (25.43 to 51.07)
ALL 2006–15	Large uncertainty (45 to >10 ⁴)			
1-in-100-yr events				
ALL 2017	12.09 (9.60 to 15.46)	19.25 (15.46 to 25.27)	23.97 (18.88 to 32.46)	20.23 (15.89 to 26.56)
NAT 2017	55.28 (40.02 to 88.93)	74.26 (49.45 to 131)	1945 (523 to >10 ⁴)	56.93 (39.13 to 96.06)
ALL 2006–15	Large uncertainty (100 to >10 ⁴)			

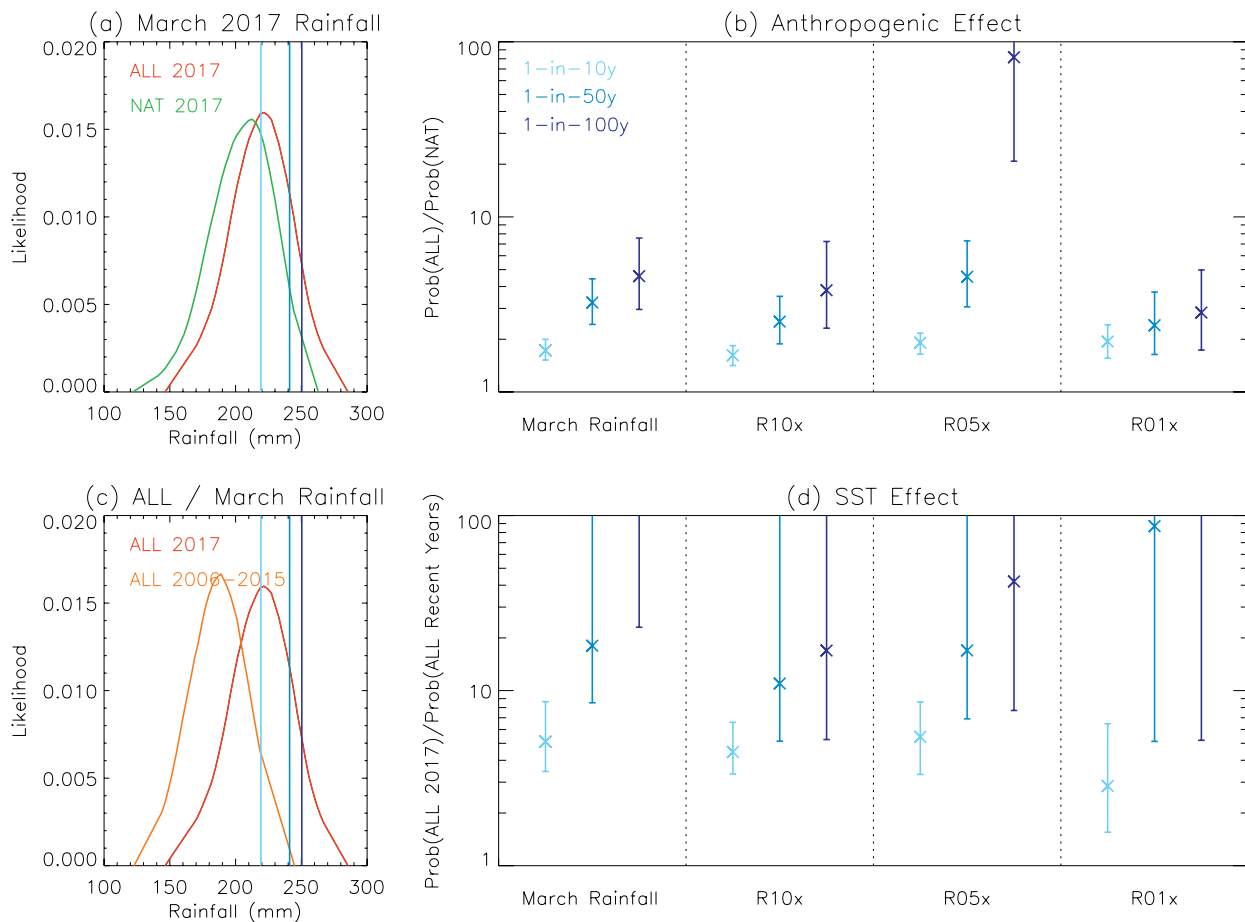


FIG. 2. (a) Normalized distributions of the March 2017 mean rainfall in Peru constructed with data from the ALL (red) and NAT (green) experiments. Events with different climatological return times (1-in-10-, 1-in-50-, and 1-in-100-yr) are represented by the vertical blue lines. (b) Risk ratio estimates showing the effect of human influence on March rainfall, R10x, R05, and R01x extremes. Events with different climatological return times are represented by different shades of blue. The best estimate (50th percentile) is marked by a cross and the 5%–95% uncertainty range by whiskers. (c) As in (a), but for distributions constructed with data from the ALL experiments for March 2017 (red line) and the same month in years 2006–15 (orange line). (d) As in (b), but for the effect of the 2017 SST anomalies on rainfall extremes.

uncertainties related to the boundary conditions and model's ability to represent regional rainfall are also present and will affect to some extent the attribution results shown here.

Conclusions. Coastal El Niño conditions and man-made climate change both favor extreme rainfall in Peru. When the effect of large positive SST anomalies similar to 2017 is factored in, wet extremes are estimated to be at least 1.5 times more likely to happen (or 2–3 times for more rare events) compared to pre-industrial times. The coastal El Niño is estimated to increase the likelihood of extremes 3–6 times (best estimate), or more than 10 times for rarer events. Although model dependency, and in particular the uncertainty in the NAT boundary conditions, may affect the estimated probabilities (Christidis and

Stott 2014), it was verified that the modeled oceanic warming used in this study to produce the boundary conditions is broadly consistent with observed SST trends in the region, which increases confidence in the results. Uncertainty about the accuracy of the simulated rainfall in the region remains the major caveat of this study, traced to the lack of reliable observational datasets for a detailed model evaluation. Hence, the attribution results reported here only provide a useful first assessment of the event's main drivers rather than a definitive measure of their effect. Moving toward the integration of the Hadley system into an attribution service that outputs assessments of extremes on a regular basis, could be key to well-informed decision-making, especially in the aftermath of catastrophic events like the one investigated here.

ACKNOWLEDGMENTS. This work was supported by the Joint DECC/Defra Met Office Hadley Centre Climate Programme (GA01101) and the EUPHEME project, which is part of ERA4CS, an ERA-NET initiated by JPI Climate and co-funded by the European Union (Grant 690462).

REFERENCES

- Christidis, N., and P. A. Stott, 2014: Change in the odds of warm years and seasons due to anthropogenic influence on the climate. *J. Climate*, **27**, 2607–2621, <https://doi.org/10.1175/JCLI-D-13-00563.1>.
- , —, A. Scaife, A. Arribas, G. S. Jones, D. Copsey, J. R. Knight, and W. J. Tennant, 2013: A new HadGEM3-A based system for attribution of weather- and climate-related extreme events. *J. Climate*, **26**, 2756–2783, <https://doi.org/10.1175/JCLI-D-12-00169.1>.
- , A. Ciavarella, and P. A. Stott, 2018: Different ways of framing event attribution questions: The example of warm and wet winters in the United Kingdom similar to 2015/16. *J. Climate*, **31**, 4827–4845, <https://doi.org/10.1175/JCLI-D-17-0464.1>.
- Ciavarella, A., and Coauthors, 2018: Upgrade of the HadGEM3-A based attribution system to high resolution and a new validation framework for probabilistic event attribution. *Wea. Climate Extremes*, **20**, 9–32, <https://doi.org/10.1016/j.wace.2018.03.003>.
- CPC, 2017: Southern Oscillation Index (SOI): (Stand Tahiti—Stand Darwin) sea level pressure data. Climate Prediction Center, accessed June 2017, www.cpc.ncep.noaa.gov/data/indices/soi.
- EM-DAT, 2017: The Emergency Events Database. Centre for Research on the Epidemiology of Disasters, accessed December 2017, www.emdat.be.
- Fraser, B., 2017: Peru's floods teach tough lessons. *Nature*, **544**, 405–406, <https://doi.org/10.1038/544405a>.
- Garreaud, R., 2018: A plausible atmospheric trigger for the 2017 coastal El Niño. *Int. J. Climatol.*, **38**, e1296–e1302, <https://doi.org/10.1002/joc.5426>.
- Huffman, G. J., R. F. Adler, D. T. Bolvin, and G. Gu, 2009: Improving the global precipitation record: GPCP version 2.1. *Geophys. Res. Lett.*, **36**, L17808, <https://doi.org/10.1029/2009GL040000>.
- Kalnay, E., and Coauthors, 1996: The NCEP/NCAR 40-Year Reanalysis Project. *Bull. Amer. Meteor. Soc.*, **77**, 437–471, [https://doi.org/10.1175/1520-0477\(1996\)077<0437:TNYRP>2.0.CO;2](https://doi.org/10.1175/1520-0477(1996)077<0437:TNYRP>2.0.CO;2).
- Lavado Casimiro, W. S., J. Ronchail, D. L. Labat, J. C. Espinoza, and J. L. Guyot, 2012: Basin-scale analysis of rainfall and runoff in Peru (1969–2004): Pacific, Titicaca and Amazonas drainages. *Hydrol. Sci. J.*, **57**, 625–642, <https://doi.org/10.1080/02626667.2012.672985>.
- Rayner, N. A., D. E. Parker, E. B. Horton, C. K. Folland, L. V. Alexander, D. P. Rowell, E. C. Kent, and A. Kaplan, 2003: Global analyses of sea surface temperature, sea ice, and night marine air temperature since the late nineteenth century. *J. Geophys. Res.*, **108**, 4407, <https://doi.org/10.1029/2002JD002670>.
- Rhein, M., and Coauthors, 2013: Observations: Ocean. *Climate Change 2013: The Physical Science Basis*, T. F. Stocker et al., Eds., Cambridge University Press, 255–315.
- Sanabria, J., L. Bourrel, B. Dewitte, F. Frappart, P. Rau, O. Solis, and D. Labat, 2018: Rainfall along the coast of Peru during strong El Niño events. *Int. J. Climatol.*, **38**, 1737–1747, <https://doi.org/10.1002/joc.5292>.
- Schneider, U., M. Ziese, A. Meyer-Christoffer, P. Finger, E. Rustemeier, and A. Becker, 2016: The new portfolio of global precipitation data products of the Global Precipitation Climatology Centre suitable to assess and quantify the global water cycle and resources. *Proc. IAHS*, **374**, 29–34, <https://doi.org/10.5194/piahs-374-29-2016>.
- Stott, P. A., and Coauthors, 2016: Attribution of extreme weather and climate-related events. *Wiley Interdiscip. Rev.: Climate Change*, **7**, 23–41, <https://doi.org/10.1002/wcc.380>.
- Trenberth, K., and Coauthors, Eds., 2016: The Climate Data Guide: Nino SST Indices (Nino 1+2, 3, 3.4, 4; ONI and TNI). NCAR/UCAR, accessed March 2018, <https://climatedataguide.ucar.edu/climate-data/nino-sst-indices-nino-12-3-34-4-oni-and-tni>.
- Vautard, R., and Coauthors, 2018: Evaluation of the HadGEM3-A simulations in view of detection and attribution of human influence on extreme events in Europe. *Climate Dyn.*, <https://doi.org/10.1007/s00382-018-4183-6>.

8 CONTRIBUTION OF ANTHROPOGENIC CLIMATE CHANGE TO APRIL–MAY 2017 HEAVY PRECIPITATION OVER THE URUGUAY RIVER BASIN

RAFAEL C. DE ABREU, CHRISTOPHER CUNNINGHAM, CONRADO M. RUDORFF, NATALIA RUDORFF, ABAYOMI A. ABATAN, BUWEN DONG, FRASER C. LOTT, SIMON F. B. TETT, AND SARAH N. SPARROW

Anthropogenic climate change has increased the risk of the April–May 2017 extreme rainfall in the Uruguay River basin, which has caused extensive flood and major socioeconomic impacts, by at least twofold with a most likely increase of about fivefold.

INTRODUCTION. The Uruguay River is a trans-boundary river of great economic importance in South America. Its headwaters lie in southern Brazil, the middle reach forms part of the Brazil–Argentina border, the lower reach forms the Argentina–Uruguay border, and it then empties into the La Plata River with a catchment area of 3.65×10^5 km². The river basin has a temperate climate with annual mean precipitation of 1,750 mm with little seasonality. During the late twentieth century, the Uruguay basin had a positive trend in precipitation (Barros et al. 2008) and streamflow (Pasquini and Depetris 2007). Based on hydrological modeling, Saurral et al. (2008) attributed the 1960–2000 streamflow trend mainly to the increase in precipitation rather than land cover

change. The upper Uruguay River catchment has relatively high relief, low soil storage capacity, and land use is mostly pasture and cropland. Therefore, the catchment has a fast hydrologic response in which flood occurrence is more dependent on meteorology than on initial conditions of soil moisture and flow (Tucci et al. 2003). A cascade of hydroelectric dams is used for flood control operations. However, when more persistent and intensive rainfall systems develop over the upper catchment, the high soil moisture, fast rainfall runoff response, and limited storage capacity of reservoirs overwhelm the flood control operations and result in downstream flooding. Flood related impacts have also increased, resulting in a growing concern regarding the need to identify the causes of increased flood frequency and establish effective mitigation efforts.

Explaining the increase in flood frequency requires assessing the role of climate change in shifting the likelihood of extreme rainfall events over the catchment and building more detailed understanding of ongoing changes in the linkage between rainfall and hydrological mechanisms that cause flooding in this flow regulated catchment. To address the former, we analyzed the influence of anthropogenic climate change on the likelihood of the heavy rainfall that occurred in April–May 2017, which led to widespread overbank flooding along the Uruguay River that peaked in June, causing significant impacts such as direct economic loss in Brazil of 102 million U.S. dollars (FAMURS 2017) and displacement of more than 3,500 people in Uruguay (BBC 2017).

DATA AND METHODS. The Climate Prediction Center (CPC) Global Unified Precipitation data (Chen et al. 2008) with a spatial resolution of $0.5^\circ \times 0.5^\circ$ were

AFFILIATIONS: DE ABREU—Department of Atmospheric Sciences, Universidade de São Paulo, São Paulo, Brazil; CUNNINGHAM AND C. RUDORFF—Centro Nacional de Monitoramento e Alertas de Desastres Naturais, São José dos Campos, Brazil; N. RUDORFF—Centro de Previsão do Tempo e Estudos Climáticos, Instituto Nacional de Pesquisas Espaciais, São José dos Campos, Brazil; ABATAN AND TETT—School of Geosciences, University of Edinburgh, Edinburgh, United Kingdom; DONG—National Centre for Atmospheric Science, University of Reading, Reading, United Kingdom; LOTT—Met Office Hadley Centre, Exeter, United Kingdom; SPARROW—Oxford e-Research Centre, University of Oxford, Oxford, United Kingdom

CORRESPONDING AUTHOR: Rafael C. de Abreu, rafael.abreu@iag.usp.br

DOI:10.1175/BAMS-D-18-0102.1

A supplement to this article is available online (10.1175/BAMS-D-18-0102.2)

© 2019 American Meteorological Society

For information regarding reuse of this content and general copyright information, consult the [AMS Copyright Policy](#).

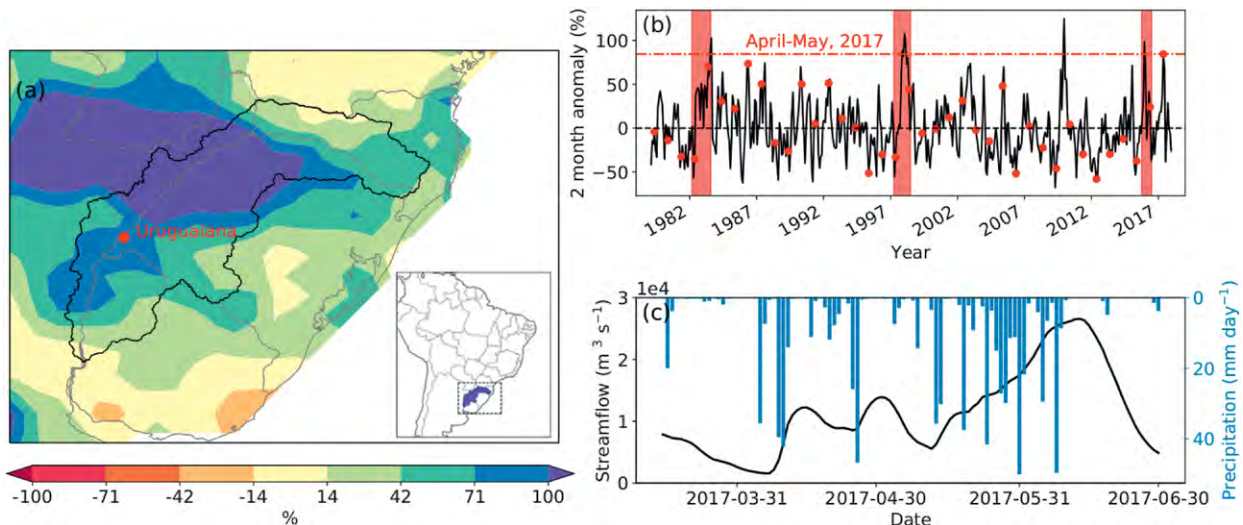


FIG. 1. (a) 2017 April and May anomalous precipitation in the Uruguay basin as percentage difference from a 1979–2013 climatology, based on the Climate Prediction Center (CPC) Global Unified Precipitation data. The gray borders indicates the geographic boundaries for coastlines, countries and Brazilian states, while black line indicates the boundaries of the Uruguay River basin. (b) Two-month precipitation anomaly related to the period of 1979–2017 as percentage difference from the 1979–2013 climatology, based on the Uruguay catchment average calculated using the CPC data (black line). Red bars in (b) highlight very strong El Niño events, where the Oceanic Niño Index (ONI) was greater than 2°C for more than 3 consecutive months; red dots indicate April–May precipitation anomaly and the red dashed dotted line the 2017 April–May anomaly. (c) Daily streamflow from Uruguiana (black line) and daily precipitation for the average CPC data in the catchment area upstream of Uruguiana (blue line).

used to characterize the precipitation over the Uruguay River catchment for the period 1979–2017 (Fig. 1). We applied the Met Office Hadley Centre atmosphere-only general circulation model HadGEM3-A (Ciavarella et al. 2018) at N216 resolution (approximately 60 km in the midlatitudes) to assess the influence from anthropogenic forcings. For 1980–2013 two ensembles of 15 members were used. The first ensemble (“Actual”) is driven by both natural (variability in the solar irradiance in the top of the atmosphere and volcanic activity) and anthropogenic forcings [greenhouse gases (GHG), zonal-mean ozone concentrations, aerosol emissions, and land use changes], with sea surface temperatures (SSTs) and sea ice coverage from HadISST (Rayner et al. 2003). The second ensemble (“Natural”) is driven only by natural atmospheric forcings, and has the estimated impact of anthropogenic forcings removed from SST and sea ice patterns using the attribution method described in Pall et al. (2011) and Christidis et al. (2013). To estimate the change in likelihood of the 2017 heavy precipitation, we analyze the extensions of these ensembles (denoted “ActualExt” and “NaturalExt”) that were available from March to August 2017 with 525 ensemble members each.

The Actual and Natural ensemble members are multidecadal simulations, from 1960 to 2013,

designed primarily for model validation, while the ActualExt and NaturalExt are shorter simulations with a higher number of ensemble members used for attribution assessments. The “Ext” simulations are continuations of the 1959–2013 runs, with the ensemble members increased by producing batches of members branching from the end of a single multidecadal simulation, which therefore share the initial conditions of the small size ensemble but are different in the realization of the stochastic physics (Ciavarella et al. 2018).

To establish how representative the precipitation in the climate model is for our study region we applied a nonparametric two-sample Kolmogorov–Smirnov (KS) test to verify if the CPC precipitation and the “Actual” model simulations from 1979 to 2013 were from the same distribution (Wilks 2006). Gamma distributions were fitted to ActualExt and NaturalExt to estimate the risk ratio (RR). To test sensitivity to the fitted distribution we also fitted a generalized extreme value (GEV) distribution to both distributions. Risk ratio is a metric recommended for use in attribution (National Academies of Sciences, Engineering, and Medicine 2016) to indicate the change in probability of an event with climate change, and is simply the ratio of the actual probability to the natural. Uncertainties

within the simulations were computed using a bootstrap resampling method (Efron and Tibshirani 1993).

RESULTS AND DISCUSSION. The region is characterized by monthly precipitation distributed equally throughout the year, and is susceptible to floods year round. However, April–May 2017 precipitation was the largest April–May anomaly and the eighth highest anomaly for a two-month consecutive period since 1979 (Fig. 1b). It resulted from a succession of intense events from synoptic scale to mesoscale in the region (CPTEC 2017a,b). A major component was the interaction of midlatitude meteorological systems with the low-level jet to the east of the Andes that supplied additional moisture from tropical regions, enhancing the associated convection. April events enhanced the streamflow in the basin (Fig. 1c) and also led to increased soil moisture and reservoir levels. In May, more heavy rainfall over the hydrological wet conditions resulted in flooding that peaked in the beginning of June with a return period of 40 years, causing great economic impacts.

Unlike most of the large anomalies in Fig. 1b, April–May 2017 coincided with a neutral phase of El Niño. However, the austral summer of 2017 was characterized by an unusual fast warming of the far eastern Pacific, denominated by a coastal El Niño (Garreaud 2018). Generally, positive precipitation anomalies in southern Brazil are expected during El Niños (Grimm et al. 1998, 2000), which can cause significant floods (Pasquini and Depetris 2007). Because of the low streamflow in the end of March (Fig. 1c),

the low soil moisture storage, and the fast response of the basin, no preconditioning of soil moisture from earlier months would have had a significant impact on the flood. However, we cannot reject the hypothesis that this El Niño increased the frequency of the low-level jet (Silva et al. 2009), which is a key component in producing precipitation in the region.

To avoid a selection effect we consider 1986 April–May precipitation as a threshold for record-breaking events. Although this was a moderate El Niño year, the 1986 flood occurred in April of that year and had similar meteorological conditions to 2017, with heavy precipitation events in the headwater of the basin during a two-month period, resulting in the second highest April–May anomaly on record for the CPC dataset with 517 mm and a positive anomaly of 73%.

At the 5% significance level, the KS test indicated that we cannot reject the hypothesis that both datasets, the CPC observations and “Actual” historical simulations (1980–2013), were drawn from the same distribution (p value = 0.9). This suggests that the Actual simulations were able to correctly reproduce the statistics of April–May historical precipitation over the catchment area of the Uruguay River (see also online supplemental material). When the same test was used to check whether “Actual” and “Natural” simulations were different, the result indicated that they were not drawn from the same distribution (p value = 0.005), suggesting a difference between the simulations over the catchment area.

The fitted probability distribution functions (Fig. 2a) indicates different shapes for ActualExt

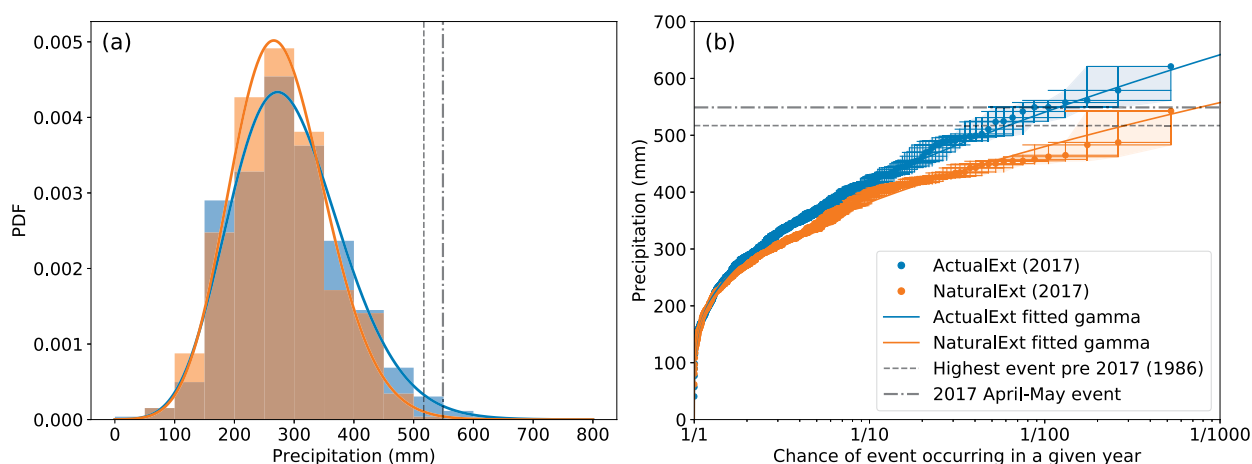


FIG. 2. (a) Probability distribution function for fitted gamma distributions of ActualExt and NaturalExt simulations of 2017 April and May accumulated precipitation in the Uruguay basin. (b) Return time for the ActualExt and NaturalExt experiments. Each marker represents an ensemble member and the blue and orange lines are the fitted gamma return period for the ActualExt and NaturalExt, respectively. The errors bars indicate the 95% confidence interval using bootstrap resampling. Black dashed line indicating the 517 mm threshold based on the 1986 event and the 2017 rainfall of 549 mm as dashed dotted line.

and NaturalExt, with a high narrower PDF in the NaturalExt world in comparison to the ActualExt world. On the other hand, ActualExt shows increased probabilities in the right tail of the distribution, indicating greater chance of extreme events due to anthropogenic forcings, such as the 1986 and the 2017 thresholds. ActualExt also shows a 61-yr return time (Fig. 2b) for the 1986 threshold while NaturalExt indicates a return period of 285 years according to the fitted gamma distributions. Furthermore, for the 61-yr return time, NaturalExt has 11% lower precipitation than ActualExt.

We assessed the risk ratio using the fitted gamma distributions for ActualExt and NaturalExt. The value obtained was about 4.6, suggesting that the chance of occurrence of a 1986-like event is about 5 times greater in ActualExt than in the NaturalExt. Uncertainty in the RR was estimated using bootstrapping. For each model ensemble 1,000 samples, with replacement, were produced and gamma distributions fitted. They were used to calculate the probability of exceeding the threshold, for both the ActualExt and NaturalExt simulations. In this case, the RR distribution had a median of 5.2 with 5 and 95% percentiles of 2.6 and 10.4, respectively. Using a GEV fit and identical methodology we find that the RR distribution was highly skewed with a median of 4.7 with 5 and 95% percentiles of 2.0 and 17.7 respectively.

The historical record of CPC alone (Fig. 1b) did not seem to foresee the anomalous event of 2017, with 13 years since 2000 experiencing close to or below average anomalies in April–May. However, the increase in probability of enhanced precipitation events in ActualExt is consistent with the findings of Soares and Marengo (2009). They investigated the South American low-level jet in a warming climate due to anthropogenic influence and found an increase in the meridional moisture transport from the Amazonian region to the south part of Brazil, where the Uruguay River basin is located, mainly because of an increased temperature gradient between tropical and subtropical South America.

CONCLUSIONS. This article examined the April–May 2017 extreme rainfall in a historical context, and analyzed the influence of anthropogenic climate change on the likelihood of such an event that led to severe flooding of the Uruguay River. We found that anthropogenic climate change has increased the risk of the April–May 2017 extreme rainfall in this catchment by at least 2 times with a median increase of about 5 times. However, when considering event attribution it is necessary to consider methodological

limitations. The removal of the anthropogenic effect in the SST and SIC is a major source of uncertainty, as well as land use changes. Also, there is a need for a more thorough evaluation of the circulation patterns in the model simulations for that particular region that is beyond the scope of this paper.

Our study made reference to the 2017 flooding of the Uruguay River as the main impact caused by extreme rainfall over a two-month period. The length of the period was defined based on the prerequisite of high levels in the reservoirs for the occurrence of high-impact floods. The flood wave travel time from the upper to middle catchment toward the end of the period after heavy rainfall over antecedent high soil moisture and high reservoir levels was of the order of 5 to 6 days. Hence an analysis based on precipitation outputs on a daily to weekly scale would also be important to track individual heavy rainfall events more specifically. Future research to understand the linkage between rainfall and hydrological mechanisms that cause flooding in this flow-regulated catchment is necessary to fully explain the increase in flood frequency.

ACKNOWLEDGMENTS. This study was carried out during a workshop on Operational Attribution at the University of Oxford sponsored by the Newton Fund through the Met Office Climate Science for Service Partnership Brazil (CSSP Brazil) and the U.K.–China Research and Innovation Partnership Fund through the CSSP China. RCA acknowledges support from CNPq. AA, BD, and ST were funded by CSSP Brazil. FCL and SS were funded by CSSP China.

REFERENCES

- Barros, V. R., M. E. Doyle, and I. A. Camilloni, 2008: Precipitation trends in southeastern South America: Relationship with ENSO phases and with low-level circulation. *Theor. Appl. Climatol.*, **93**, 19–33, <https://doi.org/10.1007/s00704-007-0329-x>.
- BBC, 2017: Uruguay floods displace thousands. British Broadcasting Corporation, accessed 12 January 2018, www.bbc.com/news/world-latin-america-40171998.
- Chen, M., W. Shi, P. Xie, V. Silva, V. E. Kousky, R. W. Higgins, and J. E. Janowiak, 2008: Assessing objective techniques for gauge-based analyses of global daily precipitation. *J. Geophys. Res.*, **113**, D04110, <https://doi.org/10.1029/2007JD009132>.
- Christidis, N., P. A. Stott, A. A. Scaife, A. Arribas, G. S. Jones, D. Copsey, J. R. Knight, and W. J. Tennant, 2013: A new HadGEM3-A-based system for attribution of weather- and climate-related extreme events.

- J. Climate*, **26**, 2756–2783, <https://doi.org/10.1175/JCLI-D-12-00169.1>.
- Ciavarella, A., and Coauthors, 2018: Upgrade of the HadGEM3-A based attribution system to high resolution and a new validation framework for probabilistic event attribution. *Wea. Climate Extremes*, **20**, 9–32, <https://doi.org/10.1016/j.wace.2018.03.003>.
- CPTEC, 2017a: Casos significativos de abril de 2017 [Significant cases from April 2017]. Centro de Previsão de Tempo e Estudos Climáticos [Center for Weather Forecasting and Climate Studies], 6 pp., accessed in 28 May 2018, https://s3.cptec.inpe.br/webdop/static/resources/sites/tempo/assets/pdf/caso_sig_abril_2017.pdf.
- , 2017b: Casos significativos de maio de 2017 [Significant cases from May 2017]. Centro de Previsão de Tempo e Estudos Climáticos [Center for Weather Forecasting and Climate Studies], 3 pp., accessed in 28 May 2018, https://s3.cptec.inpe.br/webdop/static/resources/sites/tempo/assets/pdf/caso_sig_maio_2017.pdf.
- Efron, B., and R. J. Tibshirani, 1993: *An Introduction to the Bootstrap*. Chapman and Hall, 456 pp.
- FAMURS, 2017: Sobe para R\$ 339 milhões o valor dos prejuízos com o temporal no RS. Federação das Associações dos Municípios do Rio Grande do Sul, accessed 12 January 2018, www.famurs.com.br/noticias/sobe-para-r-339-milhoes-o-valor-dos-prejuizos-com-o-temporal-no-rs/.
- Garreaud, R. D., 2018: A plausible atmospheric trigger for the 2017 coastal El Niño. *Int. J. Climatol.*, **38**, e1296–e1302, <https://doi.org/10.1002/joc.5426>.
- Grimm, A. M., S. E. T. Ferraz, and J. Gomes, 1998: Precipitation anomalies in southern Brazil associated with El Niño and La Niña events. *J. Climate*, **11**, 2863–2880, [https://doi.org/10.1175/1520-0442\(1998\)011<2863:PAISBA>2.0.CO;2](https://doi.org/10.1175/1520-0442(1998)011<2863:PAISBA>2.0.CO;2).
- , V. R. Barros, and M. E. Doyle, 2000: Climate variability in southern South America associated with El Niño and La Niña events. *J. Climate*, **13**, 35–58, [https://doi.org/10.1175/1520-0442\(2000\)013<0035:CVISSA>2.0.CO;2](https://doi.org/10.1175/1520-0442(2000)013<0035:CVISSA>2.0.CO;2).
- National Academies of Sciences, Engineering, and Medicine, 2016: *Attribution of Extreme Weather Events in the Context of Climate Change*. The National Academies Press, 186 pp., <https://doi.org/10.17226/21852>.
- Pall, P., T. Aina, D. A. Stone, P. A. Stott, T. Nozawa, A. G. Hilberts, D. Lohmann, and M. R. Allen, 2011: Anthropogenic greenhouse gas contribution to flood risk in England and Wales in autumn 2000. *Nature*, **470**, 382–385, <https://doi.org/10.1038/nature09762>.
- Pasquini, A. I., and P. J. Depetris, 2007: Discharge trends and flow dynamics of South American rivers draining the southern Atlantic seaboard: An overview. *J. Hydrol.*, **333**, 385–399, <https://doi.org/10.1016/j.jhydrol.2006.09.005>.
- Rayner, N., D. E. Parker, C. K. Folland, E. B. Horton, L. V. Alexander, and D. P. Rowell, 2003: The global sea-ice and sea surface temperature (HadISST) data sets. Accessed December 2017, <https://rda.ucar.edu/datasets/ds277.3/>.
- Saurral, R. I., V. R. Barros, and D. P. Lettenmaier, 2008: Land use impact on the Uruguay River discharge. *Geophys. Res. Lett.*, **35**, L12401, <https://doi.org/10.1029/2008GL033707>.
- Silva, G. A. M., T. Ambrizi, and J. A. Marengo, 2009: Observational evidences on the modulation of the South American low level jet east of the Andes according the ENSO variability. *Ann. Geophys.*, **27**, 645–657, <https://doi.org/10.5194/angeo-27-645-2009>.
- Soares, W. R., and J. A. Marengo, 2009: Assessments of moisture fluxes east of the Andes in South America in a global warming scenario. *Int. J. Climatol.*, **29**, 1395–1414, <https://doi.org/10.1002/joc.1800>.
- Tucci, C. E. M., R. T. Clarke, W. Collischonn, P. L. da Silva Dias, and G. S. de Oliveira, 2003: Long-term flow forecasts based on climate and hydrologic modeling: Uruguay River basin. *Water Resour. Res.*, **39**, 1181, <https://doi.org/10.1029/2003WR002074>.
- Wilks, D. S., 2006: *Statistical Methods in the Atmospheric Sciences*. Academic Press, 592 pp.

DECEMBER 2016: LINKING THE LOWEST ARCTIC SEA-ICE EXTENT ON RECORD WITH THE LOWEST EUROPEAN PRECIPITATION EVENT ON RECORD

JUAN C. ACOSTA NAVARRO, PABLO ORTEGA, JAVIER GARCÍA-SERRANO, VIRGINIE GUEMAS, ETIENNE TOURIGNY, RUBÉN CRUZ-GARCÍA, FRANÇOIS MASSONNET, AND FRANCISCO J. DOBLAS-REYES

Our study suggests that record-breaking low precipitation over parts of western Europe during December 2016 may have been favored by an unprecedented reduction of Arctic sea ice, likely driven by anthropogenic climate change.

INTRODUCTION. Extreme warm Arctic temperatures during November–December 2016 can only be understood in the context of human influence on climate (Kam et al. 2018; see also Fig. ES1 in the online supplemental information). In the same months, the total Arctic sea ice extent experienced a historical low value with negative anomalies in most of the Arctic, but especially strong in the Barents and Kara Seas (BK; Figs. 1a,c). In addition, a high pressure blocking pattern developed over Europe during December 2016 (Vautard et al. 2017) and caused the total amount of precipitation to be the lowest in the last 116 years (Figs. 1b,d).

Human influence on climate likely includes intensification of precipitation extremes (Min et al. 2011). Furthermore, in the last decade several studies have found causal links between low sea ice cover in late autumn and extreme midlatitude climate anomalies in the following winter. Baroclinic instability generated through enhanced surface heat fluxes due to

sea ice reduction promotes planetary wave activity in the troposphere and the troposphere–stratosphere interface that could potentially affect the atmospheric flow, and thus modify midlatitude weather and climate at the surface [see Cohen et al. (2014) and Screen et al. (2018) for a review]. We used three sets of tailored retrospective forecasts to attribute the role of extremely reduced Arctic sea ice conditions (mostly over BK) with regard to the 2016 extremely low precipitation event in Europe.

DATA AND METHODS. We used observationally based gridded fields of monthly mean sea ice concentration (SIC) for the period 1980–2016 (Cavalieri et al. 1996) and European precipitation for the period 1901–2016 (Haylock et al. 2008; Harris et al. 2014). Sea level pressure for the period 1980–2016 was taken from ERA-Interim (Dee et al. 2011). The BK region (red box in Fig. 1a) was defined as the area within 15°–100°E, 68°–82°N, while Europe (red box in Fig. 1b) was defined as the area within 10°W–30°E, 38°–60°N.

Using the fully coupled climate model EC-Earth3 in forecast mode (i.e., initialized simulations; Doblas-Reyes et al. 2013) with the Autosubmit workflow manager (Manubens-Gil et al. 2016) we simulated the climate of November–December 2016 in three sets of ensemble retrospective predictions, specifically conceived to isolate the preconditioning role of sea ice state. We first produced a set of 100-member forecasts with the observed initial conditions from 1 November 2016 (Forecast16) to describe the baseline skill of the model to predict the 2016 extreme in precipitation. The contribution of sea ice was then assessed by repeating the same experiments, but using sea ice conditions from 1 November 2014, which were chosen due to their closeness to the 1980–2015 climatology in the BK region (Forecast16_Ice14). Previous studies

AFFILIATIONS: ACOSTA NAVARRO, ORTEGA, GARCÍA-SERRANO, GUEMAS, TOURIGNY, CRUZ-GARCÍA—Barcelona Supercomputing Centre, Barcelona, Spain; MASSONNET—Georges Lemaître Centre for Earth and Climate Research, Earth and Life Institute, Université catholique de Louvain, Louvain-la-Neuve, Belgium, and Barcelona Supercomputing Centre, Barcelona, Spain DOBLAS-REYES—Barcelona Supercomputing Centre and Catalan Institution for Research and Advanced Studies (ICREA), Barcelona, Spain

CORRESPONDING AUTHOR: Juan C. Acosta Navarro, jacosta@bsc.es

DOI:10.1175/BAMS-D-18-0097.1

A supplement to this article is available online (10.1175/BAMS-D-18-0097.2)

© 2019 American Meteorological Society

For information regarding reuse of this content and general copyright information, consult the [AMS Copyright Policy](#).

suggest that 100-member ensembles are sufficiently large to separate the atmospheric response to sea ice changes from the noise caused by internal variability (e.g., Screen et al. 2014). For the period 1980–2015, an additional set of 10-member November–December retrospective predictions (Hindcast) was initialized every 1 November with atmospheric, oceanic, and sea ice initial conditions representative of each year to assess the model capability to simulate and predict the mean climate of the period and to establish a baseline to compare the extreme event of 2016 in all forecasts. All model experiments used atmospheric initial conditions adapted from ERA-Interim (Dee et al. 2011), oceanic initial conditions adapted from ORAS4 (Balmaseda et al. 2013), and sea ice conditions from a historical reconstruction using assimilation of SIC from Satellite Application Facility on Ocean and Sea Ice (OSISAF) and the European Space Agency (ESA; <http://esa-cci.nersc.no>).

CHARACTERIZING THE EXTREME EVENTS. A breakpoint in sea ice loss (i.e., an accelerated decline) over the BK region took place in the early 2000s (Close et al. 2015). Here we use the 15-yr period 2001–15 as representative of this marked change, not including the extreme autumn–winter of 2016; the 15-yr period 1980–94 is used as baseline for sea ice cover before the dramatic recent sea ice loss. Between the periods 1980–94 and 2001–15 there is a clear shift in the probability distribution of observed sea ice cover in the BK region (Fig. 1c), a shift that has previously been related to anthropogenic climate change (Bindoff et al. 2013). BK SIC in 2016 was the lowest for the period November–December since satellite observations began in 1979 and twice as low as the lowest value in the period 1980–94. The EC-Earth3 hindcasts also exhibit a BK sea ice cover shift between 1980–94 and 2001–15, but less marked than in the observations (Fig. 1c). Indeed, while the observed 2016 SIC remains unlikely but plausible with respect to the 2001–15 hindcasts and Forecast16 distributions, it is virtually impossible when compared to the 1980–94 distribution. Note likewise that the ensemble-mean SIC of Forecast16 lies on the tail of Hindcast 1980–94.

Following the extreme sea ice conditions, December 2016 was characterized by a persistent, abnormally high sea level pressure system centered in northwestern Europe (Fig. 1b) exceeding the December mean (since the early 1900s) by over two standard deviations (Vautard et al. 2017) and leading to reduced humidity transport into Europe from the North Atlantic. As a result, the mean precipitation in Europe was the lowest

on record for that month since 1901. Most locations experienced anomalous precipitation well below one standard deviation from the historical mean for December (Fig. 1b). The probability distribution of precipitation barely changed over the observational period (1901–2016). We also compared the same 15-yr periods for precipitation than for sea ice, but we show 1980–2015 due to the lack of long-term trends and higher natural variability (Fig. ES2).

Although EC-Earth3 shows a dry bias in precipitation as compared to observations for the periods 1980–2015 (blue vs gray lines in Fig. 1d), the variability in the model and the observations is practically the same, allowing for a non-bias-corrected analysis of extreme events (Bellprat and Doblas-Reyes 2016). Forecast16 (purple line) displays drier conditions than Hindcast, which supports the ability of the model to broadly simulate, and predict, the occurrence of such events one month in advance. Indeed, the observed spatial features of the anomalous sea level pressure and precipitation in Europe during December 2016 are tightly captured by the model in Forecast16, although with a model tendency to underestimate the observed amplitude (Figs. 1b and 2a). This underestimation is somehow expected in the forecasts, as the reproducibility of the extreme event one month ahead will degrade due to the chaotic nature of the system.

IMPACT OF BARENTS–KARA SEA ICE REDUCTION. Repeating the forecasts with 2014 sea ice (Forecast16_Ice14) initial conditions shifts the mode of the probability density function toward wetter conditions (compared to Forecast16) by about 20%, suggesting that sea ice could have a preconditioning or additive effect on the extreme event in Europe during 2016. Indeed, sea ice initialization from realistic conditions enhanced the anomalous circulation and precipitation spatial patterns in most parts of the continent, except for the southeast area (Figs. 2a,b). To assess the robustness in the mean response to the sea ice initial state we randomly sampled 1000 sub-ensembles of 50 members each from the full 100-member ensemble and computed the mean values of those sub-ensembles for the precipitation and sea level pressure differences between Forecast16 and Forecast16_Ice14 at the gridpoint level. Within the 1000 sub-ensembles there is large agreement (over 80%) on the negative sign of precipitation over most of western Europe (Fig. ES3) and on the positive sign of sea level pressure over most of the continent (Fig. ES4). Note also an important effect of sea ice reduction on western North American precipitation causing a wet south–dry north dipole as seen in

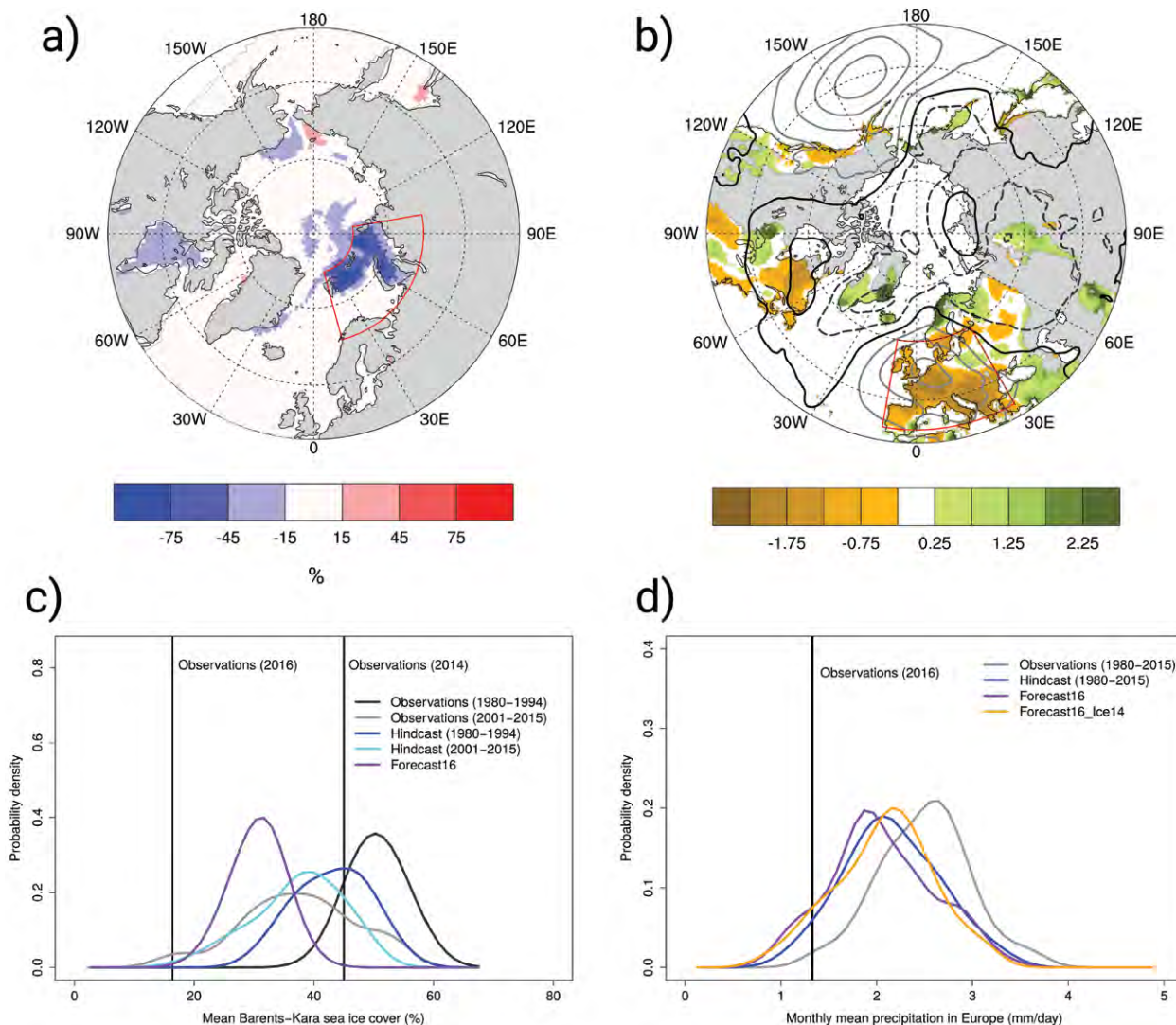


FIG. 1. (a) Observed mean November–December sea ice concentration differences between 2016 and 2014. The red box represents the Barents–Kara region. (b) Observed December 2016 standardized anomalies of total precipitation (colors) and sea level pressure (contours; with 4-hPa intervals, the solid black line is zero and the gray solid and black dashed lines represent positive and negative anomalies, respectively). Regions with mean precipitation below 1 mm day⁻¹ were excluded. All anomalies in (b) are computed with respect to the period 1980–2015. (c) Smoothed probability distribution functions (with the Nadaraya–Watson kernel regression in R) of mean November–December Barents–Kara sea ice cover in observations (gray shading) and model experiments (colors). (d) Smoothed probability distribution functions of mean December precipitation in Europe in observations (gray shading) and model experiments (colors).

observations (Fig. 1c). Having a different experimental setup, focusing only on December and having the largest differences in sea ice in BK Seas, could cause somewhat different mean circulation and precipitation responses to sea ice loss in this study than in previous ones (Deser et al. 2016; Hay et al. 2018).

The influence of initial conditions on extremely low precipitation is further explored in Figs. 2c and 2d as an odds ratio. This is defined as the ratio between the probability to be in the lowest quintile, the middle three quintiles (also called the interquintile range),

or the upper quintile for each 2016 forecast and the climatological probability of the same three categories in Hindcast (i.e., 20%, 60% and 20%, respectively). Each grid point is attributed to the category with highest odds ratio. The point is drawn in gray if it is attributed to the interquintile range. If the point is attributed to the lower (upper) quintile category, the corresponding odds ratio is plotted as negative (positive). The odds ratio represents how anomalous the probability of a given event is. Comparing Figs. 2c and 2d confirms that Forecast16 captures an increase

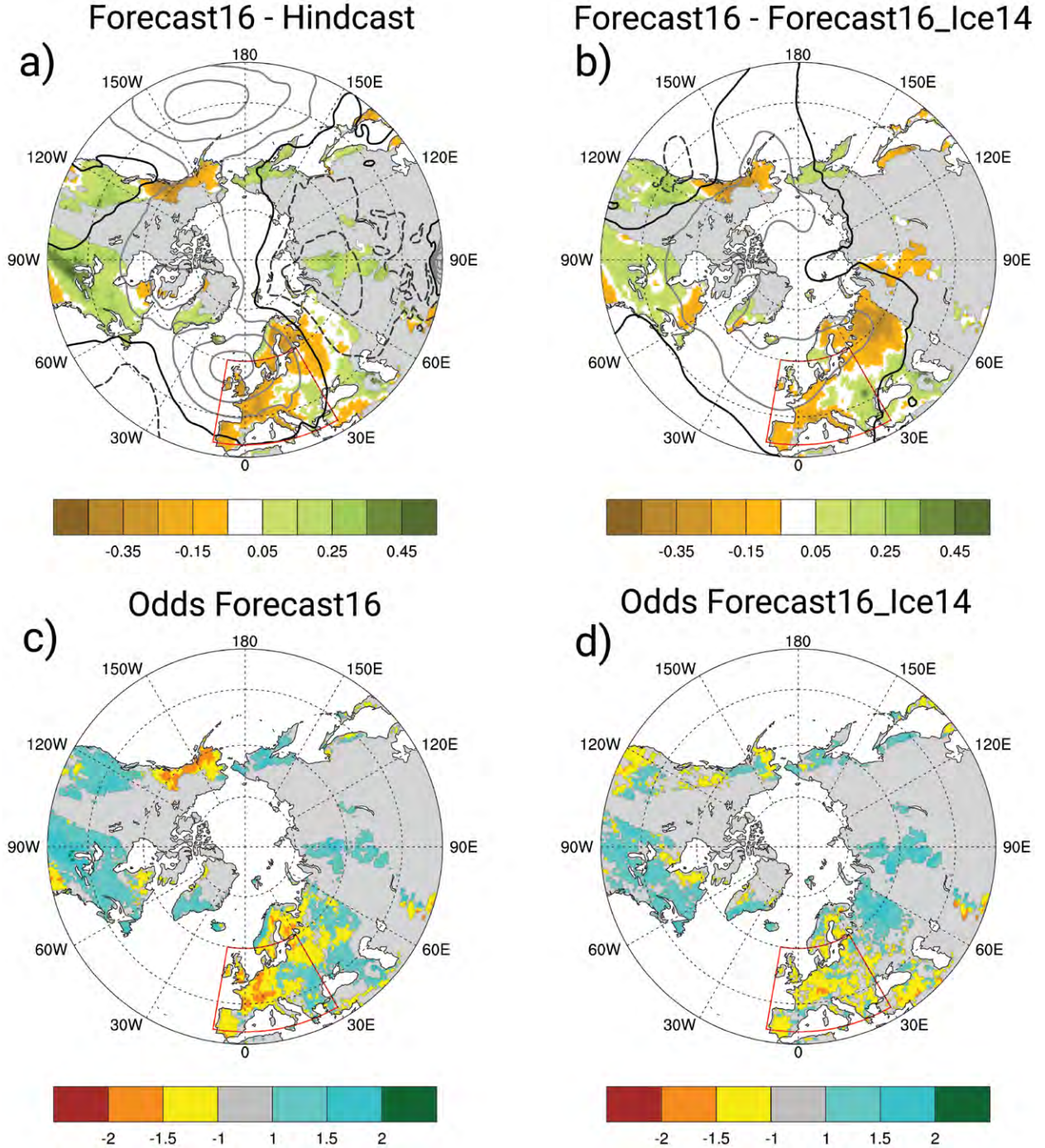


FIG. 2. (a) Mean modeled December 2016 standardized anomalies of total precipitation (colors) and sea level pressure (lines) for all members in Forecast16 (lines every 1 hPa). (b) As in (a), but for Forecast16-Forecast16_Ice14 (lines every 1 hPa). All anomalies in (a) and (b) are computed with respect to 1980–2015. (c) Precipitation odds in Forecast16, which describe the ratio between the probability to be in the lower quintile, the interquintile range, or the upper quintile for the forecast and the probability of the same categories in Hindcast. Each point is attributed to the category with highest odds ratio. The point is gray if attributed to the interquintile range and negative (positive) if attributed to the lower (upper) quintile. (d) As in (c), but for Forecast16_Ice14. Regions with precipitation below 1 mm day⁻¹ were excluded in all plots.

in likelihood of extreme dry conditions over western Europe, with many regions showing an increment in the odds of over 1.5. The dry conditions are also present in Forecast16_Ice14, indicating that either the ocean or the atmosphere was important for capturing the event. However, the response in Forecast16_Ice14 is weaker than in Forecast16 in western and north-western Europe, showing that realistic ice conditions were important to better reproduce the event in these locations.

DISCUSSION AND CONCLUSIONS. EC-Earth3 experiments targeting the low December 2016 precipitation event in Europe indicate that while realistic ocean and atmosphere conditions had a key role in preconditioning and capturing the extremely low precipitation event, initializing the model with actual sea ice conditions increased the likelihood of occurrence over many parts of the continent. The role of internally generated chaotic variability was only indirectly addressed here, by producing and exploring an ensemble of predictions with perturbed initial conditions.

ACKNOWLEDGMENTS. This work was funded by the EU projects APPLICATE (Grant 727862), PRIMAVERA (Grant 641727), and ESA/CMUG-CCI3. We acknowledge the E-OBS dataset from the EU-FP6 project ENSEMBLES and the data providers in the ECA&D project (www.ecad.eu), and KNMI for Climate Explorer (<https://climexp.knmi.nl>). We acknowledge PRACE for awarding us access to MareNostrum at Barcelona Supercomputing Center (BSC), Spain.

REFERENCES

- Balmaseda, M. A., K. Mogensen, and A. T. Weaver, 2013: Evaluation of the ECMWF ocean reanalysis system ORAS4. *Quart. J. Roy. Meteor. Soc.*, **139**, 1132–1161, <https://doi.org/10.1002/qj.2063>.
- Bellprat, O., and F. Doblas-Reyes, 2016: Attribution of extreme weather and climate events overestimated by unreliable climate simulations. *Geophys. Res. Lett.*, **43**, 2158–2164, <https://doi.org/10.1002/2015GL067189>.
- Bindoff, N. L., and Coauthors, 2013: Detection and attribution of climate change: From global to regional. *Climate Change 2013: The Physical Science Basis*, T. F. Stocker et al., Eds., Cambridge University Press, 867–952.
- Cavalieri, D., C. Parkinson, P. Gloersen, and H. Zwally, 1996: Sea ice concentrations from Nimbus-7 SMMR and DMSP SSM/I-SSMIS passive microwave data, version 1. NASA National Snow and Ice Data Center Distributed Active Archive Center, accessed April 2018, <https://doi.org/10.5067/8GQ8LZQVL0VL>.
- Close, S., M.-N. Houssais, and C. Herbaut, 2015: Regional dependence in the timing of onset of rapid decline in Arctic sea ice concentration. *J. Geophys. Res. Oceans*, **120**, 8077–8098, <https://doi.org/10.1002/2015JC011187>.
- Cohen, J., and Coauthors, 2014: Recent Arctic amplification and extreme mid-latitude weather. *Nat. Geosci.*, **7**, 627–637, <https://doi.org/10.1038/ngeo2234>.
- Dee, D. P., and Coauthors, 2011: The ERA-Interim Reanalysis: Configuration and performance of the data assimilation system. *Quart. J. Roy. Meteor. Soc.*, **137**, 553–597, <https://doi.org/10.1002/qj.828>.
- Deser, C., and Coauthors, 2016: Does ocean coupling matter for the northern extratropical response to projected Arctic sea ice loss? *Geophys. Res. Lett.*, **43**, 2149–2157, <https://doi.org/10.1002/2016GL067792>.
- Doblas-Reyes, F., and Coauthors, 2013: Initialized near-term regional climate change prediction. *Nat. Commun.*, **4**, 1715, <https://doi.org/10.1038/ncomms2704>.
- Harris, I., P. Jones, T. Osborn, and D. Lister, 2014: Updated high-resolution grids of monthly climatic observations—The CRU TS3.10 dataset. *Int. J. Climatol.*, **34**, 623–642, <https://doi.org/10.1002/joc.3711>.
- Hay, S., P. J. Kushner, R. Blackport, and K. E. McCusker, 2018: On the relative robustness of the climate response to high-latitude and low-latitude warming. *Geophys. Res. Lett.*, **45**, 6232–6241, <https://doi.org/10.1029/2018GL077294>.
- Haylock, M., N. Hofstra, A. Klein Tank, E. Klok, P. Jones, and M. New, 2008: A European daily high-resolution gridded data set of surface temperature and precipitation for 1950–2006. *J. Geophys. Res.*, **113**, D20119, <https://doi.org/10.1029/2008JD010201>.
- Kam, J., T. R. Knutson, F. Zeng, and A. T. Wittenberg, 2017: CMIP5 model-based assessment of anthropogenic influence on highly anomalous Arctic warmth during November–December 2016 [in “Explaining Extreme Events of 2016 from a Climate Perspective”]. *Bull. Amer. Meteor. Soc.*, **99** (1), S34–S38, <https://doi.org/10.1175/BAMS-D-17-0115.1>.
- Manubens-Gil, D., J. Vegas-Regidor, C. Prodhomme, O. Mula-Valls, and F. J. Doblas-Reyes, 2016: Seamless management of ensemble climate prediction experiments on HPC platforms. *2016 IEEE Conf. on High Performance Computing & Simulation (HPCS)*, Innsbruck, Austria, IEEE, <https://doi.org/10.1109/HPCSim.2016.7568429>.
- Min, S.-K., X. Zhang, F. W. Zwiers, and G. C. Hegerl, 2011: Human contribution to more-intense pre-

- precipitation extremes. *Nature*, **470**, 378, <https://doi.org/10.1038/nature09763>.
- Screen, J. A., C. Deser, I. Simmonds, and R. Tomas, 2014: Atmospheric impacts of Arctic sea-ice loss, 1979–2009: Separating forced change from atmospheric internal variability. *Climate Dyn.*, **43**, 333–344, <https://doi.org/10.1007/s00382-013-1830-9>.
- , and Coauthors, 2018: Consistency and discrepancy in the atmospheric response to Arctic sea-ice loss across climate models. *Nat. Geosci.*, **11**, 155–163, <https://doi.org/10.1038/s41561-018-0059-y>.
- Vautard, R., A. Colette, E. Van Meijgaard, F. Meleux, G. Jan, F. O. Oldenborgh, I. Tobin, and P. Yiou, 2017: Attribution of wintertime anticyclonic stagnation contributing to air pollution in western Europe [in “Explaining Extreme Events of 2016 from a Climate Perspective”]. *Bull. Amer. Meteor. Soc.*, **99** (1), S70–S75, <https://doi.org/10.1175/BAMS-D-17-0113.1>.

THE EXCEPTIONAL SUMMER HEAT WAVE IN SOUTHERN EUROPE 2017

SARAH F. KEW, SJOUKJE Y. PHILIP, GEERT JAN VAN OLDENBORGH, FRIEDRIKE E. L. OTTO,
ROBERT VAUTARD, AND GERARD VAN DER SCHRIER

Across the Euro-Mediterranean the likelihood of a heat wave at least as hot as summer 2017 is now on the order of 10%. Anthropogenic climate change has increased the odds at least threefold since 1950.

INTRODUCTION. Summer 2017 in western Europe and the Euro-Mediterranean was remarkable in particular for its very hot heat waves. Following an exceptionally warm June (Otto et al. 2017) in western Europe, the heat returned to southern Spain in July and contributed to substantial forest fires. Madrid (Retiro) hit 40.6°C on July 13, equaling the 2012 record. Heat episodes continued into August, extending to many areas in southern Europe (see Fig. 1b).

Early August saw a particularly intense heat wave that was described as the “worst heat wave since 2003” (BBC 2017) in southern Europe and became dubbed as “Lucifer,” with local maximum temperatures in Italy and the Balkans topping 40°C for several days. Several countries issued code red alerts (Fig. 1a). Records were broken in southern France (4 August, Nîmes-Courbessac, 41.6°C), for example, and in Corsica and Croatia, where nighttime temperatures exceeded 30°C. Widespread heat and lack of precipitation triggered a severe drought in many areas, persisting into fall.

Southern Europe is familiar with very hot summer days. However, sustained extreme temperatures

become hazardous, particularly for the very young and elderly and those suffering from heart conditions, high blood pressure, or asthma (IFRC 2017), or tourists unaccustomed to high temperatures. High energy and water consumption during prolonged heat waves also puts strain on supplies.

There were some reports of deaths associated with the August heat wave, but usually the full impact is only evident after analyzing and attributing the total mortality excesses (e.g., D’Ippoliti et al. 2010; Mitchell et al. 2016). Increased hospital admissions with people suffering from heat-related conditions were also reported. The agricultural industry bore the brunt of the hot and dry summer season, with Bosnia, Serbia, and Italy experiencing major losses (Zuvela and Vasovic 2017). In Italy, grape harvests (Horowitz 2017) were carried out weeks in advance to reduce risk of heat damage.

Here, we investigate the return period and changing risk of heat waves like those of summer 2017 in the Euro-Mediterranean, seeking a spatial and temporal event definition related to the impacts that society experienced (Otto et al. 2018). We analyze the annual maxima of 3-day-mean area-averaged daily maximum temperatures (TX3X) for a box over southeast Europe (“SE-box”; 8°–24°E, 36°–48°N; Fig. 1b), using the European daily high-resolution gridded dataset (E-OBS; 1950–present; Haylock et al. 2008). This spatial event definition is closely linked to impacts on the national scale, as the SE-box corresponds well with the early August 2017 Metealarm red-alert regions (Fig. 1a)—warnings issued by national weather services and therefore related to how weather is nationally perceived—for which there is good data homogeneity (up to 48°N). The 3-day temporal definition is representative of the period of time that sustained high temperatures became more hazardous (D’Ippoliti et al. 2010). Local station data are generally more homogeneous

AFFILIATIONS: KEW AND PHILIP—Royal Netherlands Meteorological Institute (KNMI), De Bilt, and Department of Water and Climate Risk, Institute for Environmental Studies (IVM), Amsterdam, Netherlands; VAN OLDENBORGH, AND VAN DER SCHRIER—Royal Netherlands Meteorological Institute (KNMI), De Bilt, Netherlands; OTTO—University of Oxford, Oxford, United Kingdom; VAUTARD—Laboratoire des sciences du climat et de l’environnement, Institut Pierre Simon Laplace, Gif sur Yvette, France

CORRESPONDING AUTHOR: Sarah F. Kew, sarah.kew@vu.nl

DOI:10.1175/BAMS-D-18-0109.1

A supplement to this article is available online (10.1175/BAMS-D-18-0109.2)

© 2019 American Meteorological Society

For information regarding reuse of this content and general copyright information, consult the [AMS Copyright Policy](#).

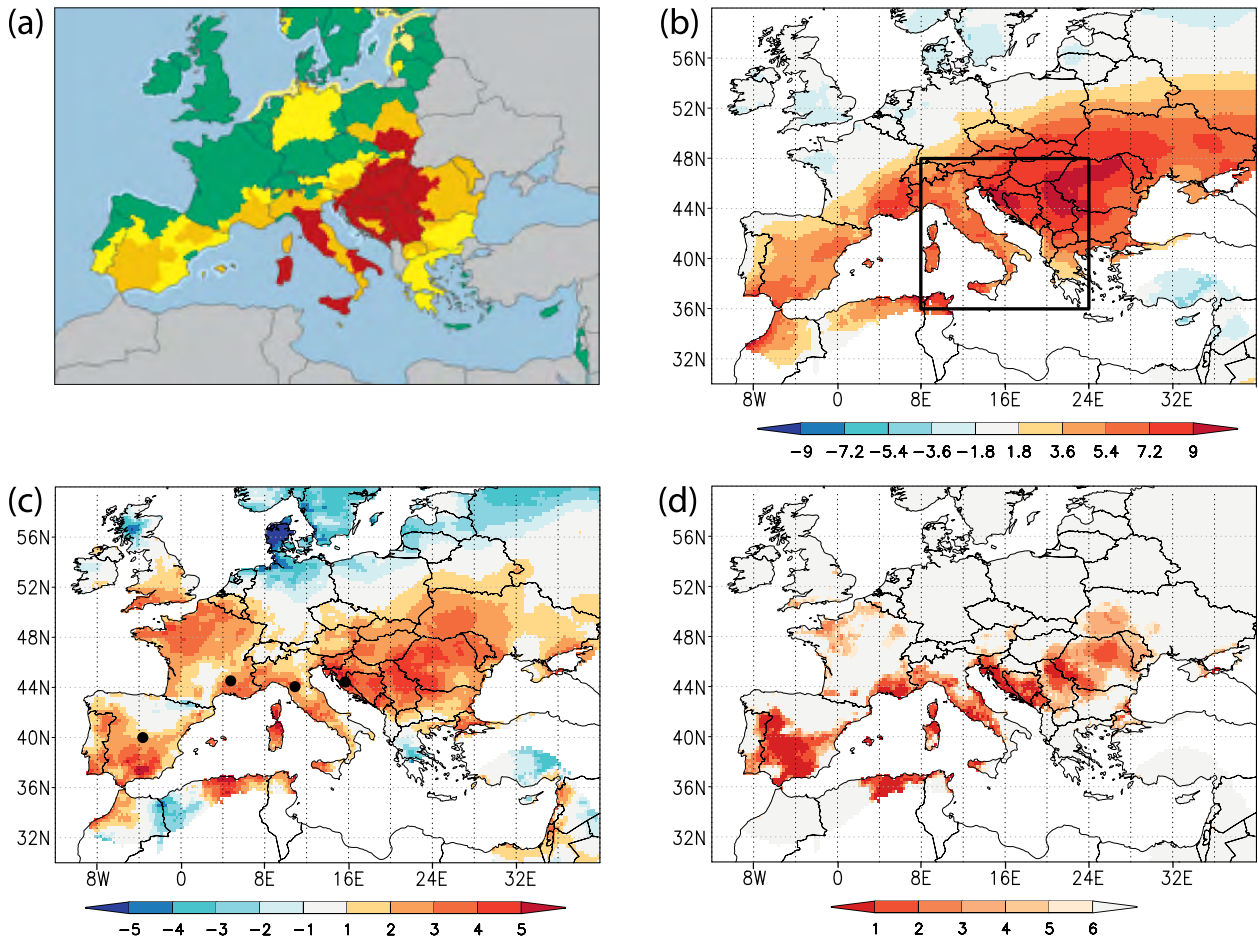


FIG. 1. Context of the event in maps. (a) Meteocalarm weather alerts for 1420 CET 4 Aug 2017. Note that maps are issued every 20 min; regions experiencing an alarm varied slightly during the heat wave of 3–5 August. All red warnings, and also the orange and yellow warnings in southern Europe, are for extreme high temperature. (b) 3-day averaged Tmax anomalies (w.r.t 1981–2010) for 3–5 Aug 2017, with box illustrating the area selected for analysis. Also shown are annual maxima of 3-day averaged Tmax as (c) anomalies w.r.t 1981–2010 and (d) rank of the year 2017 in the 1950–2017 series. Locations of the stations used in Spain, France, Italy, and Croatia (black markers) are given in (c). Source: E-OBS data.

in their time series than gridded observations, which can suffer from varying variability (heteroscedasticity) due to varying numbers of input stations per grid box over time: more stations can average out some of the noise, and no stations gives climatology. A resulting artificial change in variability over time could be incorrectly interpreted as a change in the frequency of extremes due to global warming. We therefore additionally analyze homogenized station series of TX3X, based on the European Climate Assessment and Dataset (ECA&D; Klein Tank et al. 2002), for four stations (see dots in Fig. 1c): Madrid-Cuatro Vientos Airport (Spain), Montélimar (France), Monte Cimone (Italy), and Gospić (Croatia). The record heat wave conditions were to the south of the stations analyzed here in Spain and France (see ranking of 2017 TX3X in Fig. 2d), but we could not

find (by visual inspection of the TX3X time series) non-coastal stations without discontinuities in those regions and the models we use cannot resolve the required coastal effects.

To determine the return periods of TX3X, we fit the temperature observations to a generalized extreme value (GEV) distribution, with μ being the position parameter, σ the scale parameter, and ξ the shape parameter. Global warming is factored in by allowing the GEV fit to shift with the (low-pass filtered) global mean surface temperature (T_{global}), that is, $\mu = \mu_0 + \alpha T_{\text{global}}$, with α being the fitted trend in K K^{-1} and with σ and ξ fixed. This assumption, that global warming influences only the mean of the distribution and not the variability or shape, is checked in climate models with enough data to analyze the distributions of the past and present climate in independent time

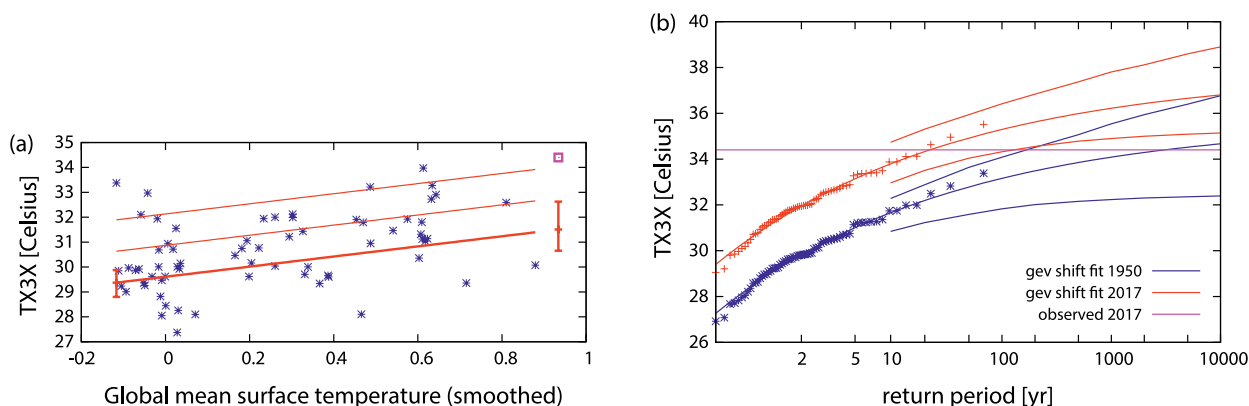


FIG. 2. An example of the results for the observed TX3X for the SE-box. (a) The fit applied to observations, where asterisks mark the observations, the thick line denotes the time-varying mean (fitted position parameter), the thin lines mark 1σ and 2σ (with σ the fitted scale parameter) above the mean, and the two vertical red whiskers show the 95% confidence interval of the fitted position parameter for the climates of 1950 (leftmost) and 2017 (rightmost). (b) Return period distributions shifted to the climates of 2017 (red lines and crosses) and the past (1950; blue lines and asterisks), including error margins (red and blue bounding curves). The purple square in (a) and horizontal line in (b) indicate the 2017 value (not included in the fits).

slices/experiments. Confidence intervals are estimated using a 1000-member non-parametric bootstrap.

After validations on several model ensembles (weather@home, the European Consortium Earth System Model (EC-Earth), the Hadley Centre Global Environment Model, version 3a, (HadGEM-3A), and the European branch of the Coordinated Regional Downscaling Experiment (EURO-CORDEX)) we perform a standard analysis to attribute changes in the return period to climate change, and synthesize the results. Similar methods, including the GEV approach described above, have been applied in van Oldenborgh et al. (2015), Uhe et al. (2016), Philip et al. (2018), and van Oldenborgh et al. (2018).

RESULTS. Our observational analysis shows that the 2017 SE-box TX3X peaked for 3–5 August at 34.4°C (3.4°C higher than the average 3-day heat wave in 1981–2010) in the E-OBS dataset. The return period in 2017 is about 20 years [95% confidence interval (CI): 7–130 yr], whereas in 1950 the (extrapolated) return period is about 3000 years (97.5% CI: at least 160 yr); see Fig. 2. The ratio of these return periods gives a best estimate of the risk ratio (RR) between 1950 and 2017 of roughly 140 (97.5% CI: at least 5), and a change in magnitude of about 2.1°C (95% CI: 0.9° – 3.7°C).

In this particular study, model validation (see the online supplemental information) revealed that the models overestimate the variability found in the SE-box-averaged TX3X observations. Therefore we cannot provide RRs for models or a synthesis

combining observations and models for the SE-box. It is nevertheless clear that there is an increase in the occurrence of heat waves like those of summer 2017. Observations revealed that, since 1950, the risk at least quintupled, but probably increased much more. We emphasize communication of the conservative lower limit of “at least 5” to avoid results dependent on large extrapolations. A formal attribution to anthropogenic climate change is therefore not possible but is very plausible given the attributed rise in seasonal mean temperatures (Stott et al. 2004).

The results for the station analysis are listed in Table 1. As expected, the return periods for Madrid-Cuatro Vientos and Montélimar are not extreme, but in Monte Cimone and Gospić the 2017 heat wave was the highest on record. All stations show a significant trend toward more frequent extremes ($p < 0.025$). We also include model results (Table 1) for models evaluated (see the supplement) to perform adequately at the individual station locations. Three out of the four stations are located outside of the SE-box, which explains part of the different outcome in the models’ performance. Note that the signal-to-noise ratio of the observations will be smaller for individual stations than for an area average. Model systematic errors may therefore fall within uncertainty ranges of the observations more easily at single locations. A synthesized (weighted average) result for each station combining observed and available validated model results is given in the final column of Table 1. This provides estimates of the lower and upper bounds (95% CI) of the risk ratio between 1950 and 2017. In general, the

TABLE 1. Summary of observational and validated model results in TX3X for the station locations.

Station	Observed 2017 TX3X and anomaly w.r.t. 1981–2010	Return period in current climate (95% CI)	Year of comparison for risk ratio	Risk ratio (95% CI)	Synthesized results: Risk ratio for 2017/1950
Spain: Madrid-Cuatro Vientos (1945–now)	39.5°C, 6.3°C	6 yr (3 ... 19 yr)	1950	13 (2 ... 1300)	6 ... 50
EURO-CORDEX			1971–2000	5 (3 ... 7)	
France: Montélimar (1921–2017)	37.9°C, 8.0°C	6 yr (3 ... 20 yr)	1950	3.3 (1.1 ... 9.5)	3 ... 8
EC-Earth			1950	4.9 (3.8 ... 6.3)	
EURO-CORDEX			1971–2000	4.2 (2.5 ... 5.8)	
Italy: Monte Cimone (1951–2017 with gap)	23.5°C, 14.7°C	20 yr (6 ... 500 yr)	1950	220 (1.9 ... ∞)	3.5 ... 8
EC-Earth			1950	4.7 (3.6 ... 5.8)	
EURO-CORDEX			1971–2000	3.5 (2.5 ... 7.5)	
Croatia: Gospić (1906–2017 with gaps)	37.5°C, 10.4°C	40 yr (4 ... ∞ yr)	1950	60 (4 ... ∞)	3 ... 7
EC-Earth			1950	4.4 (3.3 ... 5.4)	

lower bounds of the observations and model results are of the same order of magnitude but the upper bounds and best estimates differ with large differences in sample sizes and higher variability in the models. Besides providing a formal attribution, the effect of the model results in the synthesis is to confine the large uncertainty range on the upper bound.

In general, observations and models agree on a tendency toward more frequent 3-day summer temperature extremes like in summer 2017, at the selected individual station locations. Accounting also for the observed increase in risk in the SE-box, we estimate that probabilities in 2017 are at least 3.5 times higher compared to 1950 (and at least 4 times higher compared to 1900).

DISCUSSION. Our impact-based approach to attribution for last summer's Euro-Mediterranean heat waves yielded a return time in the current climate of around 20 years for southeastern Europe, the region suffering the greatest impacts. This is similar to King (2017), indicative that results are insensitive to minor differences in event definition. Significant trends in the likelihood of 3-day heat waves can be seen not only in area-averaged observations but also in individual station series. Foundational attribution work on European *seasonal* temperature extremes (e.g., Stott et al. 2004; Schär et al. 2004; Christidis et al. 2015) has led to a general view that the “heat wave attribution problem” is largely solved. On the *daily* time scale however, this is not the case: Models confirm an increase in likeli-

hood with global warming but fail to reproduce some key features of the observed distribution of heat waves [variability in southeastern Europe (this study) and trends and variability in northern Europe (Sippel et al. 2016; Min et al. 2013)]. Future research is necessary to reveal the mechanisms. Possible hypotheses are over-efficient model moisture recycling leading to spatial, and over time, temporal, temperature heterogeneity, insufficient moisture transport, or an incorrect variability in boundary layer height.

ACKNOWLEDGMENTS. This study was conducted as part of the World Weather Attribution (WWA) funded by the MacArthur Foundation and was also supported in part by the EUPHEME project, which is part of ERA4CS, an ERA-NET initiated by JPI Climate and co-funded by the European Union (Grant 690462).

REFERENCES

- BBC, 2017: Europe heatwave sparks health warnings as temperatures soar. BBC, 4 August 2017, www.bbc.com/news/world-europe-40825668.
- Christidis, N., G. S. Jones, and P. A. Stott, 2015: Dramatically increasing chance of extremely hot summers since the 2003 European heatwave. *Nat. Climate Change*, **5**, 46–50, <https://doi.org/10.1038/nclimate2468>.
- D'Ippoliti, D., P. Michelozzi, C. Marino, and Coauthors, 2010: The impact of heat waves on mortality in 9

- European cities: Results from the EuroHEAT project. *Environ. Health*, **9**, 37, <https://doi.org/10.1186/1476-069X-9-37>.
- Haylock, M. R., N. Hofstra, A. M. G. Klein Tank, E. J. Klok, P. D. Jones, and M. New, 2008: A European daily high-resolution gridded data set of surface temperature and precipitation for 1950–2006. *J. Geophys. Res.*, **113**, D20119, <https://doi.org/10.1029/2008JD010201>.
- Horowitz, J., 2017: In Italy's drought-hit vineyards, the harvest of a changing climate. 22 August 2017, *New York Times*, www.nytimes.com/2017/08/22/world/europe/barolo-italy-wine-climate-change.html?mcubz=0&r=0.
- IFRC, 2017: IFRC warns of serious health risks as extreme heatwave sweeps across Europe. 4 August 2017, International Federation of Red Cross and Red Crescent Societies, <http://media.ifrc.org/ifrc/press-release/ifrc-warns-serious-health-risks-extreme-heatwave-sweeps-across-europe/>.
- King, A., 2017: Southeast Europe swelters through another heatwave with a human fingerprint. *The Conversation*, accessed 19 March 2018, <https://theconversation.com/southeast-europe-swelters-through-another-heatwave-with-a-human-fingerprint-82139>.
- Klein Tank, A. M. G., and Coauthors, 2002: Daily dataset of 20th-century surface air temperature and precipitation series for the European Climate Assessment. *Int. J. Climatol.*, **22**, 1441–1453, <https://doi.org/10.1002/joc.773>.
- Min, E., W. Hazeleger, G. J. van Oldenborgh, and A. Sterl, 2013: Evaluation of trends in high temperature extremes in north-western Europe in regional climate models. *Environ. Res. Lett.*, **8**, 014011, <https://doi.org/10.1088/1748-9326/8/1/014011>.
- Mitchell, D., and Coauthors, 2016: Attributing human mortality during extreme heat waves to anthropogenic climate change. *Environ. Res. Lett.*, **11**, 074006, <https://doi.org/10.1088/1748-9326/11/7/074006>.
- Otto, F. E. L., and G. J. van Oldenborgh, R. Vautard, and C. Schwierz, 2017: Record June temperatures in western Europe. World Weather Attribution, accessed 30 March 2018, www.worldweatherattribution.org/analyses/european-heat-june-2017/.
- , S. Philip, S. Kew, S. Li, A. King, and H. Cullen, 2018: Attributing high-impact extreme events across timescales—A case study of four different types of events. *Climatic Change*, **149**, 399–412, <https://doi.org/10.1007/s10584-018-2258-3>.
- Philip, S. Y., S. F. Kew, M. Hauser, B. P. Guillod, A. J. Teuling, K. Whan, P. Uhe, and G. J. van Oldenborgh, 2018: Western US high June 2015 temperatures and their relation to global warming and soil moisture. *Climate Dyn.*, **50**, 2587–2601, <https://doi.org/10.1007/s00382-017-3759-x>.
- Schär, C., P. L. Vidale, D. Lüthi, C. Frei, C. Häberli, M. A. Liniger, and C. Appenzeller, 2004: The role of increasing temperature variability in European summer heatwaves. *Nature*, **427**, 332–336, <https://doi.org/10.1038/nature02300>.
- Sippel, S., F. E. L. Otto, M. Flach, and G. J. van Oldenborgh, 2016: The role of anthropogenic warming in 2015 central European heat waves [in “Explaining Extreme Events of 2015”]. *Bull. Amer. Meteor. Soc.*, **97**, S51–S56, <https://doi.org/10.1175/BAMS-D-16-0150.1>.
- Stott, P. A., D. A. Stone, and M. R. Allen, 2004: Human contribution to the European heatwave of 2003. *Nature*, **432**, 610–614, <https://doi.org/10.1038/nature03089>.
- Uhe, P., F. E. L. Otto, K. Haustein, G. J. van Oldenborgh, A. D. King, D. C. H. Wallom, M. R. Allen, and H. Cullen, 2016: Comparison of methods: Attributing the 2014 record European temperatures to human influences. *Geophys. Res. Lett.*, **43**, 8685–8693, <https://doi.org/10.1002/2016GL069568>.
- van Oldenborgh, G. J., R. Haarsma, H. de Vries, and M. R. Allen, 2015: Cold extremes in North America vs. mild weather in Europe: The winter of 2013–14 in the context of a warming world. *Bull. Amer. Meteor. Soc.*, **96**, 707–714, <https://doi.org/10.1175/BAMS-D-14-00036.1>.
- , and Coauthors, 2018: Extreme heat in India and anthropogenic climate change. *Nat. Hazards Earth Syst. Sci.*, **18**, 365–381, <https://doi.org/10.5194/nhess-18-365-2018>.
- Zuvela, M., and A. Vasovic, 2017: 'Lucifer' heat wave holds Italy, eastern Europe in fiery grip. 4 August 2017, Reuters, www.reuters.com/article/us-europe-weather-heatwave/lucifer-heat-wave-holds-italy-eastern-europe-in-fiery-grip-idUSKBN1AK1I8.

11 EXAMINING THE POTENTIAL CONTRIBUTIONS OF EXTREME “WESTERN V” SEA SURFACE TEMPERATURES TO THE 2017 MARCH–JUNE EAST AFRICAN DROUGHT

CHRIS FUNK, ANDREW HOELL, SHARON NICHOLSON, DIRIBA KORECHA, GIDEON GALU, GULEID ARTAN, FETENE TESHOME, KINFE HAILERMARIAM, ZEWDU SEGELE, LAURA HARRISON, ABEBE TADEGE, ZACHARY ATHERU, CATHERINE POMPOSI, AND DIEGO PEDREROS

Anthropogenic warming of Western V sea surface temperatures contributed to East African drought. Extremely warm ($FAR = 1$) Western V SST doubled the probability of drought, contributing to widespread food insecurity.

INTRODUCTION. During March–June (MAMJ) 2017 East Africa (EA; 35°–50°E, 12°S–9°N) experienced an extensive drought across Tanzania, Ethiopia, Kenya, and Somalia that contributed to extreme food insecurity (Funk et al. 2018, hereafter F18) approaching near-famine conditions (FEWSNET 2017a; FSNAU 2017). Effective forecasts, monitoring, and mitigation by the Intergovernmental Authority on Development (IGAD) Climate Predictions and Applications Centre and international partners (FEWSNET 2017a) motivated effective humanitarian responses. When the 2017 MAMJ rains failed, humanitarian assistance was already arriving, stabilizing food prices (FEWSNET 2017b).

Climate simulations indicate (F18) that strong El Niños may often be followed by exceptional warming in the western Pacific, creating the potential for

northeastern Ethiopian/southern African droughts followed by La Niña-like dry conditions during October–December and MAMJ in eastern EA, as in 1999–2001, 2010/11, and 2016/17. While 2016 October–December precipitation deficits do not appear to be significantly influenced by climate change (Uhe et al. 2018), prior research finds that human influence increased the probability of drought during the last severe drought in 2011 (Lott et al. 2013).

Here, we examine EA climate trends and drivers (Fig. 1) and then formally attribute the 2017 EA rainfall deficits and SST extrema (Fig. 2).

EA MAMJ RAINFALL TRENDS. Figure 1a shows standardized EA rainfall anomalies based on the 1900–2014 Centennial Trends (CenTrends; Funk et al. 2015b) dataset and 2015–17 Climate Hazards group Infrared Precipitation with Stations (CHIRPS; Funk et al. 2015c) values. As noted by many authors (Funk et al. 2005; Williams and Funk 2011; Lyon and DeWitt 2012; Nicholson et al. 2012; Funk et al. 2013; Hoell and Funk 2014; Liebmann et al. 2014; Lyon 2014; Nicholson 2014; Yang et al. 2014; Nicholson 2016; Hoell et al. 2017; Liebmann et al. 2017; Nicholson 2017; Funk et al. 2018) and many datasets (Sun et al. 2018), EA has experienced a large increase in the frequency of droughts. Since 1999 only two EA MAMJ seasons were above normal. Figure 1b also shows EA data from the Global Precipitation Climatology Centre (GPCC; Schneider et al. 2014) and a new Ethiopian dataset created by combining CHIRPS with ~150 quality-controlled gauge observations. These also indicate substantial severe declines. Note that the EA region presented is very large and may not be homogeneous across the entire domain or MAMJ season (Nicholson 2017),

AFFILIATIONS: FUNK AND PEDREROS—U.S. Geological Survey, Earth Resources Observation and Science Center; FUNK, KORECHA, GALU, HARRISON, POMPOSI, AND PEDREROS—University of California Santa Barbara Climate Hazards Center, Physical Sciences Division; HOELL—NOAA Earth Systems Research Laboratory; NICHOLSON—Florida State University, Department of Meteorology, Earth, Ocean, and Atmospheric Science; KORECHA AND GALU—Famine Early Warning Systems Network; ARTAN, SEGELE, TADEGE, AND ATHERU—Intergovernmental Authority on Development (IGAD) Climate Prediction and Applications Centre; TESHOME AND HAILERMARIAM—National Meteorological Agency of Ethiopia
CORRESPONDING AUTHOR: Chris Funk, chris@geog.ucsb.edu

DOI:10.1175/BAMS-D-18-0108.1

A supplement to this article is available online (10.1175/BAMS-D-18-0108.2)

© 2019 American Meteorological Society

For information regarding reuse of this content and general copyright information, consult the [AMS Copyright Policy](#).

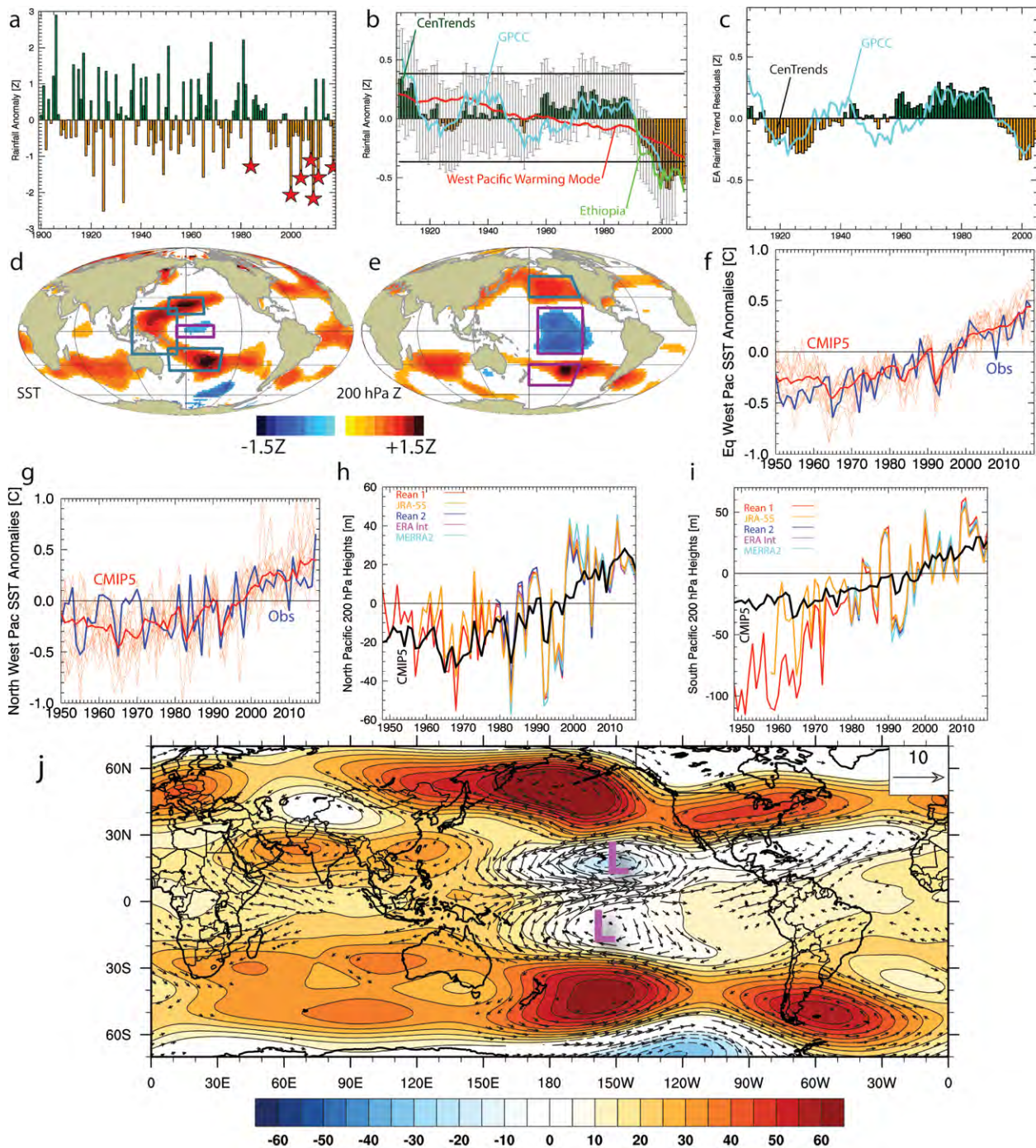


FIG. 1. (a) Standardized EA rainfall from CenTrends/CHIRPS; stars denote droughts. (b) 20-yr EA rainfall with bootstrapped confidence intervals and standard errors. Vertical error bars denote CenTrends kriging standard errors. Horizontal lines indicate deviations significant at $p = 0.05$, based on 10,000 bootstrapped samples. Red line indicates west Pacific warming mode regression estimates. Ethiopia time series averaged over Ethiopia southeast of 9°N , 35°E . (c) EA decadal rainfall decadal variability, based on WPWM regression residuals. (d),(e) Dry season composites of MAMJ SST and Reanalysis I 200-hPa heights. Screened for significance at $p = 0.1$. (f),(g) MAMJ SST time series. (h),(i). MAMJ 200-hPa heights from multiple reanalyses. (j) Changes in CAM5 200-hPa heights and winds during 1981–2016 vs 1921–80 WNP warm events, screened for significance at $p = 0.1$ (Funk et al. 2018).

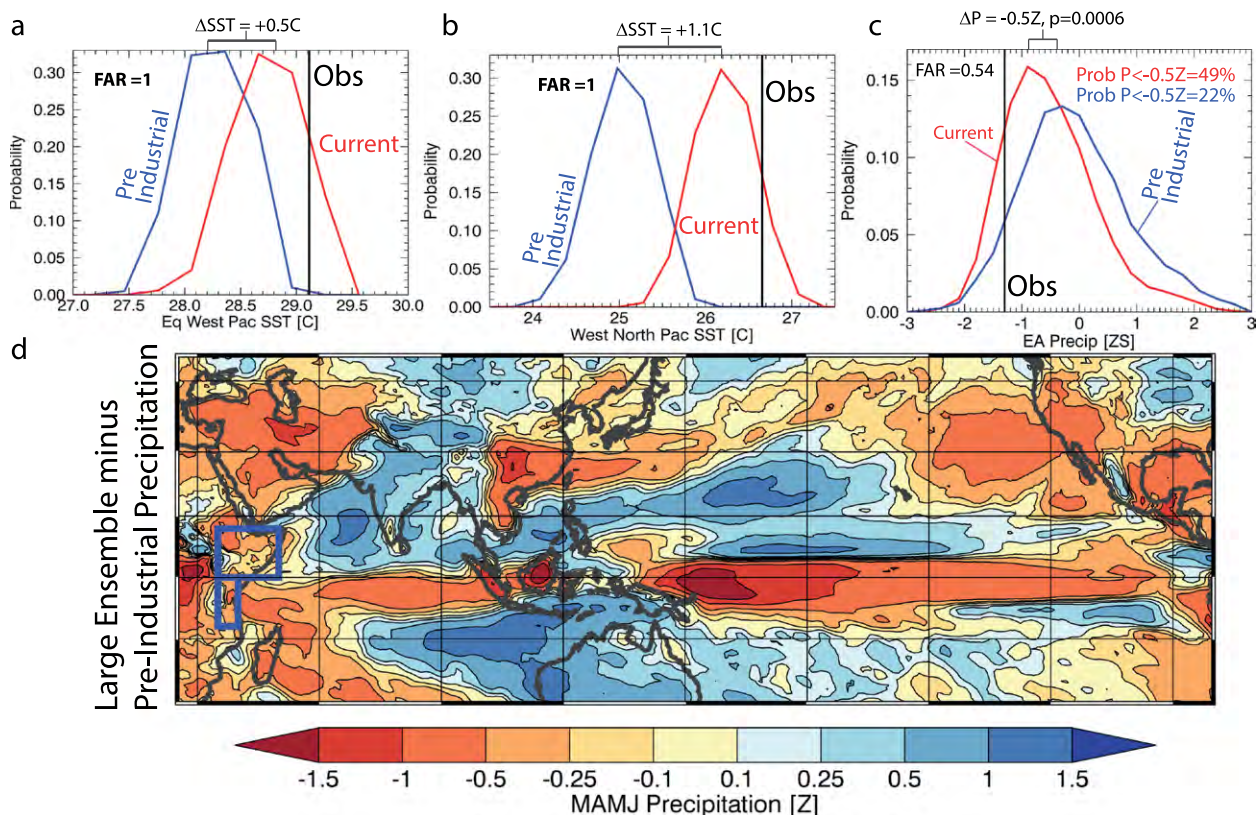


FIG. 2. (a),(b) Preindustrial and 2016–18 distributions for **WEP** and **WNP** SST. 2017 ERSSTv4 values are shown with vertical lines. CESMI SST bias adjusted based on the 1920–2017 LE and observed SST averages. (c) EA precipitation distributions for these same analog seasons. Rainfall based on blue boxes in Fig. 2d. The $-0.5Z$ distribution shift is highly significant ($p = 0.0006$). (d) A map of the difference in precipitation for the 43 large ensemble analog seasons (WVG $< -1Z$ and Niño-4 values between 0 and 1Z) and 674 preindustrial analogs (Niño-4 values between 0 and 1Z). When strong WVG conditions occur along with neutral-warm Niño-4 SST, we find a La Niña-like response associated with dry EA conditions.

but most of this region has experienced substantial declines (Funk et al. 2015b), and analysis of a more homogeneous eastern EA region identifies similar changes (F18).

Several recent studies (Lyon 2014; Yang et al. 2014) have suggested that Pacific decadal variability (Lyon et al. 2014) primarily accounts for the recent decrease in rainfall. These studies, however, are based on analyses of detrended EA precipitation. These trends are large (Funk et al. 2015b; Nicholson 2017) and should not be discounted. The red line in Fig. 1b shows an estimate of the EA rainfall trend based on a regression with the west Pacific warming mode—the first principal component of global SST after the influence ENSO has been removed (Funk and Hoell 2015). It has been shown that increases in this mode have been associated with an enhanced Walker circulation, drying over East Africa, and a characteristic “Western V” Pacific SST warming pattern (Funk and Hoell 2015, 2017). The so-called Western V stretches poleward and eastward from a

point near the Maritime Continent (Fig. 1d). Our EA trend estimate indicates a $-0.5Z$ decline between 1900 and 2017 (throughout Z stands for standardized anomaly or Z score). CenTrends and GPCC residuals from this trend mode (Fig. 1c) also exhibit similar and substantial decadal variations. Between 1900–1919 and 1998–2017, the observed EA time series declines from $+0.3Z$ to $-0.5Z$; $\sim 0.5Z$ of this decline may be associated with the trend mode, and $\sim 0.3Z$ may be associated with decadal changes.

We can explore these changes further by compositing (Figs. 1d,e) Extended Reconstructed SST version 4 (ERSSTv4; Huang et al. 2015) standardized MAMJ SSTs and NCEP–NCAR Reanalysis 1 200-hPa heights for recent EA drought years (stars in Fig. 1a). We see a distinct Western V structure and a La Niña-like temperature dipole in ocean temperatures (Fig. 1d). In the upper atmosphere we find La Niña-like upper-level cyclonic lows over the equatorial eastern Pacific. Poleward of these lows we also see upper-level height increases (Fig. 1e). These height gradients produce

vigorous easterly disruptions of the subtropical westerly jet that converge near the date line, enhancing subsidence, decreasing precipitation over the central equatorial Pacific (F18), and enhancing the Indian Ocean branch of the Walker circulation (Williams and Funk 2011; Liebmann et al. 2014, 2017). See upper-level winds and velocity potential changes in Fig. ES1 in the online supplemental material.

Observed SST from the western equatorial Pacific (WEP; 20°S–20°N, 120°–170°E) and western North Pacific (WNP; 13°–30°N, 160°E–140°W) have experienced very large increases ($>+0.6Z$) since the 1950s (Figs. 1f,g) that track closely with estimates from a multimodel CMIP5 climate change ensemble (see Table ES1 in the online supplemental material). According to ERSSTv4, 2017 MAMJ WEP and WNP SST values were the second warmest or warmest on record. This is consistent with WEP/WNP warming that tends to follow strong El Niños (F18); since 1981, large jumps in west Pacific SST have followed in six out of the eight strongest El Niños. As recently noted (Newman et al. 2018), the 2015/16 El Niño produced exceptionally warm Niño-4 SSTs.

Upper-level midlatitude Pacific height fields from five reanalyses (Figs. 1h,i) indicate enhanced ridging to the northeast and southeast of the Western V SST anomalies. Such ridging would enhance the impact of La Niña-like upper-level equatorial lows, diverting the subtropical westerly jet and increasing subsidence near the date line (Fig. ES1). Composites of the differences in the Community Atmosphere Model version 5 (CAM5) upper-level height and winds (Fig. 1j) during strong versus moderate WNP events (see F18) emphasize how such remote height changes modulate the Walker circulation by enhancing date line subsidence.

These observational results (Fig. 1) indicate that EA MAMJ droughts are associated with warm WNP/WEP SST and stronger Walker circulation anomalies.

SST AND PRECIPITATION ATTRIBUTION.

We next use simulations from the Community Earth System Model version 1 (CESM1; Hurrell et al. 2013) to examine WEP/WNP SST extremes and EA rainfall. The CESM1 represents mean SST conditions and ENSO variations well (Flato et al. 2013; Hurrell et al. 2013). CESM1 west Pacific warming trends and the associated negative teleconnection to EA rainfall is similar to that found in observations (Funk and Hoell 2017).

To characterize 2017 WEP and WNP SST, we use 40 “historic” simulations for 2016, 2017, and 2018; these realizations represent a world with climate

change. These simulations can be contrasted with simulations representing preindustrial conditions (Figs. 2a,b), identifying substantial warming. Note that the historic CMIP5 multimodel ensemble also indicates rapid warming in these regions [Figs. 1f,g and Table ES1; see also Table 7 of Funk et al. (2018)]. The influence of climate change, measured by the fraction of attributable risk (FAR), can be defined as $FAR = 1 - (P_0/P_1)$, where P_0 is the modeled probability of the event in a climate without anthropogenic influence, and P_1 is the probability in a climate with anthropogenic influence (Allen 2003; Stott et al. 2004). Here, the FAR values are 1 in both cases. These temperature extremes would be extremely unlikely without human-induced climate change.

We next use the CESM1 to explore “Western V gradient” (WVG) impacts. This approach is similar to previous attribution analyses (Funk et al. 2015a) based on the WPG, except that we extend the gradient definition to incorporate the WNP, since extratropical heating and height disruptions (Figs. 1d,e) help intensify the Walker circulation (Fig. 1j), producing subsidence over EA (Fig. ES1). Note that we use the precipitation simulations directly, rather than using a statistical “two-step” approach. The WVG is defined as the standardized difference between Niño-4 and Western V SST: $WV = [Z(WEP) + Z(WNP)]/2$, where $Z()$ denotes standardization. *The core of our attribution analysis is that we use the modeled EA CESM1 rainfall distributions to evaluate the impact of the WVG.*

Most WVG values since 1999 have been below normal, and the 2017 WVG value was $-1.4Z$, indicating a strong gradient. The 2017 season, however, stands out as unique, given that it also exhibited warm ($+0.8Z$) Niño-4 SST conditions. Extreme Western V SST coexisted with modestly warm east Pacific SST (F18). While such a unique event is hard to evaluate using observations, F18 suggests that CESM1 simulations indicate substantial increases in the frequency of very warm west Pacific SSTs (see Fig. 9I in F18), as do all the CMIP5 models (as in Table 7 in F18 and Table ES1 herein). Here we contrast similar events (WVG values of $<-1Z$ and Niño-4 SST between 0 and $+1Z$; 43 events between 2016 and 2018) with similar preindustrial conditions absent Western-V warming (Niño-4 SST between 0 and $+1Z$; 674 events).

Examining the precipitation differences, we find a La Niña-like precipitation response (Fig. 2d), despite neutral-warm Niño-4 SST. In the presence of extreme Western V warming we find dry EA conditions, event without cool La Niña SST. Figure 2c expresses this tendency using EA rainfall distributions based on the

43 and 674 2016–18 and preindustrial analog events. *Warm “Western V” conditions double the probability of EA droughts*. Approximately one-half (49%) of the 2016–18 versus one-quarter (26%) of the preindustrial simulations were dry ($<-0.5Z$). The simulations indicate that strong WVG conditions, produced by exceptionally ($FAR = 1$) warm WEP and WNP SST, doubled the chance of EA experiencing a drought in 2017. It should be noted, however, that this study relies on a single model. The National Academies recommends the use of a multimethod or multimodel approach (National Academies of Sciences 2016); as more large ensembles become available, this approach will be expanded. Here, we have shown that warm WV SST can produce EA drying on decadal (Fig. 1) and seasonal (Fig. 2) time scales. Enhanced early warning systems, risk reduction strategies, and climate services may help cope with these more frequent droughts.

ACKNOWLEDGMENTS. Support was provided by the USAID Famine Early Warning Systems Network and the U.S. Geological Survey Drivers of Drought program. Simulations were obtained from the ESRL Facility for Climate Assessments (FACTS) and the KNMI Climate Explorer. Reanalysis time series were obtained from the ESRL Web-based Reanalysis Intercomparison Toolkit (WRIT).

REFERENCES

- Allen, M. R., 2003: Liability for climate change. *Nature*, **421**, 891–892, <https://doi.org/10.1038/421891a>.
- FEWS NET, 2017a: Somalia: Persistent drought leads to major food security crisis. Famine Early Warning Systems Network, World Food Programme, accessed 23 March 2018, www.wfp.org/news/news-release/somalia-persistent-drought-leads-major-food-security-crisis-0.
- , 2017b: Decreases in staple food prices likely due to humanitarian assistance. Famine Early Warning Systems Network, World Food Programme, accessed 23 March 2018, <http://fewsn.net/east-africa/somalia/key-message-update/march-2017>.
- Flato, G., and Coauthors, 2013: Evaluation of climate models. *Climate Change 2013: The Physical Science Basis*, T. F. Stocker et al., Eds., Cambridge University Press, 741–866.
- FSNAU, 2017: Risk of Famine (IPC Phase 5) persists in Somalia. Food Security and Nutrition Analysis Unit–Somalia, accessed 23 March 2018, www.fsnau.org/in-focus/fewsn-fsnau-joint-somalia-food-security-outlook-february-september-2017.
- Funk, C., and A. Hoell, 2015: The leading mode of observed and CMIP5 ENSO-residual sea surface temperatures and associated changes in Indo-Pacific climate. *J. Climate*, **28**, 4309–4329, <https://doi.org/10.1175/JCLI-D-14-00334.1>.
- , and —, 2017: Recent climate extremes associated with the west Pacific warming mode. *Climate Extremes: Patterns and Mechanisms*, S. Y. Wang et al., Eds., Wiley, 165–176, <https://doi.org/10.1002/9781119068020.ch10>.
- , and Coauthors, 2005: Recent drought tendencies in Ethiopia and equatorial–subtropical eastern Africa. Vulnerability to Food Insecurity: Factor Identification and Characterization Rep. 01/2005, FEWS NET, 12 pp., <https://reliefweb.int/report/ethiopia/recent-drought-tendencies-ethiopia-vulnerability-food-insecurity-factor>.
- , and Coauthors, 2013: Attribution of 2012 and 2003–12 rainfall deficits in eastern Kenya and southern Somalia [in “Explaining Extreme Events of 2012 from a Climate Perspective”]. *Bull. Amer. Meteor. Soc.*, **94**, 45–48, <https://doi.org/10.1175/BAMS-D-13-00085.1>.
- , S. Shukla, A. Hoell, and B. Livneh, 2015a: Assessing the contributions of East African and west Pacific warming to the 2014 boreal spring East African drought [in “Explaining Extreme Events of 2014 from a Climate Perspective”]. *Bull. Amer. Meteor. Soc.*, **96**, S77–S82, <https://doi.org/10.1175/BAMS-D-15-00106.1>.
- , S. E. Nicholson, M. Landsfeld, D. Klotter, P. Peterson, and L. Harrison, 2015b: The Centennial Trends Greater Horn of Africa precipitation dataset. *Sci. Data*, **2**, 150050, <https://doi.org/10.1038/sdata.2015.50>.
- , and Coauthors, 2015c: The Climate Hazards Infrared Precipitation with Stations—A new environmental record for monitoring extremes. *Sci. Data*, **2**, 150066, <https://doi.org/10.1038/sdata.2015.66>.
- , and Coauthors, 2018: Examining the role of unusually warm Indo-Pacific sea surface temperatures in recent African droughts. *Quart. J. Roy. Meteor. Soc.*, <https://doi.org/10.1002/qj.3266>, in press.
- Hoell, A., and C. Funk, 2014: Indo-Pacific sea surface temperature influences on failed consecutive rainy seasons over eastern Africa. *Climate Dyn.*, **43**, 1645–1660, <https://doi.org/10.1007/s00382-013-1991-6>.
- , M. Hoerling, J. Eischeid, X.-W. Quan, and B. Liebmann, 2017: Reconciling theories for human and natural attribution of recent East Africa drying. *J. Climate*, **30**, 1939–1957, <https://doi.org/10.1175/JCLI-D-16-0558.1>.
- Huang, B., and Coauthors, 2015: Extended reconstructed sea surface temperature version 4 (ERSST. v4). Part

- I: Upgrades and intercomparisons. *J. Climate*, **28**, 911–930, <https://doi.org/10.1175/JCLI-D-14-00006.1>.
- Hurrell, J. W., and Coauthors, 2013: The Community Earth System Model: A framework for collaborative research. *Bull. Amer. Meteor. Soc.*, **94**, 1339–1360, <https://doi.org/10.1175/BAMS-D-12-00121.1>.
- Liebmann, B., and Coauthors, 2014: Understanding recent eastern Horn of Africa rainfall variability and change. *J. Climate*, **27**, 8630–8645, <https://doi.org/10.1175/JCLI-D-13-00714.1>.
- , and Coauthors, 2017: Climatology and interannual variability of boreal spring wet season precipitation in the eastern Horn of Africa and implications for its recent decline. *J. Climate*, **30**, 3867–3886, <https://doi.org/10.1175/JCLI-D-16-0452.1>.
- Lott, F. C., N. Christidis, and P. A. Stott, 2013: Can the 2011 East African drought be attributed to human-induced climate change? *Geophys. Res. Lett.*, **40**, 1177–1181, <https://doi.org/10.1002/grl.50235>.
- Lyon, B., 2014: Seasonal drought in the Greater Horn of Africa and its recent increase during the March–May long rains. *J. Climate*, **27**, 7953–7975, <https://doi.org/10.1175/JCLI-D-13-00459.1>.
- , and D. G. DeWitt, 2012: A recent and abrupt decline in the East African long rains. *Geophys. Res. Lett.*, **39**, L02702, <https://doi.org/10.1029/2011GL050337>.
- , A. G. Barnston, and D. G. DeWitt, 2014: Tropical Pacific forcing of a 1998–1999 climate shift: Observational analysis and climate model results for the boreal spring season. *Climate Dyn.*, **43**, 893–909, <https://doi.org/10.1007/s00382-013-1891-9>.
- National Academies of Sciences, 2016: *Attribution of Extreme Weather Events in the Context of Climate Change*. National Academies Press, 186 pp.
- Newman, M., A. T. Wittenberg, L. Cheng, G. P. Compo, and C. A. Smith, 2018: The extreme 2015/16 El Niño, in the context of historical climate variability and change [in “Explaining Extreme Events of 2016 from a Climate Perspective”]. *Bull. Amer. Meteor. Soc.*, **99**, S16–S20, <https://doi.org/10.1175/BAMS-D-17-01116.1>.
- Nicholson, S. E., 2014: A detailed look at the recent drought situation in the Greater Horn of Africa. *J. Arid Environ.*, **103**, 71–79, <https://doi.org/10.1016/j.jaridenv.2013.12.003>.
- , 2016: An analysis of recent rainfall conditions in eastern Africa. *Int. J. Climatol.*, **36**, 526–532, <https://doi.org/10.1002/joc.4358>.
- , 2017: Climate and climatic variability of rainfall over eastern Africa. *Rev. Geophys.*, **55**, 590–635, <https://doi.org/10.1002/2016RG000544>.
- , A. K. Dezfuli, and D. Klotter, 2012: A two-century precipitation dataset for the continent of Africa. *Bull. Amer. Meteor. Soc.*, **93**, 1219–1231, <https://doi.org/10.1175/BAMS-D-11-00212.1>.
- Schneider, U., A. Becker, P. Finger, A. Meyer-Christoffer, M. Ziese, and B. Rudolf, 2014: GPCC’s new land surface precipitation climatology based on quality-controlled in situ data and its role in quantifying the global water cycle. *Theor. Appl. Climatol.*, **115**, 15–40, <https://doi.org/10.1007/s00704-013-0860-x>.
- Stott, P. A., D. A. Stone, and M. R. Allen, 2004: Human contribution to the European heatwave of 2003. *Nature*, **432**, 610–614, <https://doi.org/10.1038/nature03089>.
- Sun, Q., C. Miao, Q. Duan, H. Ashouri, S. Sorooshian, and K.-L. Hsu, 2018: A review of global precipitation data sets: Data sources, estimation, and intercomparisons. *Rev. Geophys.*, **56**, 79–107, <https://doi.org/10.1002/2017RG000574>.
- Uhe, P., and Coauthors, 2018: Attributing drivers of the 2016 Kenyan drought. *Int. J. Climatol.*, **38**, e554–e568, <https://doi.org/10.1002/joc.5389>.
- Williams, P., and C. Funk, 2011: A westward extension of the warm pool leads to a westward extension of the Walker circulation, drying eastern Africa. *Climate Dyn.*, **37**, 2417–2435, <https://doi.org/10.1007/s00382-010-0984-y>.
- Yang, W., R. Seager, M. A. Cane, and B. Lyon, 2014: The East African long rains in observations and models. *J. Climate*, **27**, 7185–7202, <https://doi.org/10.1175/JCLI-D-13-00447.1>.

RISKS OF PRE-MONSOON EXTREME RAINFALL EVENTS OF BANGLADESH: IS ANTHROPOGENIC CLIMATE CHANGE PLAYING A ROLE?

RUKSANA H. RIMI, KARSTEN HAUSTEIN, EMILY J. BARBOUR, AND MYLES R. ALLEN

Anthropogenic climate change doubled the likelihood of the 2017 pre-monsoon extreme 6-day rainfall event at northeast Bangladesh. The magnitude of this contribution is sensitive to the climatological period in use.

INTRODUCTION. Northeastern Bangladesh (NEB; 90.5°–92.5°E, 24°–25.5°N) has unique low-land areas known as *haors*. The “Boro” paddy (rice) crop is cultivated in these haors in dry winter season (December–February) and harvested during April–May. Boro accounted for ~55% of national rice production per annum during 2011–16 and NEB contributed to ~15% of the total Boro rice production over this period (FAO 2017). NEB receives highest annual mean rainfall of >4,300 mm, in contrast to western Bangladesh, which receives 1,400 mm (Shahid 2010). Topographic uplifting of the south-westerly flow by the Meghalaya Plateau and other surrounding mountains triggers heavy convective rainfall at NEB in the pre-monsoon season (Murata et al. 2008, 2011; Sanderson and Ahmed 1979; Shahid 2010). Pre-monsoon rainfall during March–April facilitates growth of Boro but events >150 mm of total 6-day rainfall can cause early flash floods and damage crops. On 27 March 2017, extreme rainfall over NEB triggered the earliest flash flood since 2000 (Ahmed et al. 2017). Subsequently, ~850,000 households were affected and ~220,000 ha of nearly harvestable Boro were damaged. Crop failure in 2017 contributed to a record 30% rice price hike compared

to 2016 (FAO 2017). Analyzing NOAA’s Climate Prediction Center (CPC) observation data, we find that during 16 March–15 April 2017, 6-day total rainfall over NEB amounted to 225 mm (i.e., 33.33% higher than the flash flood triggering threshold of 150 mm). The highest positive rainfall anomaly (up to 100 mm day⁻¹; relative to 1979–2017) during 16 March–15 April 2017 is found at NEB (see red box in Fig. 1a). To determine how rare this event is, we apply a generalized Pareto (GP) distribution fit to CPC data exceeding 90th percentile values, and find a return time of ~70 years (Fig. 1d).

Most of the attribution studies are done for mid-latitude extreme events of the developed countries while very few of them focus on the tropical region (Marthews et al. 2015; Otto et al. 2015; Otto 2017) or developing countries, even though these countries experience extreme events and have the least capacity to adapt with the consequent impacts (IPCC 2013).

To understand the drivers behind the 2017 floods, here we investigate the probabilities of extreme 6-day rainfall during pre-monsoon season in Bangladesh and analyze whether or not anthropogenic climate change has changed the odds of such events occurring (Allen 1999). We utilize the very large weather@home regional climate model (RCM) ensemble based on HadRM3P. We also investigate the potential contribution of radiative cooling from anthropogenic aerosols as their presence can counterbalance the greenhouse gas (GHG) induced intensification of the hydrological cycle (Li et al. 2016). Niño-3.4 and Indian Ocean dipole (IOD) indices are used to quantify the role of two key climate modes. Additionally, two global climate models (GCMs) of MIROC5 and ETH_CAM4 are used to test the robustness of our results.

DATA AND METHODS. We use daily rainfall data from Asian Precipitation Highly Resolved Observational Data Integration toward Evaluation of Water Resources (APHRODITE) covering 1979–2007

AFFILIATIONS: RIMI, HAUSTEIN, AND ALLEN—Environmental Change Institute, School of Geography and the Environment, University of Oxford, Oxford, United Kingdom; BARBOUR—Environmental Change Institute, School of Geography and the Environment, University of Oxford, Oxford, United Kingdom, and CSIRO Land and Water, Canberra, ACT 2601, Australia.

CORRESPONDING AUTHOR: Ruksana H. Rimi, ruksana.rimi@ouce.ox.ac.uk

DOI:10.1175/BAMS-D-18-0152.1

A supplement to this article is available online (10.1175/BAMS-D-18-0152.2)

© 2019 American Meteorological Society

For information regarding reuse of this content and general copyright information, consult the [AMS Copyright Policy](#).

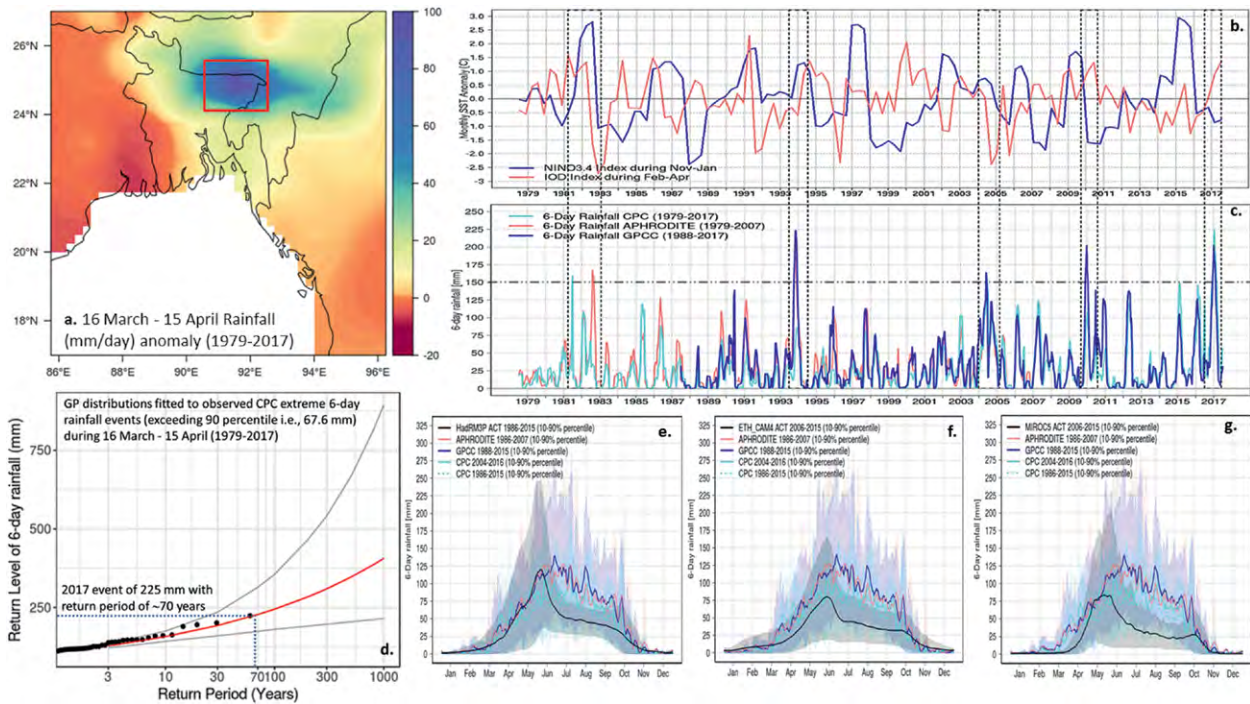


FIG. 1. (a) Spatial distribution of CPC rainfall (mm day⁻¹) over Bangladesh during 16 March–15 April 2017 relative to climatology (1979–2017). The red box indicates the study area of NEB. (b) Niño-3.4 (November–January) and IOD (February–April) indices during 1979–2017. The horizontal dashed black line in (c) indicates the threshold value for heaviest rainfall events. The vertical dashed black rectangles in (b) and (c) indicate the association between the heaviest rainfall events and IOD (Niño-3.4). (d) Return level plot of GP distribution fitted to CPC observed extreme 6-day rainfall events exceeding a 90th percentile threshold. (e)–(g) Annual cycles of 6-day rainfall over NEB as in models and observations (HadRM3P, ETH_CAM4 and MIROC5, respectively), with CPC (1979–2017 and 2004–16), GPCC (1988–2017), and APHRODITE (1979–2007).

(Yatagai et al. 2012), CPC global 0.5° analysis of daily rain gauge measurements covering 1979–2017 (Chen et al. 2008), and Global Rainfall Climatology Centre (GPCC) daily rainfall data covering 1988–2017 (Schamm et al. 2015). The higher-resolution (50 km) weather@home HadRM3P RCM is nested in the global atmosphere-only HadAM3P model [an atmospheric general circulation model (AGCM)] and is driven by prescribed SSTs and sea ice concentration (SIC) (Massey et al. 2015; Guillod et al. 2017) and radiative forcing. Following Schaller et al. (2016), we use 75,000 (30 × 2500) simulations for “Actual March 2017” under factual conditions with observed 2017 GHG concentrations, OSTIA SSTs, and SIC (Donlon et al. 2012) and 15,7500 (30 × 5250) simulations for “Natural March 2017” under conditions that might have been in a counterfactual world without past GHG emissions and other pollutants. We also use 2,160,000 (360 × 30 × 200) simulations for each of the Actual, Natural, and GHG-only climatology over the 30 years (1986–2015) of reference period. Here the GHG-only scenario has current levels of GHGs but the anthropogenic aerosols are set to pre-industrial

levels. In addition, we use smaller ensembles from two GCMs, with 1500 (30 × 50) simulations from MIROC5 and 15,000 (30 × 500) simulations from ETH_CAM4 representing Actual and Natural March during a 10-yr (2006–15) period [see Mitchell et al. (2017) for more details]. All model and observation data are regridded using bilinear interpolation method and then area-averaged rainfall statistics over NEB are analyzed. We use the Niño-3.4 index (Rayner et al. 2003) to determine the lagged correlation with March rainfall over NEB, and with the IOD index (Huang et al. 2017).

We quantified the change in the occurrence probability of rainfall event, the risk ratio (RR), as $RR = P_f / P_{cf}$, where the probability of the event in the factual climate is denoted by P_f and the probability of the same event in a counterfactual climate without anthropogenic climate change is denoted by P_{cf} (NAS 2016). An exception to this is the GHG-only scenario, where RR is calculated using P_{cf} = actual climate instead of natural climate.

As far as the HadRM3P’s performance with regard to APHRODITE, GPCC, and CPC is concerned, the

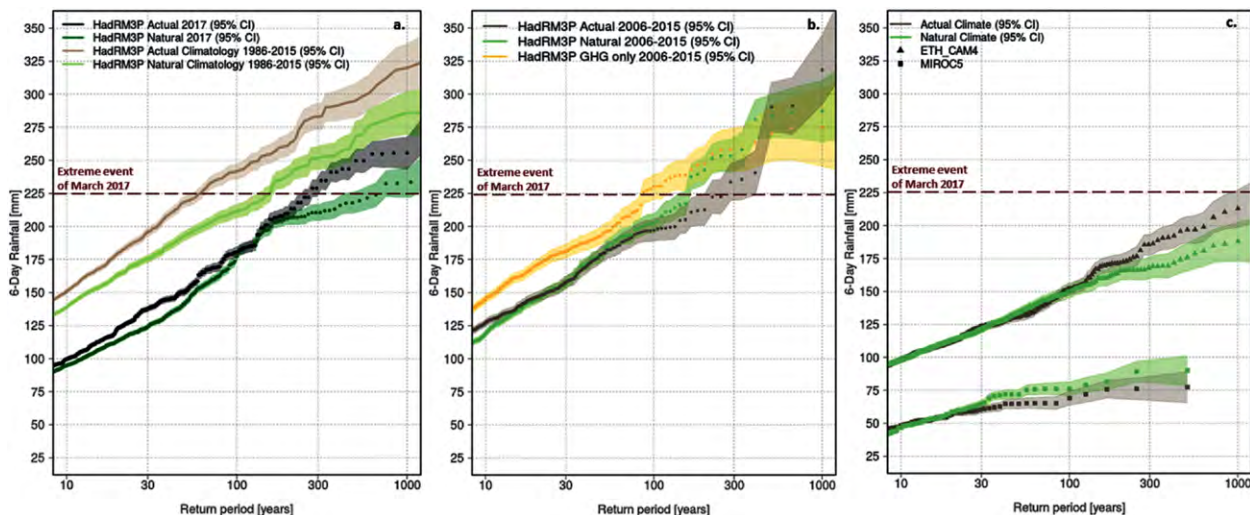


FIG. 2. Return periods for 6-day rainfall events in March over NEB showing (a) HadRM3P Actual 2017 (black) and Natural 2017 (dark green) vs Actual climatology 1986–2015 (gray) and Natural climatology 1986–2015 (light green) ensembles. (b) Actual climatology 2006–15 (gray), Natural climatology 2006–15 (light green), and GHG-only climatology 2006–15 (yellow). (c) Actual climatology 2006–15 (gray) and Natural climatology 2006–15 (light green) but as in MIROC5 (squares) and ETH_CAM4 (triangles) model ensembles. Each dot, triangle, or square represents one simulation of the HadRM3P, MIROC5, or ETH_CAM4 model, respectively, and the shaded polygon shows 95% confidence intervals. The horizontal dashed deep brown line in each panel indicates the extreme event of March 2017.

model reproduces the annual rainfall cycle with satisfactory agreement. However, monsoon rainfall is underestimated in HadRM3P by $\sim 30\%$ (Fig. 1e) with an early onset. We are using model data for March rather than mid-March to mid-April to remove this bias. MIROC5 is biased dry (Fig. 1g) in March ($\sim 50\%$), whereas ETH-CAM4 (Fig. 1f) is biased extremely dry ($\sim 40\%$ in March and $\sim 25\%$ – 50% throughout the monsoon season).

RESULTS AND DISCUSSION. Figure 2 illustrates how the return periods of March extreme 6-day rainfall events have changed from natural counterfactual climate to actual climate scenarios. The likelihood of extreme 6-day rainfall event under 2017 SST conditions in March has increased by $\sim 20\%$ (Fig. 2a) in HadRM3P compared to natural conditions. We find RR of ~ 2 (100% increase) for the 1986–2015 climatology period (Fig. 2a), but then unaltered risks for the shorter 2006–15 period (for events < 200 mm; Fig. 2b). This suggests that there are interesting nonlinear dynamic feedbacks at play, which depend on the state of the climate (i.e., ENSO or IOD variability). For March and the preceding winter (DJF 2016/17), very weak La Niña conditions were present (see Fig. ES2c in the online supplemental material). While not conclusive, HadRM3P results indicate that La Niña made drier conditions more

likely over NEB (Fig. ES1c). Such feedback arises from global teleconnections, which can be detected in the upper-level zonal wind anomaly fields, in HadRM3P and reanalysis (not shown). In general, we find a moderate correlation ($r = 0.4$ to 0.6 ; no lag) between Niño-3.4 and NEB rainfall in March (Fig. ES2g). Regarding the interplay between ENSO and IOD itself, we argue that ENSO leads most IOD changes as notable particularly during strong El Niño events (Figs. 1b,c) because correlation between Niño-3.4 during November to January and IOD during February and March ($r = 0.467$; 4 months' lead time; $p = 0.0081$ at 95% confidence level) is significant. While positive IOD events tend to weaken the El Niño impact on the rainfall (e.g., Behera and Ratnam 2018), we obtain mixed results for the five heavy rainfall events (vertical dashed rectangles through Figs. 1b and 1c) exceeding the 150-mm threshold. Only two out of five events were associated with positive IOD and El Niño conditions. March 2017 is drier not only from an ENSO but also from an IOD point of view. Since March is in the beginning of the pre-monsoon season, small changes can cause drastically different outcomes. Matsumoto (1997) and Ashfaq et al. (2009) identified an early onset of the rainy days at NEB on 8 April and 21 May, respectively. We speculate that the current warming has shifted the pre-monsoon heavy rain's onset to even an earlier start. We notice

a decreasing risk for the extreme rainfall event of March 2017 (225 mm) from Natural to Actual climate but then an increasing risk from natural to GHG-only climate conditions during 2006–15. This result demonstrates a considerable contribution of the anthropogenic aerosols for March 2006–15 (Fig. 2b); however, this is not the same for 1986–2015 (not shown). MIROC5 and ETH_CAM4 simulate much smaller changes in risk, with ETH_CAM4 even suggesting a drying trend, but none of these GCMs captured the observed extreme event of 2017 (Fig. 2c).

CONCLUSIONS. Based on the results from HadRM3P model only (for 1986–2015), we conclude that anthropogenic climate change doubled the likelihood of extreme pre-monsoon rainfall (~100% more likely) over NEB. Interestingly, the attribution signal in March is sensitive to the chosen climatology period. Natural ENSO and IOD variability influence interannual changes in rainfall risks, yet both indices made the 2017 rainfall event less likely. The anthropogenic aerosol cooling effect is noticeably observed during the recent decade (2006–15). How the interplay between the two competing forces of GHGs and the anthropogenic aerosols influences the risks of extreme rainfall events should be explored more. For the first time, this study presents attribution assessment for pre-monsoon extreme rainfall event for Bangladesh. Understanding the physical mechanisms behind such event and using a multimodel approach to incorporate associated uncertainties can be useful for further studies.

ACKNOWLEDGMENTS. This paper was supported in part by the UKIERI-DST project. We thank our colleagues at the Oxford e-Research Centre for their technical expertise, the Met Office Hadley Centre PRECIS team for their technical and scientific support for the development and application of weather@home, and all the volunteers who have donated their computing time to weather@home.

REFERENCES

- Allen, M.: 1999: Do-it-yourself climate prediction. *Nature*, **401**, 642, <https://doi.org/10.1038/44266>.
- Ahmed, R., K. R. Rahaman, A. Kok, and Q. K. Hassan, 2017: Remote sensing-based quantification of the impact of flash flooding on the rice production: A case study over northeastern Bangladesh. *Sensors*, **17**, E2347, <https://doi.org/10.3390/s17102347>.
- Ashfaq, M., Y. Shi, W.-W. Tung, R. J. Trapp, X. Gao, J. S. Pal, and N. S. Diffenbaugh, 2009: Suppression of South Asian summer monsoon precipitation in the 21st century. *Geophys. Res. Lett.*, **36**, L01704, <https://doi.org/10.1029/2008GL036500>.
- Behera, S. K., and J. V. Ratnam, 2018: Quasi-asymmetric response of the Indian summer monsoon rainfall to opposite phases of the IOD. *Sci. Rep.*, **8**, 123, <https://doi.org/10.1038/s41598-017-18396-6>.
- Black, M. T., and Coauthors, 2016: The weather@home regional climate modelling project for Australia and New Zealand. *Geosci. Model Dev.*, **9**, 3161–3176, <https://doi.org/10.5194/gmd-9-3161-2016>.
- Chen, M., W. Shi, P. Xie, V. Silva, V. Kousky, R. Higgins, and J. Janowiak, 2008: Assessing objective techniques for gauge-based analyses of global daily precipitation. *J. Geophys. Res.*, **113**, D04110, <https://doi.org/10.1029/2007JD009132>.
- Donlon, C. J., M. Martin, J. Stark, J. Roberts-Jones, E. Fiedler, and W. Wimmer, 2012: The Operational Sea Surface Temperature and Sea Ice Analysis (OS-TIA) system. *Remote Sens. Environ.*, **116**, 140–158, <https://doi.org/10.1016/j.rse.2010.10.017>.
- FAO, 2017: Bangladesh: Severe floods in 2017 affected large numbers of people and caused damage to the agriculture sector. Food and Agriculture Organization of the United Nations, 6 pp., www.fao.org/3/a-i7876e.pdf.
- Guillod, B. P., and Coauthors, 2017: weather@home 2: Validation of an improved global-regional climate modelling system. *Geosci. Model Dev.*, **10**, 1849–1872, <https://doi.org/10.5194/gmd-10-1849-2017>.
- Hansen, J., R. Ruedy, M. Sato, and K. Lo, 2010: Global surface temperature change. *Rev. Geophys.*, **48**, RG4004, <https://doi.org/10.1029/2010RG000345>.
- Huang, B., and Coauthors, 2017: Extended Reconstructed Sea Surface Temperature, version 5 (ERSSTv5): Upgrades, validations, and intercomparisons. *J. Climate*, **30**, 8179–8205, <https://doi.org/10.1175/JCLI-D-16-0836.1>.
- IPCC, 2013: *Climate Change 2013: The Physical Science Basis*. T. F. Stocker et al., Eds., Cambridge University Press, 1535 pp.
- Li, Z., and Coauthors, 2016: Aerosol and monsoon climate interactions over Asia. *Rev. Geophys.*, **54**, 866–929, <https://doi.org/10.1002/2015RG000500>.
- Marthews, T. R., F. E. L. Otto, D. Mitchell, S. J. Dadson, and R. G. Jones, 2015: The 2014 drought in the horn of Africa: Attribution of meteorological drivers [in “Explaining Extreme Events of 2014 from a Climate Perspective”]. *Bull. Amer. Meteor. Soc.*, **96**, S83–S88, <https://doi.org/10.1175/BAMS-D-15-00115.1>.
- Massey, N., and Coauthors, 2015: weather@home—Development and validation of a very large ensemble modelling system for probabilistic event attribution. *Quart. J. Roy. Meteor. Soc.*, **141**, 1528–1545, <https://doi.org/10.1002/qj.2455>.

- Matsumoto, J., 1997: Seasonal transition of summer rainy season over Indochina and adjacent monsoon region. *Adv. Atmos. Sci.*, **14**, 231–245, <https://doi.org/10.1007/s00376-997-0022-0>.
- Mitchell, D., K. and Coauthors, 2017: Half a degree additional warming, prognosis and projected impacts (HAPPI): Background and experimental design. *Geosci. Model Dev.*, **10**, 571–583, <https://doi.org/10.5194/gmd-10-571-2017>.
- Murata, F., T. Terao, T. Hayashi, H. Asada, and J. Matsumoto, 2008: Relationship between atmospheric conditions at Dhaka, Bangladesh, and rainfall at Cherrapunjee, India. *Nat. Hazards*, **44**, 399–410, <https://doi.org/10.1007/s11069-007-9125-2>.
- , and Coauthors, 2011: Daytime thermodynamic and air flow structures over northeast Bangladesh during the pre-monsoon season: A case study on 25 April 2010. *J. Meteor. Soc. Japan*, **89A**, 167–179, <https://doi.org/10.2151/jmsj.2011-A11>.
- NAS, 2016: *Attribution of Extreme Weather Events in the Context of Climate Change*. National Academies of Sciences, Engineering and Medicine, 186 pp.
- Otto, F. E. L., 2017: Attribution of weather and climate events. *Annu. Rev. Environ. Resour.*, **42**, 627–646, <https://doi.org/10.1146/annurev-environ-102016-060847>.
- , R. James, and M. Allen, 2015: The science of attributing extreme weather events and its potential contribution to assessing loss and damage associated with climate change impacts. Environmental Change Institute, 4 pp., https://unfccc.int/files/adaptation/workstreams/loss_and_damage/application/pdf/attributingextremeevents.pdf.
- Rayner, N. A., D. E. Parker, E. B. Horton, C. K. Folland, L. V. Alexander, D. P. Rowell, E. C. Kent, and A. Kaplan, 2003: Global analyses of sea surface temperature, sea ice, and night marine air temperature since the late nineteenth century. *J. Geophys. Res.*, **108**, 4407, <https://doi.org/10.1029/2002JD002670>.
- Sanderson, M., and R. Ahmed, 1979: Pre-monsoon rainfall and its variability in Bangladesh: A trend surface analysis. *Hydrol. Sci. Bull.*, **24**, 277–287, <https://doi.org/10.1080/02626667909491867>.
- Schaller, N., and Coauthors, 2016: Human influence on climate in the 2014 southern England winter floods and their impacts. *Nat. Climate Change*, **6**, 627–634, <https://doi.org/10.1038/nclimate2927>.
- Schamm, K., M., Ziese, K. Raykova, A. Becker, P. Finger, A. Meyer-Christoffer, and U. Schneider, 2015: GPCC full data daily version 1.0 at 1.0°: Daily land-surface precipitation from rain-gauges built on GTS-based and historic data, accessed 10 Dec 2017, https://doi.org/10.5676/DWD_GPCC/FD_D_V1_100.
- Shahid, S., 2010: Rainfall variability and the trends of wet and dry periods in Bangladesh. *Int. J. Climatol.*, **30**, 2299–2313, <https://doi.org/10.1002/joc.2053>.
- Yatagai, A., K. Kenji, A. Osamu, H. Atsushi, Y. Natsuko, and K. Akio, 2012: APHRODITE: Constructing a long-term daily gridded precipitation dataset for Asia based on a dense network of rain gauges. *Bull. Amer. Meteor. Soc.*, **93**, 1401–1415, <https://doi.org/10.1175/BAMS-D-11-00122.1>.

THE EFFECTS OF NATURAL VARIABILITY AND CLIMATE CHANGE ON THE RECORD LOW SUNSHINE OVER JAPAN DURING AUGUST 2017

CHIHARU TAKAHASHI, HIDEO SHIOGAMA, YUKIKO IMADA, YU KOSAKA, MASATO MORI, MIKI ARAI, YUICHI KAMAE, AND MASAHIRO WATANABE

The record low sunshine over Japan during August 2017 was mainly attributed to a blocking high and Pacific–Japan pattern. Anthropogenic warming and decaying El Niño contributed to an increase in the probability of occurrence.

INTRODUCTION. Early August in 2017 had record poor sunshine in northern Japan with anomalously cool and rainy conditions, which damaged agriculture and the economy. There was very low sunshine for one week at several observation sites on the Pacific side of northern Japan, the longest duration in July and August since 1961 (Figs. 1a,b). Observational analysis indicates that the prolonged cloudy days were caused by cold northeasterly winds in that region (Fig. 1d; see also Figs. ES1a and ES1b in the online supplemental information). These cold winds are associated with two possible factors. One is the surface Okhotsk high associated with a blocking high over East Siberia (Figs. 1c–e). The Okhotsk high often causes anomalously cold summers in northern Japan (Kodama 1997; Nakamura and Fukamachi 2004). The prominent Okhotsk high in August 2017 formed in association with the propagation of a stationary Rossby wave in the middle-upper troposphere from Europe through East Siberia (Fig. ES1c), as shown by Sato and Takahashi

(2007). The other possible factor of the cold winds is the Pacific–Japan (PJ) teleconnection pattern (Nitta 1987; Kosaka and Nakamura 2006, 2010) induced by anomalously suppressed convective activity over the Philippine Sea (Fig. 1e; see also Figs. ES1b,d,e) associated with a northward-propagating intraseasonal oscillation from the tropics (Figs. ES1f,g). In advance of the event, tropical cyclones (T1705 and T1711) developed as a part of the PJ teleconnection and could have provided an initial moist condition in Japan. The PJ pattern and anomalous Okhotsk high often co-occur (Wakabayashi and Kawamura 2004; Hirota and Takahashi 2012), and the resultant tripolar pattern of atmospheric circulation has been known to cause sunshine deficits such as that observed in August 2017 (Figs. ES1h,i).

It has been suggested that greater anthropogenic warming in the Far East land area than the surrounding ocean intensifies the anticyclonic circulation throughout the troposphere over eastern Siberia and the Okhotsk Sea (Kimoto 2005; Arai and Kimoto 2008; Kamae et al. 2014). The intensified anticyclone leads to strengthened easterly winds into northern Japan (Fig. ES1j). Geopotential height at 500 hPa (Z_{500}) and its deviation from the zonal mean (Z'_{500}) have an increasing trend of 7.2 and 2.1 m decade⁻¹, respectively, over eastern Siberia and the sea of Okhotsk (orange box in Fig. 1e) in July–August for 1961–2017 (Fig. ES1j). Sunshine duration has significantly decreased with a trend of -0.19 h month⁻¹ decade⁻¹ (Fig. 1b). Therefore, we can expect that anthropogenic warming has influenced the likelihood of the unusual blocking and Okhotsk high, which led to the 2017 extreme event.

Apart from the human influence, seasonal weather in Japan is strongly influenced by atmospheric variability forced by sea surface temperature (SST) variation in the tropics such as El Niño–Southern Oscillation (ENSO; Fig. ES1k). Although La Niña was gradually

AFFILIATIONS: TAKAHASHI, ARAI, AND WATANABE—Atmosphere and Ocean Research Institute, The University of Tokyo, Chiba, Japan; SHIOGAMA—Center for Global Environmental Research, National Institute for Environmental Studies, Tsukuba, Japan; IMADA—Meteorological Research Institute, Japan Meteorological Agency, Tsukuba, Japan; KOSAKA AND MORI—Research Center for Advanced Science and Technology, The University of Tokyo, Tokyo, Japan; KAMAE—Faculty of Life and Environmental Sciences, University of Tsukuba, Tsukuba, Ibaraki, Japan
CORRESPONDING AUTHOR: Chiharu Takahashi, chiha@aori.u-tokyo.ac.jp

DOI:10.1175/BAMS-D-18-0107.1

A supplement to this article is available online (10.1175/BAMS-D-18-0107.2)

© 2019 American Meteorological Society

For information regarding reuse of this content and general copyright information, consult the [AMS Copyright Policy](#).

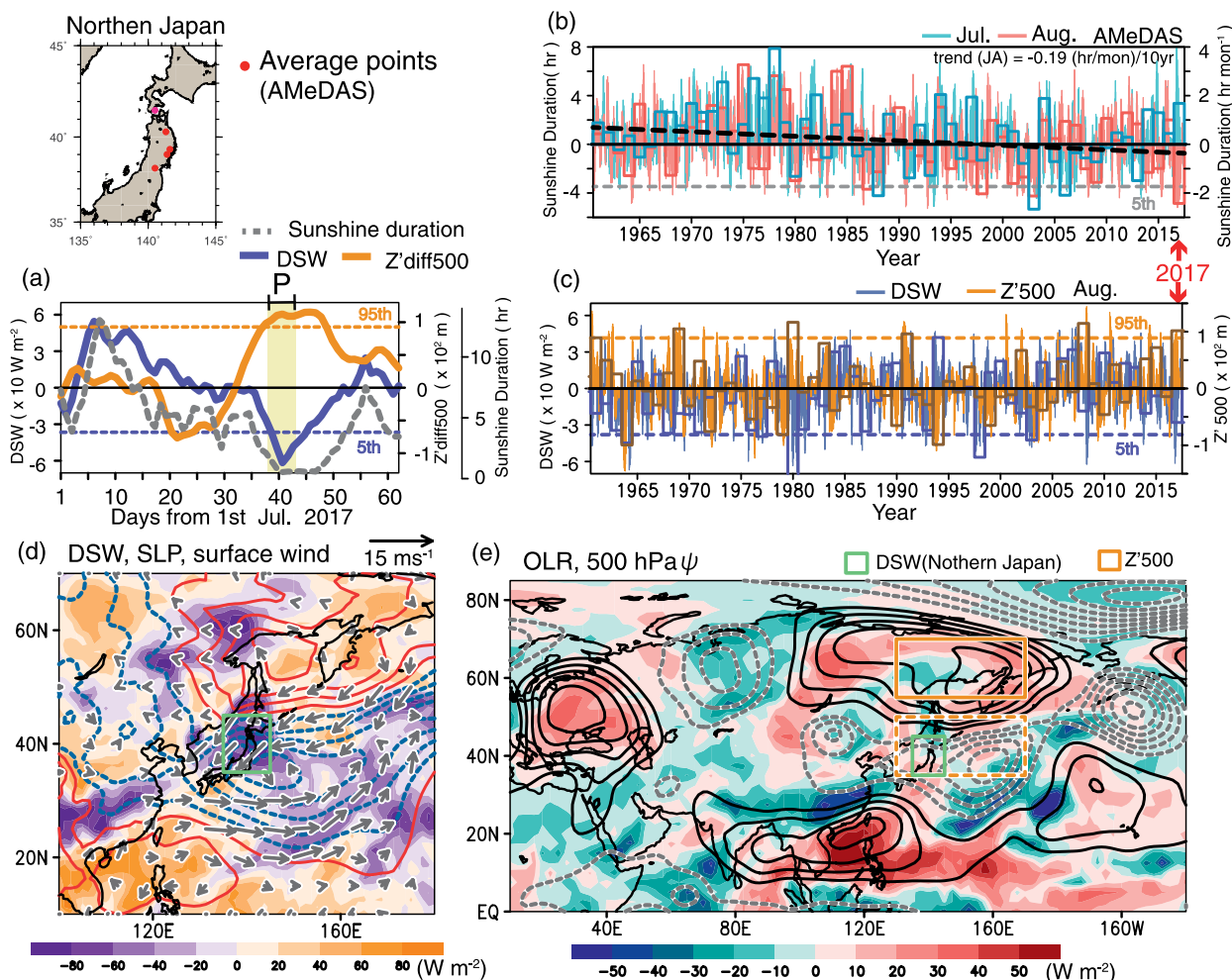


FIG. 1. (a) Time series of observed sunshine duration (gray) averaged at five observations sites (red circles in map of Japan) and anomalies of DSW (purple) over northern Japan (35° – 45° N, 135° – 145° E, green boxes in Figs. 1d,e) and $Z'_{\text{diff}}500$ (difference in $Z'500$ between orange and dashed boxes in Fig. 1e) in July–August 2017. (b) As in (a), but for sunshine duration in July (blue) and August (pink). (c) As in (a) but anomalies of $Z'500$ over East Siberia and the Okhotsk Sea (solid box in Fig. 1e) and DSW in August for 1961–2017. The shading in (a) indicates the analysis period P (8–12 August). In (b) and (c), curves show 5-day running mean anomalies (with the axis in the left) and bars indicate monthly mean (the right axis). Also shown are observed patterns of the 5-day mean anomalies during the period P in (d) DSW (shading), sea level pressure (contours; 1.0-hPa interval), and surface winds (vectors) and (e) OLR (shading) and 500-hPa streamfunction (contours; $2 \times 10^6 \text{ m}^2 \text{ s}^{-1}$ interval). Dashed contours indicate negative anomalies.

developing in August 2017, the Niño-3.4 SST anomaly was still positive (about 0.26°C) like El Niño in July (Fig. ES2a), which potentially contributed to the development of the PJ pattern. Thus, we examine the contributions of anthropogenic warming and ENSO on the occurrence of the extreme low sunshine event in northern Japan in early August 2017 using an atmospheric general circulation model (AGCM).

METHODS. We have performed several sets of 100-member ensemble simulations for 2017 using the AGCM of MIROC5 (T85L40, Watanabe et al. 2010). Each member was started from different initial condi-

tions. ALL is the all-forcing run forced by the observed historical SST and sea ice derived from the HadISST dataset (Rayner et al. 2003). NAT1 and NAT2 are natural forcing runs driven by detrended HadISST based on 1870–2012 linear trends (NAT1; Christidis and Stott 2014) and by removing the anthropogenic changes in SST/sea ice based on attribution experiments from phase 5 of the Coupled Model Intercomparison Project (CMIP5) (NAT2; D. Stone and P. Pall 2017, unpublished manuscript: http://portal.nersc.gov/c20c/pub/StoneDA_PallP_2017.pdf). Details of ALL, NAT1, and NAT2 are described in Shiogama et al. (2013, 2014). ALLnoENSO is the same as ALL, but the monthly SST

anomalies regressed onto Niño-3.4 SST anomaly have been subtracted (Takahashi et al. 2016) in order to suppress the influence of ENSO in 2017. The SSTs that drive each experiment are shown in Fig. ES2. We have also performed a 10-member long-term ALL experiment, called ALL-LNG for 1949–2016, to define a threshold of the event. We used the daily JRA-55 reanalysis dataset (Kobayashi et al. 2015; Harada et al. 2016), outgoing longwave radiation (OLR) from NOAA (Liebmann and Smith 1996), and surface observations from the Automated Meteorological Data Acquisition System (AMeDAS) by the Japan Meteorological Agency.

Since MIROC5 does not provide sunshine duration diagnostics, we employ a surface downward solar radiation (DSW) index averaged over northern Japan (35°–45°N, 135°–145°E; green box in Figs. 1d,e) as a proxy, which is the same approach as in Christidis et al. (2016). Observed sunshine duration is highly correlated (at 0.76) with the DSW index in July–August for 1961–2017 based on JRA-55. The extreme event with very low sunshine duration is defined as the 5-day period of 8–12 August 2017 (indicated as “P” in Fig. 1a) centering around the minimum index day, when the DSW index fell outside the 5th percentile (Figs. 1a,c) based on the 5-day running-mean statistics for July–August of 1961–2017.

The Z'_{500} anomaly averaged over eastern Siberia and the Okhotsk Sea (orange box in Fig. 1e) also exceeds the 95th percentile (Fig. 1c). We assess the relative contribution of anthropogenic forcing and ENSO to the occurrence of the 2017 extreme event by estimating the fraction of attributable risk (FAR; Allen 2003), defined as $1 - (P_0/P_1)$, where P_1 and P_0 are probabilities exceeding a given threshold in ALL and NAT1/NAT2/ALLnoENSO simulations (each 100-member ensemble), respectively, and estimated based on probability density functions (PDFs) of the mean value for the period P . The threshold in each index is defined based on PDFs of 5-day running mean anomalies estimated from the 10-member ensemble of ALL-LNG for July–August 1961–2016. The best estimate (50th percentile) and 95% confidence interval (CI) of the probabilities are estimated through the bootstrap random resampling (each 1000 samples).

RESULTS. The observed DSW index averaged for the period P is -61.8 W m^{-2} (Fig. 2a). This value corresponds to the 0.3th percentile of the 5-day running mean index in July–August for the recent 57 years. Therefore, we adopt the first percentile (-75.0 W m^{-2}) as the threshold of the DSW index in ALL-LNG run. The best estimate in occurrence probability (95% CI) of the extreme DSW index that falls below the thresh-

old is 1.3% (0.0–3.4%), 0.17% (0.0–0.51%), 0.046% (0.0–0.40%), and 0.11% (0.0–0.40%) for ALL, NAT1, NAT2, and ALLnoENSO, respectively (Fig. 2a). The estimated FAR_{ANTH} (anthropogenic effect) and FAR_{ENSO} (ENSO effect) is 0.89–0.97 and 0.90, respectively. These results indicate that the anthropogenic warming contributed to increase of the chance of the 2017 extreme low sunshine by 7.7–29 times, suggesting that this event would hardly have happened without human influence. Besides, it is suggested that ENSO acted to raise the chance by about 12 times.

Ensemble-mean differences between ALL and NAT1/NAT2 can represent influence of anthropogenic forcing on the 2017 event, forced by SSTs (Figs. ES2c,d). The changes in Z'_{500} due to anthropogenic effect show enhanced anticyclonic circulation with lower-tropospheric warming in the extratropics covering eastern Siberia and the Okhotsk Sea (Fig. 2c and Fig. ES3a) and anomalous cyclonic circulation in the ocean to the east of Japan, which is consistent with previous studies (e.g., Kamae et al. 2014). These changes are similar to the ensemble-mean trends in ALL-LNG in July–August 1961–2017 (Fig. ES3b). The composite of extreme DSW members (below the second percentile) in ALL well represents the tripolar circulation pattern as in observations, with significantly weaker amplitudes in NAT1/NAT2 (Figs. ES3c–h).

We also evaluate likelihood of the extreme Okhotsk high related to the blocking ($Z'_{\text{diff},500}$), which is defined as difference of Z'_{500} anomalies between the eastern Siberia–Okhotsk sea sector (55°–70°N, 130°–170°E) and the area to its south (35°–50°N, 130°–170°E). The observed $Z'_{\text{diff},500}$ anomaly averaged in the period P is 112.3 m (Figs. 1a and 2b), corresponding to 97.2th percentile of 5-day running mean in July–August for the recent 57 years. The threshold of $Z'_{\text{diff},500}$ is thus defined as 107.0 m, which is equivalent to the 97th percentile in ALL-LNG. The best estimate (95% CI) in occurrence probability of extreme $Z'_{\text{diff},500}$ exceeding this threshold is 5.5% (2.3–9.3%), 2.2% (0.89–4.3%), 1.7% (0.41–3.4%), and 3.3% (1.0–6.5%) for ALL, NAT1, NAT2, and ALLnoENSO, respectively (Fig. 2b). The estimated FAR_{ANTH} and FAR_{ENSO} are 0.57–0.70 and 0.39, respectively. The results suggest that the anthropogenic warming contributed to raise the occurrence probability of the 2017 extreme Okhotsk high by 2.5–3.2 times, whereas ENSO influence was weaker (1.7 times).

The impact of ENSO in 2017 is represented by the difference of ensemble means between ALL and ALLnoENSO (Fig. 2d), which feature a teleconnection pattern similar to that occurs in July–August for El Niño years (Fig. ES1k). The decaying El Niño signal remained

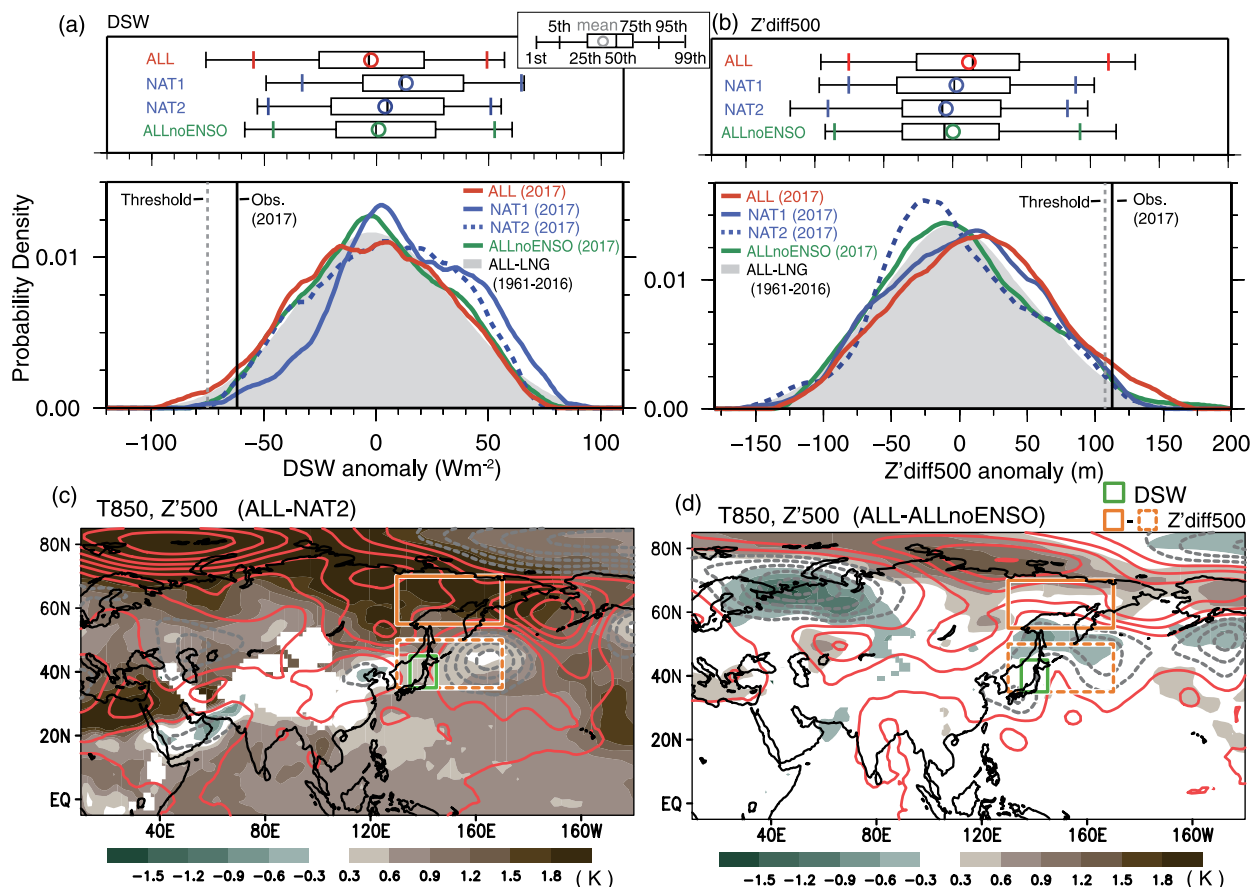


FIG. 2. (a),(b) Box-and-whisker plots and PDFs of (a) 5-day (the period P) average DSW anomalies over northern Japan (green boxes in Figs. 2c,d) and (b) $Z'_{\text{diff}500}$ anomalies (difference in $Z'500$ anomalies between orange solid and dashed boxes in Figs. 2d,e) in the 2017 event for ALL (red), NAT1 (blue solid), NAT2 (blue dashed), ALLnoENSO (green), and 5-day running mean anomalies in ALL-LNG for July–August, 1961–2016 (shading). The black and gray dashed lines indicate the 2017 observed anomalies and threshold, respectively. (c) Ensemble mean difference in 5-day average 850-hPa temperature (shading) and $Z'500$ anomalies (contours; 5-m interval with negative dashed) between ALL and NAT2. (d) As in (c), but for the difference between ALL and ALLnoENSO.

in the SST anomalies in July 2017 (Fig. ES2e), which probably led to the intensification of PJ teleconnection and $Z'500_{\text{diff}P}$ and acted to increase the likelihood of occurrence of extreme event. It is expected that extremely prolonged cloudy and little sunshine days over northern Japan will happen more frequently due to the Okhotsk high intensified by human-induced warming in the future, although the results are based on a single model. Further investigation with other models is required.

CONCLUSIONS. The record prolonged low sunshine in northern Japan in early August of 2017 was mainly attributed to the persistent cold inflow along the anomalous cyclone over Japan, which is simultaneously induced by an extraordinary development of the Okhotsk high associated with blocking over eastern Siberia and the intraseasonal PJ teleconnection pat-

tern. Interestingly, it is found that this extreme event would hardly have occurred without anthropogenic warming, which is linked to increased probability of occurrence of extremely enhanced anticyclones in the Okhotsk Sea by 2.5–3.2 times due to human-induced warming. The 2017 decaying El Niño also increased the event occurrence through the amplification of tripolar pattern, although it was a smaller contribution than the human influence.

ACKNOWLEDGMENTS. This work was supported by the Program for Integrated Research Program for Advancing Climate Models (TOUGOU program) from the Ministry of Education, Culture, Sports, Science and Technology (MEXT), Japan. The MIROC5 simulations were performed using the Earth Simulator at JAMSTEC and the NEC SX at NIES.

REFERENCES

- Allen, M. R. 2003: Liability for climate change. *Nature*, **421**, 891–892, <https://doi.org/10.1038/421891a>.
- Arai, M., and M. Kimoto, 2008: Simulated interannual variation in summertime atmospheric circulation associated with the East Asian monsoon. *Climate Dyn.*, **31**, 435–447, <https://doi.org/10.1007/s00382-007-0317-y>.
- Christidis, N., and P. A. Stott, 2014: Change in the odds of warm years and seasons due to anthropogenic influence on the climate. *J. Climate*, **27**, 2607–2621, <https://doi.org/10.1175/JCLI-D-13-00563.1>.
- , M. McCarthy, A. Ciavarella, and P. A. Stott, 2016: Human contribution to the record sunshine of winter 2014/15 in the United Kingdom. *Bull. Amer. Meteor. Soc.*, **97**, S47–S50, <https://doi.org/10.1175/BAMS-D-16-0143.1>.
- Harada, Y., and Coauthors, 2016: The JRA-55 Reanalysis: Representation of atmospheric circulation and climate variability. *J. Meteor. Soc. Japan*, **94**, 269–302, <https://doi.org/10.2151/jmsj.2016-015>.
- Hirota, N., and M. Takahashi, 2012: A tripolar pattern as an internal mode of the East Asian summer monsoon. *Climate Dyn.*, **39**, 2219–2238, <https://doi.org/10.1007/s00382-012-1416-y>.
- Kamae, Y., M. Watanabe, M. Kimoto, and H. Shiogama, 2014: Summertime land–sea thermal contrast and atmospheric circulation over East Asia in a warming climate—Part I: Past changes and future projections. *Climate Dyn.*, **43**, 2553–2568, <https://doi.org/10.1007/s00382-014-2073-0>.
- Kimoto, M., 2005: Simulated change of the East Asian circulation under global warming scenario. *Geophys. Res. Lett.*, **32**, L16701, <https://doi.org/10.1029/2005GL023383>.
- Kobayashi, S., and Coauthors, 2015: The JRA-55 Reanalysis: General specifications and basic characteristics. *J. Meteor. Soc. Japan*, **93**, 5–48, <https://doi.org/10.2151/jmsj.2015-001>.
- Kodama, Y.-M., 1997: Air mass transformation of the Yamase air-flow in the summer of 1993. *J. Meteor. Soc. Japan*, **75**, 737–751, https://doi.org/10.2151/jmsj.1965.75.3_737.
- Kosaka, Y., and H. Nakamura, 2006: Structure and dynamics of the summertime Pacific–Japan teleconnection pattern. *Quart. J. Roy. Meteor. Soc.*, **132**, 2009–2030, <https://doi.org/10.1256/qj.05.204>.
- , and —, 2010: Mechanisms of meridional teleconnection observed between a summer monsoon system and a subtropical anticyclone. Part I: The Pacific–Japan pattern. *J. Climate*, **23**, 5085–5108, <https://doi.org/10.1175/2010JCLI3413.1>.
- Liebmann, B., and C. A. Smith, 1996: Description of a complete (interpolated) outgoing longwave radiation dataset. *Bull. Amer. Meteor. Soc.*, **77**, 1275–1277.
- Nakamura, H., and T. Fukamachi, 2004: Evolution and dynamics of summertime blocking over the Far East and the associated surface Okhotsk high. *Quart. J. Roy. Meteor. Soc.*, **130**, 1213–1233, <https://doi.org/10.1256/qj.03.101>.
- Nitta, T., 1987: Convective activities in the tropical western Pacific and their impact on the Northern Hemisphere summer circulation. *J. Meteor. Soc. Japan*, **65**, 373–390, https://doi.org/10.2151/jmsj.1965.65.3_373.
- Rayner, N. A., D. E. Parker, E. B. Horton, C. K. Folland, L. V. Alexander, D. P. Rowell, E. C. Kent, and A. Kaplan, 2003: Global analyses of sea surface temperature, sea ice, and night marine air temperature since the late nineteenth century. *J. Geophys. Res.*, **108**, 4407, <https://doi.org/10.1029/2002JD002670>.
- Sato, N., and M. Takahashi, 2007: Dynamical processes related to the appearance of the Okhotsk high during early midsummer. *J. Climate*, **20**, 4982–4994, <https://doi.org/10.1175/JCLI4285.1>.
- Shiogama, H., M. Watanabe, Y. Imada, M. Mori, M. Ishii, and M. Kimoto, 2013: An event attribution of the 2010 drought in the south Amazon region using the MIROC5 model. *Atmos. Sci. Lett.*, **14**, 170–175, <https://doi.org/10.1002/asl2.435>.
- , —, —, —, Y. Kamae, M. Ishii, and M. Kimoto, 2014: Attribution of the June–July 2013 heat wave in the southwestern United States. *SOLA*, **10**, 122–126, <https://doi.org/10.2151/sola.2014-025>.
- Takahashi, C., M. Watanabe, H. Shiogama, Y. Imada, and M. Mori, 2016: A persistent Japanese heat wave in early August 2015: Role of natural variability and human-induced warming [in “Explaining Extreme Events of 2015 from a Climate Perspective”]. *Bull. Amer. Meteor. Soc.*, **97**, S107–S112, <https://doi.org/10.1175/BAMS-D-16-0157.1>.
- Wakabayashi, S., and R. Kawamura, 2004: Extraction of major teleconnection patterns possibly associated with the anomalous summer climate in Japan. *J. Meteor. Soc. Japan*, **82**, 1577–1588, <https://doi.org/10.2151/jmsj.82.1577>.
- Watanabe, M., and Coauthors, 2010: Improved climate simulation by MIROC5: Mean states, variability, and climate sensitivity. *J. Climate*, **23**, 6312–6335, <https://doi.org/10.1175/2010JCLI3679.1>.

ANTHROPOGENIC CONTRIBUTION TO THE 2017 EARLIEST SUMMER ONSET IN SOUTH KOREA

SEUNG-KI MIN, YEON-HEE KIM, IN-HONG PARK, DONGHYUN LEE, SARAH SPARROW,
DAVID WALLOM, AND DÁITHÍ STONE

Large-ensemble RCM and GCM simulations suggest a significant anthropogenic contribution to the observed warmest May and earliest summer onset in South Korea, increasing the risk of its occurrence by 2–3 times.

INTRODUCTION. During May 2017, South Korea experienced the hottest recorded temperature since 1973 (the beginning of the observations from 45 stations; Fig. 1a). This was the culmination of four consecutive years of record-breaking May temperatures (Fig. 1b). Responding to the early heat, in 2015 the Korean Meteorological Administration (KMA) started to issue heat wave warnings throughout the year rather than only during June–September (KMA 2015). Based on multiple coupled climate models (CMIP5; see below) the probability of having an extremely hot May (exceeding +1.5 standard deviation; red dashed line in Fig. 1b) for four consecutive years is extremely low, corresponding to a 1-in-1000-yr event without anthropogenic forcing and a 1-in-100-yr event with anthropogenic influences (Fig. ES1). This is consistent with the results for consecutive global record-breaking temperatures (Mann et al. 2017).

The warmer May temperatures were observed across South Korea (Fig. 1a), with the station mean being 1.5°C higher than 1987–2010 climatology (17.2°C; note a short period for climatology due to the

w@h model experiment; see below). The hottest May coincides with the earliest summer onset about 8 days earlier than climatology (as defined in the Data and methods section below; see the green line in Fig. 1b), exerting huge societal impacts for health, economy, and leisure activities (*Korea Herald*,¹ *Korea Times*²). Indeed, the correlation between Korea May temperature and summer onset day is very strong ($r = -0.78$). A simple analysis suggests that this relation is a result of an overall warming throughout the seasons rather than a shift in the seasonality (Fig. 1c). Warmer May and earlier summer onset were also observed over the northern China (Figs. 1d,e), with 2°C warmer and 8–10 days earlier onset than climatology (refer to Fig. ES2 for climatology patterns). This regional summer lengthening has important implications for the overall midlatitudes (e.g., for agriculture; Qian et al. 2016), in terms of systematic changes in the annual cycle (Park et al. 2018).

This study examines human contribution to the 2017 extreme May heat and the earliest summer onset in South Korea. To consider small spatial scales, we use high-resolution large-ensemble regional climate model (RCM) and global climate model (GCM) simulations available for the year 2017, each performed with and without anthropogenic forcings. The risk ratio (RR) and fraction of attributable risk (FAR) are analyzed to assess changes in the probabilities of occurrence of the extreme summer onset between the real and counterfactual worlds.

DATA AND METHODS. We use daily mean temperatures (T_{mean}) from 45 South Korean weather stations for 1973–2017. To check regional-scale responses, we use monthly surface air temperature from

AFFILIATIONS: MIN, KIM, PARK, AND LEE—Division of Environmental Science and Engineering, Pohang University of Science and Technology, Pohang, South Korea; SPARROW AND WALLOM—Oxford e-Research Centre, Department of Engineering, University of Oxford, Oxford, United Kingdom; STONE—Global Climate Adaptation Partnership, Oxford, United Kingdom

CORRESPONDING AUTHOR: Seung-Ki Min, skmin@postech.ac.kr

DOI:10.1175/BAMS-D-18-0096.1

A supplement to this article is available online (10.1175/BAMS-D-18-0096.2)

© 2019 American Meteorological Society

For information regarding reuse of this content and general copyright information, consult the [AMS Copyright Policy](#).

¹ www.koreaherald.com/view.php?ud=20170623000779&ACE_SEARCH=1

² http://koreatimes.co.kr/www/news/biz/2017/05/602_228786.html

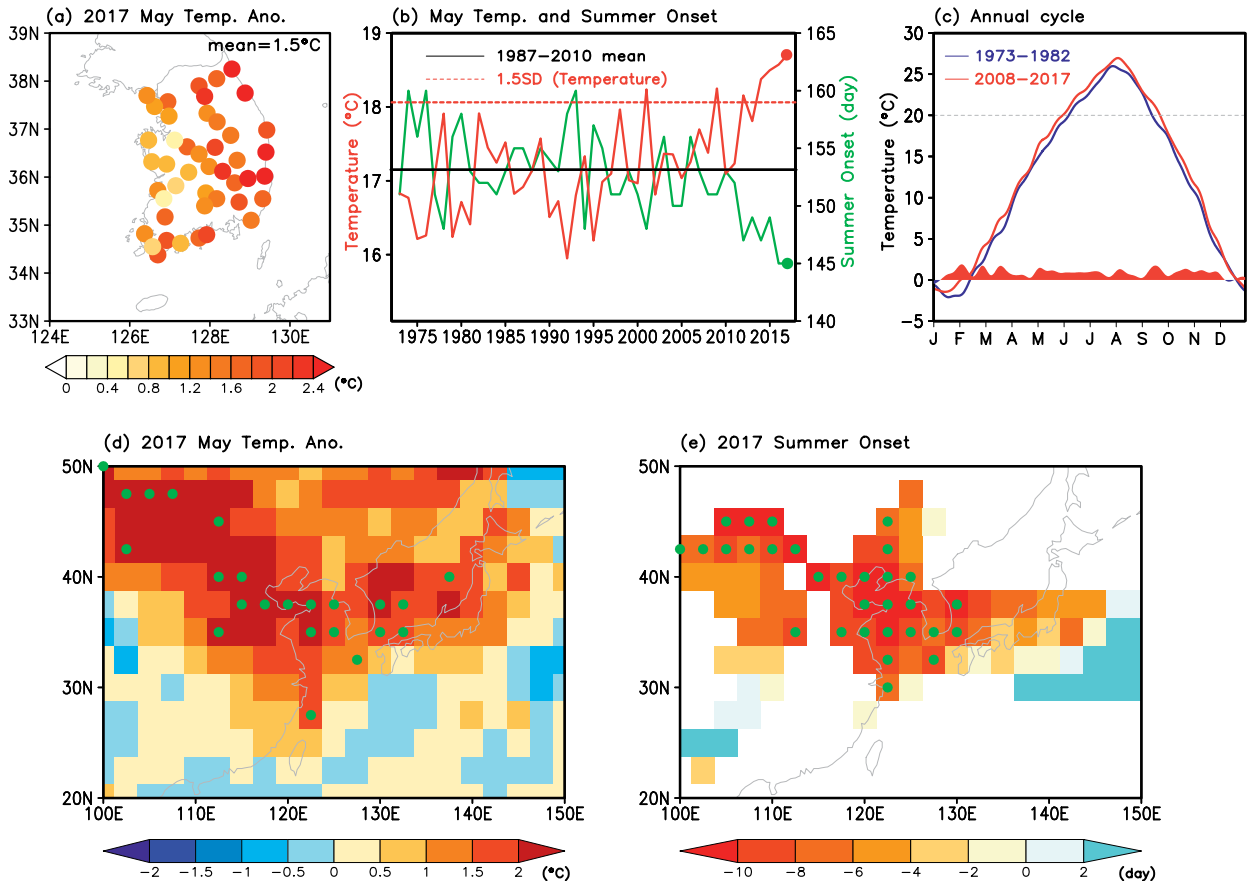


FIG. 1. (a) Distribution of May mean temperature anomalies observed at 45 stations over South Korea in 2017. Anomalies are with respect to 1987–2010 mean. (b) Time series of May mean temperature (red) and summer onset day (green) averaged over 45 stations for 1973–2017. Black solid line indicates 1987–2010 mean for both temperature and summer onset and red dashed line represents 1.5 standard deviation of temperature. (c) Annual cycle of South Korean temperature during 1973–82 and 2008–17 and their differences (red filled line). Also shown are the spatial distributions of (d) 2017 May mean temperature anomalies and (e) 2017 summer onset anomalies obtained from ERA-Interim reanalysis with 2.5° spatial resolution. In (e), areas are displayed only where May–June mean temperature are within 17° – 23°C , having a similar summer onset to South Korea (see Fig. ES2b in the online supplemental information). Green dotted grids in (d) and (e) indicate the record high temperature and record early summer onset in 2017.

the ERA-Interim reanalysis. RCM data are obtained from the weather@home (w@h) East Asia project, which uses the HadRM3P RCM (the Hadley Centre Regional Climate Model, version 3, with improved physics parameterizations) nested in the HadAM3P atmospheric GCM (similar expansion; Massey et al. 2015; Guillod et al. 2017). Observed sea surface temperature (SST), sea ice coverage, greenhouse gas, and aerosol were prescribed for the real world simulations (referred to as ALL). The counterfactual world simulations without human influences (NAT) were conducted with an adjusted SST, which was made by removing anthropogenic warming from the observed SST and using preindustrial levels of external forcings (see Table ES1 in the online supplemental material; Schaller et al. 2016). The RCM domain covers East

Asia and Indian Ocean, consistent with Freychet et al. (2018), with a 50-km resolution. For GCM data, we use a large ensemble simulation of CAM5.1 that participated in the C20C+ D&A project, which was run at a resolution of $1^\circ \times 1^\circ$ (Neale et al. 2012; Stone et al. 2018). The ALL and NAT simulations were conducted with prescribed observed and adjusted external forcings and boundary conditions, similarly to w@h experiment but with some differences (see Table ES1 for details). We also use the multimodel data from phase 5 of the Coupled Model Intercomparison Project (CMIP5; Taylor et al. 2012). RCP4.5 simulations for 2008–27 are used as ALL and natural forcing only runs for 1986–2005 are used as NAT (Table ES1). Anomalies for observations and all model data are calculated with respect to 1987–2010 means

(using ALL climatology for model data) to be matched with the data period from w@h runs.

The analysis domain for South Korea is 34°–38°N, 125°–130°E and a land–sea mask from each model is considered, regarding a grid with land fraction > 0.15 as land. Summer onset day is defined as the date with a smoothed May Tmean value over 20°C, which is determined adaptively and uniquely (Qian et al. 2009; 2011) by the ensemble empirical mode decomposition (EEMD) method (Wu and Huang 2009). All models used in this study can capture the observed summer onset day with Tmean of 20°C occurring during May–June (not shown). To quantify the anthropogenic contribution to the increased probability of occurrence of the extreme heat event, we analyze the risk ratio and fraction of attributable risk, which are defined as $RR = P_{ALL}/P_{NAT}$ and $FAR = 1 - (P_{NAT}/P_{ALL})$, where P_{ALL} and P_{NAT} are probability of extreme events in ALL and NAT simulations, respectively (e.g., Easterling et al. 2016).

RESULTS. Figures 2a–c display frequency distributions of the Tmean and summer onset anomalies both individually (upper and right histograms) and combined (contours). The probability exceeding the observed value is calculated from fitted kernel distributions (using a Gaussian kernel function) for each variable. For w@h (Fig. 2a), the probability (P) of Tmean anomalies higher than the observed (+1.5°C) is 16.65% in ALL and 4.03% in NAT. For summer onset anomalies, P_{ALL} is also higher (32.55%) than P_{NAT} (12.17%). The resulting FAR values are 0.76 and 0.63, respectively (Table ES1), indicating a dominant contribution of anthropogenic forcings to the 2017-like extreme warming and early start of summer season. Joint probability exceeding the 2017 observations is found to be 9.86% in ALL and 2.79% in NAT, respectively. The corresponding FAR is 0.72 ($RR = 3.53$), indicating that the extreme risk increases about 3 to 4 times due to the anthropogenic forcing. CAM5.1 results (Fig. 2b) show that anthropogenic influences have increased the risk of extreme May Tmean and summer onset by about 17 times and 2–3 times, respectively (Table ES1). Results from CMIP5 are overall similar to those from w@h RCMs with FAR values being 0.89 and 0.63 for Tmean and summer onset, respectively (Fig. 2c). In conclusion, the 2017 record warm May and earliest summer start in South Korea are largely due to anthropogenic influences, at least doubling the likelihood ($FAR > 0.5$).

RR obtained from w@h, CAM5.1, and CMIP5 ensembles is summarized with corresponding uncertainty ranges (Figs. 2d,e). For May Tmean anomalies,

all models show RR clearly above one, indicating that human influence is detectable. The stronger RR in CAM5.1 is related to its lower P_{NAT} , which seems to be associated with the smaller interensemble Tmean variability (Fig. 2b). The w@h simulations exhibit different RRs for Tmean according to different delta-SST patterns prescribed (ALL minus NAT; see Table ES2 for corresponding CMIP5 models). Results for summer onset show generally positive RR, which is relatively small compared to the Tmean case (Fig. 2e), with different RRs observed for different prescribed SSTs as well. Using the w@h ensemble, we examine the relationship between RR for Tmean and RR for summer onset (both on the logarithm scale). Results show a strong positive Tmean–summer onset relation ($r = 0.90$) in RR across different delta-SSTs (Fig. 2f), which represents influences of different CMIP5 models (see Table ES2). In this regard, a recent study found that intermodel spread in anthropogenic signals in South Korea is largely determined by intermodel spread in aerosol sensitivity (Kim et al. 2018). To check whether the same explanation can apply here, we compare the RR (log scale) from different delta-SST with the aerosol effective radiative forcing (AER) from the corresponding CMIP5 models (Fig. 2g). We find a statistically significant intermodel correlation ($r = 0.74$) such that models having larger cooling responses to aerosol forcing tend to have smaller RR and vice versa. Essentially identical results are observed between AER and delta-SST itself (not shown). This suggests an important role of aerosol cooling in determining uncertainties in the risk assessment over South Korea and possibly over East Asia. Further related analysis indicates a large difference in delta-SST patterns between w@h (weak) and CAM5.1 (strong; similar to CMIP5) ensembles (not shown). However, ALL–NAT differences in South Korean May Tmean are similar between the two models (around 0.7°–0.8°C; Figs. 2a,b), and this implies a stronger aerosol cooling effect in CAM5.1 than in w@h RCM (cf. Kim et al. 2018).

CONCLUDING REMARKS. The probability of an extremely warm May and unusually early summer onset in South Korea is compared between real world (ALL) and counterfactual world (NAT) conditions using the datasets from high-resolution large-ensemble simulations from an atmospheric RCM (w@h) and an atmospheric GCM (CAM5.1). Results with multiple coupled climate models (CMIP5) with a coarse resolution are also compared. All models consistently show increases in the likelihood of a 2017-like extreme event by about 2 to 3 times when including anthropogenic

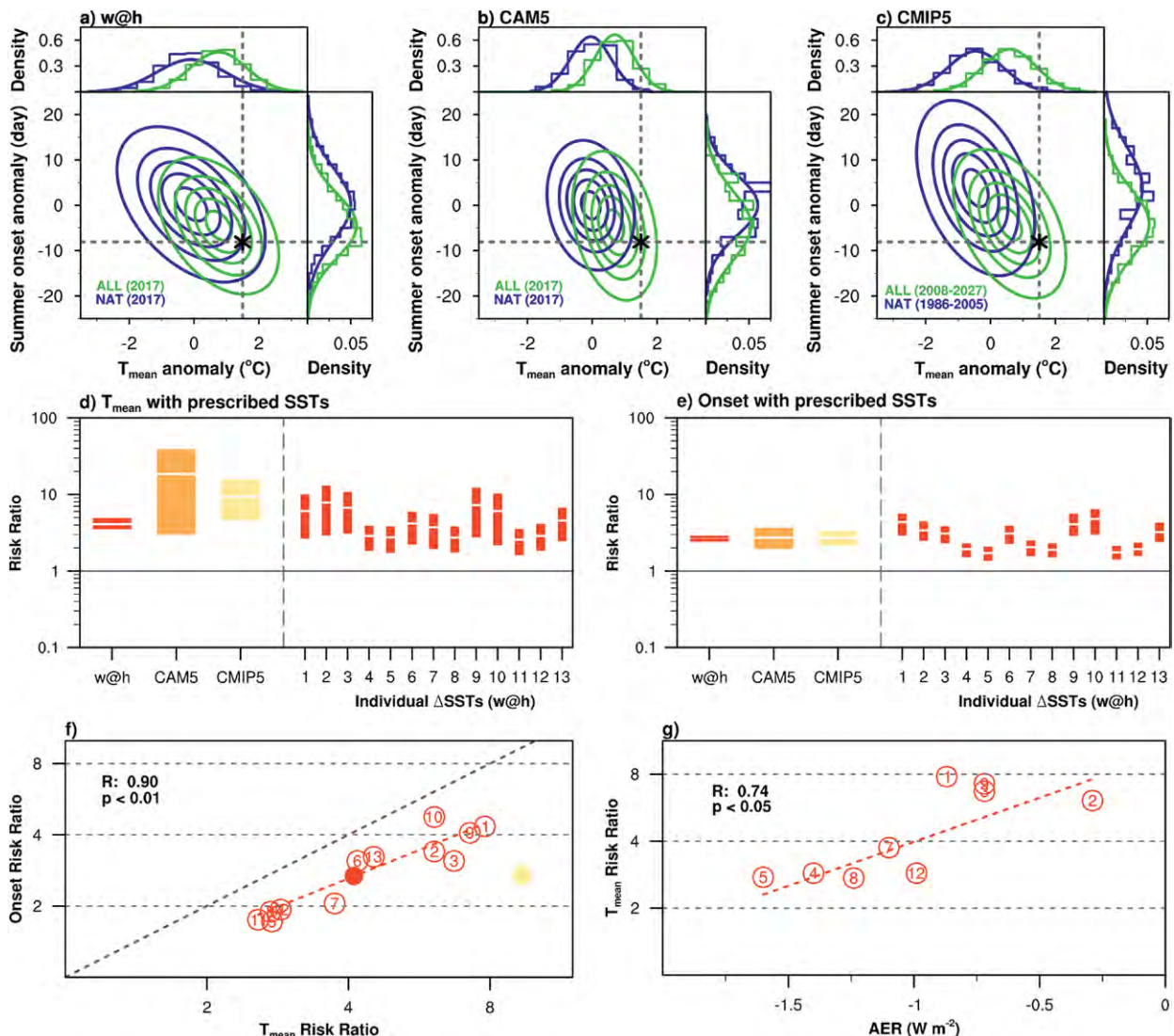


FIG. 2. Joint probability distribution of the May T_{mean} and summer onset anomalies from ALL (green) and NAT (blue) simulations from the (a) w@h, (b) CAM5, and (c) CMIP5 ensembles. Black asterisks and dashed lines represent observed values. Also shown are risk ratios for w@h, CAM5, and CMIP5 of (d) T_{mean} and (e) summer onset where left-hand side bars are from all simulations and right-hand side bars with numbers represent w@h results from different prescribed delta-SSTs (No. 1–12 obtained from different CMIP5 models and No. 13 with CMIP5 multimodel means as indicated in Table ES2). The 90% confidence interval of RR is estimated using the “basic bootstrap” method with 1,000 random samples (Paciorek et al. 2018) and the 90% confidence interval of the FAR is obtained by converting the log RR percentiles into FAR values. (f) Scatterplot between risk ratios of temperature and summer onsets. Red and yellow closed circles indicate w@h and CMIP5 ensemble means, respectively. (g) Scatterplot between for aerosol forcing [AER; obtained from Allen and Ajoku (2016)] and risk ratios of temperature. In (f) and (g), numbered circles represent values from w@h ensemble with different delta-SSTs as explained above.

forcing (mainly due to greenhouse gas increases). When repeating our analysis using a subset of CMIP5 models that provide both ALL and NAT runs (models marked with an asterisk in Table ES2), attribution results remain similar (not shown), indicating a weak influence of the different set of models for ALL and NAT runs. Further, it is suggested that differences in the attribution results among different boundary SSTs (or GCMs)

are partly due to the intermodel difference in aerosol cooling effects, supporting previous findings. Our multimodel assessment provides a convincing evidence that human influence has contributed to the stronger and earlier heat wave by better considering intermodel uncertainties. Physical mechanisms responsible for the observed advance of summer onset and its uncertainty need to be further investigated.

ACKNOWLEDGMENTS. This work was supported by the Korea Meteorological Administration Research and Development Program under Grants KMI2018-03610 and KMA2018-00321 and by a National Research Foundation of Korea (NRF) grant funded by the Korean government (MSIT) (NRF-2018R1A5A1024958). This material is based upon work supported by the U.S. Department of Energy, Office of Science, Office of Biological and Environmental Research, under Contract DE-AC02-05CH11231.

REFERENCES

- Allen, R. J., and O. Ajoku, 2016: Future aerosol reductions and widening of the northern tropical belt. *J. Geophys. Res.*, **121**, 6765–6786, <https://doi.org/10.1002/2016JD024803>.
- Easterling, D. R., K. E. Kunkel, M. F. Wehner, and L. Sun, 2016: Detection and attribution of climate extremes in the observed record. *Wea. Climate Extremes*, **11**, 17–27, <https://doi.org/10.1016/j.wace.2016.01.001>.
- Freychet, N., S. Sparrow, S. Tett, M. J. Mineter, G. Hegerl, and D. C. H. Wallom, 2018: Impacts of anthropogenic forcings and El Niño on Chinese extreme temperatures. *Adv. Atmos. Sci.*, **35**, 994–1002, <https://doi.org/10.1007/s00376-018-7258-8>.
- Guilliod, B. P., and Coauthors, 2017: weather@home 2: Validation of an improved global–regional climate modeling system. *Geosci. Model Dev.*, **10**, 1849–1872, <https://doi.org/10.5194/gmd-10-1849-2017>.
- Kim, Y.-H., S.-K. Min, D. A. Stone, H. Shiogama, and P. Wolski, 2018: Multi-model event attribution of the summer 2013 heat wave in Korea. *Wea. Climate Extremes*, **20**, 33–44, <https://doi.org/10.1016/j.wace.2018.03.004>.
- KMA, 2015: Early heat wave warning issued throughout the year (in Korean). Korean Meteorological Administration, accessed 10 April 2018, http://web.kma.go.kr/notify/press/kma_list.jsp?bid=press&mode=view&num=1193019&page=1&field=subject&text=%C6%F8%BF%B0.
- Mann, M. E., S. K. Miller, S. Rahmstorf, B. A. Steinman, and M. Tingley, 2017: Record temperature streak bears anthropogenic fingerprint. *Geophys. Res. Lett.*, **44**, 7936–7944, <https://doi.org/10.1002/2017GL074056>.
- Massey, N., and Coauthors, 2015: weather@home—Development and validation of a very large ensemble modelling system for probabilistic event attribution. *Quart. J. Roy. Meteor. Soc.*, **141**, 1528–1545, <https://doi.org/10.1002/qj.2455>.
- Neale, R. B., and Coauthors, 2012: Description of the NCAR Community Atmosphere Model (CAM 5.0). NCAR Tech. Note, NCAR/TN-486+STR, 289 pp., www.cesm.ucar.edu/models/cesm1.0/cam/docs/description/cam5_desc.pdf.
- Paciorek, C. J., D. A. Stone, and M. F. Wehner, 2018: Quantifying uncertainty in the attribution of human influence on severe weather. *Wea. Climate Extremes*, **20**, 69–80, <https://doi.org/10.1016/j.wace.2018.01.002>.
- Park, B.-J., Y.-H. Kim, S.-K. Min, and E.-P. Lim, 2018: Anthropogenic and natural contributions to the lengthening of the summer season in the Northern Hemisphere. *J. Climate*, **31**, 6803–6819, <https://doi.org/10.1175/JCLI-D-17-0643.1>.
- Qian, C., C. Fu, Z. Wu, and Z. Yan, 2009: On the secular change of spring onset at Stockholm. *Geophys. Res. Lett.*, **36**, L12706, <https://doi.org/10.1029/2009GL038617>.
- , —, —, and —, 2011: The role of changes in the annual cycle in earlier onset of climatic spring in northern China. *Adv. Atmos. Sci.*, **28**, 284–296, <https://doi.org/10.1007/s00376-010-9221-1>.
- , G. Ren, and Y. Zhou, 2016: Urbanization effects on climatic changes in 24 particular timings of the seasonal cycle in the middle and lower reaches of the Yellow River. *Theor. Appl. Climatol.*, **124**, 781–791, <https://doi.org/10.1007/s00704-015-1446-6>.
- Schaller, N., and Coauthors, 2016: Human influence on climate in the 2014 southern England winter floods and their impacts. *Nat. Climate Change*, **6**, 627–634, <https://doi.org/10.1038/nclimate2927>.
- Stone, D. A., and Coauthors, 2018: A basis set for exploration of sensitivity to prescribed ocean conditions for estimating human contributions to extreme weather in CAM5.1-1degree. *Wea. Climate Extremes*, **19**, 10–19, <https://doi.org/10.1016/j.wace.2017.12.003>.
- Taylor, K. E., R. J. Stouffer, and G. A. Meehl, 2012: An overview of CMIP5 and the experiment design. *Bull. Amer. Meteor. Soc.*, **93**, 485–498, <https://doi.org/10.1175/BAMS-D-11-00094.1>.
- Wu, Z., and N. E. Huang, 2009: Ensemble empirical mode decomposition: A noise-assisted data analysis method. *Adv. Adapt. Data Anal.*, **1**, 1–41, <https://doi.org/10.1142/S1793536909000047>.

ANTHROPOGENIC INFLUENCE ON THE HEAVIEST JUNE PRECIPITATION IN SOUTHEASTERN CHINA SINCE 1961

YING SUN, SIYAN DONG, XUEBIN ZHANG, PETER STOTT, AND TING HU

Anthropogenic influence has increased the chance of an extreme heavy precipitation event like that in June 2017 in southeastern China by about twofold, from a 0.6% probability to a 1.2% probability.

INTRODUCTION. In June 2017, southeastern China experienced heavy and long-lasting precipitation. The total precipitation amount was the highest on record since 1961 (Fig. 1) and was about 60% more than the 1961–90 average for June in the region. The normalized precipitation departure exceeds 3.0 sigma from the 1961–2017 mean. In Hunan province, which is located in central southeastern China, the persistent heavy rainfall at the end of June affected more than 7.8 million people, with 34 fatalities and about 0.8 million people displaced. The affected area of the crops was 605,000 hectares, with a total of 116,000 hectares without harvest. A total of 32,000 houses collapsed and 41,000 were severely damaged. The direct economic loss was 24.12 billion Chinese Yuan (CMA 2017; NCC 2017). It is therefore important to provide a timely answer as to the reasons for this heavy precipitation and if it is related to human influence.

Human-induced increases in greenhouse gases have contributed to the observed intensification of heavy precipitation events in many land areas (Zhang et al. 2007; Min et al. 2011; Zhang et al. 2013). Several studies have investigated the influence of external forcing on some heavy precipitation events in China (e.g., Zhou et al. 2013; Burke et al. 2016). In one case, human influence may have contributed to the occurrence probability of heavy precipitation in southeastern China in May (Burke et al. 2016) whereas in another case there was no clear evidence of human influence of heavy precipitation in northern China (Zhou et al. 2013). There is also evidence of human influence that results in a shift toward heavy precipitation over eastern China (Ma et al. 2017). Here, we use outputs from the large ensemble simulations conducted with the Canadian Earth System Model version 2 (CanESM2; Arora et al. 2011) to investigate possible human influence on heavy precipitation like the June 2017 precipitation event in southeastern China.

DATA AND METHODS. The precipitation event mainly covered the area 24°–32°N, 107°–124°E (box in Fig. 1). We use gauge observations of precipitation (SURF_CLI_CHN_MUL_DAY_V3.0; <http://data.cma.cn/>) that have been collected and rigorously quality controlled (Cao et al. 2016) at the China National Meteorological Information Center (NMIC). Since most Chinese stations were established after the late 1950s and the data become reliable and continuous after 1961, we use the station data in the region at about 600 stations for the period 1961–2017. We divide the region into multiple grid boxes at 2.8125° resolution, roughly consistent with the CanESM2 model grids. We average station precipitation amount within each grid. These gridded values are then averaged to obtain regional

AFFILIATIONS: SUN—National Climate Center, Laboratory for Climate Studies, China Meteorological Administration, Beijing, and Collaborative Innovation Center on Forecast and Evaluation of Meteorological Disasters, Nanjing University of Information Science and Technology, Nanjing, China; DONG AND HU—National Climate Center, Laboratory for Climate Studies, China Meteorological Administration, Beijing, China; ZHANG—Climate Research Division, Environment and Climate Change Canada, Toronto, Ontario, Canada; STOTT—Met Office Hadley Centre, Exeter, United Kingdom

CORRESPONDING AUTHOR: Ying Sun, sunying@cma.gov.cn

The abstract for this article can be found in this issue, following the table of contents.

DOI:10.1175/BAMS-D-18-0114.1

A supplement to this article is available online (10.1175/BAMS-D-18-0114.2).

© 2019 American Meteorological Society

For information regarding reuse of this content and general copyright information, consult the [AMS Copyright Policy](#).

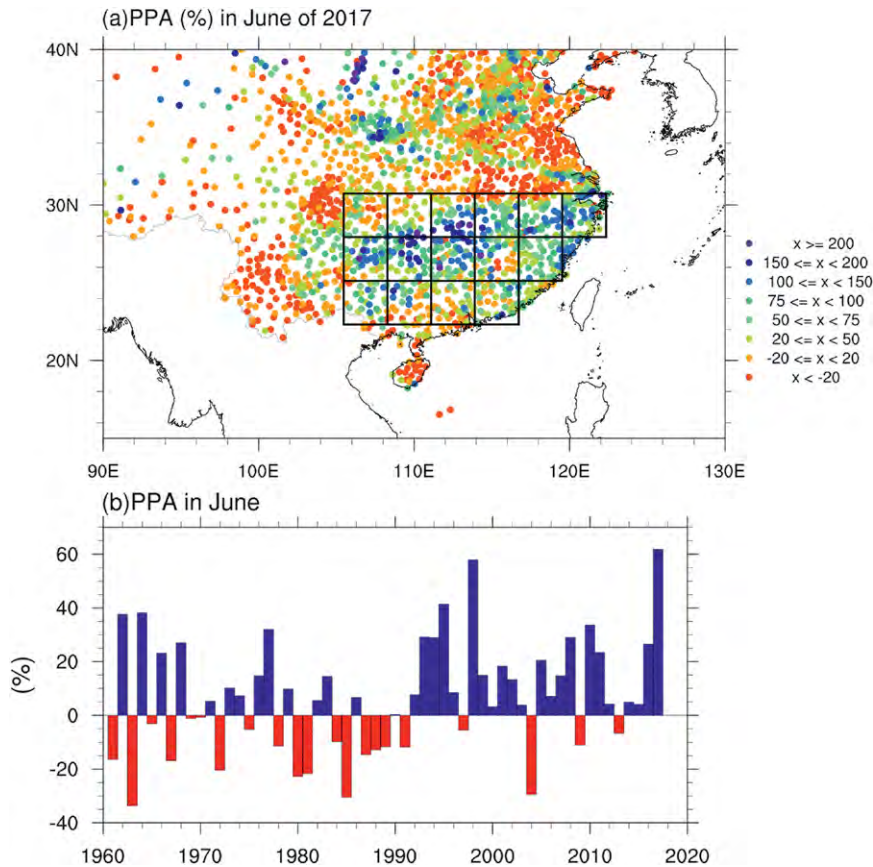


FIG. 1. Observed June percentage precipitation anomaly (PPA). (a) PPA (in percentage, relative to 1961–90 average) in June 2017 in China. The region defined as southeastern China is represented by the boxed areas. (b) Regional average of PPA in June in southeastern China during 1961–2017.

averages that are finally used to compute the percentage precipitation anomaly (PPA) relative to the 1961–90 base period.

CanESM2 was run at T63 resolution ($\sim 2.8^\circ$ longitude/latitude) and included interactive atmosphere, ocean, sea ice, land, and carbon cycle components (Arora et al. 2011). Two large initial-condition ensembles, each consisting of 50 simulations, were randomly initiated from the conditions on 1 January 1950. Two sets of experiments forced with the historical anthropogenic (greenhouse gases combined with aerosols, land use changes, etc.) and natural forcing (ALL) and with natural forcing only (NAT) were conducted. The ALL experiments finished at the end of 2004 and the RCP8.5 scenario was used to extend the ALL simulations from January 2005 onward (Fyfe et al. 2017). The NAT experiments were driven by the solar and volcanic forcings from 1950 to 2020. The solar forcing for all years after 2005 replicated the forcing data from the last solar cycle observed before 2006 and there is no explosive volcanoes forcing after 2006.

The CanESM2 has a relatively high transient climate response (TCR) of 2.4°C (IPCC 2013), leading to higher global mean surface temperature (GMST) increase than the observations. To take this higher sensitivity into account and also make the results comparable with other models, we consider simulation over a 20-yr period (1992–2011) for which the CanESM2 simulated mean GMST is 1°C above the preindustrial level as simulated for the current climate. This is because Earth’s surface has warmed about 1°C by 2017. In the following, the event probabilities in model simulations are computed based on data from the period of 1992–2011.

Our analyses include the following steps: 1) Compute the regional percentage precipitation anomaly (PPA) in June for observations and for individual ALL and

NAT forcing runs during 1961–2017. 2) Estimate the probability (P_{OBS}) for the observed June 2017 precipitation in the observational data using an empirical probability formula (Bonsal et al. 2001). This method is easy to implement and does not assume a probability distribution for the data. 3) Pool the 51 years (1950–2000) of data that occur before GMST rises by 1°C from each of the 50 ALL runs together and then estimate the PPA magnitude (PPA_{ALL}) in the pooled data corresponding to the event probability P_{OBS} , using the same probability formula. 4) Pool the 20 years (1992–2011) of data corresponding to the current climate from each of the 50 NAT runs and then estimate the probability of PPA_{ALL} in NAT simulations (P_{NAT}). 5) Compute the risk ratio $\text{RR} = P_{\text{ALL}}/P_{\text{NAT}}$. 6) Use a bootstrap method to estimate the confidence interval of the risk ratio. This involves three steps: (a) draw 50 samples of 57-yr data from the 50 ALL runs with replacement and then compute PPA_{ALL} ; (b) draw 50 samples of 20 years of data from the 50 NAT runs with replacement and then compute P_{NAT} ; and (c) compute risk ratio from the bootstrapped samples and repeat the bootstrap

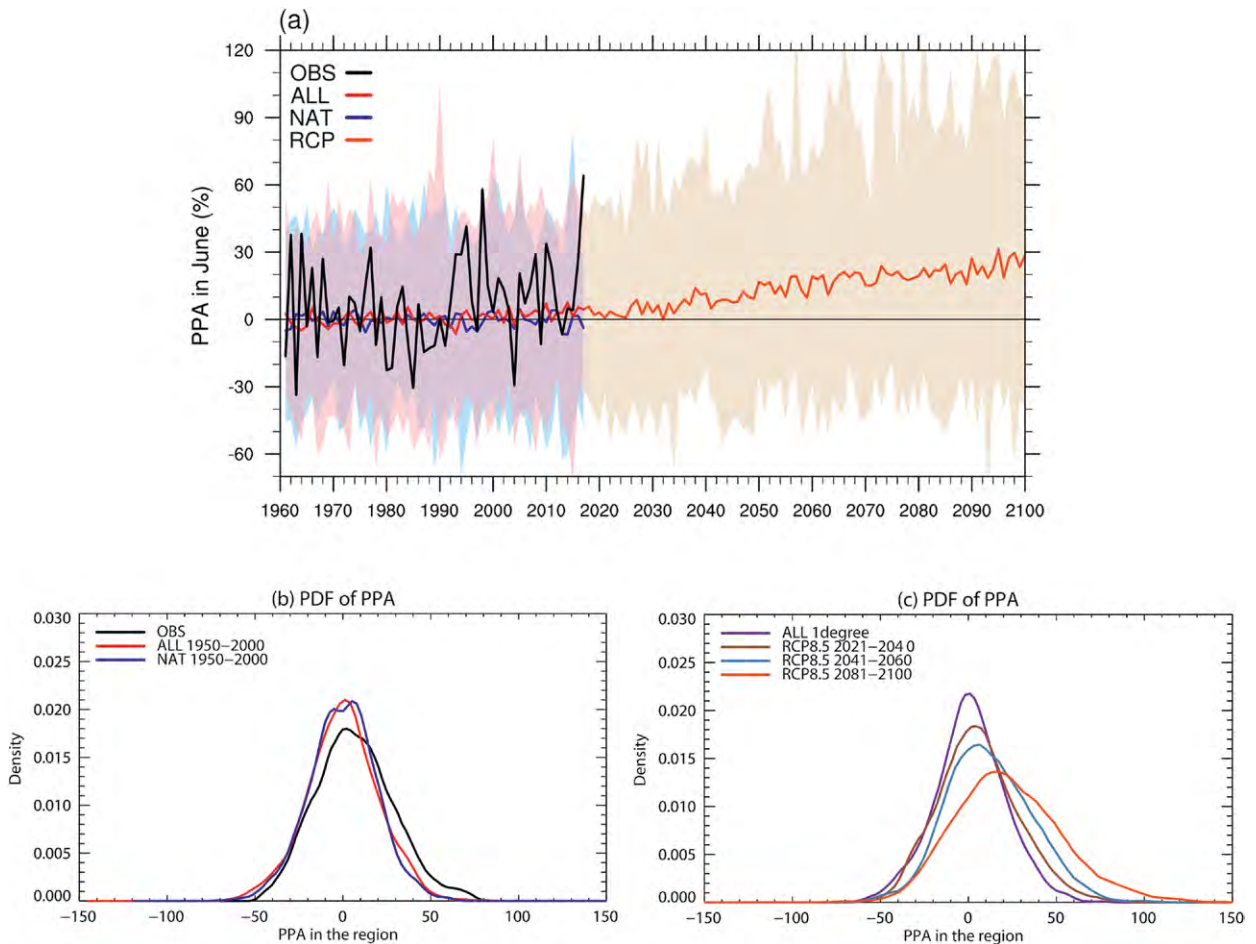


FIG. 2. Observed and simulated regional precipitation anomaly in June and relevant statistics. (a) Observed and simulated PPA for southeastern China. The black line shows the observations while the red, blue, and orange lines display the multimodel ensemble mean under ALL, NAT, and RCP8.5 forcings, respectively. Shadings indicate the ensemble spread by the 50 members. (b) Histograms of observed (black) and simulated percentage precipitation anomalies for 1961–2017 driven by ALL (purple) and NAT (blue) forcings. (c) Histograms of percentage precipitation anomaly simulated by CanESM2 under ALL (red) and RCP8.5 scenario for the future periods in 2021–40 (brown), 2041–60 (light blue), and 2081–2100 (orange).

procedure 1000 times. For the future climate under RCP8.5 scenario, the three time periods 2021–40, 2041–60, and 2081–2100 are selected to compute the occurrence probability of the events like 2017 PPA_{ALL} . The P_{RCP} can be obtained with the same method as the probability calculation P_{NAT} . Then the risk ratios for future climate are calculated as compared with the climate without anthropogenic forcing under NAT forcing (P_{RCP}/P_{NAT}) and with the current observational world (P_{RCP}/P_{OBS}).

RESULTS. Figure 1a shows that the June 2017 anomalous heavy precipitation was centered in southeastern China, especially in the region south of the Yangtze River Valley. Other areas in China experienced below-normal precipitation during this month. In the studied region, the percentage precipi-

tation anomaly in many stations (135 stations; 22% in the studied region) is higher than 100% with some stations experiencing a record-breaking amount of precipitation. The three stations with the highest June PPA (233%, 217%, and 210%) were all located in Hunan Province, where the most serious flooding disaster caused various problems for human life and society. Figure 1b shows the regional mean series for southeastern China. It is apparent that June has been very wet since the early 1990s and the June 2017 was the wettest since 1961, with a PPA_{OBS} value of 61.9%. The probability for a 2017-like event is 1.2% ($P_{OBS} = 0.012$) in the observational data, which corresponds to 1-in-83-yr event. The second largest PPA_{OBS} occurred in 1998 with a PPA value of 57.9%.

Figure 2a shows the observed (black) and simulated June precipitation anomalies under ALL (red), NAT

(blue), and RCP8.5 (orange) in southeastern China in 1961–2017 and the years after 2018 till 2100. The simulated June precipitation amount 164.6 mm (157.1–172.7 mm; Fig. ESI) is smaller than the observation (247.4 mm), but the standard deviation of June precipitation in the simulation (20.5 mm, with a 5%–95% range of 18.4–22.9 mm) is more comparable with the observed one (20.9 mm). This means that the normalized PPA would have slightly larger variations in the models than those observed. Figure 2a shows that the model results under ALL and NAT forcings cover the observed range. The ensemble mean values under ALL and NAT forcing are small, suggesting that the response of precipitation to external forcing is still very small compared with the natural internal variability. Figure 2b shows the PDF distribution of observed and simulated PPA. The observed data slightly skew rightward but this cannot be seen in the models. For the observed 2017-like event probability $P_{\text{OBS}} = 0.012$, the corresponding PPA magnitude under ALL forcing (PPA_{ALL}) is 46.5% [90% confidence interval (CI): 44.3%–52.3%]. The probability of a PPA of 46.5% under NAT forcing is 0.6% ($p = 0.006$) (90% CI: 0.003–0.011), which is a 1-in-172.4-yr event (90% CI: 92.9–369.1 yr). Correspondingly, we can estimate that the risk ratio (RR) is 2.1 (90% CI: 0.9–6.8), indicating that human-induced climate change may have increased the probability of a 2017-like event by about twofold.

Under the future RCP8.5 scenario, the ensemble mean of regional percentage precipitation anomalies simulated by CanESM2 show a clear increasing trend (Fig. 2a). Additionally, the PDFs of PPA in the early (2021–40), middle (2041–60), and late twenty-first century (2081–2100) clearly shift rightward (Fig. 2c). The distribution becomes wider and shorter compared with the observation, especially in 2081–2100. The probabilities of PPA_{ALL} in three future stages are 0.044 (90% CI: 0.033–0.057), 0.088 (90% CI: 0.072–0.103), and 0.195 (90% CI: 0.177–0.217), respectively. These correspond to 1-in-22.6-yr (90% CI: 17.3–30.9 yr), 1-in-11.3-yr (90% CI: 9.6–13.8 yr), and 1-in-5.1-yr (90% CI: 4.5–5.6 yr) events. Compared with the NAT experiments, the estimated risk ratios are 7.6 (90% CI: 3.1–26.6), 15.2 (90% CI: 6.3–51.1), and 33.8 (90% CI: 14.6–111.6). If we compare the increased probability of such an event with those that occurred in the current observational world (P_{OBS}), the risk ratio would be 3.7 (90% CI: 2.7–4.8), 7.3 (90% CI: 6.0–8.7), and 16.3 (90% CI: 14.7–18.2) under the influence of future increased human activities. All these indicate that the occurrence risk of 2017-like events will increase with the increased anthropogenic forcing. As CanESM2 has larger sensitivities, the projected

changes would be larger than median projection by CMIP5 models. The projected changes would also be less under other RCP scenarios with various mitigation efforts such as RCP4.5 or RCP2.6.

CONCLUSIONS. The human influence on the heaviest June precipitation since 1961 in southeastern China is analyzed with the observational and CanESM2 model data. The results show that the probability of extreme June precipitation that is as rare as or rarer than the June 2017 event in the ALL simulations has increased by about twofold when compared with the NAT simulations. This indicates that the anthropogenic influence may have increased the chance for such an event happening. Additionally, the model suggests that increases in regional precipitation will become more likely and probabilities for a similar event are projected to increase progressively more with future anthropogenic warming. These future projections provide additional support for the conclusion that the occurrence probability of such heavy precipitation may already be increasing due to human influence.

ACKNOWLEDGMENTS. Y.S., S. D., and T. H. are supported by China funding agencies through multiple grants: China 2018YFA0605604, NSFC 41675074 and 41775082, and CCSF201805. PAS was supported by the UK–China Research and Innovation Partnership Fund through the Met Office Climate Science for Service Partnership (CSSP) China as part of the Newton Fund, the EUCLEIA project funded by the European Union’s Seventh Framework Programme (FP7/2007–13) under Grant Agreement 607085, and the Joint UK DECCBEIS/Defra Met Office Hadley Centre Climate Programme (GA01101).

REFERENCES

- Arora, V. K., and Coauthors, 2011: Carbon emission limits required to satisfy future representative concentration pathways of greenhouse gases. *Geophys. Res. Lett.*, **38**, L05805, <https://doi.org/10.1029/2010GL046270>.
- Bonsal, B. R., X. Zhang, L. A. Vincent, and W. D. Hogg, 2001: Characteristics of daily and extreme temperatures over Canada. *J. Climate*, **14**, 1959–1976, [https://doi.org/10.1175/1520-0442\(2001\)014<1959:CODAE>2.0.CO;2](https://doi.org/10.1175/1520-0442(2001)014<1959:CODAE>2.0.CO;2).
- Burke, C., P. Stott, Y. Sun, and A. Ciavarella, 2016: Attribution of extreme rainfall in South East China during May 2015 [in “Explaining Extremes of 2015 from a Climate Perspective”]. *Bull. Amer. Meteor. Soc.*, **97**, S92–S96, <https://doi.org/10.1175/BAMS-D-16-0144.1>.
- Cao, L., Y. Zhu, G. Tang, F. Yuan, and Z. Yan, 2016: Climatic warming in China according to a homogenized

- data set from 2419 stations. *Int. J. Climatol.*, **36**, 4384–4392, <https://doi.org/10.1002/joc.4639>.
- CMA, 2017: China Climate Bulletin 2017 (in Chinese with English abstract). China Meteorological Administration, 54 pp., www.cma.gov.cn/root7/auto13139/201801/t20180117_460484.html.
- Fyfe, J. C., and Coauthors, 2017: Large near-term projected snowpack loss over the western United States. *Nat. Commun.*, **8**, 14996, <https://doi.org/10.1038/ncomms14996>.
- IPCC, 2013: *Climate Change 2013: The Physical Science Basis*. T. F. Stocker et al., Eds., Cambridge University Press, 1535 pp.
- Ma, S., and Coauthors, 2017: Detectable anthropogenic shift toward heavy precipitation over eastern China. *J. Climate*, **30**, 1381–1396, <https://doi.org/10.1175/JCLI-D-16-0311.1>.
- Min, S.-K., X. B. Zhang, F. W. Zwiers, and G. C. Hegerl, 2011: Human contribution to more-intense precipitation extremes. *Nature*, **470**, 378–381, <https://doi.org/10.1038/nature09763>.
- NCC, 2017: China Monthly Climate Bulletin for June 2017. National Climate Center of China Meteorological Administration, 18 pp, http://cmdp.ncc-cma.net/influ/moni_china.php.
- Zhang, X., F. W. Zwiers, G. C. Hegerl, F. H. Lambert, N. P. Gillett, S. Solomon, P. Stott, and T. Nozawa, 2007: Detection of human influence on twentieth-century precipitation trends. *Nature*, **448**, 461–465, <https://doi.org/10.1038/nature06025>.
- , H. Wan, F. W. Zwiers, G. C. Hegerl, and S.-K. Min, 2013: Attributing intensification of precipitation extremes to human influence. *Geophys. Res. Lett.*, **40**, 5252–5257, <https://doi.org/10.1002/grl.51010>.
- Zhou, T. J., F. F. Song, R. P. Lin, X. L. Chen, and X. Y. Chen, 2013: The 2012 North China floods: Explaining an extreme rainfall event in the context of a longer-term drying tendency [in “Explaining Extreme Events of 2012 from a Climate Perspective”]. *Bull. Amer. Meteor. Soc.*, **94**, S49–S51, <https://doi.org/10.1175/BAMS-D-13-00085.1>.

16

ATTRIBUTION OF THE PERSISTENT SPRING–SUMMER HOT AND DRY EXTREMES OVER NORTHEAST CHINA IN 2017

SHANSHAN WANG, XING YUAN, AND RENGUANG WU

Anthropogenic climate change has increased the risk of 2017 northeast China persistent spring–summer hot and dry extremes by 5%–55% and 37%–113% respectively.

INTRODUCTION. In March–July 2017, northeast China suffered a long period of intense hot and dry weather. This concurrent heat and drought extreme event affected more than 7.4×10^5 km² of crops and herbage, especially over Xilinguole and Hulunbuir Prairie, and resulted in a direct economic loss of about 70 billion renminbi (RMB) (about 10 billion U.S. dollars; Zhang et al. 2017). During this period, northeast China was under the influence of a persistent and extensive anticyclone centered around Lake Baikal (the Baikal high). Another remarkable fact is that 2017 was the third warmest year on record (WMO 2018), with the absence of El Niño conditions. Meanwhile, the Arctic sea ice extent was well below average during the preceding winter and spring, especially in the Barents Sea and its adjacent seas (WMO 2017).

The increase of greenhouse gases is likely responsible for the warming temperature and the enhancing anticyclone around Lake Baikal in recent

decades, especially after the 1970s (Zhu et al. 2012). Meanwhile, Arctic sea ice variability is a possible factor for triggering the overlying atmospheric circulation anomalies with a lagged effect, such as sustaining the Eurasian teleconnection pattern and the Baikal high system through land–air interaction (e.g., Zhao et al. 2004; Li et al. 2018; Zhang et al. 2018), thereby affecting the climate variations over northeast China (e.g., Wu et al. 2009; Wang et al. 2017; Li et al. 2018).

Therefore, in addition to assessing the contributions of anthropogenic climate change on the persistent hot and dry extremes in March–July of 2017 over northeast China, we also briefly discuss the mechanism for the occurrence of the concurrent extremes from the perspective of the changing Baikal high.

DATA AND METHODS. Monthly surface air temperature (T2M) and precipitation (PRE) observations at 839 stations provided by the National Meteorological Information Center (NMIC) at the China Meteorological Administration (CMA) were bilinearly interpolated into 1° grid cells for the period 1951–2017. Because there were limited observation stations before 1960 and the historical attribution simulations from phase 5 of the Coupled Model Intercomparison Project (CMIP5; Taylor et al. 2012) ended in 2005, T2M and PRE anomalies were calculated relative to the 1960–2005 climatology. The generalized extreme value (GEV) distribution was used to fit the March–July mean T2M and PRE distribution and to estimate the return period excluding the year 2017 in this study.

To analyze the possible reasons for the 2017 concurrent hot and dry extreme event, monthly sea ice area fraction (SIC) data from the Met Office Hadley Centre during 1870–2017 (Rayner et al. 2003) at 1° resolution were used in this study. Monthly mean 500-hPa geopotential height (HGT500) during 1979–2017 at 2.5° resolution was derived from the ERA-Interim reanalysis (Dee et al. 2011). The Baikal

AFFILIATIONS: WANG—Key Laboratory of Arid Climatic Change and Reducing Disaster of Gansu Province, and Key Open Laboratory of Arid Climate Change and Disaster Reduction, Institute of Arid Meteorology, China Meteorological Administration, Lanzhou, China; YUAN—School of Hydrology and Water Resources, Nanjing University of Information Science and Technology, Nanjing, Jiangsu, and Key Laboratory of Regional Climate–Environment for Temperate East Asia (RCE-TEA), Institute of Atmospheric Physics, Chinese Academy of Sciences, Beijing, China; WU—Center for Monsoon System Research, Institute of Atmospheric Physics, Chinese Academy of Sciences, Beijing, China

CORRESPONDING AUTHOR: Xing Yuan, yuanxing@tea.ac.cn

DOI:10.1175/BAMS-D-18-0120.1

A supplement to this article is available online (10.1175/BAMS-D-18-0120.2)

© 2019 American Meteorological Society

For information regarding reuse of this content and general copyright information, consult the [AMS Copyright Policy](#).

high intensity was defined as the mean HGT500 averaged over the region of 80°–120°E and 40°–70°N (Chen et al. 2013) during March–July.

Monthly T2M and PRE simulations from multiple CMIP5 models driven by all (ALL) and natural only (NAT) forcings during 1950–2005 were used in this study (see Table ES1 in the online supplemental information for the model list and information). All simulations were bilinearly regridded into 1° resolution and matched well with the observed distribution via a Kolmogorov–Smirnov test ($p < 0.05$). Because of the data availability, only one pair of realizations (r1i1p1) were used to assure an equal weight for different CMIP5 models. The fraction of attributable risk (FAR; Stott et al. 2004) method, which compares the event tail probabilities (P) between the CMIP5/NAT and CMIP5/ALL simulations ($\text{FAR} = 1 - P_{\text{NAT}}/P_{\text{ALL}}$), and the probability ratio ($\text{PR} = P_{\text{ALL}}/P_{\text{NAT}}$; Fischer and Knutti 2015) were both used to assess the contributions of anthropogenic climate change. FAR is the fractional contribution of human activity to a particular event, and PR is the factor by which the probability of an event has changed under anthropogenic forcing (Ma et al. 2017). Bootstrapping was performed 1000 times to estimate the FAR and PR uncertainty (Yuan et al. 2018a). To identify the significance level of the difference between ALL and NAT forcings for a given period, p values were calculated using the block bootstrap resampling approach of Singh et al. (2014). In addition, the CMIP5 model-simulated HGT500 was also used here.

In this paper, the highest 25% of regional mean T2M anomalies during each March–July were considered as the extreme hot events (as are the Baikal high intensity extremes), and the lowest 25% of the regional mean PRE anomalies were considered as the extreme dry events. If both extremes occurred in the same year (e.g., 2017), it was considered as a concurrent hot and dry extreme event.

RESULTS. Figure 1a shows the spatial distribution of March–July mean T2M anomaly during 2017. Northeast China experienced a much hotter spring and summer than normal, with anomalies exceeding 2°C over most regions. The area-averaged temperature anomaly in March–July 2017 is ranked as the first during the most recent 67 years according to the CMA/NMIC observations (Fig. 1c), with a return period of 245 years (Fig. 1e). Meanwhile, the extensive rainfall deficit occurred across northeast China (Fig. 1b), and the area-averaged rainfall anomaly in March–July 2017 was unprecedentedly low (Fig. 1d), 36% less than normal with a return period of 122 years (Fig. 1e).

The concurrent hot and dry extremes over northeast China occurred without a strong El Niño–Southern Oscillation (ENSO) signal, but in the context of record-breaking continuing global warmth of 2015–17 and the unprecedentedly low Arctic sea ice extent in the preceding winter and spring (WMO 2017, 2018). As seen from the associated circulation pattern, northeast China was dominated by a sustained anticyclone centered around Lake Baikal during this period (Fig. 1f), which lasted from March to July of 2017. Meanwhile, there were anomalous low pressure centers in both upstream (Ural Mountains) and downstream (northwest Pacific Ocean) regions. Influenced by this circulation pattern, northeast China was behind the deepened East Asian trough and before the enhanced Baikal ridge, and therefore the descending movement and the northwesterly in the upper level were prevailing, which was favorable for the abnormal hot and dry extremes (Wang et al. 2017). Meanwhile, it is also found that HGT500 exhibited a significant enhancing trend around Lake Baikal (Fig. 1g), which implies that the Baikal high has been intensifying during the past 40 years (Fig. 1h).

As mentioned in the introduction, anthropogenic warming enhances the Baikal high (Zhu et al. 2012). Meanwhile, there exists a noticeable lagged relationship between the Arctic sea ice in preceding winter and spring (particularly in spring) and the midlatitudinal circulation of Eurasia in following seasons via singular value decomposition (SVD) analysis (see Fig. ES1). As for the interannual variations, less preceding Arctic sea ice, particularly in the Barents Sea and its adjacent seas, corresponds to anomalously high pressure around Lake Baikal in the next spring and summer statistically. The lagged relationship increases significantly after 1997 ($p < 0.05$; see Fig. ES2). Recently, such a lagged effect between the Eurasian mid- to high-latitude teleconnection in summer and the interannual variations of Arctic sea ice from preceding spring to summer was also confirmed by model simulations (Li et al. 2018; Zhang et al. 2018).

To attribute the concurrent hot and dry extremes in March–July of 2017, CMIP5 model simulations with all and natural only forcings were used. Here, the probability density functions (PDFs) for extreme hot (dry) defined as those exceeding 75% (less than 75%) percentiles of the observed mean March–July T2M (PRE) averaged over northeast China were calculated by fitting GEV distributions. The FAR and PR for the March–July mean T2M hotter than 2017 is 0.23 (± 0.17) and 1.30 (0.25), with the return period decreased from 22 years to 17 years under the influence of the anthropogenic climate change (Fig. 2a).

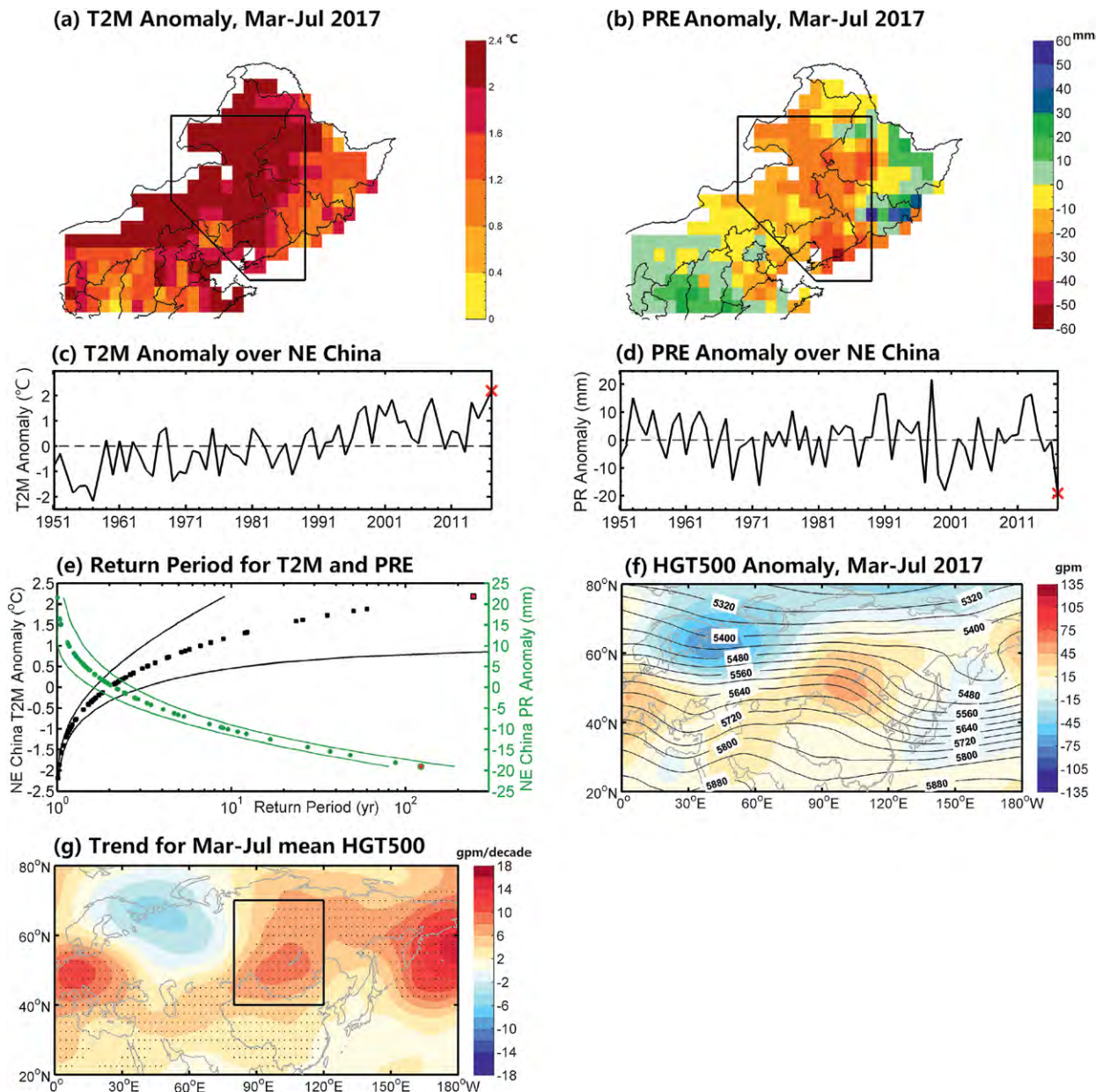


FIG. 1. (a) Temperature (T2M) anomaly (°C) and (b) precipitation (PRE) anomaly (mm) during March–July of 2017 relative to the 1960–2005 climatology based on CMA/NMIC station observations. (c),(d) Observed regional mean T2M and PRE anomalies averaged over northeast China. (e) Return periods and 95% confidence intervals for regional mean March–July T2M and PRE anomalies, where the red dots represent year 2017. (f) 500-hPa geopotential height (gpm; contours) and its anomalies (gpm; shading). (g) Trends for 500-hPa geopotential height (gpm decade⁻¹) during 1979–2017, where the stippling indicates a 95% confidence level ($p < 0.05$) using the Mann–Kendall test.

There is no significant trend for the March–July mean PRE in CMIP5 simulations (not shown), which is consistent with the observation (Fig. 1d). However, the likelihood for low precipitation extremes like that in 2017 significantly increased under anthropogenic influence, with FAR and PR values of 0.43 (± 0.12) and 1.75 (± 0.38) respectively (Fig. 2b). Meanwhile, the frequency of the concurrent hot and dry extremes

shows a visible increasing trend since the mid-1960s in ALL simulations, and the associated FAR values were positive all the time during the CMIP5 historical simulation period (Fig. 2c). In particular, ALL and NAT simulated concurrent hot and dry events were found to be different at 0.001 significance level during the most recent 30-yr period, with a FAR value of 0.22–0.25 (Fig. 2c).

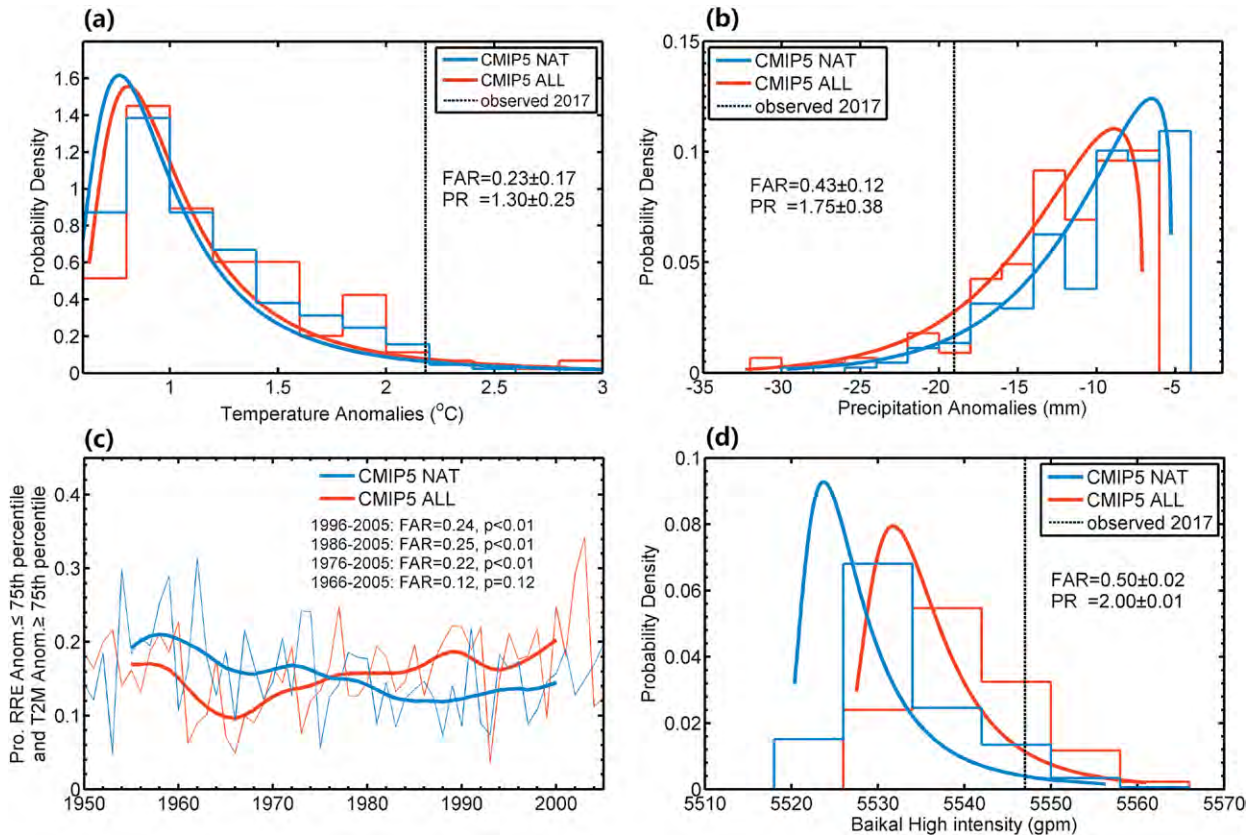


FIG. 2. Histogram (bars) and probability density functions (PDFs; curve) for northeast China March–July mean (a) temperature extremes and (b) precipitation extremes from CMIP5 simulations under all (ALL) and natural only (NAT) forcings during 1950–2005. (c) The probability of concurrent extremely low precipitation and high temperature. The bold curves show 11-yr running mean of the annual time series. (d) As in (a) and (b), but for the Baikal high intensity extremes (gpm).

The related strong Baikal high extremes of such concurrent hot and dry extreme events over northeast China were also examined with ALL and NAT simulations (Fig. 2d). The likelihood of an extremely strong Baikal high like that of 2017 increased due to anthropogenic climate forcing, with FAR and PR values of 0.5 (± 0.02) and 2.0 (± 0.01).

CONCLUSIONS. In 2017, persistent spring–summer hot and dry extremes hit northeast China, characterized by the highest temperature on record and the unprecedentedly low precipitation. Observational analysis showed that the extensive and sustained Baikal high played a crucial role in this extreme event, which was possibly contributed to by anthropogenic global warming and decreasing Arctic sea ice in preceding winter and spring. By analyzing CMIP5 model simulations, it is found that the likelihood of northeast China extremely high temperature such as that occurred in 2017 increased by about 30% due to anthropogenic climate change, and the

likelihood of extremely low precipitation increased by about 75% although its mean value showed no robust trend. Furthermore, the concurrency of such hot and dry extremes exhibited an increasing risk of 28% in the recent 30-yr period due to anthropogenic climate change.

We conjectured that the increasing risk of 2017 persistent spring–summer hot and dry extremes over northeast China was related to the enhancing Baikal high, whose likelihood was doubled in a warming climate. By analyzing pentad-mean soil moisture and temperature, Yuan et al. (2018b) reported an intensification of concurrent hot and dry extreme events over southern Africa due to anthropogenic climate change, which suggests that increasing concurrent extreme events could be very likely without any mitigation strategies.

ACKNOWLEDGMENTS. We acknowledge the World Climate Research Programme’s Working Group on Coupled Modeling, which is responsible

for CMIP. This work was supported by National Key R&D Program of China (2018YFA0606002), the Natural Science Foundation of China (41605055, 41630426), and the China Special Fund for Meteorological Research in the Public Interest (Major projects) (GYHY201506001).

REFERENCES

- Chen, D., C. Bueh, and K. Y. Zhu, 2013: Interannual and interdecadal variabilities of circulation over Lake Baikal region in late spring and their association with temperature and precipitation over China (in Chinese). *Chin. J. Atmos. Sci.*, **37**, 1199–1209.
- Dee, D. P., and Coauthors, 2011: The ERA-Interim reanalysis: Configuration and performance of the data assimilation system. *Quart. J. Roy. Meteor. Soc.*, **137**, 553–597, <https://doi.org/10.1002/qj.828>.
- Fischer, E. M., and R. Knutti, 2015: Anthropogenic contribution to global occurrence of heavy-precipitation and high-temperature extremes. *Nat. Climate Change*, **5**, 560–564, <https://doi.org/10.1038/nclimate2617>.
- Li, H., H. Chen, H. Wang, J. Sun, and J. Ma, 2018: Can Barents Sea ice decline in spring enhance summer hot drought events over northeastern China? *J. Climate*, **31**, 4705–4725, <https://doi.org/10.1175/JCLI-D-17-0429.1>.
- Ma, S. M., T. J. Zhou, D. A. Stone, O. Angélil, and H. Shiogama, 2017: Attribution of the July–August 2013 heat event in central and eastern China to anthropogenic greenhouse gas emissions. *Environ. Res. Lett.*, **12**, 054020, <https://doi.org/10.1088/1748-9326/aa69d2>.
- Rayner, N. A., D. E. Parker, E. B. Horton, C. K. Folland, L. V. Alexander, D. P. Rowell, E. C. Kent, and A. Kaplan, 2003: Global analyses of sea surface temperature, sea ice, and night marine air temperature since the late nineteenth century. *J. Geophys. Res.*, **108**, 4407, <https://doi.org/10.1029/2002JD002670>.
- Singh, D., M. Tsang, B. Rajaratnam, and N. S. Diffenbaugh, 2014: Observed changes in extreme wet and dry spells during the South Asian summer monsoon season. *Nat. Climate Change*, **4**, 456–461, <https://doi.org/10.1038/nclimate2208>.
- Stott, P. A., D. A. Stone, and M. R. Allen, 2004: Human contribution to the European heatwave of 2003. *Nature*, **432**, 610–614, <https://doi.org/10.1038/nature03089>.
- Taylor, K. E., R. J. Stouffer, and G. A. Meehl, 2012: An overview of CMIP5 and the experiment design. *Bull. Amer. Meteor. Soc.*, **93**, 485–498, <https://doi.org/10.1175/BAMS-D-11-00094.1>.
- Wang, S., X. Yuan, and Y. Li, 2017: Does a strong El Niño imply a higher predictability of extreme drought? *Sci. Rep.*, **7**, 40741, <https://doi.org/10.1038/srep40741>.
- WMO, 2017: WMO Statement on the State of the Global Climate in 2016. World Meteorological Organization, 24 pp., <https://public.wmo.int/en/resources/library/wmo-statement-state-of-global-climate-2016>.
- , 2018: WMO Statement on the State of the Global Climate in 2017. World Meteorological Organization, 35 pp., <https://public.wmo.int/en/resources/library/wmo-statement-state-of-global-climate-2017>.
- Wu, B., R. Zhang, B. Wang, and R. D'Arrigo, 2009: On the association between spring Arctic sea ice concentration and Chinese summer rainfall. *Geophys. Res. Lett.*, **36**, L09501, <https://doi.org/10.1029/2009GL037299>.
- Yuan, X., S. Wang, and Z.-Z. Hu, 2018a: Do climate change and El Niño increase likelihood of Yangtze River extreme rainfall? [in “Explaining Extreme Events of 2016 from a Climate Perspective”]. *Bull. Amer. Meteor. Soc.*, **99**, S113–S117, <https://doi.org/10.1175/BAMS-D-17-0089.1>.
- , L. Wang, and E. F. Wood, 2018b: Anthropogenic intensification of southern African flash droughts as exemplified by the 2015/16 season [in “Explaining Extreme Events of 2016 from a Climate Perspective”]. *Bull. Amer. Meteor. Soc.*, **99**, S86–S90, <https://doi.org/10.1175/BAMS-D-17-0077.1>.
- Zhang, Y., L. Zhang, S. P. Wang, and J. Feng, 2017: Drought events and their influence in summer of 2017 in China (in Chinese). *J. Arid Meteor.*, **35**, 899–905.
- Zhao, P., X. Zhang, X. Zhou, M. Ikeda, and Y. Yin, 2004: The sea ice extent anomaly in the North Pacific and its impact on the East Asian summer monsoon rainfall. *J. Climate*, **17**, 3434–3447, [https://doi.org/10.1175/1520-0442\(2004\)017<3434:TSIEAI>2.0.CO;2](https://doi.org/10.1175/1520-0442(2004)017<3434:TSIEAI>2.0.CO;2).
- Zhu, C., B. Wang, W. Qian, and B. Zhang, 2012: Recent weakening of northern East Asian summer monsoon: A possible response to global warming. *Geophys. Res. Lett.*, **39**, L09701, <https://doi.org/10.1029/2012GL051155>.

ANTHROPOGENIC WARMING HAS SUBSTANTIALLY INCREASED THE LIKELIHOOD OF JULY 2017–LIKE HEAT WAVES OVER CENTRAL EASTERN CHINA

YANG CHEN, WEI CHEN, QIN SU, FEIFEI LUO, SARAH SPARROW, FANGXING TIAN, BUWEN DONG, SIMON F. B. TETT, FRASER C. LOTT, AND DAVID WALLOM

Heat waves in central eastern China like the record-breaking July 2017 event were rare in natural worlds but have now become approximately 1-in-5-yr events due to anthropogenic forcings.

INTRODUCTION. During July 2017, an unprecedentedly intense heat wave struck central eastern China, resulting in drastically increased human morbidity/mortality, steeply reduced agriculture productivity, and serious shortage of electricity and water supply (CMA 2017). Many meteorological stations registered 15–25 hot days (daily maximum temperature over 35°C), and some even had record-high July temperatures, such as a new record of 40.9°C among historical observations since 1873 at Xu-Jia-Hui station in Shanghai (CMA 2017). The China

Meteorological Administration issued 10 high-level warnings against hot weather during 21–25 July. Such unprecedentedly frequent alarms within only 5 days attracted intense scrutiny from policy-makers, media, and the public on the relationship between this heat wave and global warming.

Previous studies usually conducted attribution analyses on seasonal warmth in central eastern China (e.g., the 2013 record-breaking summer; Sun et al. 2014), leaving attribution statements for short-term (synoptic) hot extremes sparsely reported. This study therefore attempts to answer whether and to what extent anthropogenic warming has increased the likelihood of 5-day heat waves as hot as or hotter than the 21–25 July 2017 case over central eastern China.

DATA AND METHODS. Homogenized observations of daily maximum temperatures (Tmax) during 1960–2017 from 760 meteorological stations are used [Li et al. 2015; for homogenization methods see Szentimrey (1999)]. Daily observations is interpolated onto the $0.56^\circ \times 0.83^\circ$ grid of the model via a “natural neighbor” scheme (Sibson 1981), following the model’s resolution and geography.

The upgraded HadGEM3-GA6-N216 model is employed (Christidis et al. 2013; Ciavarella et al. 2018). Model outputs include all-forced simulations conditioned on the observed 2017 sea surface temperature (SST) and sea ice from the HadISST dataset (Rayner et al. 2003) and naturalized simulations with anthropogenic signals removed from observed SSTs and with preindustrial forcings. Accordingly, occurrence probabilities and resultant attribution conclusions reported in this study are also conditioned on the 2017 SST patterns. The ensemble is generated through physics perturbations of multiple initial conditions with identical external forcings.

AFFILIATIONS: Y. CHEN—State Key Laboratory of Severe Weather, Chinese Academy of Meteorological Sciences, Beijing, China; W. CHEN—State Key Laboratory of Numerical Modeling for Atmospheric Sciences and Geophysical Fluid Dynamics, Institute of Atmospheric Physics, Chinese Academy of Sciences, Beijing, China; SU—Department of Atmospheric Sciences, Yunnan University, Kunming, China; LUO—Nansen-Zhu International Research Centre and Climate Change Research Center, Institute of Atmospheric Physics, Chinese Academy of Sciences, Beijing, China; SPARROW AND WALLOM—University of Oxford, Oxford e-Research Centre, Oxford, United Kingdom; TIAN AND DONG—National Centre for Atmospheric Science, Department of Meteorology, University of Reading, Reading, United Kingdom; TETT—School of Geosciences, University of Edinburgh, Edinburgh, United Kingdom; LOTT—Met Office Hadley Centre, Exeter, United Kingdom

CORRESPONDING AUTHOR: Dr. Wei Chen, chenwei@mail.iap.ac.cn

DOI:10.1175/BAMS-D-18-0087.1

A supplement to this article is available online (10.1175/BAMS-D-18-0087.2)

© 2019 American Meteorological Society

For information regarding reuse of this content and general copyright information, consult the [AMS Copyright Policy](#).

More specifically, historical simulations (histCLIM) consisting of 15 members over 1961–2013 are compared with interpolated observations to evaluate the model's fidelity in simulating climatological statistics (mean and variability) of the strongest 5-day heat waves. Two ensembles of 525-member simulations for the 2017 July with (hereafter histALL, as an extension of previous histCLIM runs) and without (hereafter histNAT) anthropogenic forcings are used to estimate the probability of the 21–25 July heat wave in each scenario. Denoting P_{ALL} and P_{NAT} as the occurrence probability of events equivalent to or stronger than the targeted case in 525-member histALL and histNAT ensembles, the risk ratio (RR) is expressed as P_{ALL}/P_{NAT} . The fraction of attributable risks (FAR) is expressed as $1 - P_{NAT}/P_{ALL}$.

Reference climatologies over 1961–90 are formed for both simulations (ensemble mean of 15-member

histCLIM) and observations from the hottest 5-day running mean Tmax in July. These pentad climatologies are approximately 2°–3°C warmer than July monthly-mean Tmax climatologies in both simulations and observations, and serve to distinguish especially intense 5-day heat waves from more typical 5-day cases (Figs. 1c,d). Respective climatologies are then removed from observations and simulations to create overlapping pentad Tmax anomalies (hereafter PTmax; see Fig. 1c). Based on these PTmax anomalies, both the historical distribution of the hottest 5-day heat waves and warm anomalies for the 2017 case could be well reproduced by this model (see Fig. ES1 in the online supplemental information), indicating the suitability of using this model and PTmax anomalies for attributing this 5-day heat wave. Freychet et al. (2018) also reported good performance of this model in simulating characteristics of 5-day heat waves in

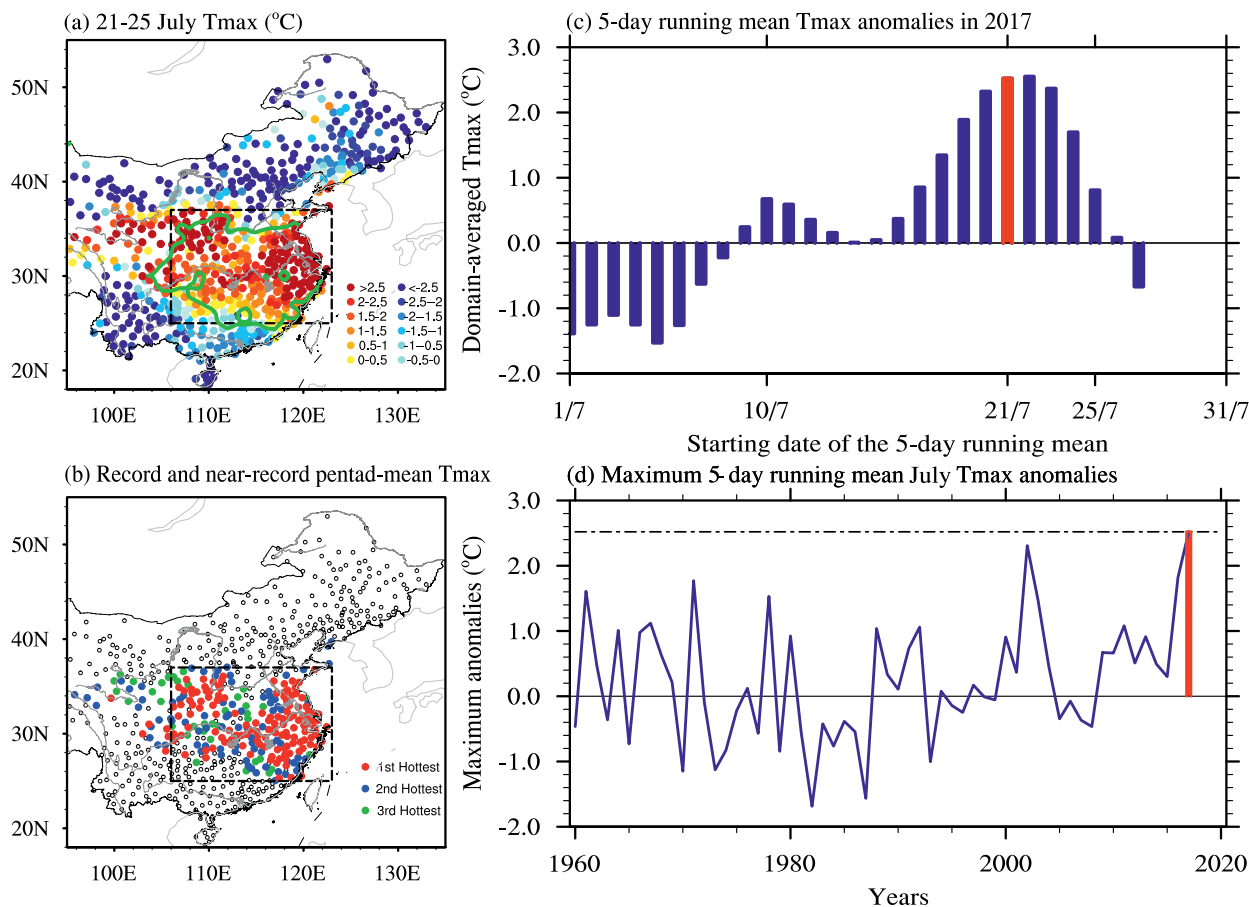


FIG. 1. (a) Observed pentad-mean (21–25 Jul 2017) Tmax anomalies (°C) relative to the 1961–90 climatology for the maximum 5-day mean Tmax. The green contour indicates the 35°C-isoline of mean Tmax during this pentad. Central eastern China is shown by the dashed rectangle. (b) Spatial distribution of stations that registered record- and near-record (since 1960) pentad-mean July Tmax during 21–25 Jul 2017. (c) Observed overlapping pentad-mean Tmax anomaly averaged over central eastern China during July 2017. Each value is indexed by the first day of the pentad. (d) Observed maximum 5-day mean Tmax anomaly averaged over central eastern China in each July over 1960–2017. The red vertical line labels the 2017 event, and the dashed line indicates its anomaly.

central eastern China, as it is capable of capturing critical mechanisms generating heat waves there. In the remainder of this paper, we used the PTmax anomaly to define the threshold.

RESULTS. During 21–25 July, almost the entirety of central eastern China had temperatures over 35°C, equivalent to 2°–6°C PTmax anomalies (Fig. 1a). Anomalies of these magnitudes produced numerous record- or near-record July PTmax (Fig. 1b). In terms of domain-averaged values, the PTmax in this pentad not only peaked during July 2017, but also set a new record among all historical July counterparts (any 5-day mean Tmax during July) since 1960 (Figs. 1c,d; note that we consider this pentad instead of 22–26 July because of its extensive social and economic repercussions). It is well known that heat waves in this area result dynamically from the persistence of anticyclonic circulations that facilitate increased surface solar radiation and adiabatic heating (Freychet et al. 2017; Chen and Lu 2015). Specific to this case, an unprecedentedly (all Julys since 1960) strong anomalous anticyclonic cell was centered above central eastern China, dynamically explaining the origin of the “record-breaking” Tmax (Fig. ES2) and its exclusive occurrence in this domain (Fig. 1a).

The PTmax anomaly from the interpolated observation (2.52°C) was used as a threshold to characterize the July 2017–like heat wave. Events of this magnitude are fairly rare ($P_{\text{NAT}} = 2.1\%$) in natural-forcing simulations (Fig. 2a, green). Without anthropogenic warming, similar heat waves should have been seen one to three times per century [mean return period: 47.7 yr; 95% confidence interval (CI): 30.8–75.0 yr; Fig. 2b, green]. By contrast, the distribution of simulated PTmax anomaly is markedly positive-displaced in all-forcing worlds, signifying substantially increased odds ($P_{\text{ALL}} = 20.1\%$) of events this hot. In the current climate, anthropogenic warming has exposed central eastern China to 2017-like heat waves about twice per decade (mean return period: 4.9 yr; 95% CI: 4.3–5.8 yr; Fig. 2b, red).

Quantitatively speaking, the risk of an event as hot or hotter increased at least tenfold ($\text{RR} = 9.8$; 95% CI: 5.9–18.9) due to anthropogenic warming. Translating into FAR, human influence accounted for at least 90% (95% CI: 83.0%–94.7%) for the presence of 2017-like heat waves. To avoid selection bias potentially introduced by using the critical threshold at the very end tail (Stott et al. 2004), we also adopted the second hottest July record (2.09°C in July 2002) as an alternative threshold. Simulated anomalies

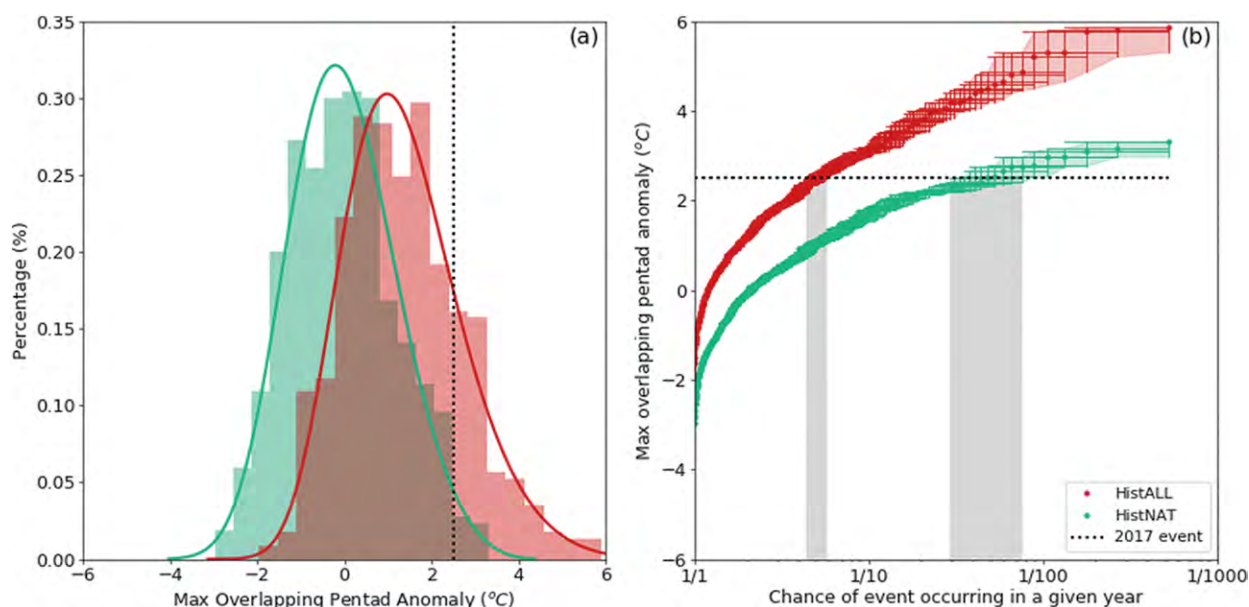


FIG. 2. (a) Distribution of domain-averaged hottest 5-day mean Tmax anomalies during July 2017 (histogram), based on 525-member histALL (red) and histNAT (green) ensembles, and their generalized extreme value (GEV)-fitted curves shown by respective colors. (b) Return periods of domain-averaged hottest 5-day mean Tmax anomalies in histALL (red) and histNAT (green) ensembles. The threshold value of 2.52°C is indicated by dashed lines in (a) and (b). In (b), vertical and horizontal bars represent the 5%–95% uncertainty interval of temperature anomalies and return periods, derived via the bootstrapping method ($N = 1000$). Gray shadings specify the uncertainty interval of return period of the threshold exceedance in histNAT and histALL runs.

exceeding this threshold are recorded 5 times more frequently ($RR = 4.5$; 95% CI: 3.4–6.5) in the all-forcing world ($P_{ALL} = 26.8\%$) than in the natural-forcing world ($P_{NAT} = 5.9\%$). These results also indicate that anthropogenic forcings contributed more to increases in the risks of rarer, more extreme heat waves. So, we reiterate that anthropogenic warming played an overarching role ($FAR = 77.8\%$; 95% CI: 70.4%–84.6%) in elevating the risk of heat waves stronger than this second-hottest threshold (e.g., the July 2017 case).

CONCLUSIONS AND DISCUSSION. In central eastern China, heat waves hotter than the July 2017 event should have had a very slim chance to occur in natural-forcing worlds. But now, forced by anthropogenic warming and conditioned on the 2017 SST pattern, a 5-day heat wave like this case has become 10 times more likely, as a 1-in-5-yr or more common event.

Although influences of anthropogenic warming could be detected and were largely attributable, attribution conclusions for a single high-impact case may be subject to some uncertainties. First, the estimated RR and FAR may be quantitatively sensitive to the selection of baseline periods (here 1961–90), as reported by Knutson et al. (2013). Still, sensitivity tests adopting varying baselines for this case indicate that the qualitative statement “increase in the likelihood of a July 2017–like heat wave could be largely attributable to anthropogenic warming” robustly holds. Second, the estimated RR and FAR only apply to the current climate. As the planet keeps warming, a higher RR of a July 2017-like case would be expected (Perkins and Gibson 2015). Future reductions in aerosols due to increasingly stricter air quality control in this area may also give a greater RR of a July 2017-like case (van Oldenborgh et al. 2018; Wang et al. 2018). This study is based only on factual and counterfactual runs in a single atmosphere-only model, with the intention of exploiting its large ensembles for calculating the statistics of rare events (Otto 2017). Estimated RRs should still be compared with those derived via other methods/models, such as observation-constrained estimates (van Oldenborgh et al. 2015), alternative atmosphere-only model-based estimates (e.g., weather@home; Massey et al. 2015), and fully coupled model-based estimates (CMIP5; Sun et al. 2014) to further clarify uncertainties.

Comparing temperatures alone in factual and counterfactual simulations, the estimated RR only delivers a general attribution message, leaving physical interpretations about how anthropogenic forcings influenced the likelihood of the heat wave and its preferential occurrence in central eastern China to

be addressed. To this end, follow-up efforts will be made to disentangle this general attribution effort into a dynamic (e.g., large-scale circulations) and a thermodynamic part (Vautard et al. 2016; Schaller et al. 2016). A critical step toward dynamic attribution is to quantify the extent to which anthropogenic warming affected the presence, location, maintenance, and amplitude of anticyclonic circulations akin to the 2017 case (Fig. ES2). Such a separation could also facilitate tracking down and communicating the source of attribution uncertainties from both dynamic and thermodynamic perspectives (Vautard et al. 2016; Wehrli et al. 2018).

ACKNOWLEDGMENTS. This study was conducted during the Operational Attribution Workshop at the University of Oxford. The study, SFBT, SS, BD, FL, and DW were supported by the U.K.–China Research and Innovation Partnership Fund through the Met Office Climate Science for Service Partnership (CSSP) China as part of the Newton Fund. Chinese authors were jointly supported by the National Key Research and Development Program (2016YFA0601504), the NSF of China (41675078, U1502233, 41320104007 and 41505037), the Youth Innovation Promotion Association of CAS (2018102), and the MOST Key Project (2016YFA0601802).

REFERENCES

- Chen, R., and R. Lu, 2015: Comparisons of the circulation anomalies associated with extreme heat weather in different regions in eastern China. *J. Climate*, **28**, 5830–5844, <https://doi.org/10.1175/JCLI-D-14-00818.1>.
- Christidis, N., P. A. Stott, A. A. Scaife, A. Arribas, G. S. Jones, D. Copsey, J. R. Knight, and W. J. Tennant, 2013: A new HadGEM3-A-based system for attribution of weather- and climate-related extreme events. *J. Climate*, **26**, 2756–2783, <https://doi.org/10.1175/JCLI-D-12-00169.1>.
- Ciavarella, A., and Coauthors, 2018: Upgrade of the HadGEM3-A based attribution system to high resolution and a new validation framework for probabilistic event attribution. *Wea. Climate Extremes*, **20**, 9–32, <https://doi.org/10.1016/j.wace.2018.03.003>.
- CMA, 2017: China Climate Bulletin 2017 (in Chinese with English abstract). China Meteorological Administration, 54 pp., www.cma.gov.cn/root7/auto13139/201801/t20180117_460484.html.
- Freychet, N., S. F. B. Tett, J. Wang, and G. C. Hegerl, 2017: Summer heat waves over eastern China: Dynamical processes and trend attribution. *Environ.*

- Res. Lett.*, **12**, 024015, <https://doi.org/10.1088/1748-9326/aa5ba3>.
- , —, G. C. Hegerl, and J. Wang, 2018: Central-eastern China persistent heat waves: Evaluation of the AMIP models. *J. Climate*, **31**, 3609–3624, <https://doi.org/10.1175/JCLI-D-17-0480.1>.
- Knutson, T. R., F. Zeng, and A. T. Wittenberg, 2013: The extreme March–May 2012 warm anomaly over the eastern United States: Global context and multimodel trend analysis [in “Explaining Extreme Events of 2012 from a Climate Perspective”]. *Bull. Amer. Meteor. Soc.*, **96**, S13–S17, <https://journals.ametsoc.org/doi/10.1175/BAMS-D-13-00085.1>.
- Li, Z., Z.-W. Yan, and H. Y. Wu, 2015: Updated homogenized Chinese temperature series with physical consistency. *Atmos. Ocean. Sci. Lett.*, **8**, 17–22, <https://doi.org/10.3878/AOSL20140062>.
- Massey, N., and Coauthors, 2015: weather@home—Development and validation of a very large ensemble modelling system for probabilistic event attribution. *Quart. J. Roy. Meteor. Soc.*, **141**, 1528–1545, <https://doi.org/10.1002/qj.2455>.
- Otto, F. E. L., 2017: Attribution of weather and climate events. *Annu. Rev. Environ. Resour.*, **42**, 627–646, <https://doi.org/10.1146/annurev-environ-102016-060847>.
- Perkins, S. E., and P. B. Gibson, 2015: Increased risk of the 2014 Australian May heatwave due to anthropogenic activity [in “Explaining Extremes of 2014 from a Climate Perspective”]. *Bull. Amer. Meteor. Soc.*, **96**, S154–S157, <https://doi.org/10.1175/BAMS-D-15-00074.1>.
- Rayner, N. A., D. E. Parker, E. B. Horton, C. K. Folland, L. V. Alexander, D. P. Rowell, E. C. Kent, and A. Kaplan, 2003: Global analyses of sea surface temperature, sea ice, and night marine air temperature since the late nineteenth century. *J. Geophys. Res.*, **108**, 4407, <https://doi.org/10.1029/2002JD002670>.
- Schaller, N., and Coauthors, 2016: Human influence on climate in the 2014 southern England winter floods and their impacts. *Nat. Climate Change*, **6**, 627–634, <https://doi.org/10.1038/nclimate2927>.
- Sibson, R., 1981: A brief description of natural neighbor interpolation. *Interpreting Multivariate Data*, V. Barnett, Ed., Wiley, 21–36.
- Stott, P. A., D. A. Stone, and M. R. Allen, 2004: Human contribution to the European heatwave of 2003. *Nature*, **432**, 610–614, <https://doi.org/10.1038/nature03089>.
- Sun, Y., X. Zhang, F. W. Zwiers, L. C. Song, H. Wan, T. Hu, H. Yin, and G. Y. Ren, 2014: Rapid increase in the risk of extreme summer heat in eastern China. *Nat. Climate Change*, **4**, 1082–1085, <https://doi.org/10.1038/nclimate2410>.
- Szentimrey, T., 1999: Multiple analysis of series for homogenization (MASH). *Proc. Second Seminar for Homogenization of Surface Climatological Data*. Budapest, Hungary, WMO, 27–46.
- van Oldenborgh, G. J., R. Haarsma, H. de Vries, and M. R. Allen, 2015: Cold extremes in North America vs. mild weather in Europe: The winter 2013–14 in the context of a warming world. *Bull. Amer. Meteor. Soc.*, **96**, 707–714, <https://doi.org/10.1175/BAMS-D-14-00036.1>.
- , and Coauthors, 2018: Extreme heat in India and anthropogenic climate change. *Nat. Hazards Earth Syst. Sci.*, **18**, 365–381, <https://doi.org/10.5194/nhess-18-365-2018>.
- Vautard, R., P. Yiou, F. Otto, P. Stott, N. Christidis, G. J. van Oldenborgh, and N. Schaller, 2016: Attribution of human-induced dynamical and thermodynamical contributions in extreme weather events. *Environ. Res. Lett.*, **11**, 114009, <https://doi.org/10.1088/1748-9326/11/11/114009>.
- Wang, J., S. F. B. Tett, Z. Yan, and J. Feng, 2018: Have human activities changed the frequencies of absolute extreme temperatures in eastern China? *Environ. Res. Lett.*, **13**, 014012, <https://doi.org/10.1088/1748-9326/aa9404>.
- Wehrli, K., B. P. Guillod, M. Hauser, M. Leclair, and S. I. Seneviratne, 2018: Assessing the dynamic vs. thermodynamic origin of climate model biases. *Geophys. Res. Lett.*, **45**, 8471–8479, <https://doi.org/10.1029/2018GL079220>.

18

ATTRIBUTION OF A RECORD-BREAKING HEATWAVE EVENT IN SUMMER 2017 OVER THE YANGTZE RIVER DELTA

CHUNLÜE ZHOU, KAICUN WANG, DAN QI, AND JIANGUO TAN

The occurrence probability of the record-breaking Yangtze River Delta heatwave in summer 2017 might be attributed to global warming (23%), the abnormal western Pacific subtropical high (32%), and the urban heat island effect (58%).

INTRODUCTION. During 11 to 28 July 2017, the Yangtze River Delta experienced a record-breaking heatwave. In particular, the Xujiahui weather station in Shanghai endured the worst heatwave in at least 145 years, with a new record of 40.9°C on 21 July 2017. The extreme heatwave left four people dead and many elderly people and children suffering from heatstroke.

Generally, the western Pacific subtropical high (WPSH) is regarded as the key anticyclone system for the occurrence of extreme heatwave events in eastern China (Yang and Li 2005; Ding et al. 2010; Wang et al. 2014; Luo and Lau 2017; Wang et al. 2016; Li and Sun 2018). The WPSH variability is modulated by tropical forcing from sea surface temperature anomalies over the equatorial Pacific Ocean (e.g., ENSO) (Tao and Xu 1962; Wang et al. 2000; He et al. 2015a; Chen and Zhou 2017) and over the tropical Indian Ocean (Yang et al. 2007; Du et al. 2009; Xie et al. 2009). During the decaying El Niño, the lasting warming over the tropical Indian Ocean can trigger an anomalous WPSH by exciting Kelvin waves eastward (Wu et al. 2009; Wu et al. 2010), resulting in a westward extension of the WPSH (Huang and Wu 1989; Zhou et al. 2009). The west-extending

WPSH induces an anomalous southwesterly flow to transport more moisture to the northern regions and then dry the atmosphere over the Yangtze River Delta (Chen and Lu 2015). This process results in decreased rainfall and increased surface incident solar radiance (Hu et al. 2012, 2013; Liu et al. 2015; Chen et al. 2016; Freychet et al. 2017), which introduce extreme heatwaves in the Yangtze River Delta, such as the one in 2013 (Li et al. 2015).

Other known factors that increase the risk of heatwaves over the Yangtze River Delta include anthropogenic global warming (Yang and Li 2005; Sun et al. 2014; Zhou et al. 2014), which meanwhile influences the variations of the WPSH by tropical oceanic warming (Zhou et al. 2009; He and Zhou 2015; He et al. 2015b), and the urban heat island effect due to local urbanization around the weather stations, which can exacerbate the heatwave by enhancing sensible heat flux and longwave radiation from the surface during the daytime (Tan et al. 2008; Sun et al. 2016; J. Wang et al. 2017).

Using the heatwave magnitude index (HWMI) and July–August mean temperature to quantify the 2017 heatwave, this study therefore tries to answer two questions: 1) How extreme is the heatwave over the Yangtze River Delta in a historical context? 2) What are the relative impacts of the WPSH, global warming, and the urban heat island on the heatwave?

DATA AND METHODS. Daily maximum air temperature (T_{\max}) from 1961 to 2017 at ~2400 meteorological stations (Fig. 1) are collected (available at <http://data.cma.cn/>). Data from 1873 to 2017 at the Xujiahui station are used to depict century-long temperature change (Tan et al. 2008). Following Russo et al. (2014), this study defines the HWMI by considering the duration and intensity of a heatwave, that is, the maximum magnitude of the heatwaves in summer (June–September), where a heatwave has at

AFFILIATIONS: ZHOU AND WANG—College of Global Change and Earth System Science, Beijing Normal University, Beijing, China; QI—National Meteorological Center, China Meteorological Administration, Beijing, China; TAN—Key Laboratory of Cities Mitigation and Adaptation to Climate Change in Shanghai, Shanghai Climate Center, Shanghai, China
CORRESPONDING AUTHOR: Kaicun Wang, kcwang@bnu.edu.cn

DOI:10.1175/BAMS-D-18-0134.1

A supplement to this article is available online (10.1175/BAMS-D-18-0134.2)

© 2019 American Meteorological Society

For information regarding reuse of this content and general copyright information, consult the [AMS Copyright Policy](#).

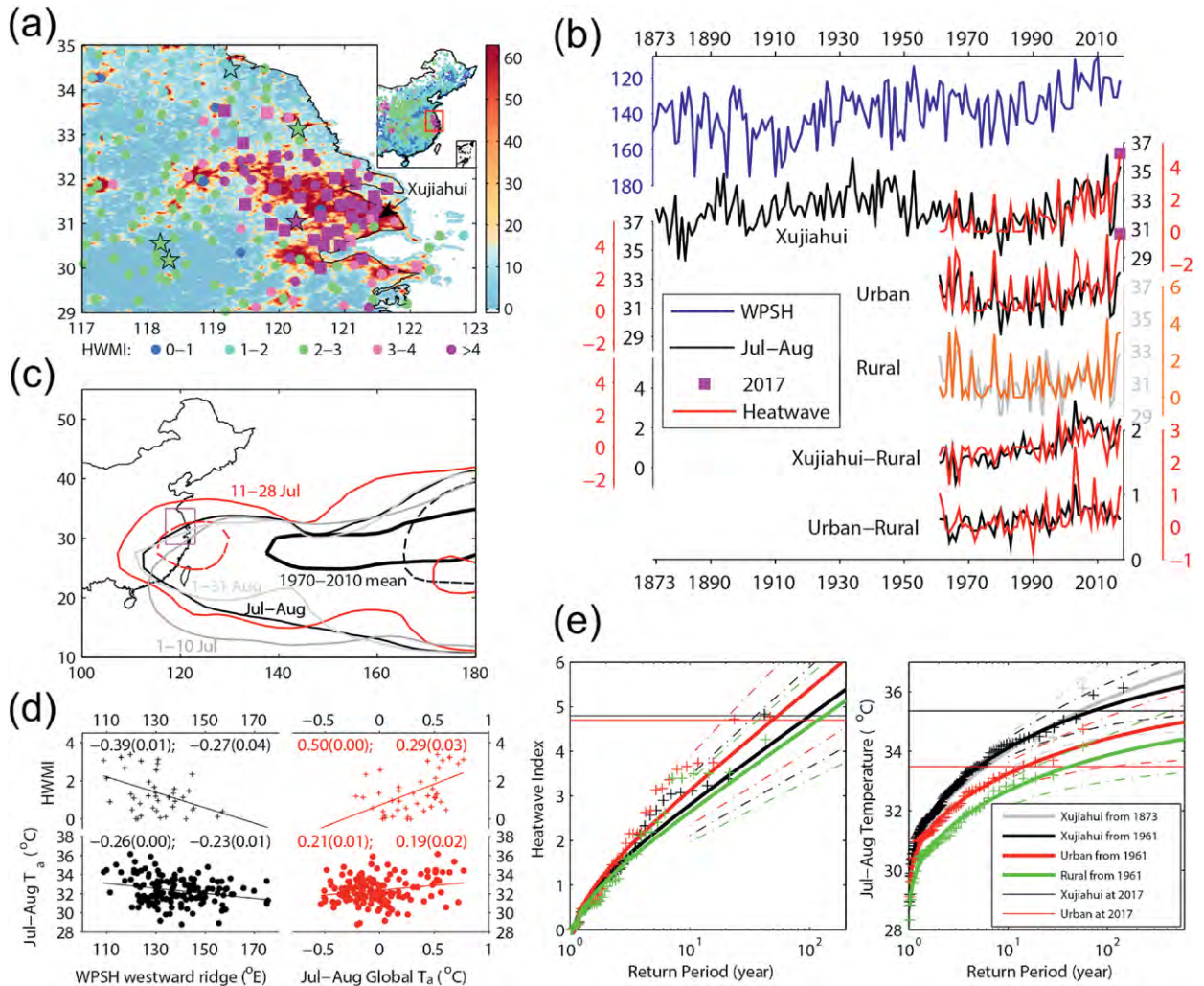


FIG. 1. (a) Spatial pattern of observed extreme heat (denoted by the HWMI) in summer of 2017 over the Yangtze River Delta, China. The stations having the record-breaking heatwave in 2017 during the period of 1961–2017 are plotted in squares. The HWMI categories are as follows: ≤ 1 normal $< 2 \leq$ moderate $< 3 \leq$ severe $< 4 \leq$ extreme. Stable lights from the defense meteorological satellite program are used to describe metropolis and rural regions. **(b)** Time series of the July–August mean west-extending ridge point position of the western Pacific subtropical high (WPSH) (in blue lines), and the July–August means of daily maximum air temperatures (in black lines) and the HWMI (in red lines) over Xujiahui station (from 1873), for urban and rural regions. Temperature differences between at Xujiahui station in the downtown area or urban stations at the edge of urban area and rural stations imply the urban heat island effect on maximum air temperature change. **(c)** Changes in the 588-dagpm contours before and after the 2017 heatwave in 11–28 July. During these days, the 588-dagpm contour centers in the Yangtze River Delta, intensifying the heatwave. **(d)** The July–August mean temperature and the HWMI show significant correlations with the July–August mean west-extending ridge point position of WPSH and global mean temperature anomalies with $p < 0.01$ before detrending (numbers in left column of each subfigure) and $p < 0.04$ after detrending the time series (numbers in right columns). **(e)** GEV fit (in solid lines) of the July–August mean temperature and the HWMI with 95% confidence intervals (in dashed lines).

least three consecutive days with T_{\max} exceeding the 90th percentile (centered on a 30-day window) for the reference period of 1971–2000 (Fischer and Schär 2010). We find that 80% of the maximum heatwaves happen in July and August (see Fig. ES1 in the online supplemental material).

Following the procedure of Ren et al. (2015), five rural stations (shown by stars in Fig. 1a) are identified in comparison with urban stations to quantify the urban heat island effect. The west-extending ridge point position (WRPP) index of the WPSH is calculated (Tao and Xu 1962; Ding 1994; Liu et al. 2012) with the

2.5° × 2.5° 500-hPa geopotential height of the NOAA-CIRES Twentieth Century Reanalysis from 1873 to 2014 (Compo et al. 2011) and extended to 2017 by that of National Centers for Environmental Prediction Reanalysis (NCEP-R1) (Kalnay et al. 1996; Zhou et al. 2018a). We define the years with a WRPP index smaller (larger) than the climatological value (e.g., 137.5°E in reanalysis) as strong (weak) WPSH years. Note that the WRPP index has a near-linear relationship with the area index of the WPSH (Fig. ES1). The WRPP index can be also estimated by use of CMIP5 experiments (Zhou and Li 2002; Dong et al. 2017). After evaluations of the all-forcings (ALL) simulations in CMIP5 archive (Taylor et al. 2012), 19 simulations in seven models (Table ES1 and Fig. ES2) with T_{\max} extended through 2017 (Sun et al. 2014) and having corresponding natural-forcings-only simulations (NAT) ending in 2012 are selected to estimate the influence of anthropogenic global warming. These detailed procedures can be found in the online supplemental information.

For consistency with the observational analysis, the model data are area-averaged over the study region (117°–123°E, 29°–35°N) (Fig. 1a). We apply several statistical techniques to assess the heatwave over the Yangtze River Delta:

- 1) A Kolmogorov–Smirnov test (K-S) is conducted to determine how well the distributions of the simulated temperature anomalies match the observed distribution.
- 2) Generalized extreme value (GEV) (Schaller et al. 2016) and scaled GEV (van der Wiel et al. 2017; Zhou et al. 2018b) distributions are determined to fit the observed and modeled HWMI and July–August temperature (see the online supplemental information).
- 3) The probability ratio (PR = $P_{\text{urban}}/P_{\text{rural}}$) is calculated to quantify urban heat island effect in the odds of extreme heat. The terms P_{urban} and P_{rural} represent the probabilities exceeding a threshold of the 2017 extreme event in two different observation scenarios (i.e., urban and rural regions). After excluding the urban heat island effect, the fraction of attributable risk (FAR = $1 - P_{\text{NAT}}/P_{\text{ALL}}$ or $1 - P_{\text{weakWPSH}}/P_{\text{strongWPSH}}$) method (Stone and Allen 2005) is used to separate the influences of global warming and the WPSH through several combinations of simulation scenarios even though it is difficult to accurately quantify their influences. We estimate the influence of global warming by setting P_{ALL} to be the probability exceeding the 2017 extreme event under the strong WPSH in ALL simulations, with P_{NAT} being the equivalent for the NAT simulations.

Accordingly, we compare the probabilities of the 2017 extreme event under strong and weak WPSHs (i.e., $P_{\text{strongWPSH}}$ and P_{weakWPSH}) in ALL simulations for estimating the WPSH influence. The 95% confidence intervals (CI) are estimated with a 1000-member bootstrap (with replacement).

RESULTS. Influence of the urban heat island. Figure 1a illustrates the spatial pattern of the 2017 extreme heatwave over the Yangtze River Delta. The record-breaking heatwave in 2017 mainly occurred in the Shanghai metropolitan area (in squares of Fig. 1a), particularly with up to 4.84 HWMI in Xujiahui station and 4.77 HWMI in the urban region (Fig. 1b). The Xujiahui station is located downtown in a built-up area with high population density (Fig. 1a), which in turn leads to higher temperatures recorded than at other stations that are located at the edge of the urban region. A GEV fit of the observed HWMI denotes that the 2017 extreme heat is a 1-in-53-yr event for in the urban region and 1-in-104-yr event for Xujiahui station (Fig. 1e). However, the HWMI in the rural region was not the maximum in 2017 (a 1-in-28-yr event; Fig. 1e), but it was in 2013 (Fig. 1b).

Temperature differences between urban and rural stations are suggested to reflect urbanization-induced warming (Sun et al. 2016). Urbanization-induced warming of the HWMI is 0.30°C decade^{−1} (significance level $p = 0.00$, accounting for 70% of the HWMI warming trend) at Xujiahui station and 0.11°C decade^{−1} ($p = 0.00$; 48%) in the urban region (Fig. 1b). For 2017, the values are 38% and 36%, respectively (Fig. 1b).

July–August temperature in 2017 is a 1-in-70-yr event in Xujiahui station and a 1-in-15-yr event for the urban region, which is not extreme in a historical context (Figs. 1b,e). Urbanization-induced July–August temperature warming is 0.35°C decade^{−1} ($p = 0.00$; 84%) at Xujiahui station and 0.05°C decade^{−1} ($p = 0.00$; 64%) in the urban region (Fig. 1b). For 2017, the values are 83% and 2% (calculated as the percentage of urbanization-induced temperature anomaly to temperature anomaly in 2017), respectively (Fig. 1b). More (less) partitioning of surface incident solar radiation into sensible (latent) heat flux induced by impervious surfaces in the urban region can largely explain the urbanization-induced warming in summer over the Yangtze River Delta (Wang and Dickinson 2013; Zhou and Wang 2016; K. Wang et al. 2017).

In addition, from the view of event occurrence probability, the urban heat island increases the likelihood of the 2017 extreme heat over the Yangtze River Delta by 2.5 times [(95% CI: 1.9–4.1) for the

HWMI; cf. 3.0 times (95% CI: 2.4–4.0) for July–August temperature] (Figs. 1e and 2c). In other words, 58% [(95% CI: 47%–76%) for the HWMI; cf. 67% (95% CI: 58%–75%) for July–August temperature] of the attributable risk of the heatwave is caused by the urban heat island.

Influence of the WPSH. The HWMI and July–August temperature anomalies show evident decadal variations (Fig. 1b), which are revealed to correlate with the WPSH ($r = -0.39$ and -0.26 , $p < 0.01$, respectively)

(Fig. 1d). The 588 dagpm (1 dagpm = 10 geopotential meters) of WPSH was located at $\sim 25^\circ\text{N}$ in early July (1–10 July 2017), and moved northward as well as extended westward to the Yangtze River Delta in middle to late July (11–28 July 2017), bringing the anomalous anticyclone over this region and favoring local heating by increasing surface incident solar radiation (Fig. 1c). After the heatwave, the WPSH retreated to $\sim 27^\circ\text{N}$ in August (Fig. 1c).

Compared with the likelihood of the HWMI between strong and weak WPSH in the ALL simulations,

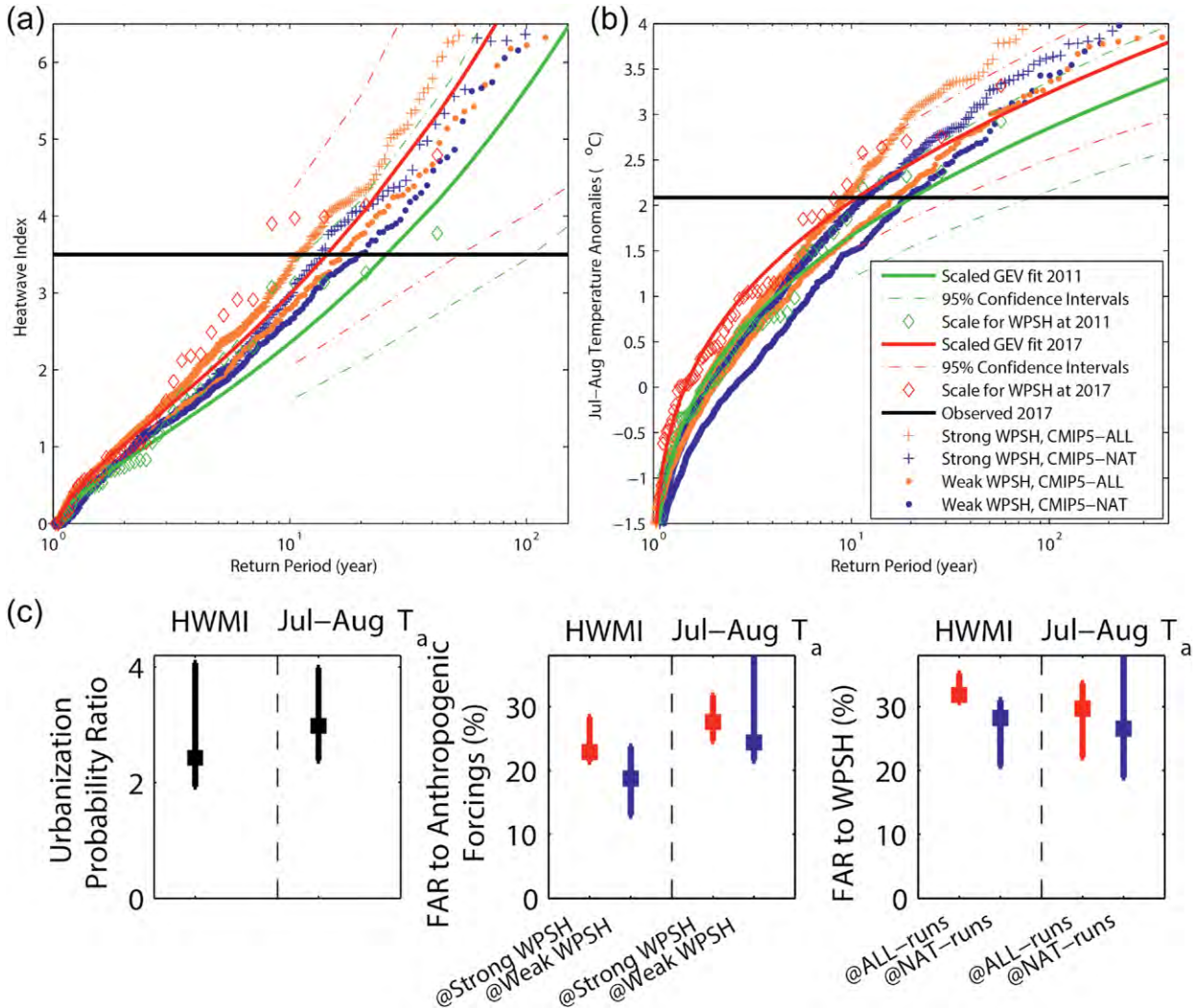


FIG. 2. (a) Return period (unit: yr) of the HWMI from the observations and models participating in phase 5 of the Coupled Model Intercomparison Project (CMIP5) under different conditions, including all forcings (ALL) and natural forcing only (NAT) simulations. The brown/blue crosses (circles) indicate strong (weak) WPSH years from the ALL and NAT simulations. The dashed lines are the 95% confidence intervals of the scaled generalized extreme value (GEV) fit to the climate in 2011 and 2017, respectively. The black thick line is the observed average HWMI of 2017 at rural regions. (b) As in (a), but for the July–August mean temperature. (c) Probability ratio (PR; %) of the HWMI and the July–August mean temperature due to urbanization and the fraction of attributable risk (FAR; %) to anthropogenic forcings and the WPSH are calculated under two different runs including the ALL and NAT simulations. Best estimates and corresponding 95% confidence intervals are calculated by the 1000-member nonparametric bootstrap.

we find 32% [(95% CI: 31%–35%) for the HWMI; cf. 30% (95% CI: 22%–33%) for July–August temperature] of the attributable risk of the 2017 extreme heatwave is attributed to the WPSH. In NAT simulations, the FAR is slightly smaller, 28% [95% CI: 20%–31% for the HWMI; cf. 26% (95% CI: 23%–34%) for July–August temperature] (Fig. 2).

Influence of anthropogenic global warming. The HWMI and July–August temperature anomalies have significantly positive correlations with July–August global mean air temperature ($r = 0.50$ and 0.21 , $p < 0.01$, respectively) (Fig. 1d), implying the footprint of global warming on the 2017 extreme heat.

To assess the influence of global warming, we compare the changes in the likelihood of the HWMI from the ALL and NAT runs (Fig. 2a). Given the strong WPSH, 23% [95% CI: 21%–28% for the HWMI; cf. 27% (95% CI: 25%–32%) for July–August temperature] of the attributable risk of such events as the 2017 extreme heatwave is attributed to global warming (Fig. 2). Given the weak WPSH, the FAR is slightly smaller (i.e., 18%) [95% CI: 11%–24% for the HWMI; cf. 24% (95% CI: 21%–32%) for July–August temperature, calculated from the return periods of approximately 15 and 20 years in ALL and NAT runs] (Fig. 2).

CONCLUSIONS AND DISCUSSION. Our analysis based on the HWMI indicates that the record-breaking heatwave event of 2017 is a 1-in-104-yr event at the Xujiahui station and a 1-in-58-yr event over the Yangtze River Delta. CMIP5-based FAR analyses suggest that approximately 23% (95% CI: 21%–28%) of the risk of such events might be attributed to global warming and 32% (95% CI: 31%–35%) of the risk might be due to the WPSH. The urban heat island over the metropolis increases the likelihood of such events by 2.5 times and contributes 36% of severity of the 2017 extreme heatwave over the Yangtze River Delta. In a word, the westward extension of the WPSH likely leads to the formation of the extreme heatwave, and global warming as well as the urban heat island would further increase the severity of the heatwave.

Zhou et al. (2014) pointed out but did not disentangle the role of global warming and internal climate variability in the 2013 extreme heat over middle and lower reaches of the Yangtze River. Zhou et al. (2014) reported 58% of attributable risk to global warming, which is near the sum ($27\% + 30\% = 57\%$) of attributable risk to global warming and the WPSH in the 2017 extreme heat over the Yangtze River Delta.

We find that the FAR of such events over the Yangtze River Delta to the WPSH is relatively higher

than that to global warming. In a strong WPSH (often leading to the extreme heat), global warming will have a slightly larger role in increasing the likelihood of such events as the 2017 extreme heat than that in a weak WPSH. In ALL simulations (often leading to the extreme heat), the role of the WPSH is also slightly higher than that in NAT runs. These results above further imply that both global warming and the WPSH will increase the likelihood of such events as the 2017 extreme heat over the Yangtze River Delta.

ACKNOWLEDGMENTS. This study was funded by the National Key R&D Program of China (2017YFA0603601) and the National Natural Science Foundation of China (41525018). Dan Qi was supported by the National Natural Science Foundation of China (41475044). The latest temperature data were obtained from the China Meteorological Administration (CMA; <http://data.cma.cn/>). Considerable gratitude is owed to several working teams, including the National Oceanic and Atmospheric Agency (NOAA) and the University of Colorado's Cooperative Institute for Research in Environmental Sciences (CIRES) for providing the atmospheric fields (www.esrl.noaa.gov/), the National Geophysical Data Centers of NOAA for providing stable nighttime light data (<http://ngdc.noaa.gov/eog/dmsp/>), the World Climate Research Programme's Working Group on Coupled Modelling (<http://cmip-pcmdi.llnl.gov/cmip5/>), and the Royal Netherlands Meteorological Institute (<https://climexp.knmi.nl/>) for the CMIP5 model output. Chunlue Zhou dedicates this in loving memory of his kind father and his heartwarming encouragement forever.

REFERENCES

- Chen, R., and R. Lu, 2015: Comparisons of the circulation anomalies associated with extreme heat in different regions of eastern China. *J. Climate*, **28**, 5830–5844, <https://doi.org/10.1175/JCLI-D-14-00818.1>.
- , Z. Wen, and R. Lu, 2016: Evolution of the circulation anomalies and the quasi-biweekly oscillations associated with extreme heat events in southern China. *J. Climate*, **29**, 6909–6921, <https://doi.org/10.1175/JCLI-D-16-0160.1>.
- Chen, X., and T. Zhou, 2017: Relative contributions of external SST forcing and internal atmospheric variability to July–August heat waves over the Yangtze River valley. *Climate Dyn.*, <https://doi.org/10.1007/s00382-017-3871-y>.
- Compo, G. P., and Coauthors, 2011: The Twentieth Century Reanalysis Project. *Quart. J. Roy. Meteor. Soc.*, **137**, 1–28, <https://doi.org/10.1002/qj.776>.

- Ding, T., W. Qian, and Z. Yan, 2010: Changes in hot days and heat waves in China during 1961–2007. *Int. J. Climatol.*, **30**, 1452–1462, <https://doi.org/10.1002/joc.1989>.
- Ding, Y., 1994: The summer monsoon in East Asia. *Monsoons over China*, Springer, 1–90.
- Dong, X., F. Fan, R. Lin, J. Jin, and R. Lian, 2017: Simulation of the western North Pacific subtropical high in El Niño decaying summers by CMIP5 AGCMs. *Atmos. Oceanic Sci. Lett.*, **10**, 146–155, <https://doi.org/10.1080/16742834.2017.1272404>.
- Du, Y., S.-P. Xie, G. Huang, and K. Hu, 2009: Role of air–sea interaction in the long persistence of El Niño–induced north Indian Ocean warming. *J. Climate*, **22**, 2023–2038, <https://doi.org/10.1175/2008JCLI2590.1>.
- Fischer, E., and C. Schär, 2010: Consistent geographical patterns of changes in high-impact European heatwaves. *Nat. Geosci.*, **3**, 398–403, <https://doi.org/10.1038/ngeo866>.
- Freychet, N., S. Tett, J. Wang, and G. Hegerl, 2017: Summer heat waves over eastern China: Dynamical processes and trend attribution. *Environ. Res. Lett.*, **12**, 024015, <https://doi.org/10.1088/1748-9326/aa5ba3>.
- He, C., and T. Zhou, 2015: Responses of the western North Pacific subtropical high to global warming under RCP4.5 and RCP8.5 scenarios projected by 33 CMIP5 models: The dominance of tropical Indian Ocean–tropical western Pacific SST gradient. *J. Climate*, **28**, 365–380, <https://doi.org/10.1175/JCLI-D-13-00494.1>.
- , —, and B. Wu, 2015a: The key oceanic regions responsible for the interannual variability of the western North Pacific subtropical high and associated mechanisms. *J. Meteor. Res.*, **29**, 562–575, <https://doi.org/10.1007/s13351-015-5037-3>.
- , —, A. Lin, B. Wu, D. Gu, C. Li, and B. Zheng, 2015b: Enhanced or weakened western North Pacific subtropical high under global warming? *Sci. Rep.*, **5**, 16771, <https://doi.org/10.1038/srep16771>.
- Hu, K., G. Huang, X. Qu, and R. Huang, 2012: The impact of Indian Ocean variability on high temperature extremes across the southern Yangtze River valley in late summer. *Adv. Atmos. Sci.*, **29**, 91–100, <https://doi.org/10.1007/s00376-011-0209-2>.
- , —, and R. Wu, 2013: A strengthened influence of ENSO on August high temperature extremes over the southern Yangtze River valley since the late 1980s. *J. Climate*, **26**, 2205–2221, <https://doi.org/10.1175/JCLI-D-12-00277.1>.
- Huang, R., and Y. Wu, 1989: The influence of ENSO on the summer climate change in China and its mechanism. *Adv. Atmos. Sci.*, **6**, 21–32, <https://doi.org/10.1007/BF02656915>.
- Kalnay, E., and Coauthors, 1996: The NCEP/NCAR 40-Year Reanalysis Project. *Bull. Amer. Meteor. Soc.*, **77**, 437–471, [https://doi.org/10.1175/1520-0477\(1996\)077<0437:TNYRP>2.0.CO;2](https://doi.org/10.1175/1520-0477(1996)077<0437:TNYRP>2.0.CO;2).
- Li, J., T. Ding, X. Jia, and X. Zhao, 2015: Analysis on the extreme heat wave over China around Yangtze River region in the summer of 2013 and its main contributing factors. *Adv. Meteor.*, **2015**, 706713, <https://doi.org/10.1155/2015/706713>.
- Li, R.-X., and J.-Q. Sun, 2018: Interdecadal variability of the large-scale extreme hot event frequency over the middle and lower reaches of the Yangtze River basin and its related atmospheric patterns. *Atmos. Ocean. Sci. Lett.*, **11**, 63–70, <https://doi.org/10.1080/16742834.2017.1335580>.
- Liu, G., R. Wu, S. Sun, and H. Wang, 2015: Synergistic contribution of precipitation anomalies over northwestern India and the South China Sea to high temperature over the Yangtze River Valley. *Adv. Atmos. Sci.*, **32**, 1255–1265, <https://doi.org/10.1007/s00376-015-4280-y>.
- Liu, Y., W. Li, W. Ai, and Q. Li, 2012: Reconstruction and application of the monthly western Pacific subtropical high indices. *J. Appl. Meteor. Sci.*, **23**, 414–423.
- Luo, M., and N.-C. Lau, 2017: Heat waves in southern China: Synoptic behavior, long-term change and urbanization effects. *J. Climate*, **30**, 703–720, <https://doi.org/10.1175/JCLI-D-16-0269.1>.
- Ren, G., and Coauthors, 2015: An integrated procedure to determine a reference station network for evaluating and adjusting urban bias in surface air temperature data. *J. Appl. Meteor. Climatol.*, **54**, 1248–1266, <https://doi.org/10.1175/JAMC-D-14-0295.1>.
- Russo, S., and Coauthors, 2014: Magnitude of extreme heat waves in present climate and their projection in a warming world. *J. Geophys. Res.*, **119**, 12 500–12 512, <https://doi.org/10.1002/2014JD022098>.
- Schaller, N., and Coauthors, 2016: Human influence on climate in the 2014 southern England winter floods and their impacts. *Nat. Climate Change*, **6**, 627–634, <https://doi.org/10.1038/nclimate2927>.
- Stone, D. A., and M. R. Allen, 2005: The end-to-end attribution problem: From emissions to impacts. *Climatic Change*, **71**, 303–318, <https://doi.org/10.1007/s10584-005-6778-2>.
- Sun, Y., X. Zhang, F. W. Zwiers, L. Song, H. Wan, T. Hu, H. Yin, and G. Ren, 2014: Rapid increase in the risk of extreme summer heat in eastern China. *Nat. Climate Change*, **4**, 1082–1085, <https://doi.org/10.1038/nclimate2410>.
- , —, G. Ren, F. W. Zwiers, and T. Hu, 2016: Contribution of urbanization to warming in China. *Nat. Climate Change*, **6**, 706–710, <https://doi.org/10.1038/nclimate2956>.

- Tan, J., Y. Zheng, L. Peng, S. Gu, and J. Shi, 2008: Effect of urban heat island on heat waves in summer of Shanghai. *Plateau Meteor.*, **27**, 144–149.
- Tao, S., and S. Xu, 1962: Circulation characteristics in association with persistent summer drought and flood in the Yangtze-Huaihe River reaches. *Acta Meteor. Sin.*, **32**, 1–18.
- Taylor, K. E., R. J. Stouffer, and G. A. Meehl, 2012: An overview of CMIP5 and the experiment design. *Bull. Amer. Meteor. Soc.*, **93**, 485–498, <https://doi.org/10.1175/BAMS-D-11-00094.1>.
- van der Wiel, K., and Coauthors, 2017: Rapid attribution of the August 2016 flood-inducing extreme precipitation in south Louisiana to climate change. *Hydrol. Earth Syst. Sci.*, **21**, 897–921, <https://doi.org/10.5194/hess-21-897-2017>.
- Wang, B., R. Wu, and X. Fu, 2000: Pacific–East Asian teleconnection: How does ENSO affect East Asian climate? *J. Climate*, **13**, 1517–1536, [https://doi.org/10.1175/1520-0442\(2000\)013<1517:PEATHD>2.0.CO;2](https://doi.org/10.1175/1520-0442(2000)013<1517:PEATHD>2.0.CO;2).
- Wang, J., Z. Yan, X.-W. Quan, and J. Feng, 2017: Urban warming in the 2013 summer heat wave in eastern China. *Climate Dyn.*, **48**, 3015–3033, <https://doi.org/10.1007/s00382-016-3248-7>.
- Wang, K., and R. E. Dickinson, 2013: Contribution of solar radiation to decadal temperature variability over land. *Proc. Natl. Acad. Sci. USA*, **110**, 14 877–14 882, <https://doi.org/10.1073/pnas.1311433110>.
- , S. Jiang, J. Wang, C. Zhou, X. Wang, and X. Lee, 2017: Comparing the diurnal and seasonal variabilities of atmospheric and surface urban heat islands based on the Beijing urban meteorological network. *J. Geophys. Res.*, **122**, 2131–2154, <https://doi.org/10.1002/2016JD025304>.
- Wang, W., W. Zhou, and D. Chen, 2014: Summer high temperature extremes in southeast China: Bonding with the El Niño–Southern Oscillation and East Asian summer monsoon coupled system. *J. Climate*, **27**, 4122–4138, <https://doi.org/10.1175/JCLI-D-13-00545.1>.
- , —, X. Li, X. Wang, and D. Wang, 2016: Synoptic-scale characteristics and atmospheric controls of summer heat waves in China. *Climate Dyn.*, **46**, 2923–2941, <https://doi.org/10.1007/s00382-015-2741-8>.
- Wu, B., T. Zhou, and T. Li, 2009: Seasonally evolving dominant interannual variability modes of East Asian climate. *J. Climate*, **22**, 2992–3005, <https://doi.org/10.1175/2008JCLI2710.1>.
- , T. Li, and T. Zhou, 2010: Relative contributions of the Indian Ocean and local SST anomalies to the maintenance of the western North Pacific anomalous anticyclone during the El Niño decaying summer. *J. Climate*, **23**, 2974–2986, <https://doi.org/10.1175/2010JCLI3300.1>.
- Xie, S.-P., K. Hu, J. Hafner, H. Tokinaga, Y. Du, G. Huang, and T. Sampe, 2009: Indian Ocean capacitor effect on Indo–western Pacific climate during the summer following El Niño. *J. Climate*, **22**, 730–747, <https://doi.org/10.1175/2008JCLI2544.1>.
- Yang, H., and C. Li, 2005: Diagnostic study of serious high temperature over south China in 2003 summer. *Climate Environ. Res.*, **10**, 80–85.
- Yang, J., Q. Liu, S. P. Xie, Z. Liu, and L. Wu, 2007: Impact of the Indian Ocean SST basin mode on the Asian summer monsoon. *Geophys. Res. Lett.*, **34**, L02708, <https://doi.org/10.1029/2006GL028571>.
- Zhou, C., and K. Wang, 2016: Biological and environmental controls on evaporative fractions at AmeriFlux sites. *J. Appl. Meteor. Climatol.*, **55**, 145–161, <https://doi.org/10.1175/JAMC-D-15-0126.1>.
- , Y. He, and K. Wang, 2018a: On the suitability of current atmospheric reanalyses for regional warming studies over China. *Atmos. Chem. Phys.*, **18**, 8113–8136, <https://doi.org/10.5194/acp-18-8113-2018>.
- , K. Wang, and D. Qi, 2018b: Attribution of the July 2016 extreme precipitation event over China's Wuhang [in “Explaining Extreme Events of 2016 from a Climate Perspective”]. *Bull. Amer. Meteor. Soc.*, **99**, S107–S112, <https://doi.org/10.1175/BAMS-D-17-0090.1>.
- Zhou, T., and Z. Li, 2002: Simulation of the East Asian summer monsoon using a variable resolution atmospheric GCM. *Climate Dyn.*, **19**, 167–180, <https://doi.org/10.1007/s00382-001-0214-8>.
- , and Coauthors, 2009: Why the western Pacific subtropical high has extended westward since the late 1970s. *J. Climate*, **22**, 2199–2215, <https://doi.org/10.1175/2008JCLI2527.1>.
- , S. Ma, and L. Zou, 2014: Understanding a hot summer in central eastern China: Summer 2013 in context of multimodel trend analysis [in “Explaining Extreme Events of 2013 from a Climate Perspective”]. *Bull. Amer. Meteor. Soc.*, **95**, S54–S57, <https://doi.org/10.1175/1520-0477-95.9.S1.1>.

THE ROLE OF NATURAL VARIABILITY AND ANTHROPOGENIC CLIMATE CHANGE IN THE 2017/18 TASMAN SEA MARINE HEATWAVE

S. E. PERKINS-KIRKPATRICK, A. D. KING, E. A. COUGNON, M. R. GROSE, E. C. J. OLIVER,
N. J. HOLBROOK, S. C. LEWIS, AND F. POURASGHAR

Two GCM ensembles indicate that the record sea surface temperatures during the 2017/18 Tasman Sea marine heatwave were virtually impossible without anthropogenic influence. However, natural variability was important in the atmospheric initiation of the event.

CLIMATOLOGICAL CONTEXT. Commencing in November 2017, a marine heatwave (MHW) developed over a very large area extending from west of Tasmania to east of New Zealand (ABoM and NIWA 2018). However, unlike in 2015/16, which was due largely to intensification of the southward transport in the East Australian Current Extension (Oliver et al. 2017) and mainly localized along the southeast Australian coast, the 2017/18 event was more closely tied with local air–sea heat fluxes (see the online supplemental material). The 2017/18 event was more

widespread compared to the 2015/16 event, including covering the entire Tasman Sea. Moreover, the mixed layer depth in the Tasman Sea was at a record shallow level during the 2017/18 event, allowing for very warm SSTs to develop, whereas during the 2015/16 event this depth was close to average. Coincident with the MHW was New Zealand’s hottest summer on record, and Tasmania’s hottest November on record (ABoM and NIWA 2018). Figure ES1 in the online supplemental material demonstrates that the 2015/16 event was the longest (308 days) and the 2017/18 event was the most intense (2.5° vs 1.8°C maximum intensity).

Based on remotely sensed sea surface temperatures (SSTs) available back to 1982, and application of the MHW definition developed by Hobday et al. (2016), this surface-intensified MHW was the most intense (maximum intensity of 2.5°C above climatology) and second-longest on record (221 days between October 2017 to April 2018) for the region of interest (see the methods section and the online supplemental material). The event was also remarkable in that most of the event warming was confined to shallow depths (<30 m), in particular around the western Tasman Sea. Unlike the 2015/16 southeast Australia MHW, which warmed through the water column to at least 100–200-m depth (Oliver et al. 2017), we note that the 2017/18 event deepened below 30-m depth in mid-December in the western Tasman Sea, but always remained <100 m for this area. The event coincided with another outbreak of Pacific Oyster Mortality Syndrome, caused by a virus in the Pacific oyster exacerbated by temperature stress (see Green et al. 2014; Ugalde et al. 2018).

During November 2017, mean sea level pressure (MSLP) was persistently high in the Tasman Sea

AFFILIATIONS: PERKINS-KIRKPATRICK—Climate Change Research Centre, and ARC Centre of Excellence for Climate Extremes, University of New South Wales, Sydney, Australia; KING—ARC Centre of Excellence for Climate System Science, and School of Earth Sciences, University of Melbourne, Melbourne, Australia; COUGNON AND HOLBROOK—Institute for Marine and Antarctic Studies, and ARC Centre of Excellence for Climate Extremes, University of Tasmania, Hobart, Tasmania, Australia; GROSE—CSIRO Oceans and Atmosphere, Hobart, Tasmania, Australia; OLIVER—Department of Oceanography, Dalhousie University, Halifax, Nova Scotia, Canada; LEWIS—ARC Centre of Excellence for Climate System Science, University of Melbourne, Melbourne, and Australian National University, Canberra, ACT, Australia; POURASGHAR—Institute for Marine and Antarctic Studies, and ARC Centre of Excellence for Climate System Science, University of Tasmania, Hobart, Tasmania, Australia

CORRESPONDING AUTHOR: Sarah Perkins-Kirkpatrick, sarah.kirkpatrick@unsw.edu.au

DOI:10.1175/BAMS-D-18-0116.1

A supplement to this article is available online (10.1175/BAMS-D-18-0116.2)

© 2019 American Meteorological Society

For information regarding reuse of this content and general copyright information, consult the [AMS Copyright Policy](#).

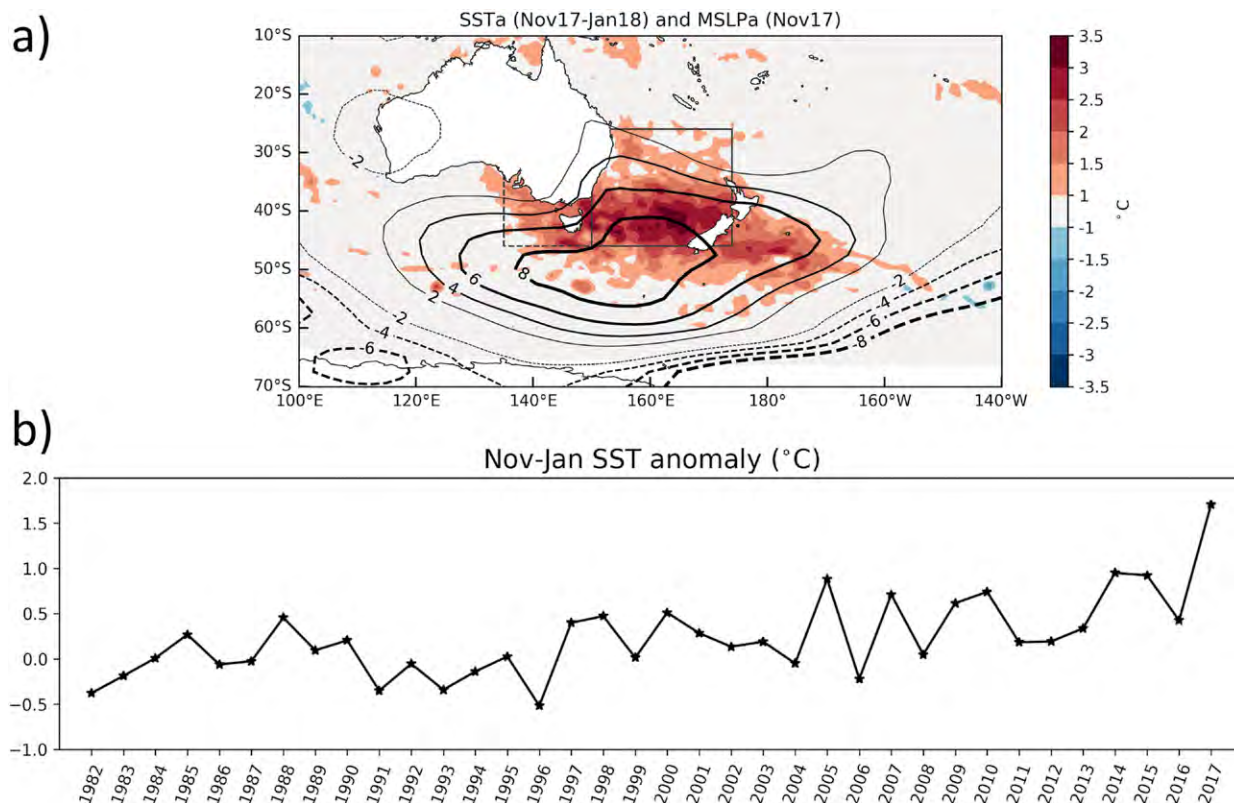


FIG. 1. (a) Average sea surface temperature anomalies from November 2017 to January 2018 (colors), and November mean sea level pressure anomalies (solid and dashed contours), relative to the background climatology from 1961–90. The Tasman Sea region is indicated by the solid box, with the western extension indicated by the dotted box. (b) Time series of regionally averaged November–January SST anomalies based on the daily NOAA OI SST v2 gridded dataset. For details on how the SST anomalies were calculated in NOAA OI SST relative to 1961–90, please see Oliver et al. (2017, 2018a).

(Fig. 1a). Although the driving atmospheric pattern ceased at the end of November 2017, warm SSTs persisted well into 2018 (ABoM and NIWA 2018). This very high atmospheric pressure initiated the event, which persisted under strong atmospheric blocking (Pook and Gibson 1999) and brought clear skies and weak winds conducive to intense ocean surface warming for a number of weeks (ABoM and NIWA 2018). An atmospheric heatwave also occurred during the third week of November 2017, which most likely generated strong atmosphere–ocean heat fluxes into the near-surface layer of the ocean. Given the atmospheric priming of the MHW, it is of interest to determine whether there is an anthropogenic signal behind the setup, and the resulting SST signature. Using two different general circulation model (GCM) ensembles, we demonstrate a substantial anthropogenic influence on the record magnitude of the Tasman MHW, as well as a continually significant role of climate variability on the underpinning atmospheric mechanisms.

DATA AND METHODS. For the SST analysis, we define our region as the Australian Bureau of Meteorology’s Tasman Sea region (26°–46°S, 150°–174°E), but with the western boundary extended westward to 135°E to also include the observed warming off Tasmania’s west coast (see Fig. 1a). We analyzed monthly average SST anomalies from November 2017 to January 2018 (Fig. 1a). We employed the daily NOAA OI SST v2 0.25° gridded dataset, which spans 1982–2018 (Banzon et al. 2016), and monthly HadISST 1° gridded data (Kennedy et al. 2011a,b), which span 1871–2017. Following Oliver et al. (2017, 2018a), we applied a correction to the OI SST anomalies so that they are referenced to a 1961–90 baseline. Based on this calculation, the average SST anomaly for the Tasman region over November 2017–January 2018 was +1.70°C. This is the hottest November–January anomaly since at least the start of our SST series (Fig. 1b).

Thresholds for November MSLP and the monthly mean blocking index (BI; see the supplemental material) were calculated from NCEP–NCAR Reanalysis

(NCEP1) data (Kalnay et al. 1996). We note that shortcomings in NCEP1 have been characterized in previous studies (e.g., Angéil et al. 2018). However, at the time of writing, no other reanalysis product included published data to the end of 2017, which also dated back to pre-1979. During November, the respective BI and MSLP anomalies of 15.5 m s^{-1} and $+5.2 \text{ hPa}$ relative to 1961–90 were computed for 150°E and the smaller Tasman Sea region (26° – 46°S , 150° – 174°E).

Our analysis employed two GCM model ensembles. The Community Earth System Model (CESM) Large Ensemble (see supplemental material and Kay et al. 2015), where skin temperature (TS; a proxy for SST), MSLP and the zonal wind at 500 hPa (U500; from which the BI was computed), were extracted and relevant monthly anomalies for each simulation against 1961–90 were calculated and averaged. Eight CMIP5 models were utilized (see the supplemental material; Taylor et al. 2012) for the analysis of monthly anomalies of SST and MSLP, calculated against each model's historical 1961–90 period.

Using two GCM ensembles allows for a more robust attribution statement. CMIP5 provides an estimate of human influence accounting for differences across various models, such as climate sensitivity, model physics and parameterization schemes, and resolution. The large ensemble of CESM provides an estimate accounting for the influence of internal variability. We initially performed a standard fraction of attributable risk (FAR) analysis (Allen 2003) for each variable, based on the observed and reanalysis anomalies defined above. For each period, 10,000 FAR values were calculated by bootstrapping with replacement of 50% of the relative ensemble sample size. However, given the rarity of the Tasman Sea MHW and the initiating synoptic system (see the results section), a FAR analysis did not produce much useful information. SST FAR values yielded 1, due to the non-occurrence of the Tasman MHW in the relative HistoricalNat and Control simulations. We therefore present the likelihood of extreme SSTs and MSLP and BI values exceeding those of the 2017/18 event showing best estimate values based on all available model data.

RESULTS. Figure 2 shows the observed and modeled probability density functions (PDFs) of November–January SST/TS and November MSLP anomalies for the natural and current (2008–27 under RCP8.5 simulations) worlds. Especially for SST/TS, there is a clear shift in the PDFs (Fig. 2a) toward much warmer conditions under anthropogenic forcing in both model ensembles. MSLP (Fig. 2b) shows a slight shift toward more positive conditions. Figure 2c displays

the changes in likelihood in SST/TS, MSLP, and BI. According to both ensembles, the overall intensity of the 2017/18 Tasman MHW could not have occurred without anthropogenic influences: the observed anomaly did not occur within the CESM control experiment, or any of the CMIP5 HistoricalNat simulations. This is a much stronger signal than that detected for many atmospheric heatwaves (e.g., Otto et al. 2012; Lewis and Karoly 2013; Christidis et al. 2015). Moreover, according to CMIP5 (CESM) the overall magnitude of the Tasman Sea MHW had very little (no) chance of occurring under current anthropogenic influence, highlighting the remarkable and extreme nature of the observed event. In the case of CESM, the response to anthropogenic forcing is not enough during the current period (or until at least 2035) to simulate the intensity of the Tasman MHW. This could be due to CESM's climate sensitivity, its ocean–atmosphere coupling strength, the exclusion of key but unknown features of marine heatwaves, or a range of other reasons that should be explored in further research. The event is projected to become much more frequent by the middle of the century, increasing to a 41% (56%) chance in the period 2041–60 under the CMIP5 (CESM) high-emissions scenario, where both model ensembles experience more rapid increases in SSTs compared to earlier time periods. MHWs like the Tasman Sea event are also significantly more likely under the Paris 1.5° and 2°C global warming targets. It is worth noting that natural climate variability would have played a key role in the general occurrence of this MHW; that is, while we find that anthropogenic climate change was critical in increasing the likelihood of the event intensity, it was unlikely to be wholly responsible. Other, less intense, Tasman Sea MHWs would still occur naturally in the absence of anthropogenic influence.

The influence of climate variability is embedded in our analysis of MSLP and BI associated with this MHW. The MSLP anomaly slightly increases in likelihood in CESM to 1% and 3% in the current and future climates. There is even less change in CMIP5, with the observed anomaly not occurring under natural conditions, and only increasing to 1% under the current and all future climates. However, the respective forced and unforced MSLP PDFs are statistically significantly different, indicating a small but detectable change toward higher MSLP under enhanced greenhouse warming. The observed November BI in CESM displays a doubling in frequency between the control and current and future climates, with likelihoods of 3% and 6%. Although the observed MSLP anomaly

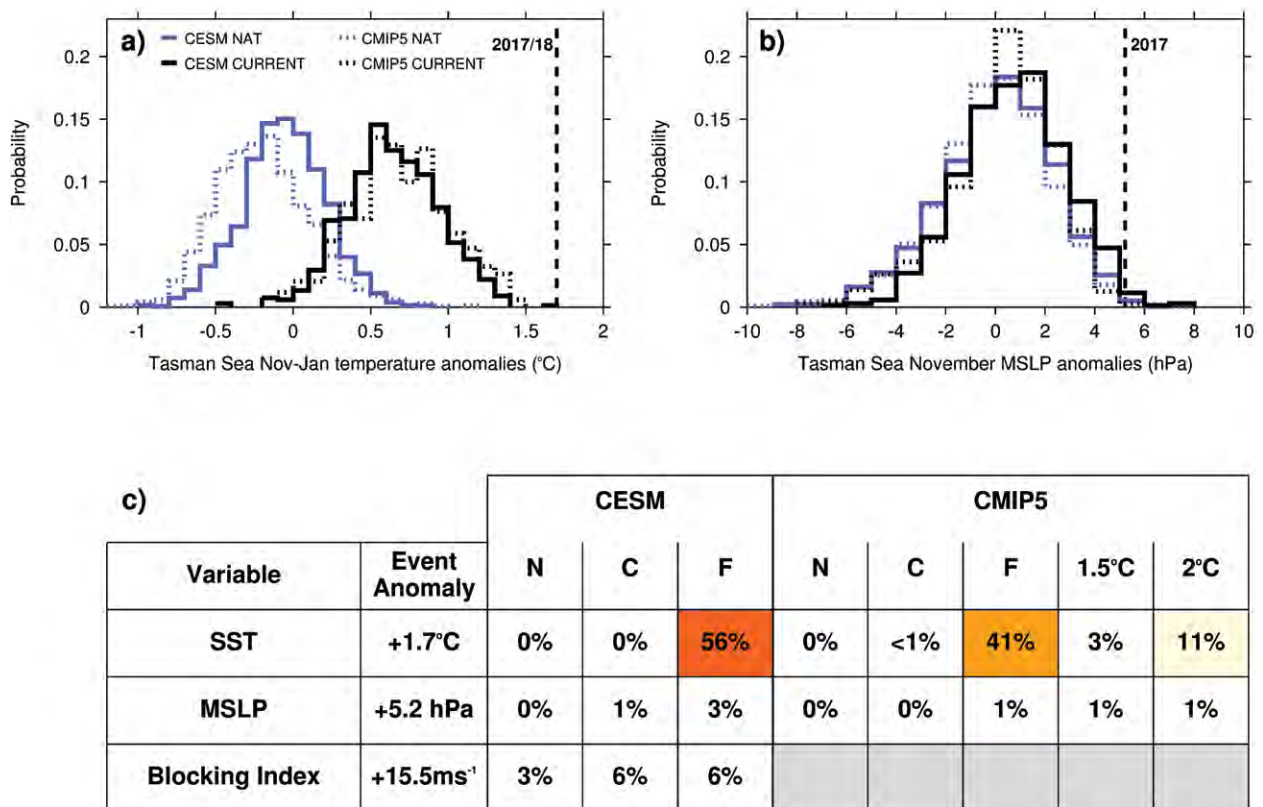


FIG. 2. Probability distributions of (a) November–January SST anomalies and (b) November MSLP anomalies over the Tasman Sea in the natural (blue) and current world (black) ensembles for both CESM (solid lines) and CMIP5 (dashed). The 2017 event is marked by a vertical dashed line. (c) Event likelihoods (best estimates), based on the SST, MSLP, and BI values associated with the event, under the natural (N) and current-world (C) ensembles, a future high-emissions world of 2050 (F), a 1.5°C world, and a 2°C world in CESM and CMIP5.

is still quite rare in the current and future periods, the measured anthropogenic influence underpinning MSLP is consistent with prior research that Southern Hemisphere pressure is tending toward a positive phase in the Southern annular mode (SAM; Gillett et al. 2013; Gillett and Fyfe 2013). A positive SAM results in anomalously high pressure over southern Australia during summer, analogous to that observed in Fig. 1. While both changes in stratospheric ozone and increases in greenhouse gases contribute to this trend, greenhouse gases will likely dominate under a high-emissions scenario (Swart and Fyfe 2012), as used here. Evidence from our analysis suggests that, while detectable, the anthropogenic influence on the initiating atmospheric pressure system is substantially less than for the record SSTs experienced during the Tasman Sea MHW. This indicates the considerable influence that climate variability has, and will continue to have, on MHWs in the Tasman Sea.

Moreover, evidence from our analysis suggests that the regional blocking aspect of the atmospheric setup was also made more likely due to human influences,

although this is also still quite rare under current and future climates.

CONCLUSIONS. Results from two GCM ensembles, which collectively strengthen the robustness of our attribution statement, indicate that the overall intensity of the 2017/18 Tasman MHW was virtually impossible without anthropogenic forcing. Both ensembles agree that events of similar magnitude dramatically increase in likelihood (become more common) in the current and especially future climates. Moreover, the fact that CESM does not simulate the intensity of the 2017/18 Tasman MHW under current levels of atmospheric greenhouse gases illustrates how unusual the event was. There is some evidence from CESM that the likelihood of the initiating surface atmospheric pressure system has also increased due to climate change, but to a lesser extent than the MHW itself. Moreover, the atmospheric blocking that was responsible for the prolonged period of high MSLP (which in turn induced SST warming) also displays some anthropogenic influence, although this detected influence is also less than that on the SST

signature. Thus, climate variability has an ongoing important role in the physical setup of Tasman Sea MHWs, which are initiated by atmospheric processes.

We therefore conclude that the majority of the anthropogenic influence on the 2017/18 Tasman MHW is embedded in the overall rising background SSTs due to global ocean warming, with a small amount of influence also on the event-initiating sea level pressure.

ACKNOWLEDGMENTS. S.E.P.-K. is supported by an Australian Research Council (ARC) Future Fellowship (Grant FT170100106). A.D.K. is supported by the ARC Centre of Excellence for Climate System Science (Grant CE110001028) and ARC DECRA (Grant DE180100638). S.C.L. is supported by an ARC DECRA (Grant DE160100092). F.P. is grateful for support from the ARC Centre of Excellence for Climate System Science (Grant CE110001028). E.A.C. and M.R.G. are supported by the Australian Government's National Environmental Science Program under the Earth Systems and Climate Change Hub. N.J.H. acknowledges funding from the ARC Centre of Excellence for Climate Extremes (Grant CE170100023).

REFERENCES

- ABoM and NIWA, 2018: Special climate statement—Record warmth in the Tasman Sea, New Zealand and Tasmania. Special Climate Statement 64, Australian Bureau of Meteorology and National Institute of Water and Atmospheric Research, 16 pp. www.bom.gov.au/climate/current/statements/scs64.pdf.
- Allen, M., 2003: Liability for climate change. *Nature*, **421**, 891–892, <https://doi.org/10.1038/421891a>.
- Angéilil, O., and Coauthors, 2018: On the nonlinearity of spatial scales in extreme weather attribution statements. *Climate Dyn.*, **50**, 2739–2752, <https://doi.org/10.1007/s00382-017-3768-9>.
- Banzon, V., T. M. Smith, T. M. Chin, C. Liu, and W. Hankins, 2016: A long-term record of blended satellite and in situ sea-surface temperature for climate monitoring, modeling and environmental studies. *Earth Syst. Sci. Data*, **8**, 165–176, <https://doi.org/10.5194/essd-8-165-2016>.
- Christidis, N., G. S. Jones, and P. A. Stott, 2015: Dramatically increasing chance of extremely hot summers since the 2003 European heatwave. *Nat. Climate Change*, **5**, 46–50, <https://doi.org/10.1038/nclimate2468>.
- Gillett, N. P., and J. C. Fyfe, 2013: Annular mode changes in the CMIP5 simulations. *Geophys. Res. Lett.*, **40**, 1189–1193, <https://doi.org/10.1002/grl.50249>.
- , —, and D. E. Parker, 2013: Attribution of observed sea level pressure trends to greenhouse gas, aerosol, and ozone changes. *Geophys. Res. Lett.*, **40**, 2302–2306, <https://doi.org/10.1002/grl.50500>.
- Green, T. J., C. Montagnani, K. Benkendorff, N. Robinson, and P. Speck, 2014: Ontogeny and water temperature influences the antiviral response of the Pacific oyster, *Crassostrea gigas*. *Fish Shellfish Immunol.*, **36**, 151–157, <https://doi.org/10.1016/j.fsi.2013.10.026>.
- Hobday, A. J., and Coauthors, 2016: A hierarchical approach to defining marine heatwaves. *Prog. Oceanogr.*, **141**, 227–238, <https://doi.org/10.1016/j.pocean.2015.12.014>.
- Kalnay, E., and Coauthors, 1996: The NCEP/NCAR 40-Year Reanalysis Project. *Bull. Amer. Meteor. Soc.*, **77**, 437–471, [https://doi.org/10.1175/1520-0477\(1996\)077<0437:TNYRP>2.0.CO;2](https://doi.org/10.1175/1520-0477(1996)077<0437:TNYRP>2.0.CO;2).
- Kay, J. E., and Coauthors, 2015: The Community Earth System Model (CESM) large ensemble project: A community resource for studying climate change in the presence of internal climate variability. *Bull. Amer. Meteor. Soc.*, **96**, 1333–1349, <https://doi.org/10.1175/BAMS-D-13-00255.1>.
- Kennedy, J. J., N. A. Rayner, R. O. Smith, D. E. Parker, and M. Saunby, 2011a: Reassessing biases and other uncertainties in sea surface temperature observations measured in situ since 1850: 1. Measurement and sampling uncertainties. *J. Geophys. Res.*, **116**, D14103, <https://doi.org/10.1029/2010JD015218>.
- , —, —, —, and —, 2011b: Reassessing biases and other uncertainties in sea surface temperature observations measured in situ since 1850: 2. Biases and homogenization. *J. Geophys. Res.*, **116**, D14104, <https://doi.org/10.1029/2010JD015220>.
- King, A. D., D. J. Karoly, and B. J. Henley, 2017: Australian climate extremes at 1.5°C and 2°C of global warming. *Nat. Climate Change*, **7**, 412, <https://doi.org/10.1038/nclimate3296>.
- Lewis, S. C., and D. J. Karoly, 2013: Anthropogenic contributions to Australia's record summer temperatures of 2013. *Geophys. Res. Lett.*, **40**, 3705–3709, <https://doi.org/10.1002/grl.50673>.
- Oliver, E. C., J. A. Benthuisen, N. L. Bindoff, A. J. Hobday, N. J. Holbrook, C. N. Mundy, and S. E. Perkins-Kirkpatrick, 2017: The unprecedented 2015/16 Tasman Sea marine heatwave. *Nat. Commun.*, **8**, 16101, <https://doi.org/10.1038/ncomms16101>.
- , S. E. Perkins-Kirkpatrick, N. J. Holbrook, and N. L. Bindoff, 2018a: Anthropogenic and natural influences on record 2016 marine heat waves [in “Explaining Extreme Events of 2016 from a Climate Perspective”]. *Bull. Amer. Meteor. Soc.*, **99** (1), S44–S48, <https://doi.org/10.1175/BAMS-D-17-0093.1>.

- , V. Lago, A. J. Hobday, N. J. Holbrook, S. D. Ling, and C. N. Mundy, 2018b: Marine heatwaves off eastern Tasmania: Trends, interannual variability, and predictability. *Prog. Oceanogr.*, **161**, 116–130, <https://doi.org/10.1016/j.pocean.2018.02.007>.
- Otto, F. E., N. Massey, G. J. van Oldenborgh, R. G. Jones, and M. R. Allen, 2012: Reconciling two approaches to attribution of the 2010 Russian heat wave. *Geophys. Res. Lett.*, **39**, L04702, <https://doi.org/10.1029/2011GL050422>.
- Pook, M. J., and T. T. Gibson, 1999: Atmospheric blocking and storm tracks during SOP-1 of the FROST Project. *Aust. Meteor. Mag.*, **48**, 51–60.
- Swart, N. C., and J. C. Fyfe, 2012: Observed and simulated changes in the Southern Hemisphere surface westerly wind-stress. *Geophys. Res. Lett.*, **39**, L16711, <https://doi.org/10.1029/2012GL052810>.
- Taylor, K. E., R. J. Stouffer, and G. A. Meehl, 2012: An overview of CMIP5 and the experiment design. *Bull. Amer. Meteor. Soc.*, **93**, 485–498, <https://doi.org/10.1175/BAMS-D-11-00094.1>.
- Ugalde, S. C., J. Preston, E. Ogier, and C. Crawford, 2018: Analysis of farm management strategies following herpesvirus (OsHV-1) disease outbreaks in Pacific oysters in Tasmania, Australia. *Aquaculture*, **495**, 179–186, <https://doi.org/10.1016/j.aquaculture.2018.05.019>.

ON DETERMINING THE IMPACT OF INCREASING ATMOSPHERIC CO₂ ON THE RECORD FIRE WEATHER IN EASTERN AUSTRALIA IN FEBRUARY 2017

PANDORA HOPE, MITCHELL T. BLACK, EUN-PA LIM, ANDREW DOWDY, GUOMIN WANG,
ACACIA S. PEPLER, AND ROBERT J. B. FAWCETT

February 2017 saw a broad region with record fire weather across central-eastern Australia. A hybrid attribution technique using modified observations and a seasonal forecast framework did not give a clear signal as to the influence of increasing atmospheric CO₂ on the fire weather.

INTRODUCTION. Studies of the climate change influence on the potential for wildfires (bushfires, as they are called in Australia) require an association to be made between meteorological and land surface metrics and wildfire risk factors such as fire weather conditions, fuel conditions, and ignition factors, as well as fire behavior, severity, or extent. Some studies assess the availability and dryness of the fuel or proxies thereof (Nicholls and Lucas 2007; Yoon et al. 2015; Partain et al. 2016; Abatzoglou and Williams 2016). Aspects of the weather of relevance to the potential for fire have also been assessed, including the intensity of fronts or the dryness of the air (Hasson et al. 2009; Grose et al. 2014; Tett et al. 2018). All of these studies found an enhancement of the potential fire danger in some regions due to ongoing climate change.

The McArthur Forest Fire Danger Index (FFDI) (McArthur 1967) combines an estimate of fuel dryness and the relevant weather features and is commonly used to describe wildfire danger in Australia (Clarke et al. 2013; Dowdy et al. 2010). Such a combined metric has not been used in an event attribution study before. Recently, a gridded FFDI dataset has been developed using winds from reanalyses

with observed rainfall and temperature for 1950 to the present (Dowdy 2018). Using this new dataset and an established event attribution technique using a seasonal forecast framework (Wang et al. 2016; Hope et al. 2016) we aim to estimate the influence of increasing levels of atmospheric CO₂ on the FFDI in eastern Australia.

THE EVENT. The first two weeks of February 2017 (late austral summer) saw unusually extreme widespread fire danger across central eastern Australia, particularly in northern New South Wales. “Eastern Australia” (east of 141°E, between 20° and 38°S) had the highest average FFDI for the first half of February in the record starting 1950 (Dowdy 2018). During this event the “Sir Ivan” fire burned 55,000 ha (www.abc.net.au/news/2017-08-16/nsw-fires-2017-sir-ivan-fire-recovery/8810284) through central northern New South Wales in fire weather conditions rated as “catastrophic” (FFDI equal to or greater than 100) by fire agencies (Fig. 1a). Intense pyrocumulonimbus was initiated by the fire, leading to subsequent fire ignition by lightning ahead of the main fire front. Extreme wildfire behavior such as this is very rare, with examples including Black Saturday in southeast Australia in 2009, the Fort McMurray fire in Alberta, Canada, in May 2016, and the Waroona fire in January 2016 in Western Australia (Ferguson 2016; Dowdy et al. 2017b). The 12 February 2017 was the highest observed daily estimate of FFDI averaged over eastern Australia for all days in the first two weeks of February. The second highest value was on 7 February 2009, Black Saturday. During this fortnight in 2017 there was no rainfall across most of the region and extremely high daily maximum temperatures (Fig. 1b), and low relative humidity (Fig. 1e).

AFFILIATIONS: HOPE, BLACK, LIM, DOWDY, WANG, AND FAWCETT—Bureau of Meteorology, Melbourne, Australia; PEPLER—Bureau of Meteorology, Sydney, Australia

CORRESPONDING AUTHOR: Pandora Hope, pandora.hope@bom.gov.au

DOI:10.1175/BAMS-D-18-0135.1

A supplement to this article is available online (10.1175/BAMS-D-18-0135.2)

© 2019 American Meteorological Society

For information regarding reuse of this content and general copyright information, consult the [AMS Copyright Policy](#).

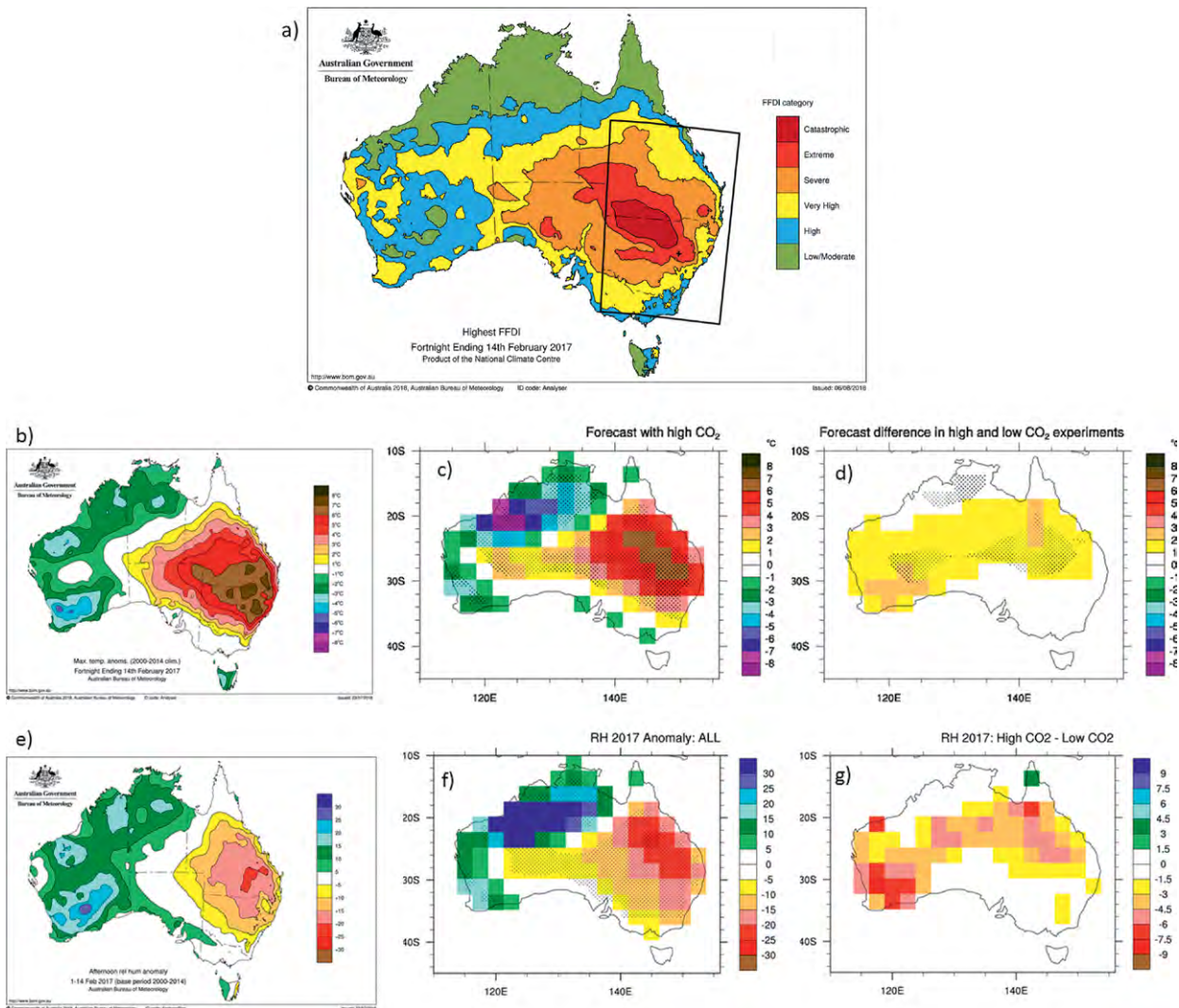


FIG. 1. (a) Observed maximum daily FFDI during 1–14 Feb 2017. The box indicates the region that defines the event and over which variables were averaged. The black dot indicates the region of the Sir Ivan fire. (b) Observed Tmax anomaly 1–14 Feb 2017 against a 2000–14 climatology (°C). (c) Forecast Tmax anomaly under current conditions; stippling indicates a significant difference from the 2000–14 mean, given the spread, at 10% level. (d) Current minus low-CO₂ anomaly. Stippling indicates a significant difference in the means, given the ensemble spread, at 10% level. (e)–(g) As in (b)–(d), but for relative humidity (%).

Prior to this period of intense fire risk, antecedent conditions were generally very dry, with many locations in the lowest 10% (decile 1) for accumulated rainfall totals since December. The summer had also been hot; New South Wales experienced its warmest summer on record, 2.56°C above the historical (1961–90) average (Bureau of Meteorology 2017).

There are known associations between large-scale climate drivers, such as ENSO, and fire risk (e.g., Black 2017). ENSO and the Indian Ocean dipole (IOD) were close to neutral during the summer of 2016/17. Indices in the preceding spring were in phases less favorable to summer extreme fire danger (Williams and Karoly 1999; Cai et al. 2009), as the

dipole mode index (www.bom.gov.au/climate/enso/indices.shtml?bookmark=iod) was negative and the Southern Oscillation index (SOI; www.bom.gov.au/climate/enso/soi/) indicated a weak La Niña, both of which are associated with increased rainfall over southeastern Australia (e.g., Risbey et al. 2009). For the subseasonal drivers, the southern annular mode (SAM; <https://legacy.bas.ac.uk/met/gjma/sam.html>) was negative in the preceding spring and the Madden–Julian oscillation was in phases 6 and 7 (www.bom.gov.au/climate/mjo/graphics/rmm.74toRealtime.txt). These phases are linked to dry conditions in central eastern Australia (Marshall et al. 2011; C. Lucas 2018, personal communication). Thus the large-

scale drivers were generally working against high fire danger conditions, although the phase of subseasonal drivers would have encouraged dry conditions.

METHOD. The event is defined as the record-breaking FFDI during 1–14 February 2017 over the east Australian region: east of 141°E, between 20° and 38°S. Below we describe a hybrid scheme used in an effort to assess the influence of increasing levels of atmospheric CO₂ on the intensity of this event.

The equation for the FFDI is as follows:

$$\text{FFDI} = 1.2753 \times \exp[0.987 \times \ln(\text{DF}) + 0.0338 \times \text{Tmax} + 0.0234 \times V - 0.0345 \times \text{RH}],$$

where Tmax is the daily maximum temperature (°C); RH is the afternoon (3 p.m.) relative humidity (%) calculated from the mixing ratio, mean sea level pressure, and temperature; and V is the afternoon (3 p.m.) 10-m wind speed (km h⁻¹) for each day of the first two weeks of February 2017. The drought factor (DF) represents a temporally accumulated antecedent soil moisture deficit derived from temperature and rainfall data from 20 days prior to the targeted fire danger period (Keetch and Byram 1968; Finkele et al. 2006).

The seasonal forecast attribution method of Wang et al. (2016) is used to assess the Tmax, RH, and wind during the first two weeks of February in the current and a low-CO₂ environment.

The seasonal forecast model, the Predictive Ocean Atmosphere Model for Australia version 2 (POAMA-2), was until recently the operational seasonal forecast system of the Australian Bureau of Meteorology. Using an observation-based DF means that the forecast can be initialized at shorter lead time (no need for the 20-day lead-in to calculate DF), and thus the forecasts are more likely to better reflect the weather associated with the event.

Eleven-member ensemble forecasts were initialized on 26 January with realistic atmosphere (including observed 2017 atmospheric CO₂ concentration of ~406 ppm), ocean, and land conditions, and verified for 1–14 February 2017. A second, low-CO₂, 11-member ensemble forecast was initialized with the same initial conditions, but from which the influence of the last 57 years of CO₂ increase was removed from the temperature and salinity through the full depth of the ocean (Fig. ES2 in the online supplemental material shows the sea surface temperature anomaly). Anomalies of change in the atmospheric temperature and humidity and also land surface temperature and soil moisture were also removed prior to initializa-

tion, following Wang et al. (2016). Atmospheric CO₂ was set to 1960 values (315 ppm). The very deep ocean might contain information from other anthropogenic forcing aside from CO₂; however, given the short lead time of the forecast used in this study, the CO₂ change will be the dominant factor.

The same forecast method was applied to create 11-member ensemble forecasts for the years 2000–14 to represent the climatology of the current climate. Atmospheric CO₂ was set to each year's value. The low-CO₂ climatology was created with starts from the same dates in 2000–14, but with the modifications used in the 2017 experiment to capture a low-CO₂ climate. CO₂ was set to 315 ppm.

For the calculation of the FFDI we developed a hybrid approach using observations to estimate the DF in the setup of a subseasonal forecast of the event. A hybrid approach was required because the forecast was good at the short lead time used, but lengthening the lead time to more than 20 days prior to the event to allow the calculation of the DF resulted in a poor forecast with this system.

The DF is calculated from observed [Australian Water Availability Project (AWAP); Jones et al. 2009] rainfall and temperature for the 20 days prior to the event and throughout the event. To account for the influence from increasing levels of atmospheric CO₂ on the DF, we apply a simple shift in the temperature data. Climate change has been shown to influence upward trends in southeast Australian daily maximum temperature (Tmax) (Karoly and Braganza 2005) and extreme heat events (Black and Karoly 2016). Observed Tmax trends since 1960 show an upward trend (Fig. ES1a), and, to account for natural variability, we choose a conservative estimate of 1°C to remove from the temperature in the low-CO₂ calculation of the FFDI. No change is applied to the precipitation as it is unclear on the direction of change in summer rainfall due to CO₂ increase (CSIRO and Bureau of Meteorology 2015), although there is a slight drying trend since 1960 (Fig. ES1b).

RESULTS. The POAMA2 forecast captured the hot and dry conditions well. For 1–14 February, the extreme heat across eastern Australia was well forecast in the current climate, with significant differences from the 2000–14 climatology at 10% level (Fig. 1c). The low-CO₂ Tmax was also well forecast when compared to the low-CO₂ climatology. Using the forecast attribution system, it was significantly warmer in the northern part of the region in the current climate compared to the same event in a low-CO₂ “1960” climate, but there was little change in the southern part of the region.

The observed relative humidity was low during this period across most of the region of interest (Fig. 1e), and it was also well forecast (Fig. 1f). The event in the current climate had lower RH than in a low-CO₂ climate in the north of the region. While the RH difference in the current minus low-CO₂ climate is large, the difference is not significant at the 10% level across the 11-member ensemble. Aspects of the wider circulation were less well forecast, but local westerly winds were evident in both the observed anomalies for the 2-week period and the forecasts, bringing dry inland air to the region of extreme FFDI (not shown).

Using the hybrid method to estimate the FFDI, the pattern is well forecast in the current climate (Fig. 2a) and reflects the observed interannual variability (Fig. ES3a). Early February 2017 had the highest FFDI anomaly compared to the climatology (Fig. ES3a). The very dry conditions captured by the observed rainfall component of the DF contributed to the high value of FFDI in 2017. The estimate of 2017 FFDI calculated with cooler temperatures and forecast in a low-CO₂ climate also reflects the observed anomaly pattern. The differences between the two estimates are small (Fig. ES3b), with strong overlap between the ensemble members.

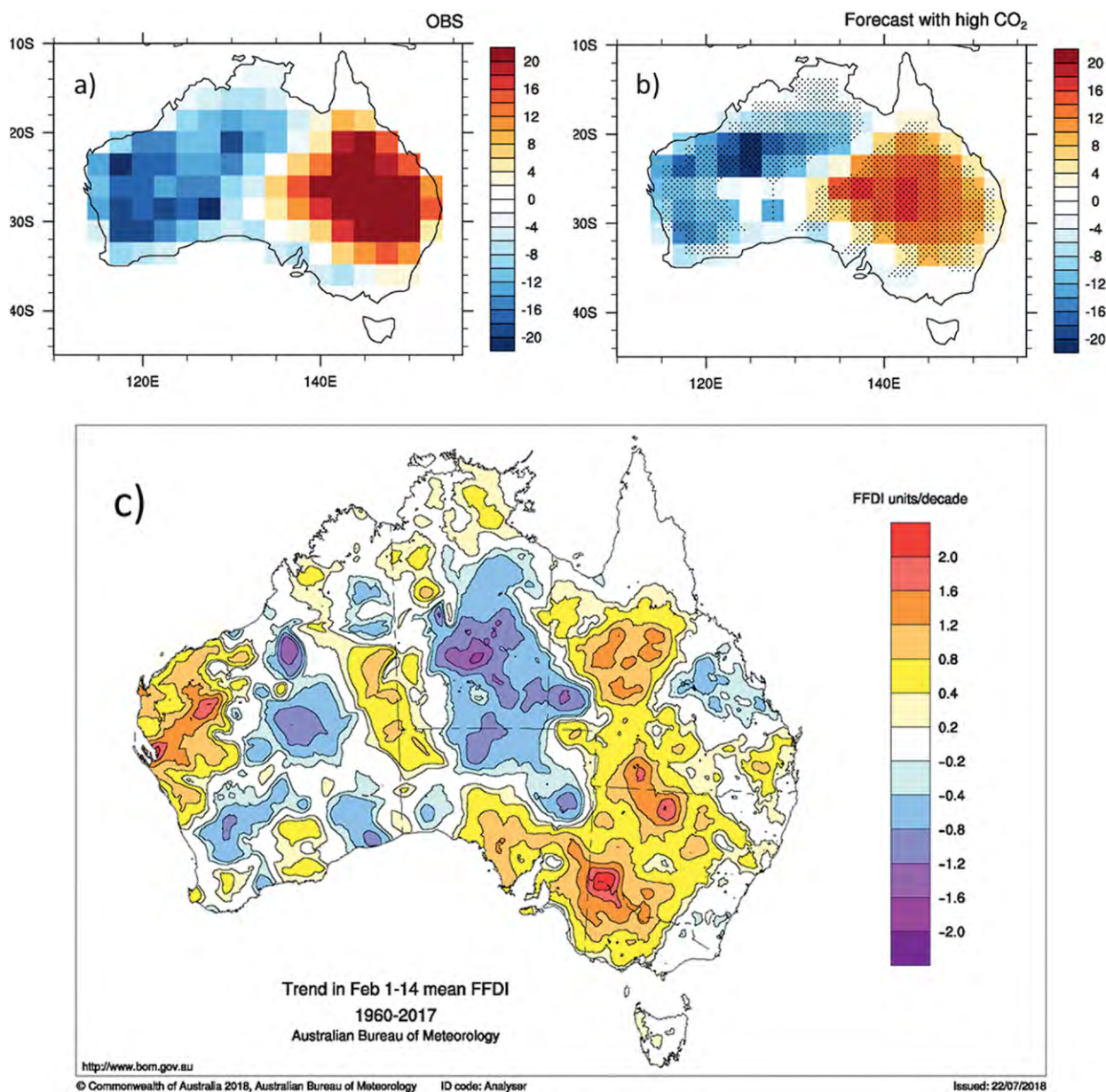


FIG. 2. (a) Observed averaged daily FFDI 1–14 Feb 2017 anomaly [Dowdy (2018) dataset; FFDI units] against a 2000–14 climatology. (b) Hybrid observed–POAMA forecast anomaly of the same event. (c) The observed linear trend 1960–2017 in observed estimated daily average FFDI (FFDI units per decade) for 1–14 Feb.

DISCUSSION. This extreme event occurred on the background of an upward trend in FFDI from 1960 to 2017 in the region (Fig. 2c). This might suggest that ongoing climate change is causing an increase in the potential for extreme fire danger in eastern Australia. However, observed trends can be influenced by other factors, including natural variability. In 2017, some measures of natural variability (ENSO and IOD) were not favoring high fire danger conditions, although the subseasonal drivers were.

Trends in some components of the FFDI metric have been attributed to increasing CO₂—notably Tmax (e.g., Williams et al. 2001). Our seasonal forecast experiments indicate that CO₂ caused an increase in Tmax in the north of the region during this particular event. Thus we can have some confidence that increasing Tmax enhanced FFDI values in the north of the region.

RH is also found to be lower for this event in the current climate than in the low-CO₂ climate in the north of the region, and thus the air was drier, although the spread across the forecast ensemble members was large. The wind was generally from the west in both the observations and forecasts, which would bring dry continental air toward the region. However, there was also large spread across the members and the timing and location of particular weather events. The magnitude of the (uncorrected) hybrid estimate of FFDI is smaller than the estimate from observations (Fig. ES3), and this is probably due to shortcomings in representing finescale features of the wind variation. Wind is difficult to include in metrics of fire danger, even for those built on observations (Lucas 2010; Clarke et al. 2013).

In developing a hybrid method to estimate the FFDI, we make assumptions about how temperature and rainfall have changed due to increasing levels of atmospheric CO₂. The change in temperature is reasonably clear, but the summer precipitation change can vary widely under future levels of CO₂ increase (CSIRO and Bureau of Meteorology 2015) and there have been no clear attribution studies of the February trends to date. The forecast precipitation from this experiment was drier through most of the region in the current climate compared to the low-CO₂ climate. Ideally, we would draw the DF from the forecast itself, if there was skill at 20 days lead time. This system did not have skill at that lead time for this event.

This preliminary study of attributing the record high fire risk fortnight to CO₂ change has produced some indication that increasing atmospheric CO₂ led to higher temperatures and reduced RH. Those factors would lead to enhanced fire danger. A full sensitivity

analysis of the importance of each component to the resultant FFDI would strengthen any statement that we might make using this system.

POAMA2, as part of the seasonal forecast attribution framework used here, has limitations in simulating the wind associated with this event, and has limited skill at lead times long enough to calculate the DF directly. A higher-resolution system forced with sea surface boundary conditions, weather@home for example (Black et al. 2016), might better represent the lead-in time required for the DF and the event itself (e.g., Black 2017). However, the ability to forecast the actual event in question is a major strength of an initialized system, particularly in an operational context. Some modeling groups already issue seasonal forecasts of fire risk indices (<https://cefa.dri.edu/CFS/fwi.php>). In Australia, a new operational seasonal forecast model with finer resolution has been shown to have skill in forecasting FFDI (Dowdy et al. 2017a). As forecast skill at longer lead time improves, the full FFDI can be calculated directly from model output, removing the need for a hybrid approach, and attribution statements could be made for extreme fire danger for every event that is well forecast.

ACKNOWLEDGMENTS. The authors received some funding from the Australian Government's National Environmental Science Programme. We would also like to thank Hua Ye for his assistance in producing the Drought Factor with a reduction of 1°C. We would also like to thank Robert Colman, Chris Lucas, and Lynette Bettio, who internally reviewed this study, our editor Stephanie Herring, and three anonymous reviewers for their helpful comments and suggestions that greatly improved this paper.

REFERENCES

- Abatzoglou, J. T., and A. P. Williams, 2016: Impact of anthropogenic climate change on wildfire across western US forests. *Proc. Natl. Acad. Sci. USA*, **113**, 11 770–11 775, <https://doi.org/10.1073/pnas.1607171113>.
- Black, M. T., 2017: An attribution study of southeast Australian wildfire risk. Ph.D. thesis. The University of Melbourne, 159 pp.
- , and D. J. Karoly, 2016: Southern Australia's warmest October on record: The role of ENSO and climate change [in "Explaining Extreme Events of 2015 from a Climate Perspective"]. *Bull. Amer. Meteor. Soc.*, **97** (12), S118–S121, <https://doi.org/10.1175/BAMS-D-16-0124.1>.
- , and Coauthors, 2016: The weather@home regional climate modelling project for Australia and New

- Zealand. *Geosci. Model Dev.*, **9**, 3161–3176, <https://doi.org/10.5194/gmd-9-3161-2016>.
- Bureau of Meteorology, 2017: Exceptional heat in south-east Australia in early 2017. Bureau of Meteorology Special Climate Statement, 61, 38 pp., www.bom.gov.au/climate/current/statements/scs61.pdf.
- Cai, W., T. Cowan, and M. Raupach, 2009: Positive Indian Ocean dipole events precondition southeast Australia bushfires. *Geophys. Res. Lett.*, **36**, L19710, <https://doi.org/10.1029/2009GL039902>.
- Clarke, H., C. Lucas, and P. Smith, 2013: Changes in Australian fire weather between 1973 and 2010. *Int. J. Climatol.*, **33**, 931–944, <https://doi.org/10.1002/joc.3480>.
- CSIRO, and Bureau of Meteorology, 2015: Climate Change in Australia—Information for Australia's Natural Resource Management Regions. Tech. Rep., CSIRO and Bureau of Meteorology, Australia, 216 pp., www.climatechangeinaustralia.gov.au/en/publications-library/technical-report/.
- Dowdy, A. J., 2018: Climatological variability of fire weather in Australia. *J. Appl. Meteor. Climatol.*, **57**, 221–234, <https://doi.org/10.1175/JAMC-D-17-0167.1>.
- , G. A. Mills, K. Finkele, and W. de Groot, 2010: Index sensitivity analysis applied to the Canadian Forest Fire Weather Index and the McArthur Forest Fire Danger Index. *Meteor. Appl.*, **17**, 298–312, <https://doi.org/10.1002/met.170>.
- , and Coauthors, 2017a: Extreme weather: Improved data products on bushfires, thunderstorms, tropical cyclones and east coast lows. M. Rumsewicz, Ed., *Research Forum 2017: Proceedings from the Research Forum at the Bushfire and Natural Hazards CRC & AFAC Conference*, Bushfire and Natural Hazards CRC, 7 pp., http://nesplclimate.com.au/wp-content/uploads/2016/03/AFAC2017-climate_extremes.pdf.
- , M. D. Fromm, and N. McCarthy, 2017b: Pyrocumulonimbus lightning and fire ignition on Black Saturday in southeast Australia. *J. Geophys. Res. Atmos.*, **122**, 7342–7354, <https://doi.org/10.1002/2017JD026577>.
- Ferguson, E., 2016: Reframing rural fire management: Report of the Special Inquiry into the January 2016 Waroona Fire. Government of Western Australia, 263 pp., <https://publicsector.wa.gov.au/document/reframing-rural-fire-management-report-special-inquiry-january-2016-waroon-fire>.
- Finkele, K., G. A. Mills, G. Beard, and D. A. Jones, 2006: National gridded drought factors and comparison of two soil moisture deficit formulations used in prediction of Forest Fire Danger Index in Australia. *Aust. Meteor. Mag.*, **55**, 183–197.
- Grose, M. R., P. Fox-Hughes, R. M. B. Harris, and N. L. Bindoff, 2014: Changes to the drivers of fire weather with a warming climate—A case study of southeast Tasmania. *Climatic Change*, **124**, 255–269, <https://doi.org/10.1007/s10584-014-1070-y>.
- Hasson, A. E. A., G. A. Mills, B. Timbal, and K. Walsh, 2009: Assessing the impact of climate change on extreme fire weather events over southeastern Australia. *Climate Res.*, **39**, 159–172, <https://doi.org/10.3354/cr00817>.
- Hope, P., G. Wang, E. P. Lim, H. H. Hendon, and J. M. Arblaster, 2016: What caused the record-breaking heat across Australia in October 2015? *Bull. Amer. Meteor. Soc.*, **97**, S122–S126, <https://doi.org/10.1175/BAMS-D-16-0141.1>.
- Jones, D. A., W. Wang, and R. Fawcett, 2009: High-quality spatial climate data-sets for Australia. *Aust. Meteor. Oceanogr. J.*, **58**, 233–248, <https://doi.org/10.22499/2.5804.003>.
- Karoly, D. J., and K. Braganza, 2005: A new approach to detection of anthropogenic temperature changes in the Australian region. *Meteor. Atmos. Phys.*, **89**, 57–67, <https://doi.org/10.1007/s00703-005-0121-3>.
- Keetch, J. J., and G. M. Byram, 1968: A drought index for forest fire control. U.S. Department of Agriculture, Forest Service, Southeastern Forest Experiment Station Res. Paper SE-38, 35 pp.
- Lucas, C., 2010: On developing a historical fire weather data-set for Australia. *Aust. Meteor. Oceanogr. J.*, **61**, 1–14, <https://doi.org/10.22499/2.6001.001>.
- Marshall, A. G., D. Hudson, M. C. Wheeler, H. H. Hendon, and O. Alves, 2011: Assessing the simulation and prediction of rainfall associated with the MJO in the POAMA seasonal forecast system. *Climate Dyn.*, **37**, 2129–2141, <https://doi.org/10.1007/s00382-010-0948-2>.
- McArthur, A., 1967: Fire behaviour in eucalypt forests. Leaflet No. 107, Department of National Development Forestry and Timber Bureau, Forest Research Institute, Canberra, 36 pp., <https://trove.nla.gov.au/work/21914760>.
- Nicholls, N., and C. Lucas, 2007: Interannual variations of area burnt in Tasmanian bushfires: Relationships with climate and predictability. *Int. J. Wildland Fire*, **16**, 540–546, <https://doi.org/10.1071/WF06125>.
- Partain, J. L., Jr., and Coauthors, 2016: An assessment of the role of anthropogenic climate change in the Alaska fire season of 2015 [in “Explaining Extreme Events of 2015 from a Climate Perspective”]. *Bull. Amer. Meteor. Soc.*, **97** (12), S14–S18, <https://doi.org/10.1175/BAMS-D-16-0149.1>.
- Risbey, J. S., M. J. Pook, P. C. McIntosh, M. C. Wheeler, and H. H. Hendon, 2009: On the remote drivers of rainfall variability in Australia. *Mon. Wea. Rev.*, **137**, 3233–3253, <https://doi.org/10.1175/2009MWR2861.1>.
- Tett, S. F. B., and Coauthors, 2018: Anthropogenic forcings and associated changes in fire risk in western

- North America and Australia during 2015/16 [in “Explaining Extreme Events of 2016 from a Climate Perspective”]. *Bull. Amer. Meteor. Soc.*, **99** (1), S60–S64, <https://doi.org/10.1175/BAMS-D-17-0096.1>.
- Wang, G., P. Hope, E.-P. Lim, H. H. Hendon, and J. M. Arblaster, 2016: Three methods for the attribution of extreme weather and climate events. Bureau of Meteorology Research Rep. 18, 31 pp., www.bom.gov.au/research/publications/researchreports/BRR-018.pdf.
- Williams, A. A. J., and D. J. Karoly, 1999: Extreme fire weather in Australia and the impact of the El Niño Southern Oscillation. *Aust. Meteor. Mag.*, **48**, 15–22.
- , D. J. Karoly, and N. Tapper, 2001: The sensitivity of Australian fire danger to climate change. *Climatic Change*, **49**, 171–191, <https://doi.org/10.1023/A:1010706116176>.
- Yoon, J. H., S.-Y. S. Wang, R. R. Gillies, L. Hipps, B. Kravitz, and P. J. Rasch, 2015: Extreme fire season in California: A glimpse into the future? [in “Explaining Extremes of 2014 from a Climate Perspective”]. *Bull. Amer. Meteor. Soc.*, **96**, S5–S9, <https://doi.org/10.1175/BAMS-D-15-00114.1>.

